

**Volume regulations by Anoctamins, Bestrophin1 and
Transmembrane Channel like proteins**



DISSERTATION ZUR ERLANGUNG DES DOKTORGRADES
DER NATURWISSENSCHAFTEN (DR.RER.NAT.)
DER FAKULTÄT FÜR BIOLOGIE UND VORKLINISCHE MEDIZIN
DER UNIVERSITÄT REGENSBURG

Vorgelegt von
Sirianant Lalida
Aus Nakhon ratchasima, Thailand

im Jahr 2016

**Das Promotionsgesuch wurde eingereicht am:
08-01-2016**

**Die Arbeit wurde angeleitet von:
Prof. Dr. Karl Kunzelmann**

Unterschrift:

SUMMARY

Volume regulation is a basic cellular property, which is required in every living organism. Cells that are subjected to hypo-osmotic shock will start to swell and subsequently will release K^+ and Cl^- through K^+ and Cl^- channels in order to restore their original volume. In 2014, two independent groups identified LRRC8A as a major component of Volume Regulated Anion Channels (VRAC). This thesis provides evidences, that in addition to LRRC8A other chloride channels, namely anoctamins or TMEM16 and bestrophin 1 are involved in volume regulation and offers a putative mechanic model for VRAC activation. Additionally, regarding the high sequence similarity between Anoctamins and TMC (Transmembrane channel like proteins), the role of TMC in volume regulation and Ca^{2+} signaling is investigated.

Patch clamp analysis of ANO6 (Anoctamin 6 or TMEM16F) overexpressing HEK 293 cells shows a two fold increase in swelling activated whole cell currents compared to control cells. These currents are inhibited by a potent inhibitor of VRAC as well as a number of inhibitors of Anoctamins. VRAC activity and RVD (Regulatory Volume Decrease) are strongly reduced when Ca^{2+} is removed and the mechanisms are depending on the activation of ANO6. In fact membrane stretch due to cell swelling activates TRP (Transient Receptor Potential) channels, therefore allowing Ca^{2+} to enter the cells. Simultaneously the intracellular Cl^- concentration is diluted due to water influx and releases ANO6 from Cl^- inhibition. In addition Ca^{2+} entering cells during cell swelling may further activate PLA₂ (phospholipase A₂). This phospholipase cleaves fatty acid from the plasma membrane and the subsequent accumulation of lysophospholipids leads to membrane tension which - together with increased Ca^{2+} levels - activates ANO6 at the junctional zone.

In addition to ANO6, ANO10 (Anoctamin 10 or TMEM16K) also plays a critical role in volume regulation. This function is identified in *Xenopus laevis* oocytes and HEK293 cells. It appears that the expression of ANO10 produces large outwardly rectifying whole cell currents when cells are subjected to hypotonic solution. On the other hands, expression of R263H-ANO10, a coding variant of ANO10, fails to produce swelling-activated whole cell

currents. ANO10 also augments Ca^{2+} signaling in HEK293 overexpressing cells, while Ca^{2+} signaling is reduced when R263H-ANO10 is expressed. These results are in agreement to the localization of ANO10 which we found to be mainly in the endoplasmic reticulum (ER). Therefore we suggest that ANO10 may facilitate volume regulation by changing Ca^{2+} signaling. Since volume regulation is known to be involved in cell migration, the role of ANO10 on macrophage migration and on their phagocytosis activity is investigated. The study shows that both migration and phagocytotic activity are reduced in the absence of ANO10. These results suggest that ANO10 is a new player in the innate immune system, controlling volume regulation and macrophage function.

Bestrophin 1 is known to be a Ca^{2+} activated Cl^- channel in the retinal pigment epithelial cells (RPE). Its role in volume regulation was also investigated. Interestingly, Best1 knock out mice show impairment related to volume regulation such as sperm morphology and motility. A study conducted in RPE cells isolated from patients with an inherited form of macular dystrophy, carrying heterozygous mutations in Best1, shows absence of swelling-activated whole cell currents, while knockdown of LRRC8A (a putative major component of VRAC) in healthy RPE cells does not affect swelling-activated whole cell currents. Therefore Best1 is suggested to be an essential component of VRAC in human RPE cells and mouse sperm.

Since TMC proteins show sequence similarities to anoctamins, we examined their role in volume regulation. However, none of the TMCs can augment swelling-activated whole cell currents. Surprisingly TMC8 largely reduced swelling-activated whole cell currents in overexpressing HEK293 cells. Not only the swelling-activated currents, but also RVD is largely compromised in the presence of TMC8. Ca^{2+} measurements reveal that TMC8 inhibits ATP-induced Ca^{2+} release without affecting Ca^{2+} level in the ER store or SOCE (Store Operated Calcium Entry). Chelation of intracellular Zn^{2+} largely inhibited ATP-induced Ca^{2+} release as well as ATP-activated ANO1 currents. These and further results suggest that upon stimulation with ATP, Zn^{2+} is co-released with Ca^{2+} and further augment Ca^{2+} release from the store. The presence of TMC8 interferes with this process, since it is known that TMC8 interacts with ZnT1-transporter and regulate Zn^{2+} re-uptake into the ER via ZnT-1.

ZUSAMMENFASSUNG

Volumenregulation ist ein grundlegender Mechanismus, der für alle lebenden Organismen notwendig ist. Zellen schwellen unter einem hypo- osmotischen Schock und aktivieren darauf die Freisetzung von K^+ und Cl^- Ionen über die Aktivierung von K^+ - und Cl^- - Kanälen, um das Ausgangsvolumen wieder herzustellen. Im Jahre 2014 wurde von zwei unabhängigen Arbeitsgruppen LRRC8A als Hauptkomponente des Volumen- Regulierten Anionen Canals (VRAC) identifiziert. Die Ergebnisse der vorliegenden Arbeit lassen aber vermuten, dass auch Anoctamine und Bestrophine an der Volumenregulation beteiligt sind. Darüber hinaus konnte für diese Proteine der Mechanismus ihrer zellvolumen-abhängigen Aktivierung geklärt werden. Zusätzlich wurde in dieser Arbeit die Rolle der TMC Proteine (TransMembrane Channel-like family of Proteins), die eine hohe Sequenzähnlichkeit zu den Anoctaminen besitzen, für die Volumenregulation und für die Regulation der intrazellulären Ca^{2+} Konzentration untersucht. Überexpression von ANO6 in HEK293 Zellen induzierte einen zweifachen Anstieg des schwellen- induzierten Ganzzellstroms im Vergleich zur Kontrolle. Dieser induzierte Strom konnte durch Blocker von VRAC und Anoctaminen inhibiert werden. Es konnte ebenfalls gezeigt werden, dass die Aktivität von VRAC und die regulatorische Volumen- Verringerung (RVD) stark reduziert waren, wenn Ca^{2+} aus dem experimentellen System entfernt wurde. Der Mechanismus zur Aktivierung von ANO6 während des Zellschwellens konnte aufgeklärt werden. Durch das Schwellen der Zellen wurden TRP Kanäle aktiviert und es kam zum Einstrom von Ca^{2+} in die Zelle. Gleichzeitig wurde die intrazelluläre Cl^- Konzentration durch den Wassereinstrom verringert und führte zur Enthemmung des Cl^- gehemmten ANO6 Kanals. Durch das Schwellen einströmendes Ca^{2+} aktivierte zusätzlich PLA_2 und damit die Freisetzung von Fettsäuren aus der Plasmamembran und dadurch zur Akkumulation von Lyso- Phospholipiden, wodurch sich die Spannung der Plasmamembran änderte. Das Zusammenspiel von Ca^{2+} und veränderter Membranspannung führte letztlich zur Aktivierung von ANO6 in Mikrodomänen.

Neben ANO6 spielte auch ANO10 eine Rolle für die Volumenregulation. Als erstes wurde die Funktion von ANO10 an der Volumenregulation in Oozyten von *Xenopus laevis* und HEK293 Zellen untersucht. Waren Zellen hypotoner Lösungen ausgesetzt erzeugte die Expression von ANO10 einen starken auswärts gerichteten Ganzzellstrom. Die Mutation von ANO10 R263H-ANO10 induzierte dagegen keinen Schwellen- induzierten Ganzzellstrom. ANO10 verstärkte den intrazelluläre Ca^{2+}

Signalweg in HEK293 Zellen. Dieser verstärkte Ca^{2+} Signalweg war in R263H-ANO10 überexprimierten Zellen reduziert. Diese Ergebnisse wurden durch die intrazelluläre Lokalisation von ANO10 im ER unterstützt. ANO10 könnte die Volumenregulation über die Verstärkung des intrazellulären Ca^{2+} Signalwegs begünstigen. Da die Regulation des Zellvolumens für die Migration und Phagozytose bei Makrophagen wichtig sein könnte, untersuchten wir den Einfluss von ANO10 auf diese Eigenschaften. Tatsächlich waren die Migrationsrate und die Aktivität der Phagozytose von Makrophagen in der Abwesenheit von ANO10 vermindert. Zusammenfassend zeigten diese Ergebnisse, dass ANO10 die Immunabwehr über eine verbesserte Volumenregulation von Makrophagen unterstützen konnte.

Die vorliegende Arbeit zeigt auch, dass Bestrophin 1 (Best1) an der Volumenregulation beteiligt sein kann. Best1 defiziente Mäuse zeigten eine abnormale Morphologie der Spermien. Zusätzlich war die Motilität der Spermien eingeschränkt, was auf eine fehlende Volumenregulation zurückzuführen war. Untersuchungen an induzierten hiRPE Stammzellen (RPE: Retinales Pigmentepithel) von Patienten mit Makuladegeneration und mutiertem pathologischem Best1 zeigten keinen Schwellen- induzierten Ganzzellstrom. In hiRPE Zellen von gesunden Patienten wurde der Schwellen- induzierte Ganzzellstrom durch das Fehlen von LRRC8A nicht beeinflusst. Daher war zu vermuten, dass Best1 eine wichtige Komponente des VRACs in humanem RPE und in Spermien der Maus ist.

Da TMC Proteine den Anoctaminen sehr ähnlich sind, wurde ihre Rolle für die Volumenregulation untersucht. Dabei wurde gefunden, dass kein Mitglied der TMCs den Schwellen- induzierten Ganzzellstrom verstärken kann. Überraschenderweise reduzierte TMC8 den Schwellen- induzierten Ganzzellstrom in TMC8 exprimierenden HEK293 Zellen. Nicht nur der Ganzzellstrom, sondern auch der RVD war stark beeinträchtigt. Messungen der intrazellulären Ca^{2+} Konzentration zeigten, dass TMC8 die ATP induzierte Speicherentleerung hemmte, aber weder die Ca^{2+} Konzentration im ER noch den store operated calcium entry veränderte. Wir konnten zusätzlich zeigen, dass auch Zn^{2+} die ATP induzierte Speicherentleerung und die Aktivierung von ANO1 hemmt. Wir vermuten, dass Zn^{2+} für eine verstärkte Freilassung von Ca^{2+} aus dem ER-Speicher notwendig ist. Es ist bekannt, dass TMC8 mit dem Zn^{2+} Transporter ZnT1 interagiert und somit die Zn^{2+} Aufnahme ins ER regulieren kann.

CONTENTS

SUMMARY.....	i
ZUSAMMENFASSUNG.....	iii
CONTENTS.....	v
CHAPTER 1 Introduction.....	1
CHAPTER 2 Cellular Volume Regulation by Anoctamin 6: Ca ²⁺ , Phospholipase A2 and osmosensing.....	17
CHAPTER 3 A coding variant of <i>ANO10</i> , affecting volume regulation of macrophages, is associated with <i>Borrelia</i> seropositivity.....	40
CHAPTER 4 Bestrophin 1 is indispensable for volume regulation in human retinal pigment epithelium cells.....	68
CHAPTER 5 TMC8 (EVER2) attenuates intracellular signaling by Zn ²⁺ and Ca ²⁺ and suppresses activation of Cl ⁻ activation.....	112
CHAPTER 6 Discussion.....	126
CONCLUDING REMARKS.....	134
REFERENCE.....	135
ACKNOWLEDGEMENTS.....	155
ERKLÄRUNGEN.....	156
CURRICULUM VITAE.....	157

CHAPTER 1

Introduction

Ion channels

The cell membrane is composed of a phospholipid bilayer, which does not allow ions and any membrane-impermeable substances to pass through. Therefore, transmembrane proteins such as transporters, pumps or ion channels are necessary to serve as a pathway for ions, water or large molecules to move across the cell membrane. An ion channel is a plasma membrane protein, which is located in all cell types and in many cellular organelles. It allows ions to pass through the lipid bilayer according to their electrochemical gradients. The ionic flow across the cell membrane can be triggered by various environmental stimuli such as voltage, ligand concentration, membrane tension, temperature.

Ion channels are categorized by their selectivity, some ion channels can be very selective that they only allow specific ions to pass through. In addition, the range of their single channel conductance, which is in the range of pico-Siemens (pS), can also be used to categorize ion channels. For example, some channels have conductance around 1 or 2 pS, while some may have conductance up to 100 pS. Lastly, ion channels can also be categorized by the mechanism of open and close state or “gating”.

Volume regulation

Volume regulation is an essential property of any living cell. Under physiological condition, the extracellular osmolarity is kept at around 280 mosmol/kg H₂O. However in some circumstances the extracellular osmolarity can be disturbed; for example, the intake of hypotonic drinks or water can change the extracellular osmolarity of intestinal epithelial cells and intestinal capillaries. Besides this, changes of the transepithelial transport activity that is controlled by hormones and mediators or accumulation of nutrients or metabolic products inside the cells can also change the intracellular osmolarity. In addition, in some pathological condition, cell volume can change due to the gradual activation of cell volume regulation processes (1). For example, under hypoxic condition, the Na⁺-K⁺-Cl⁻ cotransporter activity of

the blood-brain barrier cells is increased resulting in a higher uptake of Na^+ which leads to a slow increase in the cell volume (2). It is well known that not only when the cells encounter an osmotic change, this stimulates the volume regulation, but also other physiological processes such as cell proliferation, cell growth, cell migration, as well as the apoptotic process (1;3;4).

When cells undergo a dramatic change of the extra- or intracellular osmolarity, it can lead to cell swelling or cell shrinkage. These processes will be counteracted by the activation of ion channels or transporters which are the most effective way to regulate cell volume. For example during cell swelling K^+ channels and Volume Regulated Anion Channels (VRAC) are activated releasing KCl out of the cells. The release of these ions leads water to passively move across the cell membrane, allowing the cells to recover to their original volume. The process in which cells decrease their volume after swelling is called Regulatory Volume Decrease or RVD (Fig.1). Although other transport mechanisms are also involved in RVD (such as KCl cotransporter), the primary mechanism of RVD is the coordinated function of K^+ and Cl^- channels (5). On the contrary, in the Regulatory Volume Increase (RVI) process during cell shrinkage, the primary recovery mechanisms rely on the activation of $\text{Na}^+ - \text{K}^+ - 2\text{Cl}^-$ cotransporter, Na^+/H^+ exchanger and non-selective cation channels. Even though the loss or gain of ions is regarded as a powerful tool to regulate cell volume, there are limitations to this mechanism. Infact changes of the intracellular ions concentration can disturb the cell functions. Therefore, besides the ion movement, the movement of organic osmolytes is also necessary.

The mechanism of volume regulation has been clearly shown to be mainly dependent on ion movements through ion channels or transporter, but how do cells sense their changing of volume is still unclear. The term “osmosensor” is used to describe proteins which switch on and off according to the changing of the extra- and intracellular osmolarity. There are several studies showing that an osmosensor is able to detect 1.) Macromolecular crowding, which is an event where macromolecules such as proteins or nucleic acids are accumulated intracellularly thus changing the water content inside the cells (6) 2.) Mechanical changing of

membrane lipid bilayers or changing of cell size, which is monitored by the cytoskeleton (7) 3.) Changing of the cellular concentration of certain ions such as Cl^- (8;9). And 4.) a number of second messenger that are upregulated during the volume regulation response such as Ca^{2+} (10).

It has been reported that several types of K^+ channels are involved in volume regulation; for example, BK, IK, SK channels which possess respectively big, intermediate, and small K^+ conductance. In addition, a group of voltage-gated K^+ (Kv) channels, inwardly rectifying K^+ (Kir) channels as well as non-selective cation channels can be activated to regulate cell volume (11). Due to the abundant expression and higher basal conductance of K^+ than Cl^- therefore, swelling-activated anion, particularly, Cl^- conductance seems to play a major role in the RVD process (4). However, the molecular identity of the volume regulated anion channel (VRAC) is still in controversy.

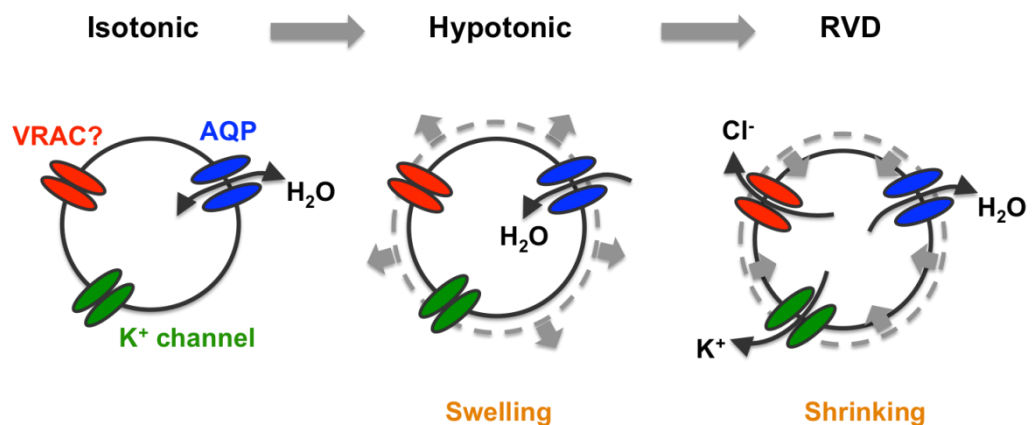


Fig 1. Regulatory Volume Decrease (RVD)

Volume regulated anion channel (VRAC)

The main characteristics of VRAC include outward rectification, time-dependency of the channel that shows inactivation by the time at positive voltage and type I Eisenmann permeability sequence $\text{I}^- > \text{Br}^- > \text{Cl}^- > \text{F}^-$ (4). Anoctamins (ANOs) is one of the protein families which are proposed as VRAC because the silencing of ANO1, ANO6, ANO8, and ANO9 in HEK293 cells showed a reduction in the swelling-activated whole cell current and also RVD (12). However some of their biophysical properties do not match with that of VRAC. In 2014, two independent groups provided strong evidences proving that LRRC8A/SWELL1 is a

major component of VRAC (13;14). However a study in RPE cells, which show a very low endogenous LRRC8A expression but a strong expression of Bestrophin1 (Best1), shows nicely swelling-activated whole cell currents. Therefore, besides LRRC8A, Best1 is also essential for volume regulation (15).

Even though a lot of effort was put into identifying the true molecular identity of VRAC, not much is known regarding its mechanism of action or activation. The role of Ca^{2+} on VRAC is intensively discussed. In 1995, Verdon B. *et al.* found that cell swelling causes Ca^{2+} influx into the cells. This is in agreement with the work from Christensen O. back in 1987, which suggested that membrane stretch during cell swelling is resulting in Ca^{2+} influx through stretch-activated channels, which were later identified as TRP channels. It was speculated that during cell swelling the Ca^{2+} influx through the TRP channels could activate swelling-activated Cl^- channel (1;10;16;17). In addition to Ca^{2+} influx, Ca^{2+} release from the ER store was also observed during cell swelling. This phenomenon was suggested to occur through autocrine release of ATP and purinergic receptor activation. The increase of the membrane fluidity by the increase of non-saturated fatty acid in the plasma membrane was also found to contribute to the activation of VRAC. Moreover, the process of hydrolyzation of phospholipids by PLA_2 , which leads to accumulation of lyso-phospholipids in the plasma membrane and the release of arachidonic acid (ArA) into the cytosol, was also known to influence the activity of VRAC (1).

Leucine-rich repeat-containing 8A (LRRC8A)

Leucine-rich repeat-containing 8 (LRRC8) proteins consist of around 800 amino acids, four transmembrane domains and a domain containing up to 17 leucine-rich repeats at the C-terminus (Fig. 2) (18). It has been shown that the leucine-rich repeat domain (LRRD) is involved in protein-protein interactions (19). LRRC8 comprises 5 paralogs, namely LRRC8A, LRRC8B, LRRC8C, LRRC8D, and LRRC8E. LRRC8A and D are abundantly expressed, while LRRC8B and LRRC8C are quite specific to the nervous and immune system respectively. LRRC8E is not strongly expressed under physiological conditions but seems to be upregulated in some tumors (18).

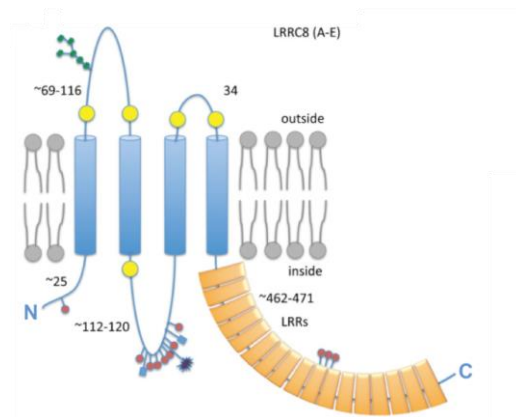


Fig 2. Proposed membrane topology of LRRC8 proteins. The conserved Cysteines are indicated at yellow circle. The orange boxes indicate leucine-rich repeats domain (LRRD). (Reprinted from “LRRC8 proteins share a common ancestor with pannexins, and may form hexameric channels involved in cell-cell communications” by Abascal F. Zardoya, R., 2012, *Bioassay*, 34, 551-560) (18)

In 2014, Qui *et al.* and Voss *et al.* identified an essential component of the VRAC by using a genome-wide small interfering RNA screen in mammalian cell lines. They made use of iodide sensitive yellow fluorescence protein (YFP) to show that only siRNA against LRRC8A could completely abolish the hypotonic-induced fluorescence quenching by iodide influx. Patch clamp experiments confirmed the elimination of swelling-activated currents when LRRC8A was knocked down in HEK293, HELA, and T lymphocyte (13;14). In addition immunocytochemistry analysis performed in HEK293 cells show a clear membrane localization of LRRC8A. Qui *et al.* (13) and Voss *et al.* (14) also studied other members of this protein family including LRRC8B-E, and found that the knock down of each of these proteins do not have effect on the swelling-activated whole cell currents (14).

Even though the results obtained from siRNA strongly prove that LRRC8A is a VRAC, the overexpression of LRRC8A alone in HEK293 and HELA cells did not increase swelling-activated whole cell currents but was rather inhibitory when compared to control cells. Taken together their results indicate that LRRC8A alone is not the VRAC; instead it seems to be an essential component of protein complex (13;14).

Anoctamins

Anoctamins (ANOs or TMEM16) form a protein family consisting of 10 members, ANO1-ANO10. Anoctamins comprise of 750-1000 amino acids with intracellular NH₂- and COOH terminus. In the beginning, anoctamins were believed to have eight transmembrane domains, and a study of a point mutation in the ANO1 sequence at the conserved region between TM5 and TM6, showed a significant reduction of the anion permeability suggesting that this is the pore forming region of anoctamins (20). However a recent study in nhTMEM, a homolog of the anoctamins protein family isolated from fungus *Nectria haematococca*, shows that anoctamins contain ten transmembrane domains and operates as a dimer with two lateral pore-like structure. The investigation in nhTMEM revealed that the binding site of Ca²⁺ is apparently buried in the hydrophobic segment close to the channel cavity (Fig. 3) (21).

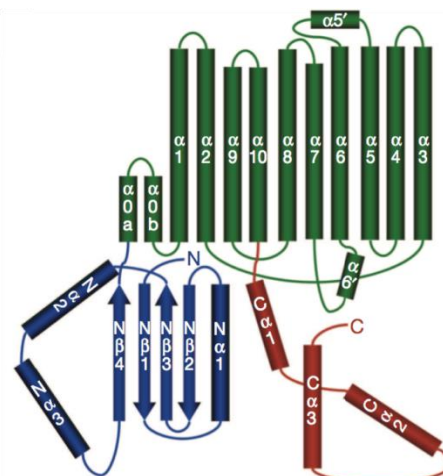


Fig 3. Topology of nhTMEM. The transmembrane domains are colored in green. N-terminal domains are in blue and the C-terminal domains are in red (Reprinted from “X-ray structure of a calcium-activated TMEM16 lipid scramblase.” by Brunner, J. D., Lim, N. K., Schenck, S., Duerst, A., Dutzler, R., 2014, *Nature*. 516, 207-212) (21)

In 2008, three independent groups used different methods to identify ANO1 as a Calcium-Activated Chloride Channel (CaCC), a channel whose physiological function has been known for decades (20;22;23). The typical characteristics of CaCC include 1.) outward rectification in current-voltage relationship with time-dependent activation 2.) activation by the increase of intracellular Ca²⁺ and 3.) type I Eisenmann permeability sequence I⁻ > Br⁻ > Cl⁻ > F⁻. In addition to ANO1, also ANO2, mostly expressed in neurons, has been found to

generate currents resembling to that of CaCC. It was shown that ANO2 is a cilia CaCC and plays a major role in olfactory signal transduction. (24-26). In 2009, Almaca *et al.* shows that knock down of ANO1 results in a large reduction of the swelling-activated whole cell currents in CFPAC, HT29, and HEK293 cells. Regulatory volume decrease (RVD) in siANO1 treated HEK293 cells was also reduced. Furthermore, electrophysiological studies also showed that swelling-activated whole cell currents were abolished in submandibular acinar cells isolated from ANO1 KO mice. Therefore, these results represent the function of ANO1 in producing volume-regulated chloride currents. ANO1 also supports Ca^{2+} activated Cl^- secretion in mouse ileum and large intestine where it is preferentially expressed (12;27).

Even though the knowledge about ANO1 and ANO2 is improving through the years, not much is known about ANO3. It has been reported that mutation of ANO3 causes autosomal dominant Craniocervical Dystonia. Calcium measurements show that ATP-induced calcium signaling in fibroblasts isolated from patients carrying a point mutation for ANO3 (W490C) is reduced when compared to control fibroblast. Nonetheless, how does mutation of ANO3 reduce calcium signaling and how does it relate to Craniocervical Dystonia need to be further investigated (28).

ANO4 has been shown to generate ATP and ionomycin-induced currents in heterologous expression systems with lower amplitude than that of ANO1 (29). Recently, ANO4 has been found to be upregulated in patients with aldosterone adenomas and pheochromocytoma, and that overexpression of ANO4 in H2965R cells leads to the increase of aldosterone secretion (30). However these data are not yet conclusive, therefore the physiological and pathological roles of ANO4 are still imprecise.

ANO5 is abundantly expressed in skeletal muscle, cardiac muscle, and bones. A recessive mutation of ANO5 has been reported to cause muscle dystrophy with the phenotype of limb-girdle muscular dystrophy 2L (LGMD2L) (31). Several groups have investigated the function of ANO5 as CaCC by using whole cell patch clamp in heterologous expression systems. Yuemin *et al.* found that 10 μM ATP are not sufficient to activate ANO5 as well as a studied by Ta To Tran *et al.*, who shows no-activation of ANO5 with 500 nM of free Ca^{2+} in

the patch pipette. However the use of ionomycin, a Ca^{2+} ionophore, clearly shows the activation of ANO5. Since ionomycin can increase the intracellular Ca^{2+} to levels beyond 100 μM , which is more than that of the ATP induced Ca^{2+} release from the ER store; the authors suggested that ANO5 requires higher concentrations of Ca^{2+} to be activated (29;32).

In addition to ANO1 and ANO2, ANO6 is another protein of this family that was gaining attention through the years. ANO6 is abundantly expressed in various tissues such as intestinal, colonic, pancreatic, salivary gland, airways submucosal glands and kidney (33). Several groups have studied the function of ANO6 as ion channel. In 2011, Martin *et al.* found that the suppression of ANO6 in Jurkat cells with siRNA led to a reduced activation of outwardly rectifying whole cell Cl^- currents by Fas ligand (FasL), a known activator of outwardly rectifying Cl^- channel (ORCC). Another known activator of ORCC, staurosporine (STS) also failed to stimulate ORCC currents in Jurkat cells with stable ANO6 suppression. They also show that the activation of ORCC by STS can be recovered by overexpression of ANO6 in these cells. Moreover, a point mutation at the putative pore region can cause a shift in the halide permeability suggesting the role of ANO6 in conducting anions. Taking these observations together, the authors conclude that ANO6 is a major component of ORCC (34).

Heterologous expression of ANO6 could generate Ca^{2+} activated Cl^- currents with lower amplitude than those generated by the CaCC-ANO1. Electrophysiological studies show that the Ca^{2+} activated outwardly rectifying current was completely abolished in megakaryocytes isolated from ANO6 KO mice (35). However the Ca^{2+} concentration required for ANO6 activation is much higher than that for ANO1 and ANO2 (29;36). Whole cell patch clamp studies by varying Ca^{2+} concentration in patch pipette from Kunzelmann's group revealed that ANO6 could generate whole cell currents only when intracellular free Ca^{2+} reached at least 10 μM . Furthermore, they found that the removal of intracellular K^+ and extracellular Na^+ resulted in a large reduction of the whole cell currents in ANO6 overexpressing HEK293 cells thus indicating the cation conductivity through ANO6. Moreover Yang H. *et al.* conducted experiments to measure the reverse potential of ANO6 under bi-ionic conditions in a heterologous system, founding that ANO6 is highly permeable

to Ca^{2+} and moderately permeable to other monovalent cations such as Li^+ , Rb^+ , K^+ , and Cs^+ (29;35). Taking together, ANO6 seems to be a Ca^{2+} activated non-selective ion channels rather than a CaCC.

ANO6 has been reported to be involved with swelling-activated Cl^- currents. Suppression of ANO6 by siRNA in HEK293 cells results in a large decrease of swelling-activated Cl^- currents. Moreover, regulatory volume decrease measured with calcein fluorescence shows an augmentation of RVD in ANO6-overexpressing HEK293 cells (12;33). However, a study by Juul C. A. *et al.* found that exogenous expression of ANO6 in EATC cells do not enhance swelling-activated Cl^- currents (37). Due to these controversial results; the role of ANO6 and its mechanism on volume regulation needed to be further investigated.

Besides the ion transport activity ANO6 is found to be a Ca^{2+} dependent phospholipid scramblase (Fig. 4). A phospholipid scramblase is a protein responsible for translocating phosphatidylserine from the inner to the outer leaflet of plasma membrane. Under physiological condition, the plasma membrane shows asymmetrical distribution of phospholipids. Phosphatidylserine (PS) and phosphatidylethanolamine (PE) can be found in the inner leaflet of the plasma membrane, while phosphatidylcholine (PC) and sphingomyelin (Sph) are dominant on outer leaflet of the plasma membrane. PS exposure is a prerequisite for several physiological processes such as blood coagulation and apoptosis (38). A mutation of ANO6 results in a defective Ca^{2+} -induced phospholipid scrambling in Scott syndrome, a rare bleeding disorder. In 2010, Suzuki *et al.* (39) generated a cell line with overactivated phospholipid scramblase activity and identified the genes which are responsible for this activity. ANO6 with D409G mutation was strongly expressed and constitutively induced phosphatidylserine exposure in these cells. In addition, increase of intracellular Ca^{2+} by A23187, a Ca^{2+} ionophore, resulted in phosphatidylserine exposure in wild-type ANO6 expressing cell line. Furthermore, an analysis of the DNA sequence from platelets and other blood cells isolated from Scott syndrome patients and their parents showed that 226 bp corresponding to the exon 13 of ANO6 are missing in Scott syndrome patients, causing a frameshift mutation, thus resulting in premature termination of the protein (39). ANO6 KO

mice show a prolonged bleeding due to lack of PS exposure, which is a prerequisite for the blood coagulation cascades. Taken together, these results suggest that ANO6 is not only an ion channel but also a phospholipid scramblase (35).

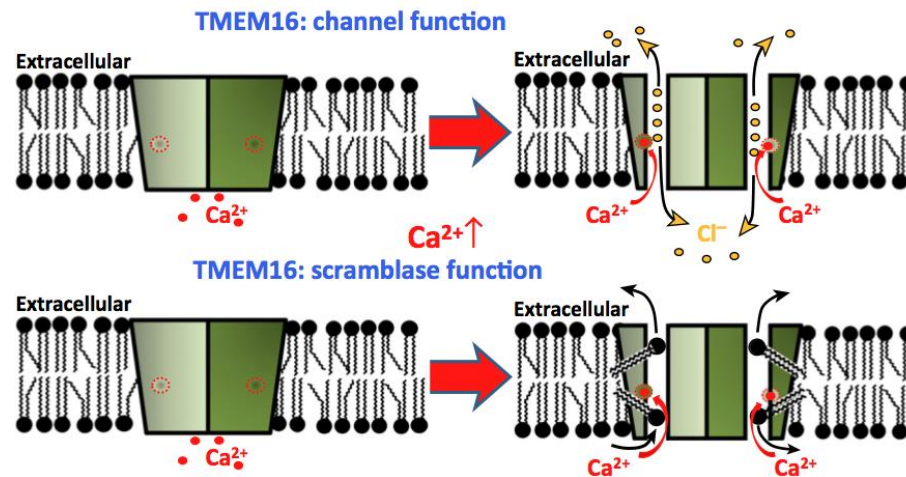


Fig 4. Phospholipids and ion transport through Anoctamins (40). The study in fungal homolog nhTMEM16 suggests a dimer with two lateral pores. These pores may provide two different functions; scramblase function and channel function. (Reprinted from “TMEM16, LRRC8A, bestrophin: chloride channels controlled by Ca^{2+} and cell volume” by Kunzelmann K., 2015, *Trends Biochem.Sci.* 40, 535-543)

ANO7, also known as NGEF, is a prostate specific plasma membrane protein. ANO7 is expressed in two different variants, which encode for two different sizes of the protein. The short form of ANO7 consists of 179 amino acids and localizes in the cytoplasm, while the long form of ANO7 consists of around 900 amino acids and localizes at the plasma membrane. A study in LNCaP cells shows that suppression of the long form of ANO7 interfere with cell aggregations, and ANO7 was found to be highly expressed at the regions where cells are in contact to each other. Therefore, the author suggested that ANO7 might be involved in cell-dependent contact interaction in prostate gland epithelial cells. ANO7 was shown to be able to generate Ca^{2+} - activated Cl^- currents in whole cell patch clamp experiments when co-expressed with P2Y_2 in HEK293 cells. However, ANO7 generated currents were of much smaller amplitude than those of ANO1 (41-44).

ANO8 and ANO9, are found in almost every tissue. Immunocytochemistry in HEK293 overexpressing cells shows a weak localization of these proteins at the plasma membrane. In addition, whole cell patch clamp studies displayed that ANO8 and ANO9 could

generate only small Ca^{2+} -activated Cl^- currents with a much more delayed activation when compared to ANO1 currents. On the other hand, ANO9 was found to inhibit ATP-induced ANO1 whole cell currents when they were coexpressed in HEK293 cells (29). Recent studies in colorectal cancer with metastasis derived cell line such as LoVo, Colo205, and SW620, found a reduction of ANO9 mRNA level. Further studies by exogenous expression of ANO9 into colorectal cancer cell lines revealed the reduction of cells growth and cells invasion. In addition exogenous ANO9 helps to promote the cells to go into apoptosis. The authors suggested that ANO9 is playing a role in tumor suppression but the mechanisms underlying this role need to be further investigated (45).

The last member of the anoctamins protein family is ANO10. Similar to ANO8 and ANO9, ANO10 is poorly expressed at the plasma membrane and gives only a small and delayed Ca^{2+} -activated Cl^- current in whole cell patch clamp experiments with overexpressing cells. ANO10 can be found in various tissues but it is highly expressed in the brain, particularly in frontal cortex, occipital cortex, and cerebellum (29;33;46). In 2010, a mutation of ANO10 was found to be the cause for the autosomal-recessive cerebellar ataxia, which is a rare neurodegenerative disorder and also involve coenzyme Q_{10} deficiency (46;47). Recently, a study in conditional ANO10 KO mice found the impairment of Ca^{2+} -induced Cl^- secretion in jejunum where ANO10 is highly expressed in wild type mice. But the mechanistic study on how ANO10 facilitates Ca^{2+} -induced Cl^- secretion is still required.

Bestrophin 1

Bestrophin1 (Best1) belongs to the bestrophin family, and consists of around 600 amino acids. A study from *Klebsiella pneumoniae* bestrophin or KpBest, which is a homolog of the human bestrophin (hBest) shows that Best consists of 4 transmembrane helices with the N- and C- terminal residues within the cytoplasm, and with five intracellular helices linked between TM2 and TM5. (Fig. 5) Moreover KpBest forms a stable pentamer, whose center provides an ion conduction pathway (48).

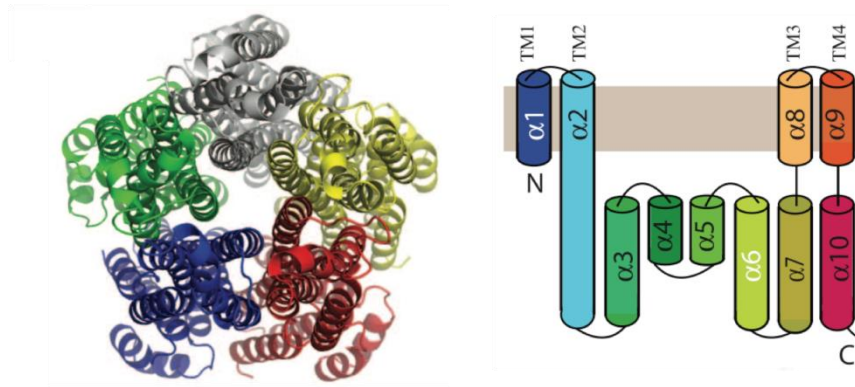


Fig 5. The left panel shows a ribbon diagram of KpBest pentamer (as view from the outside of the membrane). The right panel is a 2D topology of KpBest. The N-terminal segment is colored in blue and the C-terminal segment is colored in red. (Reprinted from “Structure and selectivity in bestrophin ion channels” by Yang, T., Liu, Q., Kloss, B., Bruni, R., Kalathur, R. C., Guo, Y., Kloppmann, E., Rost, B., Colecraft, H. M., Hendrickson, W. A., 2014, *Science*. 346, 355-359) (48)

There are four members in the family: Best1, Best2, Best3, and Best4. Many groups described Best1 as a Ca^{2+} -activated Cl^- channel in the eyes since it is highly expressed on basolateral site of retinal pigment epithelial (RPE) cells (49-53). Heterozygous mutation of Best1 results in a series of eye degenerative disorders such as Best Vitelliform Macular Dystrophy (VMD). The characteristics of VMD include the accumulation of lipofuscin within the RPE cells and the reduction of light-peak response when measured in electrooculogram (EOG). Several studies suggested that the light-peak response in human is associated with Cl^- conductance across the basolateral membrane of RPE cells. Whole cell patch clamp analysis with submicromolar free Ca^{2+} in the patch pipette revealed that overexpression of hBest1 mutant, which is responsible for VMD, results in a large reduction of whole cell basal currents when compared to wild type hBest overexpressing HEK293 cells (50;54). In addition, suppression of Best1 expression in HT29 cells using siRNA largely abolished Ca^{2+} -activated Cl^- currents (55). Along this line, mutagenesis of bestrophin shows a change in the channel gating and also in the sensitivity to DIDS, a Cl^- channel blocker (56). These findings suggested a role of Best1 as a chloride channel or a major component of it. As a result, it was proposed that defect of Best1 leads to a reduction of the light-peak response in VMD patients due to a lack of Cl^- transport across cell membrane. However RPE cells isolated from Best1 KO mice, do not show an alteration in the Ca^{2+} -activated Cl^- currents (57). In addition, it was

show that Best1 is expressed in the endoplasmic reticulum (ER) and it colocalizes with STIM1 (58). STIM1 or stromal interaction molecule 1 is a Ca^{2+} sensor protein that is able to tether the ER membrane to the plasma membrane (59;60). Best1 was shown to regulate intracellular Ca^{2+} signaling. Exogenous expression of Best1 in HEK293 cells induced augmentation of ATP-induced Ca^{2+} release from the ER. On the other hand, exogenous expression of Best1-R218C, a mutated form of Best1 found in VMD patients where expression of Best1 is normal, but its function as a Cl^- channel is impaired, largely reduced ATP-induced Ca^{2+} release. This result was also observed in siBest1 treated HEK293 cells. Since Best1 was found colocalized with Stim1, a role of Best1 on store-operated Ca^{2+} entry (SOCE) was investigated as well. In siBest1 treated porcine RPE cells, SOCE amplitude was significantly reduced when compared to non-treated or siScramble treated cells. Moreover, the alteration of Ca^{2+} signaling by Best1 results in a change of the Ca^{2+} dependent Cl^- channels activity. Activation of Best1 by Pak2 phosphorylation leads to a significant increase of ANO1 whole cell currents in HEK293 cells. These results suggested that Best1 is essential for Ca^{2+} handling in the ER and may relate to VMD not only by providing Cl^- transport across the basolateral membrane, but also acting as a counterion channel for Ca^{2+} release at the ER membrane (58;61).

Transmembrane Channel like proteins (TMC)

TMC or Transmembrane Channel like proteins belong to the TMC superfamily. In mammals, eight members of TMCs are identified as TMC1-TMC8. There is no clear function and structure of these proteins yet. However, it has been shown that TMC1 and TMC2 are required for mechanoelectrical transduction (MET) in the inner ear hair cells (62;63). Mutations of TMC1 were identified as a cause for dominant and recessive deafness in human (64). In 2009, Yoonsoon Hahn *et al.* studied the entire spectrum of anoctamins and TMCs sequences and found that TMC proteins have a sequence that is very similar to that of the anoctamins protein family; particularly where the regions of the transmembrane domains are located. It was predicted to have eight transmembrane domains similar to what it was predicted for the anoctamins topology (65). However and epitope tagged study in

heterologous expression systems predicts TMC1 to have six transmembrane domains with three extracellular loops and one large intracellular loop between TM4 and TM5 (Fig.6). Within the large intracellular loop there are two highly conserved domains among all TMC members known as TMC domains. The localization of TMC1 was shown to be intracellular and colocalized with ER proteins. However, the author stated that the ER localization of TMC1 might be due to the lack of specific membrane-localized or hair cell chaperones (66). Since TMC proteins share a similar sequence with anoctamins the question was raised whether TMCs can function as an ion channel.

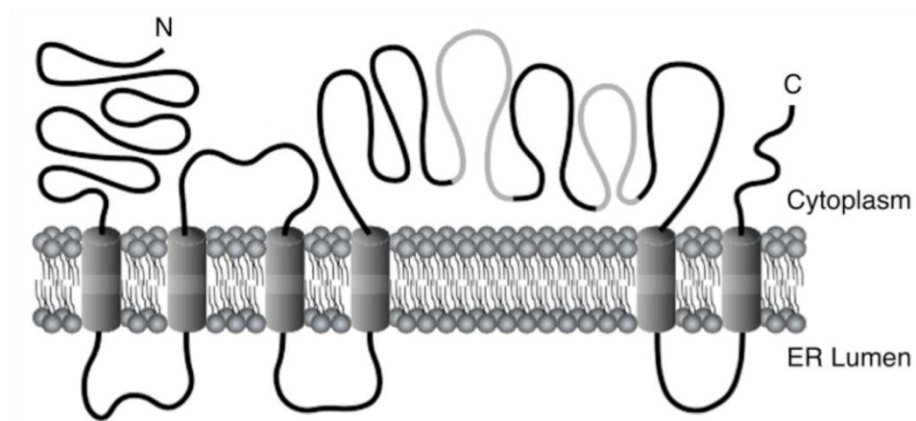


Fig 6. Topology of TMC1 (Reprinted from “Topology of transmembrane channel-like gene 1 protein” by Labay, V., Weichert, R. M., Makishima, T., Griffith, A. J., 2010, *Biochemistry*. 49, 8592-8598) (66)

A recent study from Kurima *et al.* revealed that TMC1 and TMC2 are located at the tip of stereocilia where the MET channel complex is localized (63). Expression of a mutant TMC1 in mice lacking wild type TMC1 and TMC2, which show a phenotype of defect in MET, results in a reduction of single channel MET currents and also Ca^{2+} permeability when compared to wild type mice. In addition exogenous expression of either TMC1 or TMC2 into TMC1 and TMC2 null mice could restore the MET in these mice. These data suggest the possibility of TMC1 and TMC2 as a component of MET channel complex, whether they are pore-forming channel or regulatory proteins of MET channel need to be further investigated (62;67).

Not only mutations in TMC1 cause a pathophysiology, but also mutation in TMC6 and TMC8. In fact it was reported that mutations of TMC6 and TMC8 led to a higher

susceptibility to human Papillomaviruses infection. TMC6 and TMC8, known as EVER1 and EVER2 respectively, were shown to interact with zinc transporter 1 (ZnT-1). ZnT-1 is found to be located on both plasma and ER membranes, it tightly regulates intracellular Zn^{2+} level by driving the efflux of Zn^{2+} through the plasma membrane localized ZnT-1 and reuptake of Zn^{2+} via the ER membrane localized ZnT-1. The role of TMC6/8 and ZnT-1 complex was investigated and it was found that the TMC6/8-ZnT-1 complex did not act as Zn^{2+} effluxer, but rather as a facilitator for Zn^{2+} reuptake into the ER (68). It is known that some of the HPV proteins contain Zn^{2+} binding site, and Zn^{2+} also function as a transcription factor for certain viral genes. Therefore the leakage of free Zn^{2+} from the ER and possibly into viral nucleus, due to the mutations of TMC6 or TMC8, can lead to high susceptibility to HPV infections (69). HPV infection was known to be associated with head and neck cancer, where upregulation of ANO1 was also observed. However the relationship between anoctamins and TMCs is not much investigated as well as their function as an ion channel.

Intention and outline of the present thesis

As mentioned above, volume regulation is an essential property of every living cell. This process requires the massive activation of K^+ and Cl^- channels to lower the ion concentration and to reduce cell volume, particularly during regulatory volume decrease. The macromolecular complex of VRAC and the molecular mechanism of its activation are still under debate. Although LRRC8A was identified as the essential component of VRAC, it is surprising that patients who carry mutations in LRRC8A survive and only show agammaglobulinemia, an immune disorder. Moreover LRRC8A^{-/-} mice present a relatively mild pathology (4), thus LRRC8A may not be the only transport protein that plays a role in volume regulation. The proteins mentioned above including anoctamins, bestrophin, and TMCs, were also shown to function as ion channels. Therefore, the present study is aimed to investigate the function and mechanism of action of these proteins in volume regulation. The studies in various cell types and *Xenopus laevis* oocyte in chapter 2 and 3 show that ANO6 and ANO10 augment swelling-activated whole cell currents. A coding variant of ANO10 is identified as the cause of different susceptibility to *Borrelia* seropositivity. Since macrophages

are known to have a crucial function in destroying *Borrelia*, therefore the role of ANO10 and volume regulation on macrophages function is also investigated. Given that the molecular mechanism of VRAC regulation is not much known, we, therefore examine the mechanism of ANO6 activation, since it is identified as VRAC in this thesis. Given that PLA₂ is involved in VRAC activation (1), therefore the role of PLA₂ on ANO6 activation is investigated. In addition, the significance of Ca²⁺ in VRAC activation and RVD is explored. Chapter 4 reveals that swelling-activated whole cell currents in hiRPE cells isolated from macular dystrophy patients with heterozygous Best1 mutation, +/A243V and +/Q238R, are largely reduced when compared to wild type cells. Therefore the role of Best1 in volume regulation is further investigated in *Xenopus laevis* oocytes. Best1-deficient mice do not show any defect in RPE cells, instead the sperm morphology is abnormal. Hence the role of Best1 and volume regulation in sperm function is investigated. Because TMCs have similar sequence to that of anoctamins, the role of TMCs on volume regulation and Ca²⁺ signaling is explored in chapter 5.

CHAPTER 2

Cellular Volume Regulation by Anoctamin 6: Ca²⁺, Phospholipase A2 and osmosensing

Abstract

During cell swelling, Cl⁻ channels are activated to lower intracellular Cl⁻ concentrations and to reduce cell volume, a process termed regulatory volume decrease (RVD). We show that anoctamin 6 (ANO6; TMEM16F) produces volume regulated anion currents and controls cell volume in 4 unrelated cell types. Volume regulation is compromised in freshly isolated intestinal epithelial cells from *Ano6*^{-/-} mice and also in lymphocytes from a patient lacking expression of ANO6. Ca²⁺ influx is activated and thus ANO6 is stimulated during cell swelling by local Ca²⁺ increase probably in functional nanodomains near the plasma membrane. This leads to stimulation of phospholipase A₂ (PLA₂) and generation of plasma membrane lysophospholipids, which activates ANO6. Direct application of lysophospholipids also activates an anion current that is inhibited by typical ANO6 blocker. An increase in intracellular Ca²⁺ supports activation of ANO6, but is not required when PLA₂ is fully activated, while re-addition of arachidonic acid completely blocked ANO6. Moreover, ANO6 is activated by low intracellular Cl⁻ concentrations and may therefore operate as a cellular osmosensor. High intracellular Cl⁻ concentration inhibits ANO6 and activation by PLA₂. Taken together, ANO6 supports volume regulation and volume activation of anion currents by action as a Cl⁻ channel or by scrambling membrane phospholipids. Thereby it may support the function of LRRC8 proteins.

Keywords: : Anoctamin 6; Apoptosis; RVD; Regulatory volume decrease; TMEM16F; VRAC; Volume regulation; Volume-regulated anion channel

Published in: Lalida Sirianant, Jiraporn Ousingsawat, Podchanart Wanitchakool, Rainer Schreiber and Karl Kunzelmann Cellular volume regulation by anoctamin 6: Ca²⁺, phospholipaseA2 and osmosensing. *Pflugers Arch.* 2015 October 6.

Own experimental contribution: All patch clamping experiments.

Own written contribution: Methods, Results, Parts of Introduction and Discussion.

Other contributions: Designed experiments and analyzed data.

Introduction

Volume regulation is an intrinsic property of any living cell. Cell swelling due to increase in intracellular osmolytes or by decrease in extracellular osmolarity is counteracted by volume regulated ion channels, releasing KCl to the extracellular space (1). Volume regulated anion channels (VRAC) have been studied and reviewed extensively, but the contribution of intracellular Ca²⁺ remained controversial (1;70;71). Very recently, LRRC8A has been described as an essential component of VRAC. Surprisingly, overexpression of LRRC8A rather suppressed than augmented VRAC (13;14). It was therefore concluded that other essential components are still missing to fully reproduce VRAC.

Anoctamins, a family of Ca²⁺ activated Cl⁻ channels and phospholipid scramblases (for review see (72), have been proposed to support volume regulation (12;37). Also ANO6 (anoctamin 6, TMEM16F) has pleiotropic functions, since it scrambles plasma membrane phospholipids (39;73;74) and produces Cl⁻ and nonselective cation currents (29;35;36;75), triggered by intracellular Ca²⁺ and during apoptotic cell death (34). A recent X-ray analysis of a fungal TMEM16 protein provided ideas how TMEM16 proteins may operate as phospholipid scramblases and ion channels (21). Activation of ANO6 induced cell shrinkage and subsequent swelling, and was shown to be a component of the ubiquitous outwardly rectifying Cl⁻ channel (34;37;76). Despite the evidence for a role in volume regulation and cell migration, the findings remained controversial (12;37;75;77).

Although studied extensively (for review see (1;78;79), no general concept exists for the activation of Cl⁻ currents ($I_{Cl\text{-swell}}$) during cell swelling. Also studies on LRRC8A do not provide a molecular mechanism for the regulation of this VRAC-component (13;14). In the present report we identify ANO6 as a volume regulated Cl⁻ channel and unravel the molecular mechanism of activation. Volume regulation and current measurements were done at 37 °C and in the presence of physiological extra- and intracellular ion concentrations. We found that volume regulation and proper activation of $I_{Cl\text{-swell}}$ /ANO6 requires i) lowering of the intracellular Cl⁻ concentration, ii) Ca²⁺ influx through transient receptor potential (TRP) channels, and iii) generation of membrane lysophospholipids through phospholipase A2

(PLA₂). The data suggest that ANO6 operates as an osmosensor and a Cl⁻ release channel during RVD, or may affect volume regulation by scrambling membrane phospholipids.

Materials and Methods

Animals, cells, cDNA, RT-PCR. Generation of An^{o6}^{-/-} animals and isolation of intestinal epithelial cells has been described earlier (80;81). All animal experiments were approved by the local ethics commission of the University of Regensburg and were conducted according to the guidelines of the American Physiological Society and the German law for welfare of animals. The HEK293 cells were grown as described earlier (29). The culture of EBV-transformed B lymphoblast cell lines from control subjects and Scott-UK or Scott-USA patients has been described in another report (74). Lymphocytes were grown in RPMI 1640 medium (GIBCO, 52140; Darmstadt, Germany) supplemented with 10% fetal calf serum (GIBCO) and penicillin/ streptomycin (GIBCO). LRRC8A cDNA was cloned from HEK293 cells using standard PCR techniques. Generation of cDNA for ANO6 and transfection/expression of ANO6 has been report earlier (29). RT-PCR analyses were performed using standard conditions and appropriate primers.

siRNA, solutions, materials and statistical analysis. Knockdown of ANO6 by siRNA was reported in our previous study (12). All experiments were performed 48 h after the transfection. For most experiments cells were kept initially in Ringer solution (mM): NaCl 145, KH₂PO₄ 0.4, K₂HPO₄ 1.6, D-glucose 5, MgCl₂ 1, calcium gluconate 1.3, pH 7.4. Ringer solution was then replaced by an isotonic solution (Iso) containing (mmol/l) NaCl 72.5, KH₂PO₄ 0.4, K₂HPO₄ 1.6, D-glucose 5, MgCl₂1, Ca-gluconate 1.3, mannitol 145, pH 7.4. To induce cell swelling a hypotonic solution (150 mosmol/l; 50% Hypo) was produced by removal of mannitol. Alternatively 50 or 100 mmol/l NaCl were removed to produce 17 % and 33% hypotonicity, respectively. Osmolarity was measured using an osmometer.

Western Blotting of ANO6 and COIP. Protein was isolated from wt and Scott B-lymphocytes using a sample buffer containing 50 mM Tris-HCl, 150 mM NaCl, 50 mM Tris, 100 mM dithiothreitol, 1% Nonidet P-40, 0.5% deoxycholate sodium, and 1% protease inhibitor mixture (Sigma). Proteins were separated by 8.5 % SDS-PAGE and transferred to a polyvinyl

membrane (GE Healthcare, Munich, Germany). Membranes were incubated with primary anti-ANO6 rabbit polyclonal AB (Ano6 AB P78; Davids Biotech, Regensburg, Germany) at a dilution of 1:1000 overnight at 4 °C. Proteins were visualized using horseradish peroxidase-conjugated secondary antibody and ECL detection.

For co-immunoprecipitation Cells were cotransfected with ANO6-GFP/LRRC8A or ANO6/LRRC8A-GFP. Cell lysates (NP-40 lysis buffer containing 1X protease inhibitor cocktail) was pre-cleaned with protein G-agarose at 4 °C for 1 h and incubated with 5 µg primary antibody (Rockland, Gilbertsville, PA 19525) overnight at 4 °C on a rotator. Cell lysates were incubated with protein G-agarose at 4 °C for 3 h, followed by centrifugation at 1000 g for 1 min 3 times. Pellets were collected and resuspended in 1X loading buffer. The supernatant was collected and separated by 10 % SDS-PAGE and transferred to PVDF membrane. The membrane was blocked with 5 % NFM/TBST at RT for 1 h and incubated overnight 4 °C with goat polyclonal anti-GFP AB, rabbit polyclonal anti-ANO6 AB, or rabbit polyclonal anti-LRRC8A AB (AVIVA, San Diego, USA) (1 % NFM/TBST). Subsequently, the membrane was incubated with HRP-conjugated donkey anti-goat IgG at RT for 1 h. Immunoreactive signals were visualized using supersignal chemiluminescence substrate detection kit (Pierce Biotechnology, Rockford, USA).

Measurement of [Ca²⁺]_i: The plasma membrane bound calcium sensor has been modified by the addition of a N-terminal signal peptide (20 aa) from Neuromodulin (PI-G-CaMP2). Addition of this peptide results in posttranslational palmitoylation of the protein, which facilitates anchoring of the protein to the plasma membrane. HEK293 cells were transfected on coated glass cover slips with pcDNA31 PI-G-CaMP2, and were mounted in a perfusion chamber 48 hrs after transfection. Cells were perfused with ringer solution at a rate of 8 ml/min at 37°C. Cell fluorescence measurements was measured continuously with an inverted microscope Axiovert S100 (Zeiss) using a x40 objective (Fluar 40x/1.3 Oil, Zeiss) and a high speed polychromator system (VisiChrome, Visitron, Puchheim, Germany). PI-G-CaMP2 was excited at 485 nm and 405 nm. Emission was recorded between 520 and 550 nm using a CCD-camera (CoolSnap HQ, Visitron). Control of experiments, imaging acquisition, and data

analysis were done with the software package Meta-Fluor (Universal imaging, New York, USA). Alternatively cells were loaded with Fura2 and intracellular Ca^{2+} concentrations were determined as described earlier (76).

Flow cytometry and single cell volume measurements. Cells were washed and re-dissolved in 10 ml isotonic or hypotonic Ringer solution as described for patch clamp experiments. Cells were analyzed at 37 °C / pH 7.4 using a CASY flow cytometer (Roche Diagnostics, Mannheim, Germany). Cells were analyzed at a density of 10^6 cells/ml. For single cell volume measurements cells were loaded with 1 μg of calcein-AM (Molecular Probes) and 0.01% pluronic in a standard bath solution (Ringer) for 60 min at 20–22 °C. Fluorescence intensity was measured at an excitation wavelength of 485 nm and an emission wavelength of 520–550 nm. Cell swelling and RVD were observed for 10–15 min after applying hypotonic bath solution.

Patch Clamping. Cells were patched on glass cover slips. Lymphocytes were fixed on polylysine-coated coverslips. If not indicated otherwise, patch pipettes were filled with a cytosolic-like solution containing KCl 30, K⁺-gluconate 95, NaH_2PO_4 1.2, Na_2HPO_4 4.8, EGTA 1, Ca²⁺-gluconate 0.758, MgCl_2 1.03, D - glucose 5, ATP 3, pH 7.2. The Ca^{2+} activity was 0.1 μM . Coverslips were mounted in a perfused bath chamber on the stage of an inverted microscope (IM35, Zeiss) and kept at 37 °C. The bath was perfused continuously with Ringer solution at a rate of 8 ml/min. For activation of volume dependent Cl^- currents, Ringer bath solution (mM) was first changed to Iso and then to Hypo (c.f. above). Patch clamp experiments were performed in the fast whole cell configuration. Patch pipettes had an input resistance of 2–4 $\text{M}\Omega$ when filled with the cytosolic like (physiological) solution. Currents were corrected for serial resistance. We choose this solution because it enabled swelling/shrinkage behaviour under physiological ion concentrations and allowed for direct comparison of the results from patch clamping and volume measurements. The access conductance was measured continuously and was 60–140 nS. Currents (voltage clamp) and voltages (current clamp) were recorded using a patch clamp amplifier (EPC 7, List Medical Electronics, Darmstadt, Germany), the LIH1600 interface and PULSE software (HEKA,

Lambrecht, Germany) as well as Chart software (AD Instruments, Spechbach, Germany). Data were stored continuously on a computer hard disc and analyzed using PULSE software. In regular intervals, membrane voltage (V_c) was clamped in steps of 20 mV from -100 to +100 mV from a holding voltage of -100 mV. Current density was calculated by dividing whole cell currents by cell capacitance.

Double electrode voltage clamping. Oocytes were injected with cRNA encoding aquaporin 1 (0.5 ng), Ano6 (5 ng) or both together. Water injected oocytes served as controls. 2 – 4 days after injection, oocytes were impaled with two electrodes (Clark Instruments Ltd, Salisbury, UK), which had a resistances of $< 1 \text{ M}\Omega$ when filled with 2.7 mol/l KCl. Using two bath electrodes and a virtual-ground head stage, the voltage drop across the serial resistance was effectively zero. Membrane currents were measured by voltage clamping (oocyte clamp amplifier, Warner Instruments LLC, Hamden CT) in intervals from -80 to +60 mV, in steps of 20 mV, each 1 s. The bath was continuously perfused at a rate of 5 ml/min. All experiments were conducted at 22 °C.

Materials and statistical analysis. All animal experiments were approved by local authorities and were conducted according to the guidelines of the American Physiological Society and the German law for welfare of animals. All compounds used were of highest available grade of purity and were from Sigma or Merck. NS3728 was a generous gift by NeuroSearch (Ballerup, Denmark). Data are reported as mean \pm s.e.m. Student's t-test (for paired or unpaired samples as appropriate) or ANOVA were used for statistical analysis. A p-value < 0.05 was accepted as significant difference.

Ethics statement

All animal experiments were approved by the local ethics commission of the University of Regensburg and were conducted according to the guidelines of the American Physiological Society and the German law for welfare of animals.

Results

ANO6 augments $I_{\text{Cl-swell}}$ and volume regulation in HEK293 cells

siRNA-knockdown of ANO6 in HEK293 cells was shown earlier to attenuate $I_{\text{Cl-swell}}$ by

about 50 % (12). ANO6 is a ubiquitous protein as comparably high levels of mRNA is found in all cell lines and freshly isolated cells (data not shown). We found that additional expression of exogenous ANO6 is able to augment $I_{\text{Cl-swelling}}$ activated by hypotonic bath solutions in HEK293 cells (Hypo; Fig. 1a). Patch pipettes were filled with a buffer solution of “cytosolic-like” ion composition, which is shown below to be essential for full activation of $I_{\text{Cl-swelling}}$. Hypo activated predominantly $I_{\text{Cl-swelling}}$, as K^+ channel blockers $\text{Ba}^{2+}/\text{TEA}^+$ showed little effects on Hypo-activated whole cell currents. $I_{\text{Cl-swelling}}$ was inhibited by known blockers of anoctamins, which also inhibit volume activated anion channels (VRAC), such as NPPB, NS3728 or T16_{inh}AO1 (Fig. 1a,b) (82-84). We found that extra- and intracellular Ca^{2+} was required to fully activate $I_{\text{Cl-swelling}}$. Under complete Ca^{2+} free conditions, i.e. Ca^{2+} free solution and preincubation with the Ca^{2+} chelator BAPTA-AM, $I_{\text{Cl-swelling}}$ was essentially eliminated (Fig. 1c,d).

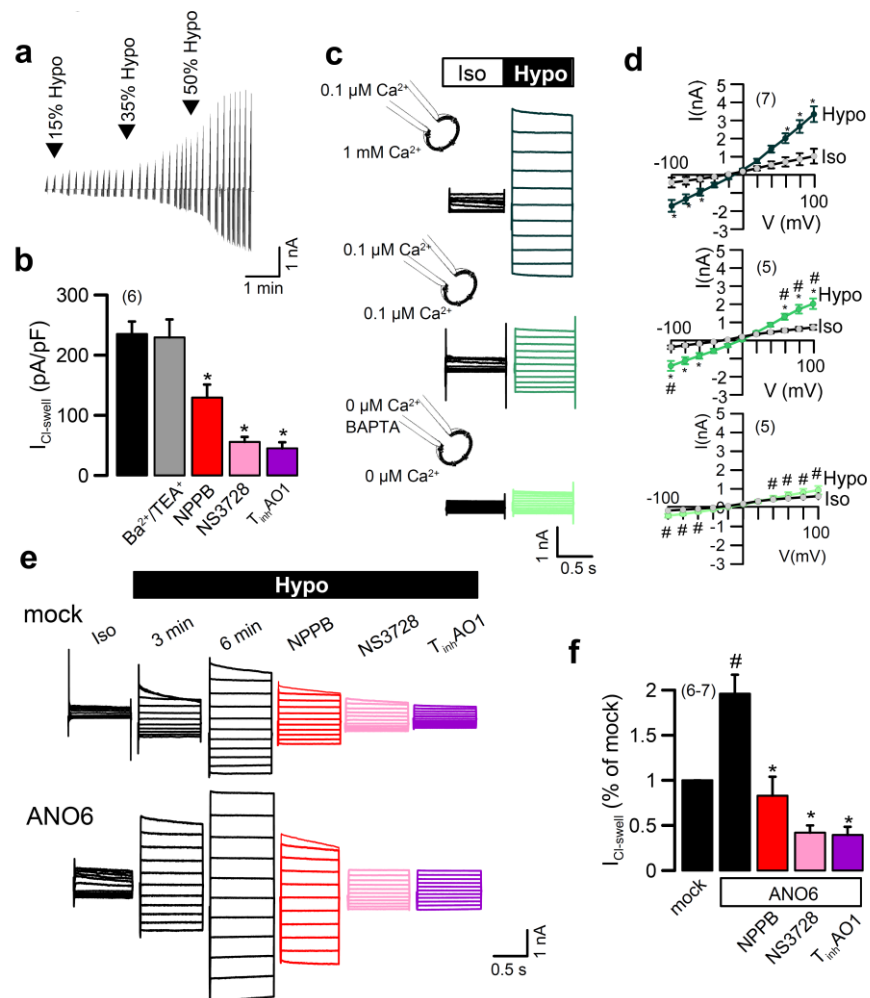


Figure 1 Cell swelling activates Anoctamin 6 (a) Continuous recording of the whole cell current ($V_c = \pm 100$

mV in steps of 20 mV) activated in mock transfected HEK293 cells, after exposure to hypotonic bath solution (Hypo; black arrowheads indicate 15, 35 and 50% hypotonicity). (b) Summary of Hypo-induced current density in mock transfected HEK293 cells and inhibition by NPPB (50 μM), NS3728 (10 μM) and T16A_{inh}AO1 (10 μM). Currents were not inhibited by K^+ channel blockers Ba^{2+} (5 mM) and TEA^+ (10 μM). (c) Inhibition of Hypo-induced whole cell currents by removal of Ca^{2+} and additional application of the Ca^{2+} chelator BAPTA (50 μM). (d) Current/voltage (i/v) relationship of the experiments shown in (c). (e) Inhibition of Hypo-induced whole cell currents by NPPB (50 μM), NS3728 (5 μM), or T16A_{inh}AO1 (10 μM) in mock transfected and ANO6-overexpressing HEK293 cells ($V_c = \pm 100$ mV in steps of 20 mV). (f) Summary of Hypo-induced current densities in mock and ANO6-overexpressing cells and effect of inhibitors.

Overexpression of ANO6 augmented $I_{\text{Cl-sw}}_{\text{well}}$. $I_{\text{Cl-sw}}_{\text{well}}$ did not show time dependent inactivation that has been reported to be characteristic for VRAC (79), but was potently blocked by typical Cl^- channel blockers (Fig. 1e,f). Volume regulation was measured by flow cytometry and in single cells using calcein fluorescence, and was augmented in ANO6-expressing cells (Fig. 1g-j). Notably, the reduced regulatory decrease (RVD) after hypotonic cell swelling was found to be attenuated in the absence of Ca^{2+} . These data indicate that proper volume regulation requires Ca^{2+} . Similar to $I_{\text{Cl-sw}}_{\text{well}}$, also apoptotic currents induced by staurosporine were augmented by overexpression of ANO6 (data not shown).

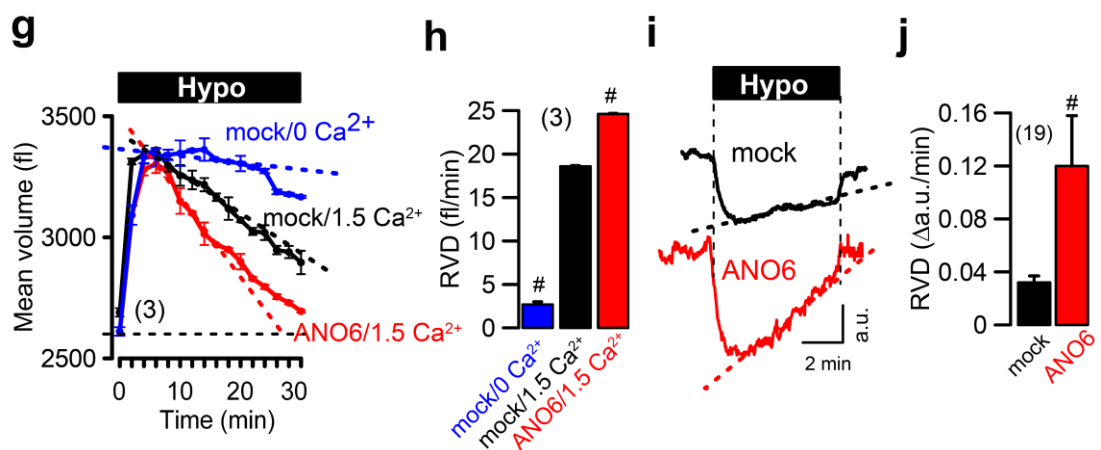
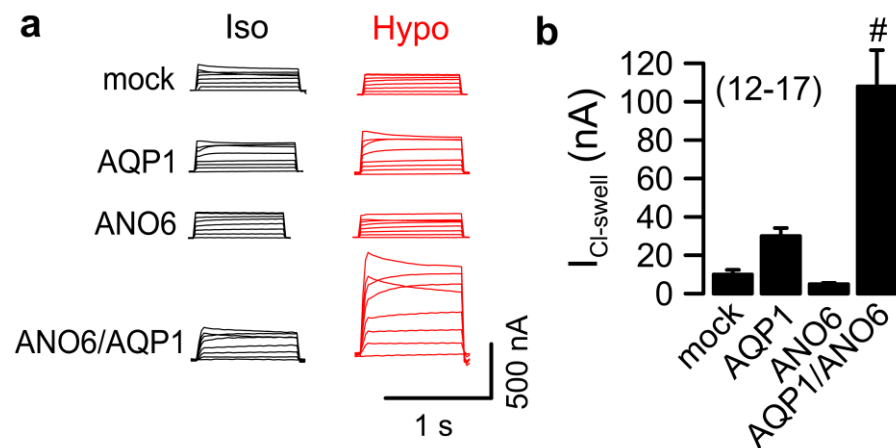


Figure 1 (cont.). Cell swelling activates Anoctamin 6 (g) Hypo-induced cell swelling and re-shrinkage (RVD) in mock transfected cells in the absence and presence of extracellular Ca^{2+} , and in ANO6-expressing cells, as measured by flow cytometry. (h) RVD calculated from initial recovery from cell swelling. (i,j) RVD in mock transfected and anoctamin-overexpressing cells as assessed by single cell volume measurements using calcein fluorescence. Mean \pm SEM; *significant inhibition by NBBP, NS3728, and T_{inh}AO1 (paired t-test). #significant difference when compared to high Ca^{2+} or mock, respectively (ANOVA). (number of cells or flow cytometry assays).

Additional evidence for the role of ANO6 in volume regulation was detected in *Xenopus*

oocytes. Hypotonic swelling can be observed in oocytes overexpressing AQP1, but not in non-injected oocytes (85). A small $I_{\text{Cl-sw}}^{\text{well}}$ was activated in AQP1-expressing oocytes by hypotonic bath solution that was, however, significantly enhanced in ANO6-coexpressing cells (Supplementary Fig. 1).



Supplementary Figure 1: $I_{\text{Cl-sw}}$ in *Xenopus* oocytes expressing ANO6.
a) Whole cell currents measured in water injected control oocytes, and oocytes expressing AQP1, ANO6 or coexpressing AQP1/ANO6. Hypotonic bath solution (50% hypotonicity; 101 mosmol/l) activated a small but significant whole cell current only in cells coexpressing AQP1/ANO6. **b)** Summary of Hypo-induced whole cell currents (at clamp voltage $V_c = +40$ mV). Mean \pm SEM. [#]significantly different when compared to AQP1 (unpaired t-test). (number of oocytes).

Ca^{2+} influx and dilution of intracellular Cl^- during hypotonic swelling is essential for activation of $I_{\text{Cl-sw}}^{\text{well}}$ /ANO6

We examined whether plasma membrane (PM) localized ANO6 (Supplementary Fig. 2a) is activated by Ca^{2+} entering the cell during cell swelling through transient receptor potential (TRP) channels. In the presence of the TRP channel inhibitor SK&F96365 (86) activation of $I_{\text{Cl-sw}}^{\text{well}}$ was largely attenuated, and the remaining $I_{\text{Cl-sw}}^{\text{well}}$ showed VRAC-typical time dependent inactivation (Fig. 2a,b). ACA, a TRP channel inhibitor and potent blocker of PLA_2 (87) completely abolished activation of $I_{\text{Cl-sw}}^{\text{well}}$, suggesting a role of PLA_2 for activation of ANO6. In contrast, the TRPM7 inhibitor NS8593 (10 μM) or the activator of TRPM7, naltriben (50 μM) had no inhibitory or activatory effects, respectively (data not shown). Notably, $I_{\text{Cl-sw}}^{\text{well}}$ was largely reduced when experiments were performed in the presence of

CsCl instead of physiological buffer solutions, and a typical time dependent inactivation was observed (Fig. 2a). Membrane voltages were depolarized in the presence of CsCl, which probably interferes with Ca^{2+} influx and activation of ANO6 (88) (data not shown). Thus the contribution of ANO6 to $I_{\text{Cl-sw}}_{\text{well}}$ cannot be properly assessed in the presence of CsCl (75).

Perfusion of the cell with high intracellular Cl^- concentrations in the patch pipette may also interfere with activation of ANO6. We therefore examined whole cell currents in ANO6-expressing cells with either low (5 mM) or high (125 mM) Cl^- in the patch pipette. In the presence of low cytosolic Cl^- we observed large whole cell currents under isotonic conditions (no cell swelling), which were strongly reduced when extracellular (bath) Cl^- was replaced by impermeable gluconate (5 Cl^-) (Fig. 2c,d left panels). Current activation by 5 Cl^- was not blocked by inhibition of TRP channels with SK&F (data not shown). In contrast, whole cell currents were low in the presence of high intracellular Cl^- (Fig. 2c,d right panels). Similar was observed when $I_{\text{Cl-sw}}_{\text{well}}$ was activated in the presence of low or high pipette Cl^- : Hypo-induced currents were large with low cytosolic Cl^- but small with high cytosolic Cl^- (Fig. 2e). We propose that dilution of the cytosolic Cl^- concentration during hypotonic cell swelling may activate ANO6.

Activation of $I_{\text{Cl-sw}}_{\text{well}}$ was largely reduced by the TRP channel inhibitor SK&F, suggesting swelling induced Ca^{2+} influx that activates ANO6 (Fig. 2a,b). Apart from TRPM7, which does not seem to contribute to activation of $I_{\text{Cl-sw}}_{\text{well}}$, TRPC1 was found to be expressed in HEK293 cells (Fig. 2f). Using the Ca^{2+} sensor Fura2, we detected a variable and transient increase in intracellular Ca^{2+} within 39.9 ± 1.5 s after applying Hypo (Fig. 2g,h). Intracellular Ca^{2+} was measured near the junctional zone, using the PM-targeted Ca^{2+} sensor PI-G-CaMP2 (89) (Supplementary Fig. 2). The delayed and transient Ca^{2+} increase caused by hypotonic cell swelling was not inhibited by SK&F96365, but was potently blocked by dantrolene, an inhibitor of ryanodine receptors (Fig. 2i). Both Ca^{2+} dependent cPLA₂ and Ca^{2+} independent iPLA₂ are expressed in HEK293 cells (Supplementary Fig. 2c,d). Nonselective PLA₂-inhibitors (ACA, aristolochic acid), pyrrophenone (inhibition of cPLA₂), and BEL (inhibition of iPLA₂) largely inhibited Ca^{2+} increase (Fig. 2 i). In contrast, inhibition of metabolic

pathways (namely PLA₂ (epoxygenase (EG), lipoxygenase (LG), cyclooxygenase (CG)) by an inhibitory cocktail neither blocked Ca^{2+} increase nor activation of ANO6, and are therefore not relevant (Fig. 2i, Supplementary Fig. 2e) (90). Thus cell swelling activates iPLA2 and cPLA₂ and releases Ca^{2+} from ryanodine- and IP3-sensitive Ca^{2+} stores into the junctional zone (Ca^{2+} nanodomain) (91-94).

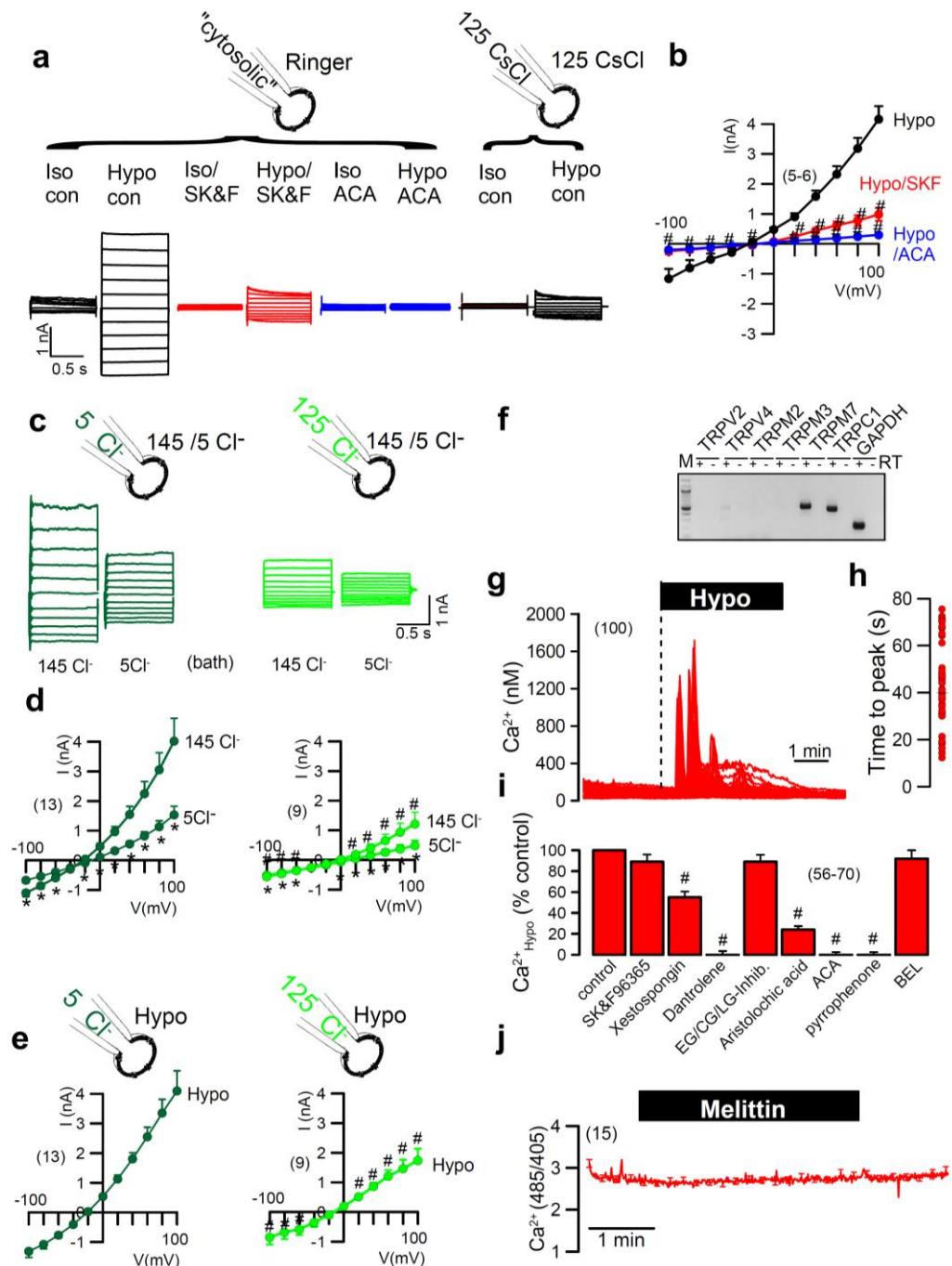
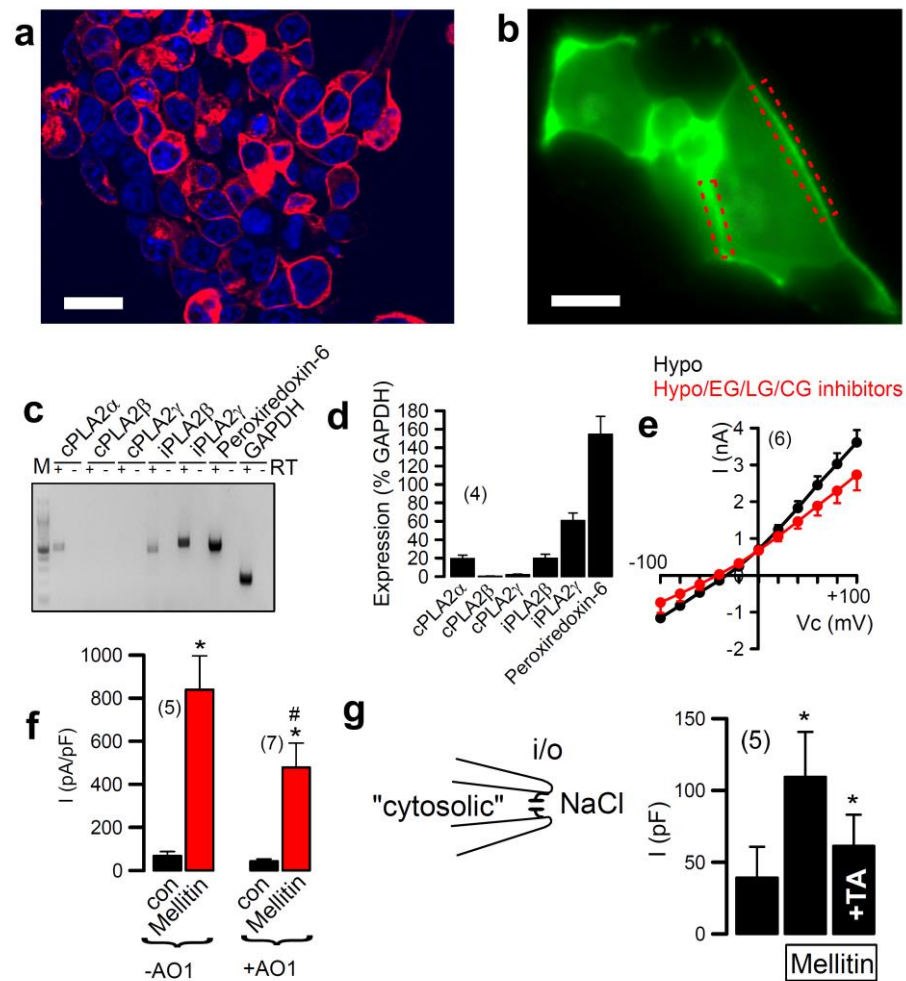


Figure 2 ANO6 is activated by hypo-induced Ca^{2+} increase. (a) Swelling induced (Hypo) whole cell currents

in ANO6-overexpressing HEK293 cells, which was inhibited by TRP channel blocker SK&F96365 (20 μ M), the TRP/PLA₂ blocker ACA (20 μ M), and the presence of CsCl in bath and pipette. **(b)** Corresponding i/v curves. **(c)** Whole cell currents in ANO6-expressing HEK293 cells with 5 or 125 mmol/l Cl⁻ in the patch pipette. **(d)** Corresponding i/v curves. **(e)** i/v curves for Hypo-induced whole cell currents in ANO6-expressing HEK293 cells with 5 or 125 mmol/l Cl⁻ in the patch pipette. **(f)** RT-PCR analysis of volume/mechanosensitive TRP channels in HEK293 cells. RT = reverse transcriptase. **(g)** Delayed Ca²⁺ increase induced by hypotonic bath solution as measured in Fura2 loaded HEK293 cells. **(h)** Time to maximal (peak) Ca²⁺ increase upon exposure to hypotonic bath solution measured in 100 individual cells. **(i)** Summary of Ca²⁺ increase near ER/plasma membrane junctional zone in HEK293 cells, using plasma membrane localized Ca²⁺ sensor PI-G-CaMP2. Effects of TRP channel inhibitor SK&F96365 (20 μ M), IP3R inhibitor xestospongin C (10 μ M), RyrR inhibitor dantrolene (10 μ M), cocktail of inhibitors of epoxygenase (EG; 100 μ M), lipoxygenase (LG; 5 μ M), and cyclooxygenase (CG; 10 μ M), broad PLA₂ inhibitors aristolochic acid (100 μ M) and ACA (20 μ M), cPLA₂ inhibitor pyrrophenone (50 nM), and iPLA₂ inhibitor BEL (30 μ M). **(j)** Continuous recording of intracellular Ca²⁺ concentration (detected as 485/405 nm fluorescence ratio) indicating lack of effects of melittin (200 nM) on intracellular Ca²⁺. Mean \pm SEM. #significantly different from Hypo, 5Cl⁻ in patch pipette or control, respectively (ANOVA). (number of cells).



Supplementary Figure 2: PLA₂ and Ca²⁺, but not pathways downstream of PLA₂ activate ANO6.

a) Immunocytochemistry of ANO6 expressed in HEK293 cells indicating membrane expression. **b)** Plasma membrane localization of the Ca²⁺ sensitive protein PI-G-CaMP2. **c)** RT-PCR analysis of Ca²⁺ sensitive and Ca²⁺ insensitive PLA₂ isoforms in HEK293 cells. **d)** Expression levels of the different PLA₂ isoforms expressed in HEK293 cells. **e)** Marginal inhibitory effects on Hypo-induced whole cell currents by simultaneous inhibition of epoxygenase (EG), lipoxygenase (LG), and cyclooxygenase (CG) with an inhibitory cocktail containing 6-(2-Propargyloxyphenyl)hexanoic acid (100 μM), nordihydroguaiaretic acid (5 μM), and indomethacin (10 μM). **f)** Summary of whole cell currents activated by melittin and inhibition by the anoctamin inhibitor AO1 (20 μM). **g)** Summary of current measurements in cell excised inside/out membrane patches from ANO6-overexpressing HEK293 cells. Pipettes were filled with "cytosolic-like" buffer solution. Activation of patch currents by 100 nM melittin and inhibition by the anoctamin inhibitor tannic acid (TA; 10 μM). Mean ± SEM. * significant current increase by melittin and inhibition by TA (paired t-test). #significantly different from -AO1 (unpaired t-test). Bath: NaCl 145, KH₂PO₄ 0.4, K₂HPO₄ 1.6, D - glucose 5, MgCl₂ 1, Ca-gluconate 1.3, pH 7.4. Patch pipette: KCl 30, K-gluconate 95, NaH₂PO₄ 1.2, Na₂HPO₄ 4.8, EGTA 1, Ca-gluconate 0.758, MgCl₂ 1.03, D -glucose 5, ATP 3 (all mM), [Ca²⁺]_i 10-7 M, pH 7.2.

Cell swelling activates ANO6 primarily through PLA₂ and accumulation of membrane lysophospholipids

Melittin, an activator of PLA₂ did not increase intracellular Ca²⁺, but strongly activated ANO6 (Fig. 2j, 3a,b). Activation of ANO6 by melittin was completely suppressed by

inhibiting iPLA_2 with BEL, which also largely attenuated RVD (Fig. 3c,d). Direct activation of ANO6 by PLA_2 through melittin did not require Ca^{2+} influx through TRP channels, as SK&F96365 did not block activation (Fig. 3e). PLA_2 -activated ANO6 whole cell currents were blocked by the anoctamin inhibitor AO1 (Supplementary Fig. 2f). Notably, membrane currents activated by melittin in inside/out excised membrane patches from ANO6-expressing HEK293 cells were blocked by tannic acid (Supplementary Fig. 2g). The data indicate that ANO6 currents can be activated by PLA_2 without influx of Ca^{2+} . In contrast complete removal of Ca^{2+} from bath and patch pipette and chelation of Ca^{2+} by 100 μM almost completely eliminated the effect of melittin (data not shown). Vice versa, activation of ANO6 by ionomycin was partially blocked by inhibition of PLA_2 with ACA (Fig. 3f).

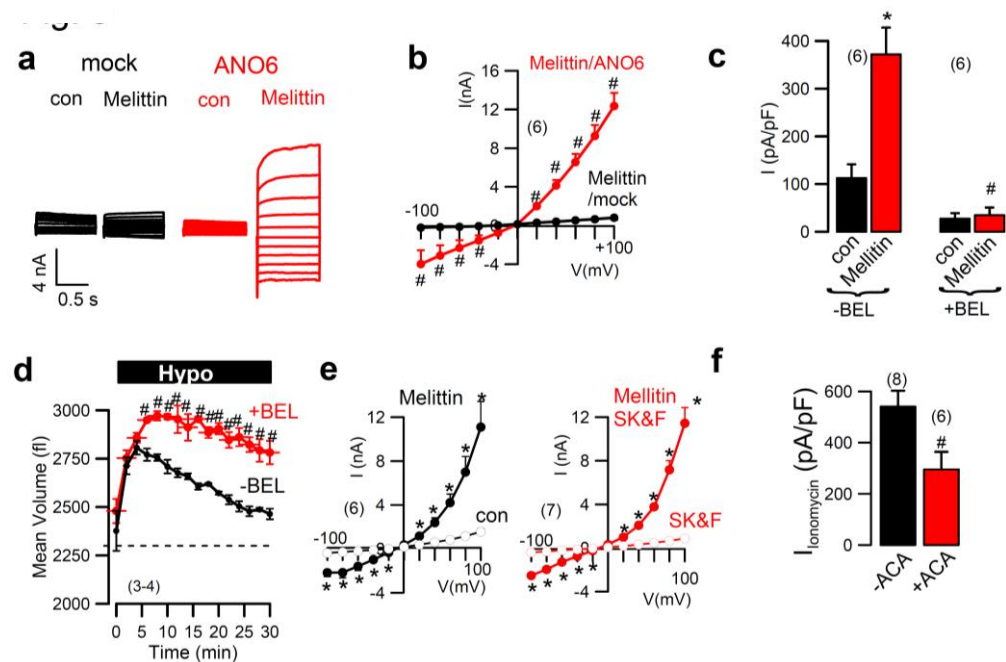


Figure 3 Cell swelling activates ANO6 through PLA_2 -generated lysophospholipids. (a,b) Activation of whole cell currents by PLA_2 -activator melittin (200 nM) in ANO6-expressing but not mock transfected cells, and corresponding i/v curves. (c) Summary of whole cell currents activated by melittin and inhibition by the iPLA_2 -inhibitor BEL (30 μM). (d) Volume regulation measured in ANO6-expressing HEK293 cells in the absence or presence of BEL. (e) I/V relationship of whole cell currents activated by melittin (200 nM) in the absence or presence of SK&F (20 μM). (f) Summary of ionomycin (1 μM) activated whole cell currents in ANO6-overexpressing HEK293 cells and inhibition by the PLA_2 -inhibitor ACA (20 μM).

We speculated that ANO6 is activated by PLA_2 through depletion of fatty acids, such as arachidonic acid (ArA), and generation of membrane lysophospholipids (LPL). The

immediate downstream product of LPL, lysophosphatidic acid (LPA), does not appear to be relevant since activation of ANO6 was not compromised in the presence of the Pan-LPA-receptor inhibitor BrP-LPA (data not shown). Accumulation of LPL within the plasma membrane is known to cause membrane tension (95), which could open ANO6. This process should be reversed by simultaneous application of fatty acids like ArA. Strikingly, activation of ANO6 by PLA_2 was much reduced in the presence of ArA (Fig. 3g,h). Moreover, as cell swelling leads to activation of PLA_2 and generation of LPL, thereby activating ANO6, I_{Cl^-} -swell was reversibly inhibited by ArA (Fig. 3i,j). Melittin, however, was unable to activate large whole cell currents in the presence of high (125 mM) intracellular Cl^- concentration (Fig. 3k). Finally, direct application of LPL (20 μM) activated an anion conductance in I^- / YFP quenching assays (Fig. 3l). This anion conductance was sensitive towards the typical anoctamin inhibitors $\text{CaCC}_{\text{inh}}\text{AO1}$, $\text{T16A}_{\text{inh}}\text{AO1}$, and tannic acid.

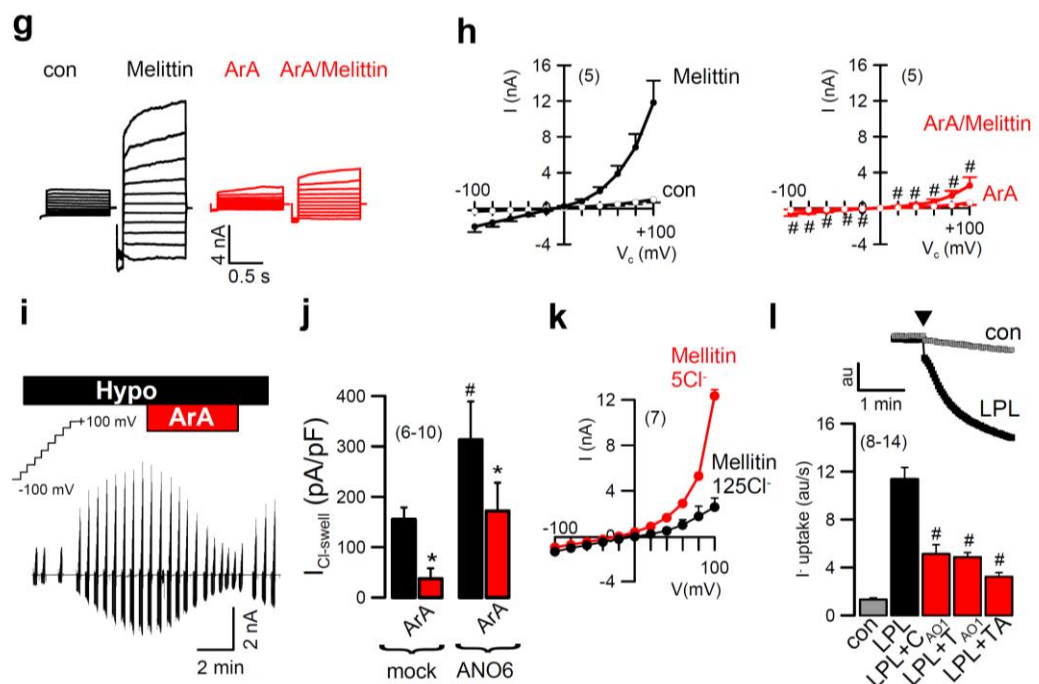


Figure 3 (cont.) Cell swelling activates ANO6 through PLA_2 -generated lysophospholipids. (g) Activation of whole cell currents in ANO6-overexpressing HEK293 cells by PLA_2 -activator melittin and inhibition by arachidonic acid (ArA; 50 μM). (h) Corresponding i/v curves. (i) Continuous recording of Hypo-induced whole cell currents and reversible inhibition of activated currents by ArA. (j) Summary of Hypo-induced current densities in mock transfected and ANO6 overexpressing HEK293 cells, and inhibition by ArA. (k) Activation of whole cell currents by melittin in the presence of low (5 mM) pipette Cl^- , which was largely reduced in the presence of high (125 mM) pipette Cl^- . (l) Activation of I^- influx in YFP fluorescence quenching assays indicating activation of an anion conductance by LPL (20 μM). The effect of LPL was suppressed by

$\text{CaCC}_{\text{inh}}\text{AO1}$ (10 μM), $\text{T16A}_{\text{inh}}\text{AO1}$ (10 μM), and tannic acid (10 μM). Mean \pm SEM; *significant activation by melittin and inhibition by ArA, respectively (paired t-test). #significantly different from mock and absence of inhibitors BEL and ACA, respectively (ANOVA). (number of cells).

ANO6 controls $I_{\text{Cl-sw}}\text{ell}$ and RVD in normal B-lymphocytes but not in lymphocytes from a patient with Scott disease

We examined activation of ANO6 by PLA_2 in B-lymphocytes from a patient with Scott disease. Scott disease is a rare inherited bleeding disorder, which is caused by a defect in ANO6 function (39;74). Cell swelling (Hypo) activated whole cell currents in normal (wt) lymphocytes, which were inhibited by the Cl^- channel blocker NPPB (Fig. 4a,b). Like in ANO6-overexpressing HEK293 cells, activation of $I_{\text{Cl-sw}}\text{ell}$ and volume regulation (RVD) was inhibited at low (10^{-7} mol/l) extracellular Ca^{2+} (Fig. 4b,c). Scott lymphocytes do not express ANO6 and demonstrated reduced $I_{\text{Cl-sw}}\text{ell}$ and defective volume regulation (Fig. 4d-f). Activation of currents was not affected by BrP-LPA, but was abolished by ACA (Fig. 4g). Lymphocytes show a PLA_2 expression pattern similar to that identified in HEK293 cells (Fig. 4h,j). Remarkably, only normal (wt) but not Scott lymphocytes activated whole cell currents during activation of PLA_2 by melittin (Fig. 4j-l). Moreover, Ca^{2+} -dependent activation ANO6 by ionomycin was also strongly attenuated by ACA (Fig. 4m). These results clearly show that also endogenous ANO6 expressed in B-lymphocytes is controlled by PLA_2 , which is activated during cell swelling.

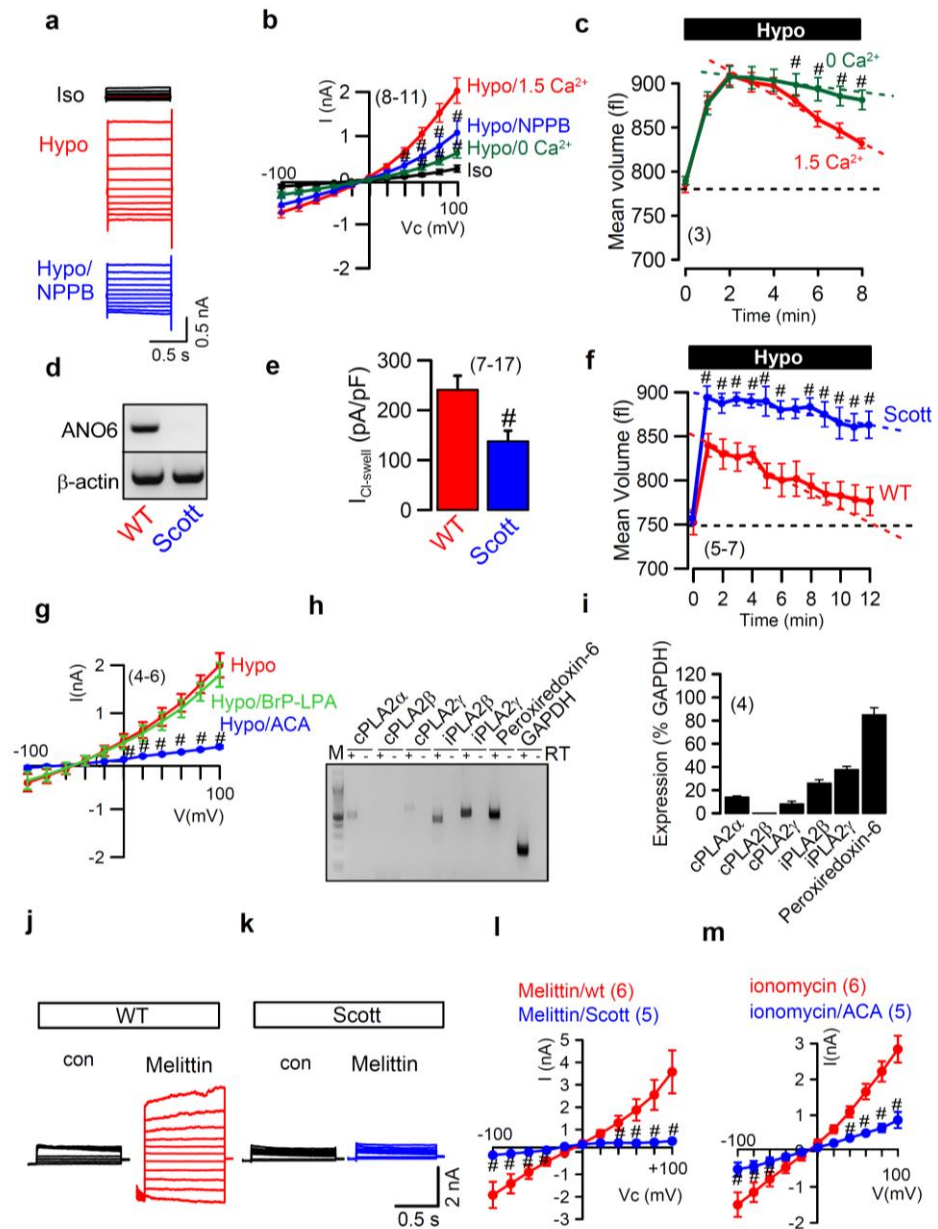


Figure 4 ANO6 is necessary for $I_{\text{Cl-swelling}}$ and RVD in human lymphocytes. (a) Hypo (50%) induced whole currents in human normal (wt) lymphocytes and inhibition by NPPB (50 μM). (b) Corresponding i/v curves, also showing the inhibitory effect of Ca^{2+} removal from the bath solution. (c) Hypo-induced cell swelling and re-shrinkage (RVD) of normal lymphocytes as measured by flow cytometry in the absence or presence (1.5 mM) extracellular Ca^{2+} . (d) Western blot indicating expression of endogenous Ano6 in normal (wt) but not in Scott lymphocytes. (e) Hypo-induced whole cell currents in wt and Scott lymphocytes. (f) Hypo-induced cell swelling and RVD in normal and Scott lymphocytes. Mean \pm SEM; # significant difference when compared to Hypo, wt, and 0 Ca^{2+} , respectively (ANOVA). (number of cells or flow cytometry assays). (g) Hypo induced whole currents in wt lymphocytes were inhibited by ACA (20 μM), but not by the Pan-LPA inhibitor BrP-LPA (5 μM). (h,i) RT-PCR analysis of PLA₂ isoforms in human B-lymphocytes. RT = reverse transcriptase. (j,l) Activation of endogenous ANO6 in wt lymphocytes, but not in Scott lymphocytes lacking expression of ANO6. (m) Inhibition of Ca^{2+} activated whole cell currents by ACA in wt lymphocytes. Mean \pm SEM; # significant difference when

compared to Hypo or wt, respectively (ANOVA). (number of cells).

Intestinal epithelial cells from An $\text{o}6^{-/-}$ mice show reduced whole cell currents and defective volume regulation

We isolated small intestinal (jejunal) epithelial cells from An $\text{o}6^{+/+}$ and An $\text{o}6^{-/-}$ mice. In these cells hypotonic bath solution activated predominantly K^+ currents in both An $\text{o}6^{+/+}$ and An $\text{o}6^{-/-}$ cells, as indicated by hyperpolarization of the membrane voltage (Fig. 5a,b). Swelling activated K^+ currents in intestinal cells have been observed earlier (96). Although swelling activated K^+ currents were identical in An $\text{o}6^{+/+}$ and An $\text{o}6^{-/-}$ cells, baseline currents under control conditions were reduced in An $\text{o}6^{-/-}$ cells, suggesting a missing Cl^- current in An $\text{o}6^{-/-}$ cells. Noteworthy, volume activated Cl^- currents were found to be partially active under isotonic conditions (79). Moreover, we reported earlier that ANO6 is partially active under control conditions (29). Despite relatively small current changes in An $\text{o}6^{-/-}$ cells, volume regulation was strongly attenuated in cells from An $\text{o}6$ knockout animals: Hypotonic cell swelling was largely enhanced and RVD was strongly delayed in An $\text{o}6^{-/-}$ cells (Fig. 5c,d). We therefore conclude that ANO6 is a volume regulated anion channel that participates in cellular volume regulation. ANO6 is activated through cell swelling induced Ca^{2+} influx, activation of PLA $_2$ and a drop in Cl^- concentration within the junctional zone. We propose that activation of ANO6 occurs by accumulation of membrane lysophospholipids generating tension within the plasma membrane bilayer (95), thereby opening the channel pore possibly by improving accessibility for Ca^{2+} ions (21). Alternatively, exposure of phospholipids like phosphatidylserine (PS) by the phospholipid scrambling property of ANO6 may lead to a conformational change allowing Cl^- transport by ANO6 or may lead to exocytosis of submembraneous channel pools.

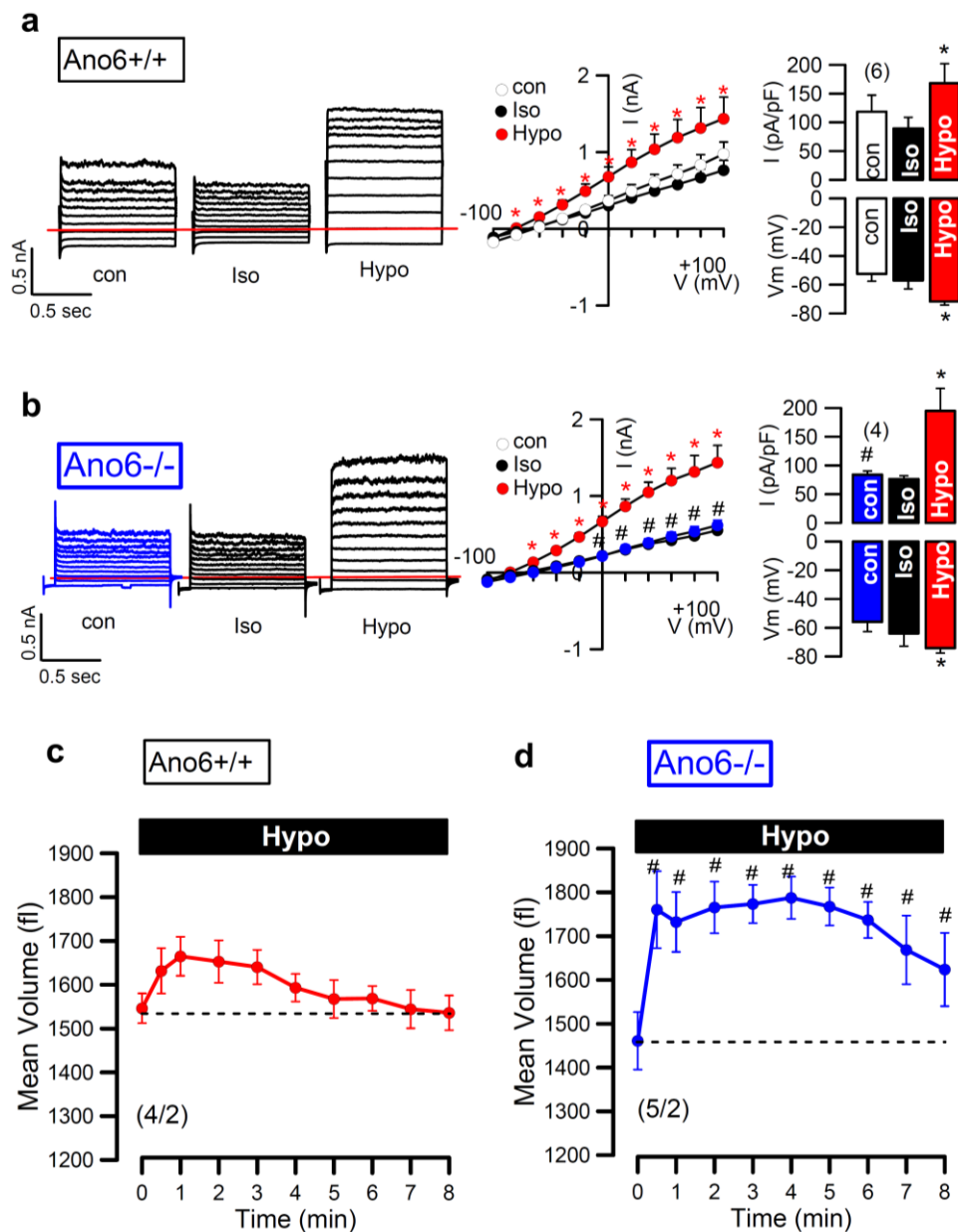


Figure 5 ANO6 controls cell volume in freshly isolated intestinal epithelial cells. (a) Whole cell currents in isolated intestinal epithelial cells from *Ano6^{+/+}* mice before and after hypotonic (35 %) cell swelling. Corresponding i/v relationships, current densities, and membrane voltages indicating activation of K^+ currents by Hypo. (b) Whole cell currents in isolated intestinal epithelial cells from *Ano6^{-/-}* mice before and after hypotonic (33 %) cell swelling. Corresponding i/v relationships, current densities, and membrane voltages. Whole cell currents are reduced under control conditions, suggesting absence of Ano6 currents which are normally active under control conditions. (c) Volume regulation (RVD) in intestinal epithelial cells from *Ano6^{+/+}* and *Ano6^{-/-}* animals, indicating rapid recovery from hypotonic cell swelling in *Ano6^{+/+}* but not *Ano6^{-/-}* cells. Enhanced increase in the cell volume and largely delayed recovery from hypotonic cell swelling in *Ano6^{-/-}* cells. Mean \pm SEM; #significant difference when compared to *Ano6^{+/+}* (unpaired t-test). (number of cells or flow cytometry assays).

Discussion

Activation of ANO6 by Ca^{2+}

The present data demonstrate that volume dependent activation of ANO6 requires Ca^{2+} , a result that corresponds well to earlier findings (37). We found that inhibition of Ca^{2+} influx through TRP channels activated by cell swelling strongly attenuated $I_{\text{Cl-swell}}$ and left behind a much smaller time dependent whole cell current (Fig. 2a). Although there is an ongoing dispute regarding the role of Ca^{2+} for volume regulated anion channels, the role of TRP channels and intracellular Ca^{2+} for cellular volume regulation received better acceptance (reviewed in (1;10;97)). Agreement exists concerning a local permissive (threshold) Ca^{2+} concentration of around 50 nM that is required to activate Cl^- channels during cell swelling (reviewed in (10;79)). Ca^{2+} influx through TRP channels appears essential to activate ANO6 during cell swelling. The data suggest Ca^{2+} induced Ca^{2+} release from dantrolene and IP_3 -sensitive stores caused by cell swelling. Ca^{2+} signaling may happen in a narrow compartmentalized space called the junctional zone (94). The concept that Ca^{2+} modulates VRAC in functional nanodomains, via colocalized store-operated Ca^{2+} influx channels has been proposed earlier (93;98;99).

Activation of ANO6 by PLA_2

Ca^{2+} -induced Ca^{2+} release was observed during cell swelling. It was paralleled by Ca^{2+} release from IP_3 -sensitive Ca^{2+} stores, probably through autocrine release of ATP and purinergic receptor signaling (12). However, ANO6 can be activated by PLA_2 without any increase in intracellular Ca^{2+} and iPLA_2 appears to be most important in this regard (Fig. 3). It is unlikely that PLA_2 and lysophospholipids (LPL) act via opening of TRP channels and Ca^{2+} influx, since i) activation of PLA_2 by melittin, which activates ANO6, does not trigger any Ca^{2+} signals, and ii) activation of ANO6 by PLA_2 was not suppressed by a TRP channel inhibitors (Fig. 3e). Notably, regulation of VRAC and RVD by cell swelling-activated PLA_2 is well recognized (1;100).

Strong activation of ANO6 through PLA_2 depolarized the membrane voltage suggesting activation of cation currents, as reported earlier (29;33;35;76;101). Our earlier work suggested

a loss of selectivity for ANO6 currents at very large intracellular Ca²⁺ concentrations and with ongoing stimulation (29;76) which was also supported by another report (36). Notwithstanding, the current activated by PLA₂ should be through ANO6 because i) melittin activated a current only in ANO6 expressing cells, 2) ACA inhibited swelling activated ANO6 currents, ACA inhibited melittin activated currents and ACA inhibited Ca²⁺ activated ANO6 currents. iii) melittin activated currents are inhibited by the ANO-inhibitors CaCC_{inh}AO1 and tannic acid, iv) melittin activated currents in ANO6-expressing wt lymphocytes, but not in Scott lymphocytes, v) melittin did not activate currents in the presence of high intracellular Cl⁻ concentration which inhibits ANO6. vi) Currents activated by ionomycin and PLA₂ are not additive

PLA₂-dependent release of Ca²⁺ from internal Ca²⁺ stores was also observed in the present study. Lambert, Hoffmann and coworkers have analyzed in detail activation and cellular redistribution of PLA₂ during hypotonic cell swelling (102-104). iPLA₂ and particularly cytosolic cPLA₂ may participate in Ca²⁺ store release and activation of ANO6 (103). Notably, iPLA₂ are characterized as being Ca²⁺ independent *in vitro*, but in fact were found to be regulated by Ca²⁺ when studied *in vivo* (105).

ANO6, an osmosensor?

We observed large Cl⁻ currents in ANO6-expressing cells, when the cytosolic Cl⁻ concentration was low (Fig. 2c-e). These currents did not require activation by Ca²⁺ or hypotonic cell swelling. In contrast, high cytosolic Cl⁻ inhibited both baseline and swelling-activated Cl⁻ currents. This has also been observed earlier for Ca²⁺ dependent activation of ANO6 by the Ca²⁺ ionophore ionomycin (29). We therefore propose that ANO6 is regulated by the intracellular Cl⁻ concentration and may therefore operate as a kind of osmosensor. The concept of regulation of I_{Cl-swel} by intracellular osmotic strength has been observed earlier (8;9). Osmosensing by TRP channels (106) is unlikely to explain the present findings, as Cl⁻ regulation of ANO6 currents is also observed in the presence of TRP channel inhibitors (data not shown). We were unable to identify a chloride binding site as described for e.g. Na⁺/Cl⁻ dependent transporters (107). It will be interesting to determine whether chloride sensitive

WNK (with no lysine [K]) kinase is controlling ANO6 activity. In fact a role of WNK3 on intracellular chloride concentration and volume regulation in HEK293 cells has been suggested earlier (108).

ANO6 and VRAC

The present data suggest that I_{Cl-swell} produced by ANO6, and the “classical” VRAC are functionally related. In fact there is no discernible difference between I_{Cl-swell} described here and VRAC, except of the pronounced difference in time dependence. In our experiments VRAC-typical time-dependent inactivation was preferentially observed when Ca²⁺-access was limited, either by removal of extracellular Ca²⁺, inhibition of Ca²⁺ influx by TRP channel blockers, or strong depolarization of the membrane voltage. The present study does not address the contribution of LRRC8A, the essential component of VRAC identified recently (13;14).

The present data identify ANO6 as a cell swelling activated anion channel and uncover a new mechanism of activation through membrane depletion of unsaturated sn-2 fatty acids and accumulation of lysophospholipids. The recently provided structure of TMEM16 from the fungus *Nectria haematococca* suggests poor accessibility of Ca²⁺ to the Ca²⁺-binding site (21). Membrane tension induced by accumulation of lysophospholipids could induce a conformational change and thereby improve accessibility for Ca²⁺ ions.

The *Ano6* null animals show a largely reduced survival rate. About 70% die before or briefly after birth, due to internal bleedings and massive malformations or asphyxia, respectively. Interestingly, the 30% survivals show expression of a splice variant of ANO6. We generated this splice variant *in vitro*, which produced normal Ca²⁺ activated whole cell currents when expressed in HEK293 cells (data not shown). The surviving animals demonstrate bone mineralization defects (80), enhanced bleeding time (27) and macrophage defects (76). Thus ANO6 is protein essential for survival and proper organ function.

Acknowledgments

Supported by DFG SFB699-A7/A12, DFG KU756/12-1, Sander-Stiftung 2013.031.1 and

Volkswagenstiftung AZ 87 499. We thank Dr. Johan Heemskerk and Dr. Eduard Bevers for supplying the lymphocyte cell lines. The excellent technical assistance by Mss. B. Wild, P. Seeberger, E. Tartler, Inês Cabrita and Mr. Simon Höllner is gratefully acknowledged.

CHAPTER 3

A coding variant of *ANO10*, affecting volume regulation of macrophages, is associated with *Borrelia* seropositivity

Abstract

In a first genome-wide association study (GWAS) approach to anti-*Borrelia* seropositivity, we identified two significant single nucleotide polymorphisms (SNP) (rs17850869, $P=4.17E-09$; rs41289586, $P=7.18E-08$). Both markers, located on chromosomes 16 and 3, respectively, are within or close to genes previously connected to spinocerebellar ataxia. The risk SNP rs41289586 represents a missense variant (R263H) of anoctamin10 (*ANO10*), a member of a protein family encoding Cl^- channels and phospholipid scramblases. *ANO10* augments volume regulated Cl^- currents (I_{Hypo}) in *Xenopus* oocytes, HEK293 cells, lymphocytes and macrophages and controls volume regulation by enhancing regulatory volume decrease (RVD). *ANO10* supports migration of macrophages, and phagocytosis of spirochetes. The R263H variant is inhibitory on I_{Hypo} , RVD and intracellular Ca^{2+} signals, which may delay spirochete clearance, thereby sensitizing adaptive immunity. Our data demonstrate for the first time that *ANO10* has a central role in innate immune defense against *Borrelia* infection.

Keywords: Anoctamin 10, Volume regulation, *Borrelia*, RVD

Published in: Hammer C, Wanitchakool P, Sirianant L, Papiol S, Monnheim M, Faria D, Ousingsawat J, Schramek N, Schmitt C, Margos G, Michel A, Kraiczy P, Pawlita M, Schreiber R, Schulz TF, Fingerle V, Tumani H, Ehrenreich H, Kunzelmann K.. A coding variant of *ANO10*, affecting volume regulation of macrophages, is associated with *Borrelia* seropositivity. *Mol Med*. 2015 Feb 23;21:26-37.

Own experimental contribution: All patch clamping and double electrode voltage clamp experiments, and part of calcium measurements.

Own written contribution: Methods, Results, Parts of Introduction and Discussion.

Other contributions: Designed experiments and analyzed data.

Introduction

Lyme borreliosis, caused by bacteria mainly transmitted by ticks of the species *Ixodes*, is the most common tick-borne disease in Europe and the United States (109). It involves many organs, predominantly skin, musculoskeletal system, heart, and nervous system (110). Central nervous system manifestations can imitate a broad range of neuropsychiatric syndromes (111), in rare cases even be indistinguishable from acute schizophrenia (112). Borreliosis is caused by a variety of species of *Borrelia burgdorferi* sensu lato complex, some of which show distinct differences in their pathogenic properties in the human host (113). *Borrelia* species have a highly complex genomic structure, and genetic variation may account for a large proportion of the variability of pathogenicity (114). However, pathogens are not only depending on their own fitness for a successful establishment of infection, but also on the genetic makeup of their hosts. The recent years have witnessed a wealth of studies elucidating the important role of human genomic variation in host defense mechanisms, both for viral and bacterial infections (115). Given the immense phenotypic variation of *Borrelia* disease symptoms, it is likely that part of it is due to differences in human immune response, originating in genomic variation. We therefore set out to (i) identify host genomic variants mediating differential susceptibility to *Borrelia* infection/seropositivity by means of a genome-wide association study (GWAS) and (ii) uncover a possible contribution of *Borrelia* seropositivity to core phenotypes of neuropsychiatric disorders. For advancing these objectives, we employed the Göttingen Research Association for Schizophrenia (GRAS) sample (116;117) comprising 1,271 healthy blood donors and 1,224 patients suffering from neuropsychiatric disease.

Material and Methods

Participants: All subject data were collected in accordance with ethical guidelines and the Helsinki Declaration. Regarding the **discovery sample** (total of N=2,495), subject selection was unbiased, i.e. sera collection concluded before specific serological analysis was planned: Schizophrenic patients (N=1,076) were recruited in 2005-2011 at 23 German sites for the

GRAS (Göttingen Research Association for Schizophrenia) data collection. Patients fulfilling DSM-IV criteria for schizophrenia (81.4%) or schizoaffective disorder (18.6%) were included regardless of disease stage (116;118). Healthy GRAS controls were anonymized blood-donors (N=1,271; Transfusion Medicine, Göttingen). Health was ensured by pre-donation screening (questionnaires, interviews, hemoglobin, blood pressure, pulse, temperature). Patients with affective disorders (N=146) were also included (ongoing GRAS extension). **Exploration sample** (N=100): In Ulm, a total of 257 patients with documented history of *Borrelia* infection were contacted in written form, resulting in 100 individuals interested to participate. The study included: (a) A comprehensive history on tick bite and borreliosis-specific symptoms; (b) a neurological examination with special emphasis on cerebellar signs and (c) drawing of blood for genetic and serological analyses. Patients were classified in 3 subgroups, based on clinical and serological findings: (i) neuroborreliosis, (ii) systemic borreliosis or (iii) laboratory-based borreliosis without typical clinical signs and symptoms.

Phenotypical analyses: Of all schizophrenic (GRAS) patients, extensive phenotypical characterization was conducted as referenced previously (116;118). Age of onset, age at first psychotic episode, positive and negative syndrome scale (PANSS) scores, chlorpromazine equivalents (CPZ), neurological symptoms (CNI; Cambridge Neurological Inventory) including fine motor skills (MacQuarrie dotting/tapping), current cognitive functioning (composite score comprising reasoning, executive function, verbal learning & memory), global assessment of functioning (GAF), Parkinsonism, hard neurological signs, motor coordination, sensory integration, and gait were employed as disease characteristics. Moreover, patient self-rating was performed using the Brief Symptom Inventory (BSI) (119). The Ulm borreliosis patients had a comprehensive clinical neurological, serological and in 81/100 patients also cerebrospinal fluid (CSF) examination. CSF diagnostics included leukocyte and differential cell count, nephelometric determination of total protein, CSF/serum ratios for albumin IgG / IgA / IgM, ELISA for *Borrelia* specific antibodies and oligoclonal IgG analysis in CSF/serum by immunoelectrophoresis.

Serological analyses: The presence of antibodies against *Borrelia* was first determined using

Enzygnost Lyme link VlsE/IgG, a quantitative immunoenzymatic method based on a mix of native *Borrelia* antigens from *B. afzelii* strain PKo and recombinant VlsE obtained from three genospecies pathogenic to humans (*B. Burgdorferi* sensu stricto, *B. garinii*, *B. afzelii*) (Siemens Healthcare-Diagnostics GmbH, Eschborn, Germany). Assays were automatically processed on BEP®III (Siemens Healthcare-Diagnostics GmbH), and interpreted (manufacturer's instructions) as positive, negative or borderline. Positive and borderline samples were re-analyzed using the EUROLINE *Borrelia*-RN-AT Immunoblot (Euroimmun, Lübeck, Germany). Only the confirmed were defined seropositive for statistical analysis and contrasted against all others. Titer levels, when mentioned in the manuscript, refer to the ELISA results. To test for specificity of association signals, the following immunoenzymatic assays were conducted: Novagnost Chlamydia pneumoniae IgG, Novagnost Chlamydia trachomatis IgG, Novagnost Mycoplasma pneumoniae IgG, Enzygnost Anti-Helicobacter pylori/IgG (all Siemens Healthcare-Diagnostics GmbH).

Genetic analyses: A semi-custom Axiom®myDesign™ genotyping array (Affymetrix, Santa Clara, CA, USA) was used. Array specifications and quality controls have been described in detail before (117). Principal components were generated using GCTA (v1.24) (120) and genetic outliers were excluded based on inspection of the first two principal components. Genomic inflation was calculated using PLINK (v1.07) (121) to ensure minimization of population stratification, excluding SNPs in the complex MHC region (chromosome 6, 29-33MB). PLINK was also used for association testing, using the following exclusion criteria: Hardy-Weinberg $P < 5E-07$, minor allele frequency < 0.01 , missingness per marker > 0.05 , and missingness per individual > 0.02 . SNPs on sex chromosomes were excluded from analysis. Variants in high linkage of genome-wide significant SNPs were identified using SNAP Proxy Search (<http://www.broadinstitute.org/mpg/snap/>), using the 1000 Genomes Pilot 1 CEU population panel and a r^2 threshold of 0.8. Patients with confirmed diagnosis of borreliosis (N=100) recruited in Ulm were genotyped using the KASP genotyping system (LGC Genomics, Berlin, Germany), after DNA isolation from blood using the JETQUICK Blood and Cell Culture Kit (Genomed, Loehe, Germany).

Cell culture, animals, cDNAs, site-directed mutagenesis, and transfection: Human *ANO10* cDNA (NM_018075.2) was purchased from OriGene (SC113757, Rockville, MD, USA), and cloned in pcDNA3.1 with a C-terminal His-Tag (Life Technologies, Darmstadt, Germany). R263H-ANO10, L510R-ANO10, L384fs-ANO10, LRRC8A and AQP1 were mutated and cloned, respectively, using standard PCR-techniques. All cDNAs were verified by sequencing. Culturing of HEK293 cells, THP-1 cells and lymphocytes, and isolation of mouse macrophages has been described earlier (76). Site-directed mutagenesis, transfection methods, and other used constructs have been described previously (12).

Fluorescent *Borrelia*: Red fluorescent *B. garinii* PRJS1009-Cherry were used to infect macrophages. In some experiments cells were exposed to TNF α (100ng/ml) for 2–6h. THP-1 monocytes were differentiated into macrophages by incubation with 100nM phorbol 12-myristate 13-acetate (PMA) (Sigma, Munich, Germany) for 48h.

Patch clamping: Cells grown on cover slips were mounted in a perfused bath on the stage of an inverted microscope (IM35, Zeiss, Munich, Germany) and kept at 37°C. The bath was perfused continuously with Ringer solution (mM: NaCl 145, KH₂PO₄ 0.4, K₂HPO₄ 1.6, D-glucose 6, MgCl₂ 1, Ca-gluconate 1.3, pH7.4) at about 10ml/min. Cell swelling was induced by removing 100mM mannitol from an isotonic (300mosmol/l) modified Ringer solution to achieve a hypotonic bath solution (Hypo, 33%, 200mosmol/l). Patch-clamp experiments were performed in the fast whole-cell configuration as described previously (76).

Two electrode voltage clamp: Oocytes were harvested from *Xenopus laevis* according to German regulations governing animal experiments. Oocytes were defolliculated for 1 h at 18°C with 1.5 mg/ml collagenase type V (Sigma). After washing oocytes were injected with cRNA encoding ANO10, R263H-ANO10, and AQP1. Preparation of cRNA and voltage clamping of the oocytes have been described earlier (76).

Measurement of [Ca²⁺]_i: The plasma membrane bound calcium sensor has been modified by the addition of a N-terminal signal peptide (20 aa) from Neuromodulin (PI-G-CaMP2). Addition of this peptide results in posttranslational palmitoylation of the protein, which facilitates anchoring of the protein to the plasma membrane. HEK293 cells were transfected

on coated glass cover slips with pcDNA31 PI-G-CaMP2, and were mounted in a perfusion chamber 48 hrs after transfection. Cells were perfused with Ringer solution at a rate of 8 ml/min at 37°C. Cell fluorescence measurements were measured continuously with an inverted microscope Axiovert S100 (Zeiss) using a x40 objective (Fluar 40x/1.3 Oil, Zeiss) and a high speed polychromator system (VisiChrome, Visitron, Puchheim, Germany). PI-G-CaMP2 was excited at 485 nm and 405 nm. Emission was recorded between 520 and 550 nm using a CCD-camera (CoolSnap HQ, Visitron). Control of experiments, imaging acquisition, and data analysis were done with the software package Meta-Fluor (Universal imaging, New York, USA). Alternatively cells were loaded with Fura2 and intracellular Ca^{2+} concentrations were determined as described earlier (76).

Flow cytometry, single cell volume measurements and migration: Cells were washed and re-dissolved in 10 ml isotonic or hypotonic Ringer solution as described for patch clamp experiments. Cells were analyzed at 37 °C / pH 7.4 using a CASY flow cytometer (Roche Diagnostics, Mannheim, Germany). Cells were analyzed at a density of 10^6 cells/ml. For single cell volume measurements cells were loaded with 1 µg of calcein-AM (Molecular Probes) and 0.01% pluronic in a standard bath solution (Ringer) for 60 min at 20-22 °C. Fluorescence intensity was measured at an excitation wavelength of 485 nm and an emission wavelength of 520–550 nm. Cell swelling and RVD were observed for 10–15 min after applying hypotonic bath solution. Cell migration was assessed in Boyden chambers as described previously (76).

Measurement of TNF α release: THP-1 cells were grown in 96 well plates and, when mentioned, treated with PMA (100nM) for 2 days. Before sample collection, cells were infected with cherry-labeled *B. garinii* (MOI 1:10) for 4h at 37°C. Following a centrifugation step the supernatant was collected and immediately stored at -20°C. TNF α was measured using Platinum ELISA kit (eBioscience Affymetrix, Vienna, Austria) according to manufacturer's instructions.

Phagocytosis assay: THP-1 cells were treated with PMA (100nM) for 2 days. Cells were infected with cherry-labeled *B. garinii* (MOI 1:10) at 37°C. After infection cells were washed

with PBS to remove remaining *Borrelia*. Cells were visualized and fluorescence was detected using an Axiovert 200 microscope/AxioVision software (Zeiss) and mean fluorescence intensity was quantified.

Annexin V binding assay. THP-1 cells treated with PMA (100nM, 48h) were grown in a 96-well plate. Cells were washed twice with cold PBS and incubated with annexin V-FITC for 15min at room temperature (FITC Annexin V Detection Kit, BD Biosciences, Heidelberg, Germany). Fluorescence intensity was detected using a plate reader (Novostar, BMG Labtech, Ortenberg, Germany). Cells were treated with TNF α (10ng/ml, 4hr) or with cherry-labeled *B. garinii* (MOI 1:10) for 4h, followed by washing with PBS and fluorescence detection, considered as time point zero. For other time points, the cells were washed to remove the remaining *Borrelia*, and kept with fresh media for the following days after infection.

Western blotting, biotinylation and immunocytochemistry: Protein was isolated from THP-1 cells grown in the absence or presence of PMA (100nM) and transfected with siRNA-ANO10 (ID# s30237, s30238, Ambion, Life Technologies, Darmstadt, Germany). Cells were lysed using lysis buffer containing 150mM NaCl, 50mM Tris, 1mM EDTA, 100mM DTT, 0,5% NP-40, and 1% protease inhibitor cocktail (Roche, Mannheim Germany). Protein separation, transfer, blotting and detection have been described previously (76). A polyclonal rabbit anti-Ano10 antibody (Aviva Systems Biology, San Diego, USA) was used at a dilution of 1:500. Rabbit anti β -actin antibody (Sigma-Aldrich, Taufkirchen, Germany) was used at a dilution of 1:1000. For biotinylation of plasma membrane proteins EZ-Link Sulfo-NHS-SS-Biotin (#89881, Pierce, Thermo Fisher Scientific, Waltham, USA) was prepared at a concentration of 1mg/ml in ice-cold phosphate-buffered saline (PBS). Biotinylated cells were lysed and 100 μ l streptavidin beads (Thermo Fisher Scientific, Waltham, USA) were added to the supernatant after centrifugation. After incubation ON at 4 °C, beads were washed 5 times with cold lysis buffer and biotinylated proteins were eluted by boiling the sample for 5 min at 95°C in SDS sample buffer. For immunocytochemistry of ANO10 the anti-ANO10 antibody was used at a dilution of 1:500.

Statistics: Group differences in categorical and continuous variables were assessed using Chi-

square or Mann-Whitney U tests. A generalized linear model was employed upon covariate inclusion. At normal distribution of continuous variables, T-tests were performed (paired and unpaired tests, respectively, for experiments in oocytes, HEK293 cells, lymphocytes and macrophages). A basic allelic test, implemented in PLINK was used to test for association between single nucleotide polymorphisms (SNPs) and *Borrelia* serological status. *P*-values < 0.05 were considered significant and multiple-testing corrected (Bonferroni) where indicated, but are displayed uncorrected. Data in Figures are expressed as mean ± SEM, in Tables as mean ± SD.

Results

Borrelia seropositivity in health and neuropsychiatric disease

We detected anti-*Borrelia* antibodies (AB) in 169 out of 2,495 individuals in total (6.8%) (Table 1).

Table 1. Cross-sectional prevalence of anti-*Borrelia* antibodies.

Study group	Anti- <i>Borrelia</i> AB status, N (%)			<i>P</i> (Pearson χ^2) ^a
	Seropositive	Seronegative	Total	
GRAS patients (schizophrenia)	85 (7.9)	991 (92.1)	1,076 (100)	0.05
Affective disorder patients ^b	16 (10.8)	132 (89.2)	148 (100)	0.07
GRAS controls (healthy subjects)	68 (5.4)	1,203 (94.6)	1,271 (100)	
Total	169 (6.8)	2,326 (93.2)	2,495 (100)	

^aCorrected for age and sex. *P* values represent results of χ^2 tests, comparing the respective patient sample with healthy controls.

^bIncluded are patients with monopolar or bipolar depression.

AB prevalence tended to be higher in schizophrenia patients (7.9%, *P*=0.05) and affective disorder patients (11.0%, *P*=0.07), when compared to psychiatrically healthy controls (5.4%). *P* values are corrected for sex and age, since male subjects are more likely to be seropositive than females (8.2% vs. 4.3%, *P*=1.96E-04, OR=1.98, Supplementary Table 1). Furthermore, groups differ significantly in mean age (Supplementary Table 2), which has to be considered because the likelihood of a past *Borrelia* infection and subsequent antibody formation increase with age (Supplementary Figure 1). We did not find a difference in mean titer levels of seropositive subjects between patient groups and controls (Supplementary Table 3).

Supplementary Table S1. Gender distribution by serostatus.

Gender	<i>Borrelia</i> antibody status - N (%)			P-value (OR, (CI)) chi ² , d.f. = 1
	Seropositive	Seronegative	Total	
Male	129 (8.2)	1,441 (91.8)	1,570 (100)	1.86-04 (1.98, (1.38 - 2.85))
Female	40 (4.3)	885 (95.7)	925 (100)	
TOTAL	169 (6.8)	2,326 (93.2)	2,495 (100)	

OR, odds ratio; CI, 95% confidence interval.

Supplementary Table S2. Mean age of study cohorts by serostatus.

Study group	<i>Borrelia</i> antibody status - Mean age in years (SD)		
	Seropositive	Seronegative	Total
Schizophrenia patients	42.5 (13.3)	39.2 (12.5) *	39.5 (12.6) *
Affective disorder patients	61.3 (15.2) *	48.3 (15.0) *	49.7 (15.5) *
Healthy controls	42.2 (14.1)	37.1 (13.1)	37.4 (13.2)
TOTAL	44.1 (14.8)	38.7 (13.2)	39.0 (13.4)

* denotes significant difference ($p \leq 0.05$) of patient group versus respective controls. P values were calculated using 2-tailed independent samples *t*-tests, equal variances not assumed in case of significant Levene's test. SD, standard deviation.

Supplementary Table S3. Anti-borrelia antibody titer distribution.

Study group (seropositives)	Mean	SD	P (GLM), corrected for gender & age
Schizophrenia patients (N=85)	165,998	184,900	0.376
Affective disorder patients (N=16)	118,063	93047	0.339
Healthy controls (N=68)	149,429	166,065	
TOTAL (N=169)	154,793	170,496	

P values represent association results, comparing the respective patient sample with healthy controls. SD, standard deviation; GLM, generalized linear model.

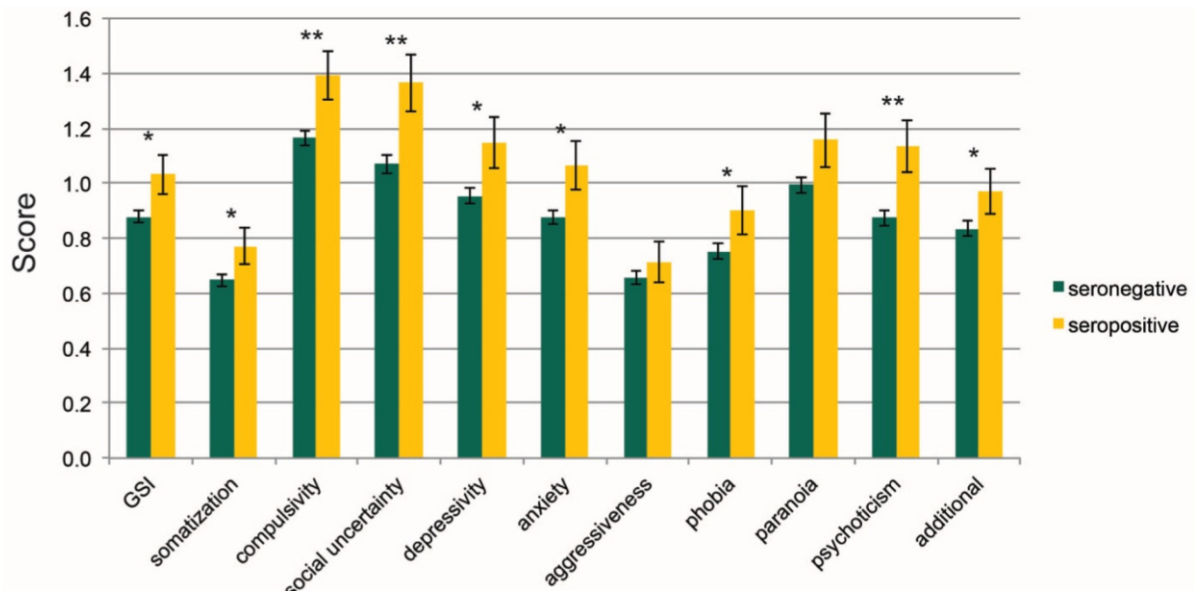
Overall, seropositive and seronegative schizophrenia patients do not show differences with respect to major disease phenotypes of schizophrenia including neurological signs as determined by the Cambridge Neurological Inventory (CNI), which should also cover symptoms of borreliosis (Supplementary Table 4). Interestingly, however, AB carriers score significantly worse throughout all scales of the Brief Symptom Inventory (BSI, corrected for age and sex as a proxy for gender) (119), an instrument based on patients' self-evaluation

(Supplementary Figure 2)

Supplementary Table S4. Baseline characteristics, according to study group.

Patient and control groups	Total sample	Borrelia-AB +	Borrelia-AB -	P (χ^2 , Z, T value) ^o
Schizophrenia patients (GRAS)	N=874-1,076 ^b	N=72-85 ^b	N=802-991 ^b	
Age, y, Mean±SD, (range)	39.46±12.59 (17-79)	42.47±13.30 (19-75)	39.21±12.50 (17-79)	0.032 (Z=-2.14)
Gender, N male (%)	721 (67.0)	62 (72.9)	659 (66.5)	0.225 ($\chi^2=1.47$)
Prodrome, N cases (%)	753 (81.0)	61 (82.4)	692 (80.8)	0.738 ($\chi^2=0.11$)
Age at first episode, y, Mean±SD, (range)	26.44±8.89 (5-68)	26.77±8.78 (15-51)	26.41±8.91 (5-68)	0.625 (Z=-0.49)
PANSS positive score, Mean±SD, (range)	13.73±6.25 (7-38)	13.78±6.31 (7-34)	13.72±6.24 (7-38)	0.962 (Z=-0.05)
PANSS negative score, Mean±SD, (range)	18.24±7.93 (7-46)	19.04±7.88 (7-37)	18.17±7.93 (7-46)	0.293 (Z=-1.05)
PANSS general score, Mean±SD, (range)	33.73±11.78 (16-82)	34.88±11.33 (16-75)	33.63±11.81 (16-82)	0.230 (Z=-1.20)
Current chlorpromazine equivalents (CPZ), Mean±SD, (range)	685.38±698.08 (0-7375)	602.90±492.97 (0-2925)	692.36±712.48 (0-7375)	0.620 (Z=-0.50)
Cambridge Neurological Inventory (CNI) ^{c,d} , Mean±SD, (range)	0.00±1.00 (-2.08-13.80)	0.01±0.86 (-1.82-2.37)	0.00±1.01 (-2.08-13.80)	0.897 (T=-0.13)
MacQuarrie Dotting ^e , Mean±SD, (range)	0.00±1.00 (-3.49-3.51)	0.04±0.98 (-1.83-3.51)	0.00±1.00 (-3.49-3.06)	0.695 (T=-0.39)
MacQuarrie Tapping ^e , Mean±SD, (range)	0.00±1.00 (-4.76-4.03)	0.17±1.00 (-1.69-3.71)	-0.01±1.00 (-4.76-4.03)	0.114 (T=-1.58)
Cognitive Composite score ^e , Mean±SD, (range)	-0.01±0.84 (-2.57-2.98)	-0.09±0.96 (-2.12-1.93)	-0.01±0.83 (-2.57-2.98)	0.390 (T=0.86)
Global Assessment of Functioning (GAF), Mean±SD, (range)	45.76±17.20 (5-90)	44.74±17.23 (8-90)	45.84±17.20 (5-90)	0.490 (Z=-0.69)
Healthy controls (GRAS)	N=1,271	N=68	N=1,203	
Age, y, Mean±SD, (range)	37.42±13.42 (18-69)	42.41±14.14 (19-67)	37.15±13.14 (18-69)	0.003 (Z=-3.01)
Gender, N male (%)	779 (61.3)	58 (85.3)	721 (59.9)	<0.001 ($\chi^2=17.45$)
Affective disorder patients	N=148	N=24	N=124	
Age, y, Mean±SD, (range)	49.68±15.49 (20-92)	61.31±15.16 (44-92)	48.27±14.98 (20-87)	0.004 (Z=-2.86)
Gender, N male (%)	70 (47.3)	9 (56.3)	61 (46.2)	0.448 ($\chi^2=0.58$)

Abbreviations: AB, antibody; CPZ, chlorpromazine equivalents; GAF, global assessment of functioning; GRAS, Göttingen Research Association for Schizophrenia; PANSS, positive and negative syndrome scale. Bolded values, P<0.05. ^oAs statistical methods, Mann-Whitney U or χ^2 tests, and for normally distributed variables, F-tests were used. ^bDue to missing data, sample sizes vary. ^cCambridge Neurological Inventory mean value if more than 95 items were available. ^dCorrected for age and CPZ. ^eCorrected for age, PANSS negative score and CPZ.



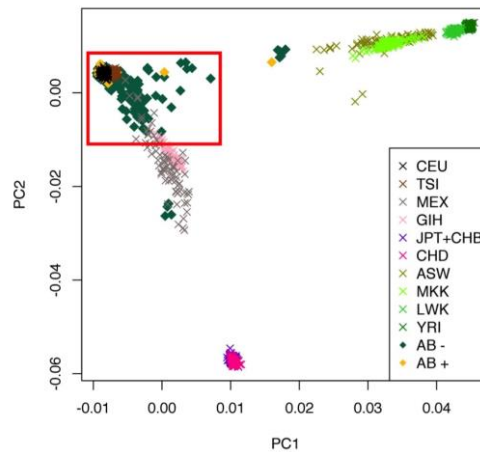
Supplementary Figure 2: Brief symptom inventory (BSI) patient self-assessment

GSI, global severity index; *, P<0.05; **, P<0.005

Reference: Franke, G.H. *Brief Symptom Inventory*, (Beltz, Göttingen, 2000).

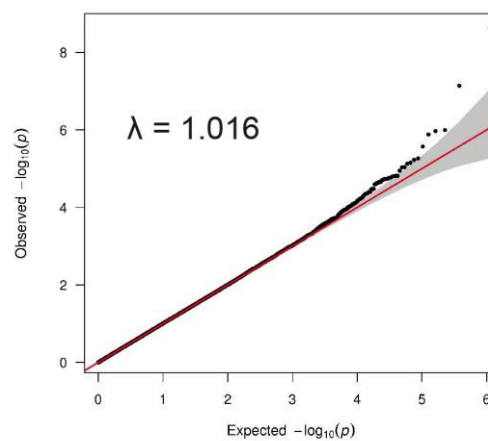
GWAS on *Borrelia* antibody seropositivity

In a principal component analysis, 19 subjects showed non-European ancestry, and were consequently excluded from genetic analyses (Supplementary Figure 3).



Supplementary Figure 3: *Principal component analysis, removal of genetic outliers*

Study participants are displayed together with Hapmap version3 r2 samples, according to their first two principal components (PC1, PC2). All subjects clustering outside the red rectangle were excluded from genetic analyses. ASW, African ancestry in Southwest USA; CEU, Utah residents with Northern and Western European ancestry from the CEPH collection; CHB, Han Chinese in Beijing, China; CHD, Chinese in Metropolitan Denver, Colorado; GIH, Gujarati Indians in Houston, Texas; JPT, Japanese in Tokyo, Japan; LWK, Luhya in Webuye, Kenya; MXL, Mexican Ancestry in Los Angeles, California; MKK, Maasai in Kinyawa, Kenya; TSI, Toscani in Italia; YRI, Yoruba in Ibadan, Nigeria; AB -, anti-*Borrelia* negative; AB +, anti-*Borrelia* positive.



Supplementary Figure 4: *Quantile-quantile plot for assessment of population stratification*

Quantile-quantile plot of association results. For each tested variant, the $-\log_{10}$ P-value is plotted against the null distribution (red line, 95% confidence intervals in gray). The highly complex MHC region (chromosome 6, 29-33MB) was removed for assessment of population stratification. λ , genomic inflation factor.

We finally analyzed a total of 2,376 individuals with available complete genotype and serological data, fulfilling all inclusion criteria. Of these, 162 (6.8%) were seropositive, and 2,214 (93.2%) seronegative. Using an allelic model, 580,108 autosomal SNPs were tested, and genomic inflation was low ($\lambda=1.016$, Supplementary Figure 4). Two SNPs (rs17850869, rs41289586) exceeded the threshold for genome-wide significance, when correcting for the number of tested SNPs ($P=8.62E-08$, Figure 1). A list of 11 SNPs with $P<1.0E-05$ is provided as Supplementary Table 5, including minor allele frequencies, association statistics, positions, and SNP classifications.

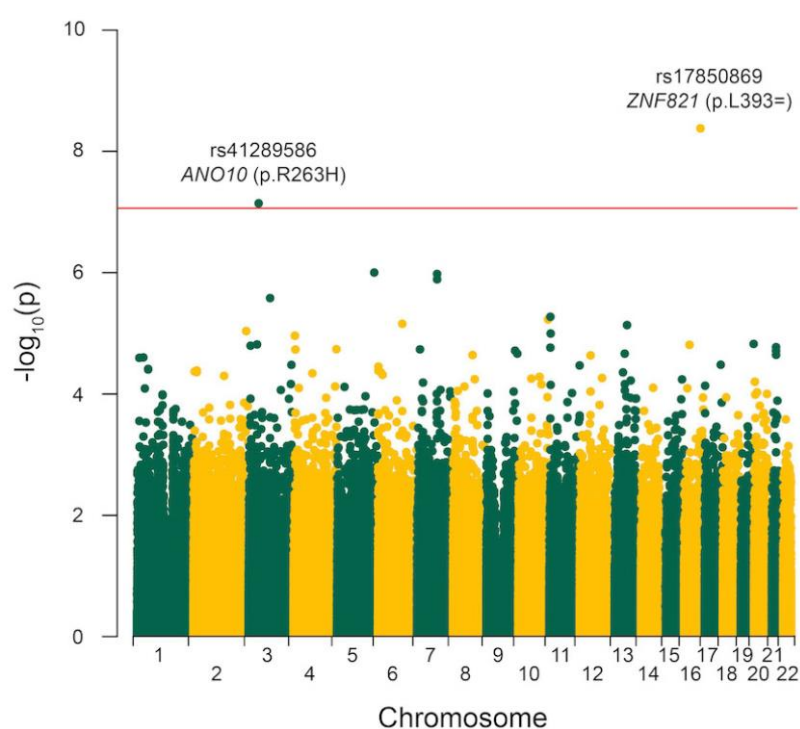


Figure 1: Manhattan plot of genome-wide association analysis. The red horizontal line designates the threshold for genome-wide significance, corrected for number of tested SNPs.

Supplementary Table S5. GWAS hits $P<1.0E-05$.

SNP	Chr.	Mb	Major / minor allele	MAF patients	MAF controls	P (allelic)	OR (95% CI)	Gene (RefSeq, hg19)	Distance (kb)	Class
rs17850869	16	71.9	C/T	0.043	0.008	4.17E-09	5.36 (2.87-10.02)	<i>ZNF821</i>	intragenic	synonymous
rs41289586	3	43.6	C/T	0.071	0.022	7.18E-08	3.38 (2.11-5.39)	<i>ANO10</i>	intragenic	missense
rs4527629	5	163.5	A/G	0.142	0.068	9.95E-07	2.25 (1.61-3.14)	<i>MAT2B</i>	522.4	
rs10267374	7	88.6	C/T	0.247	0.146	1.05E-06	1.92 (1.47-2.51)	<i>ZNF804B</i>	intragenic	intronic
rs10232922	7	88.6	A/G	0.259	0.156	1.29E-06	1.89 (1.46-2.45)	<i>ZNF804B</i>	intragenic	intronic
rs17749281	3	94.2	T/G	0.367	0.249	2.62E-06	1.75 (1.38-2.22)	<i>NSUN3</i>	307.8	
rs2499955	11	5.0	C/T	0.219	0.13	5.33E-06	1.89 (1.43-2.49)	<i>OR51L1</i>	5.6	
rs34796938	10	130.3	C/T	0.103	0.046	5.90E-06	2.38 (1.62-3.51)	<i>PREX2</i>	intragenic	intronic
rs7755387	6	106.2	G/T	0.117	0.056	7.00E-06	2.25 (1.57-3.23)	<i>PRDM1</i>	297.7	
rs4883922	13	73.7	C/T	0.345	0.234	7.30E-06	1.72 (1.36-2.19)	<i>KLF5</i>	2.2	
rs12616914	2	232.0	T/C	0.084	0.035	9.20E-06	2.54 (1.66-3.88)	<i>PSMD1</i>	intragenic	intronic

SNP, single nucleotide polymorphism; Chr., chromosome; Mb, mega base pairs; MAF, minor allele frequency; OR, odds ratio; CI, confidence interval; kb, kilo base pairs.

Genome-wide significant hits

Both genome-wide significant SNPs show a low minor allele frequency in seronegative subjects, which is significantly higher in AB carriers (rs17850869: 0.008 versus 0.043; rs41289586: 0.022 versus 0.071, Supplementary Table 5). Genotype distributions are presented in Table 2, where we also display results using additional open-access resources from the 1000 Genomes Project (122) and the Exome Variant Server (NHLBI GO Exome Sequencing Project (ESP), Seattle, WA, URL: <http://evs.gs.washington.edu/EVS/>, access date: July 17, 2014). Overall, these data are highly similar to the distribution in our seronegative population; hence an under-representation of the minor alleles is unlikely to be the source of association. As an exception, the MAF of rs17850869 is higher in the European 1000 Genomes Project study participants (MAF=0.022). This may, however, be a bias of the small number of individuals included there (Table 2).

Table 2. Genotypes and MAFs of GWAS hits.^a

Subjects or populations according to reference SNP ID	Genotypes			MAF	<i>P</i> ^b (allelic test) (OR, (95% CI))
	CC	CT	TT		
rs17850869					
Seropositive	148	14	0	0.043	
Seronegative	2,177	37	0	0.008	4.17E-09 (5.36, (2.87–10.02))
1000g (CEU)	80	5	0	0.029	0.449 (1.49, (0.53–4.21))
1000g (EUR)	362	17	0	0.022	0.061 (1.97, (0.96–4.04))
EVS (EA)	4,148	50	2	0.006	1.50E-13 (6.98, (3.84–12.70))
rs41289586					
Seropositive	140	21	1	0.071	
Seronegative	2,118	96	1	0.022	7.18E-08 (3.38, (2.11–5.39))
1000g (CEU)	80	5	0	0.029	0.058 (2.52, (0.94–6.76))
1000g (EUR)	362	17	0	0.022	1.1E-04 (3.33, (1.75–6.32))
EVS (EA)	4,074	222	4	0.027	2.47E-06 (2.78, (1.78–4.33))

One of the two genome-wide significant SNPs, rs17850869, is a synonymous coding variant of zinc finger protein 821, encoded by the *ZNF821* gene on chromosome 16 (NP_001188482.1, p.Leu393), and associated with a P value of 4.17E-09 (OR=5.36). It is in complete linkage with only one other SNP, rs74944699, an intronic variant in *PMFBP3*. Of note, the gene upstream of *ZNF821* is *ATXNIL* (ataxin 1-like), a paralog of *ATXN1* (ataxin 1),

which is associated with spinocerebellar ataxia type 1 (SCA1) (123).

The other SNP, rs41289586 ($P=7.18E-08$, $OR=3.38$), is a missense variant of anoctamin 10, encoded by the gene *ANO10* (NP_060545.3, p.R263H) on chromosome 3. It shows linkage ($r^2>0.8$) with two intronic SNPs, rs62250916 in *ANO10*, and rs11926254 in *SNRK*. Using software tools for a prediction of the effect of amino acid substitutions on protein function, the ANO10-R263H variant was predicted to be ‘probably damaging’ (score 1.000) by PolyPhen-2 (<http://genetics.bwh.harvard.edu/pph2/>), ‘deleterious’ (score -4.66) by PROVEAN, and ‘damaging’ (score 0.000) by SIFT (both <http://provean.jcvi.org/>). Notably, also mutations in *ANO10* were reported to be causative for spinocerebellar ataxia (46;124).

We investigated, but did not find an association of either SNP with antibodies against several other bacterial infections (*Helicobacter pylori*, *Mycoplasma pneumoniae*, *Chlamydia pneumoniae*, *Chlamydia trachomatis*). They were also not associated with a sum score including all five serological tests against bacterial infections in a linear regression model (Supplementary Table 6). Both SNPs are not found on commonly used genotyping arrays, and were thus not included previously in GWAS investigating other phenotypes. In our study cohort, they were not associated with the diagnosis of schizophrenia (rs41289586: $P_{\text{allelic}}=0.11$, rs17850869: $P_{\text{allelic}}=0.28$).

Supplementary Table S6. Association of genome-wide significant hits with other bacterial infections.

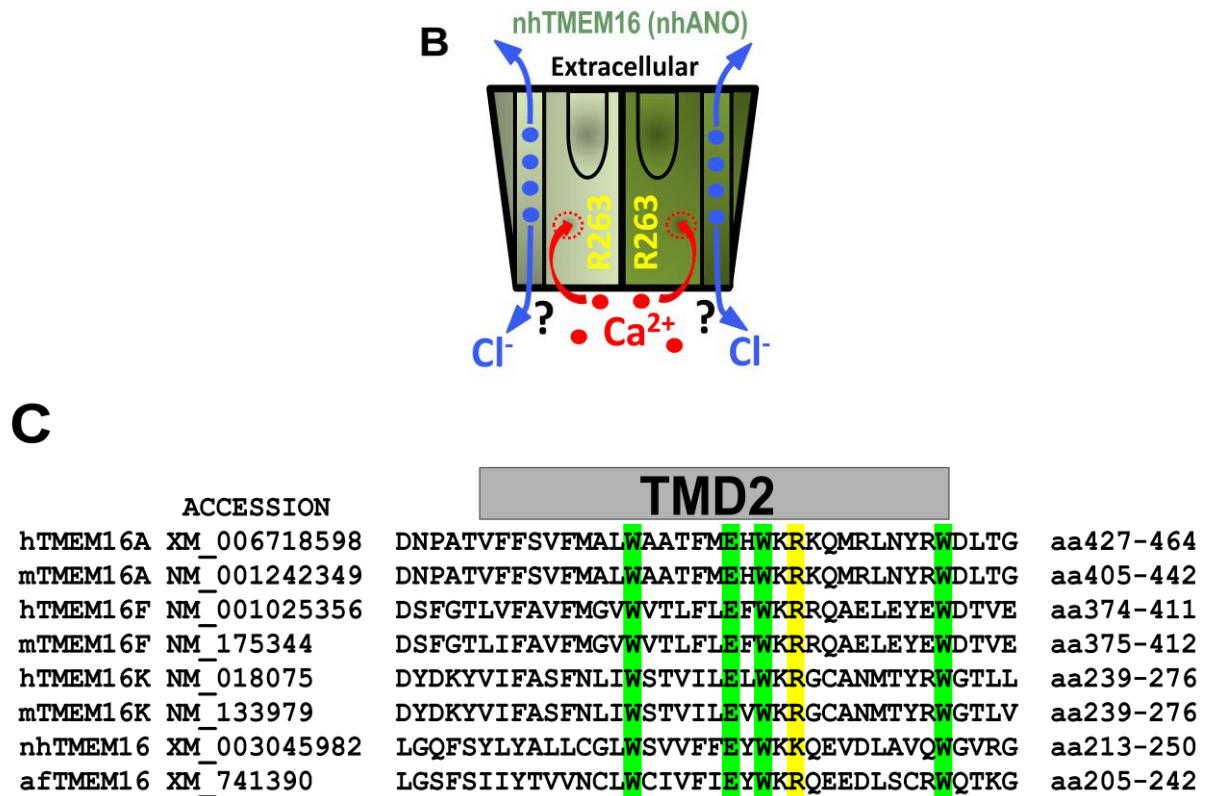
Pathogen	rs41289586	rs17850869
	<i>P</i> (allelic) (OR, (95% CI))	<i>P</i> (allelic) (OR, (95% CI))
<i>Borrelia</i>	7.18E-08 (3.38, (2.11-5.39))	4.17E-09 (5.36, (2.87-10.02))
<i>Helicobacter pylori</i>	0.64 (0.90, (0.59-1.39))	0.55 (0.82, (0.42-1.58))
<i>Mycoplasma pneumoniae</i>	0.51 (0.89, (0.62-1.26))	0.59 (1.16, (0.68-1.97))
<i>Chlamydia pneumoniae</i>	0.77 (1.06, (0.71-1.57))	0.81 (0.93, (0.51-1.71))
<i>Chlamydia trachomatis</i>	0.54 (0.87, (0.54-1.38))	0.32 (1.36, (0.74-2.50))
	<i>P</i> (linear regression) (BETA, (95% CI))	<i>P</i> (linear regression) (BETA, (95% CI))
ALL except <i>Borrelia</i> (sum score: 0-4)	0.34 (-0.14, (-0.41-0.14))	0.35 (0.20, (-0.22-0.62))

OR, odds ratio; CI, confidence interval.

Compromised cellular volume regulation by ANO10-R263H

ANO10 belongs to a family of 10 proteins which operate as Cl^- channels and phospholipid scramblases (20;22;23;39;73). Structural insights into TMEM16/noctamin proteins were provided recently (21). R263 is located close to the dimer interface and is well

conserved within the anoctamin family and between species (Supplementary Fig. 8B,C).



Supplementary Figure 8: *ANO10* in macrophages, putative structure and location of R263 **B)** Putative structure of nhTMEM16 which exists as a dimer, and location of R263 close to dimerization interface. It is currently unclear whether the two lateral subunit cavities, which serve as conductive pores for polar head groups of phospholipids during phospholipid scrambling, also form Cl⁻ conducting channels. Activation by Ca²⁺ requires Ca²⁺ to move to their binding sites deep in the membrane localized part of nhTMEM16 (Brunner et al.: X-ray structure of a calcium-activated TMEM16 lipid scramblase (2014) Nature). **C)** R263 is located in the putative 2. Transmembrane domain. R263 (related to Ano10) is conserved in ANO1, ANO6, ANO10 and afTMEM16 (highlighted in yellow). In nhTMEM16 R (Arg)263 is replaced by K (Lys) (Higgins et al: Improving the sensitivity of progressive multiple sequence alignment through sequence weighting, positionspecific gap penalties and weight matrix choice. (1994) Nucleic Acids Research).

Anoctamins have been reported earlier to be relevant for cellular volume regulation (12;34;37), which is essential for cell migration and immune defense (125). Anoctamins may be part of a channel or regulatory complex that produce volume regulated anion currents (I_{Hypo}) activated by hypotonic bath solution (Hypo). An essential component of such a complex has been identified as LRRC8 (13;14). We examined the role of ANO10 for volume regulation by coexpression with aquaporin 1 in *Xenopus* oocytes, which swell and eventually burst when exposed to Hypo (85). Expression of ANO10, but not R263H-ANO10, produced

large outwardly rectifying whole cell currents (I_{Hypo}) when oocytes were exposed to Hypo (Fig. 2A,B). Coexpression of R263H-ANO10 together with ANO10 suppressed activation of I_{Hypo} (Fig. 2C). Moreover, bursting of oocytes due to Hypo-induced swelling was reduced by ANO10 but not by R263H-ANO10 (Fig. 2D). Noteworthy, activation of phospholipase A2 by melittin, a known activator of I_{Hypo} , also activated ANO10. Moreover, coexpression of LRRC8A, which itself induced I_{Hypo} , did not further augment I_{Hypo} produced by ANO10 (Fig. 2E,F). Taken together, ANO10 but not R263H-ANO10 generates swelling activated whole cell currents in oocytes.

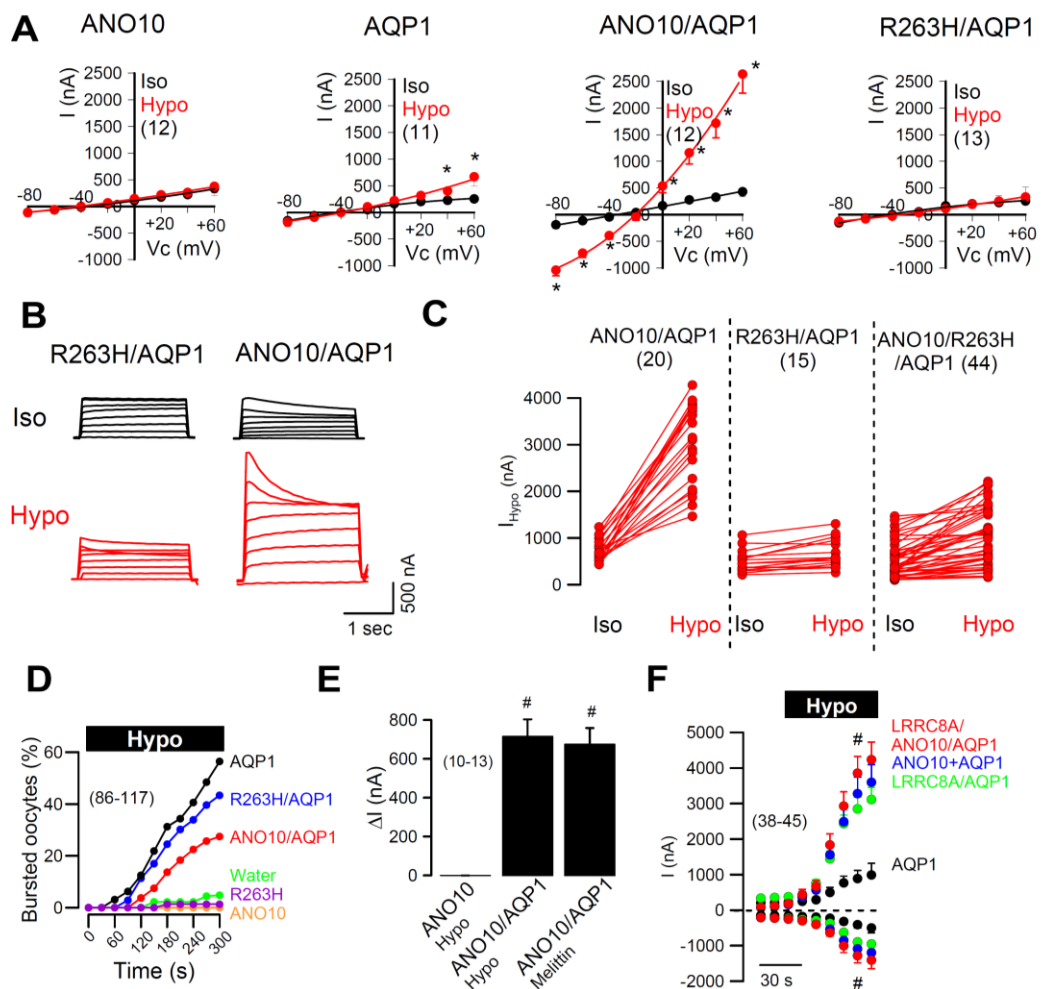


Figure 2: ANO10 but not R263H-ANO10 generates volume activated whole cell currents in *Xenopus* oocytes. **A)** Current/voltage relationships of whole cell currents activated by cell swelling (I_{Hypo} , 50 % reduced extracellular osmolarity) in *Xenopus* oocytes. R263H-ANO10 does not produce I_{Hypo} . **B)** Current overlay ($V_c = \pm 100$ mV) demonstrates typical time dependent inactivation of I_{Hypo} . **C)** I_{Hypo} in oocytes expressing AQP1/ANO10, AQP1/ANO10-R263H, and AQP1/ANO10/ANO10-R263H, respectively. Coexpression of ANO10-R263H suppressed currents produced by wt ANO10. **D)** Oocyte bursting after exposure to hypotonic bath solution. Fraction of bursted oocytes was reduced by expression of ANO10. Oocytes survived in the

absence of AQP1. **E**) Summary of whole cell currents activated by Hypo and the PLA₂-activator melittin (100 nM). **F**) Summary of time dependent activation of whole cell currents in cells expressing ANO10, LRRC8A, or coexpressing both. All oocytes expressed AQP1. Mean \pm SEM (number of oocytes); *significant activation by Hypo (paired t-test). #significant difference to ANO10 and ANO/AQP1, respectively (unpaired t-test).

We also expressed ANO10 in HEK293 cells and found enhanced whole cell currents activated by Hypo, which were inhibited by typical anoctamin blockers such as NPPB, NS3728, and T_{inh}AO1 (Fig. 3A,B). Currents could not be activated in the complete absence of Ca²⁺, but were augmented, along with an increase in volume regulation (regulatory volume decrease, RVD), when only extracellular Ca²⁺ was reduced to 0.1 μ M (Fig. 3C, Supplementary Fig. S5A,B). I_{Hypo} was inhibited by arachidonic acid, confirming earlier reports (126), and was controlled by phospholipase A2 (Supplementary Fig. S5C-F). Notably, I_{Hypo} was significantly reduced by expression of two ANO10-mutants that have been reported to cause cerebellar ataxia (46;124) (Supplementary Fig. S5G,H). Expression of ANO10 augmented RVD during exposure to Hypo, when measured by flow cytometry or single cell imaging of calcein loaded cells (Fig. 3D-G). These data establish a role of ANO10 for volume regulation in mammalian cells.

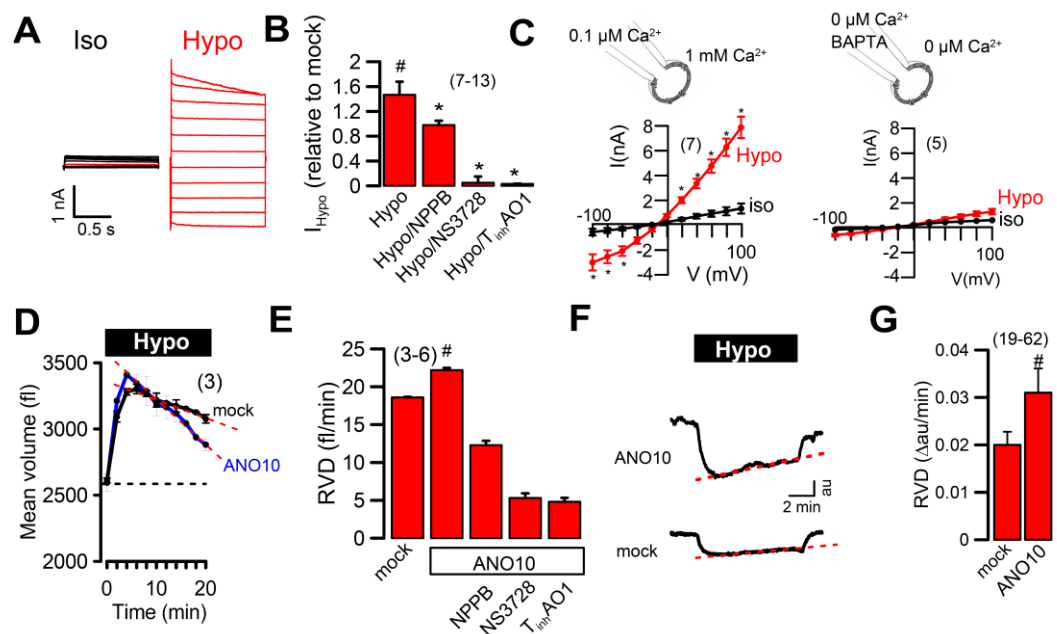
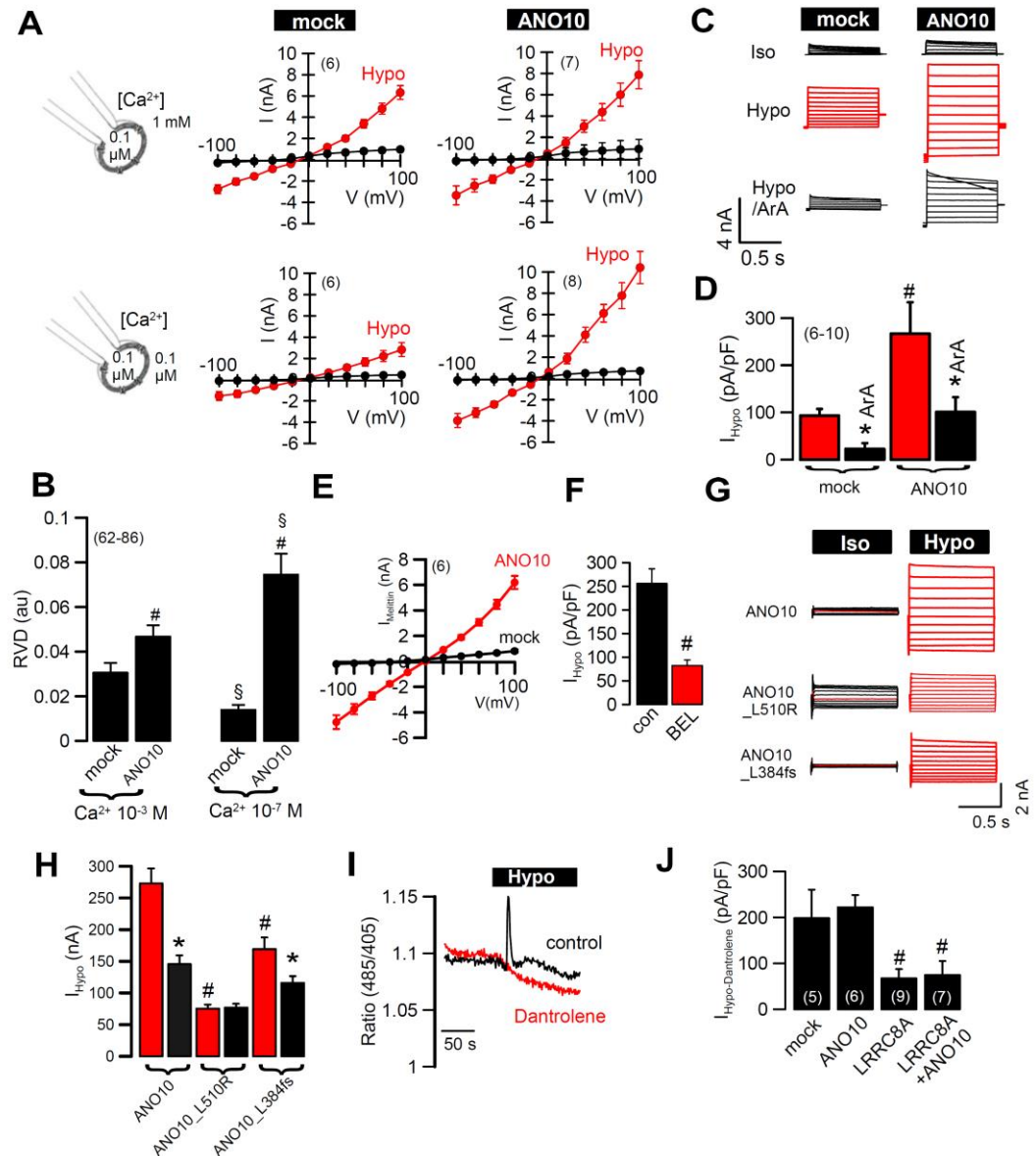


Figure 3: ANO10 affects volume activated whole cell currents in HEK293 cells. **A**) Whole cell currents ($V_c = \pm 100$ mV) activated by cell swelling (I_{Hypo}, 33% reduced extracellular osmolarity) in ANO10-expressing cells. **B**) Swelling induced currents (I_{Hypo}) in ANO10-expressing cells relative to mock transfected cells, and inhibition by NPPB (50 μ M), NS3728 (5 μ M), and T_{inh}AO1 (20 μ M). **C**) I/V curves indicating loss of I_{Hypo} with complete elimination of Ca²⁺ and preincubation with BAPTA (50 μ M, 30 min). **D**) Regulation of cell volume in the presence of Hypo (regulatory volume decrease, RVD) in mock transfected cells or cells overexpressing ANO10

(flow cytometry). **E**) RVD in mock transfected cells or cells overexpressing ANO10, and inhibition by NPPB, NS3728, and $T_{inh}AO1$. **F**) Re-shrinkage of cells exposed to hypotonic bath solution (RVD), measured in single cells loaded with calcein. **G**) Comparison of RVD (measured by calcein fluorescence) obtained in mock-transfected and ANO10-overexpressing cells. Mean \pm SEM (number of cells); *significant inhibition(paired t-test). #significant difference to mock (unpaired t-test).



Supplementary Figure 5: ANO10 increases ICI-swell and volume regulation in HEK293 cells **A**) I/V relationship of currents activated by hypotonic bath solution (I_{Hypo}) in mock-transfected and ANO10-overexpressing HEK293 cells in the presence of normal (10^{-3} M) and low (10^{-7} M) extracellular Ca^{2+} . Note that ANO10 induces larger I_{Hypo} when extracellular Ca^{2+} is low. **B**) Summary of RVD in mock-transfected and ANO10-overexpressing HEK293 cells in the presence of normal (10^{-3} M) and low (10^{-7} M) extracellular Ca^{2+} , as measured in single cell calcein fluorescence assays. **C**) Activation of I_{Hypo} in mock-transfected and ANO10-overexpressing HEK293 cells and inhibition by arachidonic acid (50 μ M). **D**) Summary of the current measurements shown in C). **E**) I/V relationship of whole cell currents activated by the PLA2 activator melittin (100 nM). **F**) Inhibition of I_{Hypo} by the inhibitor of phospholipase A2, bromoenolactone (BEL; 30 μ M). **G**) Activation of I_{Hypo} in HEK293 cells expressing wt ANO10 and two mutants reported in autosomal-recessive

cerebellar ataxia. **H)** Summary of the current measurements shown in G). **I)** Intracellular Ca^{2+} as measured by GCAMP2, showing inhibition of Hypo-induced Ca^{2+} release with dantrolene (10 μM), a blocker of the ryanodine receptor. **J)** Summary of IHypo in the presence of dantrolene. Note that i) ANO10 did not increase IHypo and ii) LRRC8A inhibited IHypo #significantly different to mock, ANO10, and con, respectively (unpaired t-test). *Significant effect of Ara and NPPB, respectively (paired t-test). §significantly different to high Ca^{2+} (unpaired t-test). (number of cells).

In contrast to wt ANO10, R263H-ANO10 failed to produce large I_{Hypo} , and compromised RVD in HEK293 cells (Fig. 4A-C). Virtually identical results were obtained when ANO10 and R263H-ANO10 were expressed in lymphocytes (Supplementary Fig. 6). Immunocytochemistry and membrane biotinylation showed weak membrane expression of ANO10 and R263H-ANO10 and suggested primarily a location of ANO10 in the endoplasmic reticulum (ER) (Fig. 4H-J). Using the plasma membrane targeted Ca^{2+} sensitive protein GCAMP2 (Fig. 4D,E), or conventional Fura2 imaging (Fig. 4F), we found that Hypo induced a delayed transient rise in intracellular Ca^{2+} which was augmented by ANO10, but reduced by R263H-ANO10. However, ANO10 does not seem to affect the filling of the ER Ca^{2+} store, since the SERCA pump inhibitor CPA induced a similar Ca^{2+} increase in the absence or presence of ANO10 (Fig. 4G). Hypo induced store release occurred through dantrolene-sensitive ryanodine receptors (127). In the presence of dantrolene, I_{Hypo} was not augmented by ANO10 (Supplementary Fig. 5aI,J). Taken together R263H-ANO10 may compromise volume regulation by participating in an ion channel complex or by controlling intracellular Ca^{2+} signaling (Supplementary Fig. 8A).

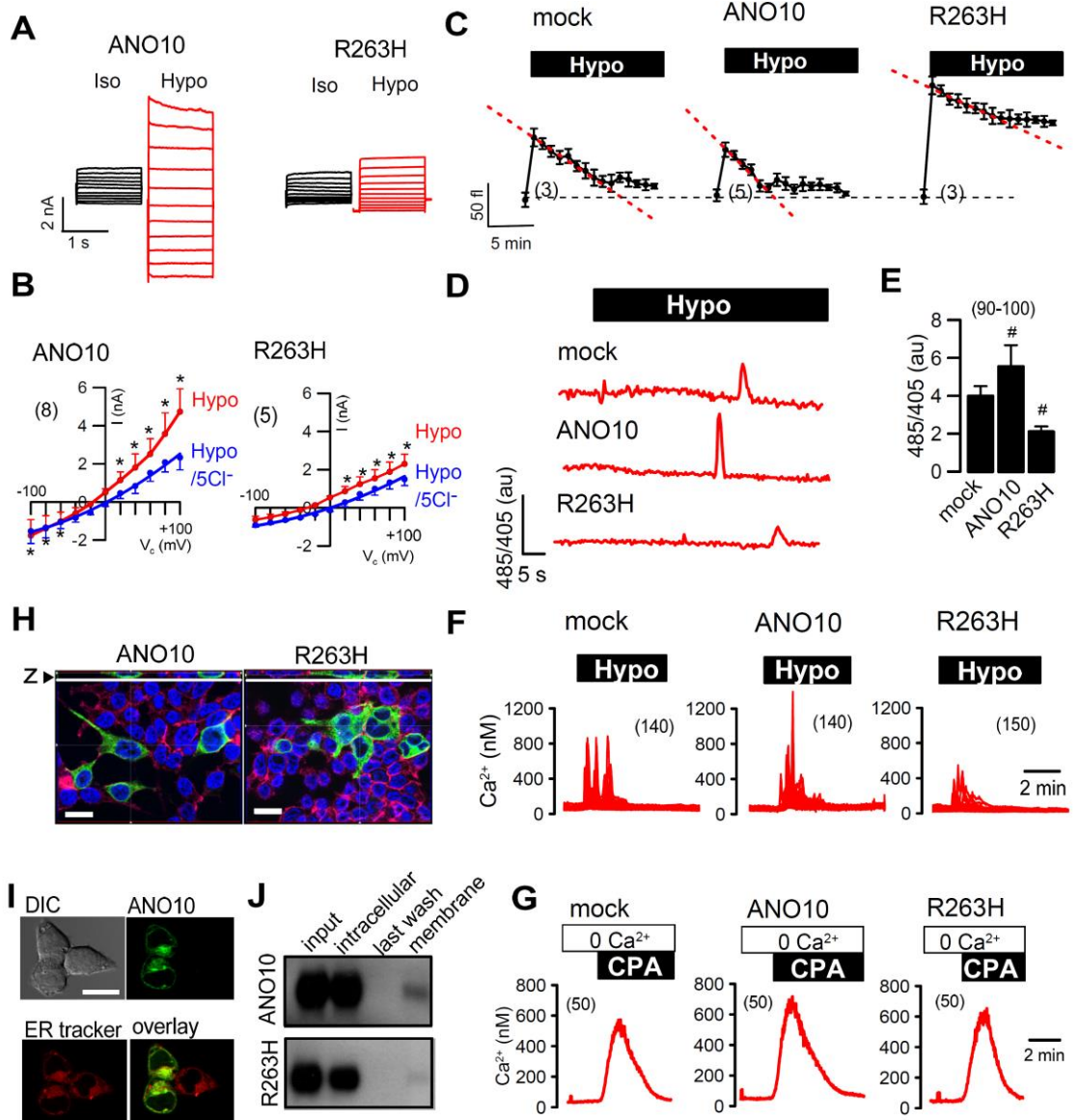
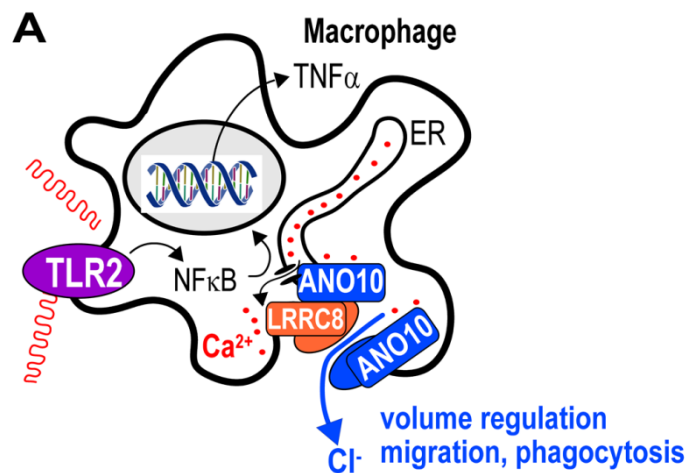


Figure 4: R263H inhibits volume regulation, I_{Hypo} , and intracellular Ca^{2+} signaling in HEK293 cells. **A)** Whole cell currents ($V_c = \pm 100$ mV) activated by cell swelling (I_{Hypo} , 33 % reduced extracellular osmolarity) in cells expressing ANO10 and R263H-ANO10 (R263H). **B)** Current/voltage relationships for I_{Hypo} and inhibition of I_{Hypo} by removal of Cl^- from the extracellular bath solution (5Cl⁻). **C)** Regulation of cell volume in the presence of Hypo (regulatory volume decrease, RVD) in cells expressing ANO10 or R263H (flow cytometry). **D)** Effect of cell swelling on intracellular [Ca^{2+}] in cells expressing ANO10 or R263H or mock transfected cells, as measured by the Ca^{2+} sensor GCAMP2. **E)** Summary of the effects of cell swelling on [Ca^{2+}]_i (485/405 fluorescence emission ratio) in ANO10 and R263H expressing cells. **F)** Collected recordings of the effects of cell swelling on [Ca^{2+}]_i, measured by Fura2. **G)** Collected recordings of the effects of ER-store emptying by cyclopiazonic acid (CPA; 10 μ M) on [Ca^{2+}]_i, measured by Fura2. **H)** Confocal images of cells expressing ANO10 or R263H suggesting weak membrane expression. **I)** Live staining of ANO10-GFP (green) and ER (ER-tracker; red) suggesting ER localization of ANO10. **J)** Membrane biotinylation of cells expressing ANO10 or R263H, suggesting low membrane expression of ANO10, which is even reduced for R263H. Mean \pm SEM (number of experiments); #significant difference when compared to mock (ANOVA); §significant difference when compared to ANO10 (ANOVA). Bar = 20 μ m. Numbers are given in the graph in parenthesis.



Supplementary Figure 8: ANO10 in macrophages, A) Hypothetical model for the role of ANO10 in immune cells such as macrophages.

Compromised macrophage function in the absence of ANO10

Macrophages are within the first line of defense during infection with *Borrelia* (128). We found that ANO10 is expressed along with ANO6 in human THP-1 macrophages as well as freshly isolated mouse peritoneal macrophages (Fig. 5A,B; Supplementary Fig. 7A,B). In THP-1 macrophages, ANO10 was located mostly intracellularly (Fig. 5C). RVD was examined in single cells by loading macrophages with calcein. Recovery from Hypo-induced cell swelling (RVD) was reduced after siRNA-knockdown of ANO10 (Fig. 5D,E). Similar results were obtained in mouse macrophages in which AnO10 expression was inhibited by siRNA or was knocked down in AnO10^{lox/lox}/E2A-cre mice (Supplementary Fig. 7C-E). The results indicate that ANO10 is important for volume regulation also in human and mouse macrophages.

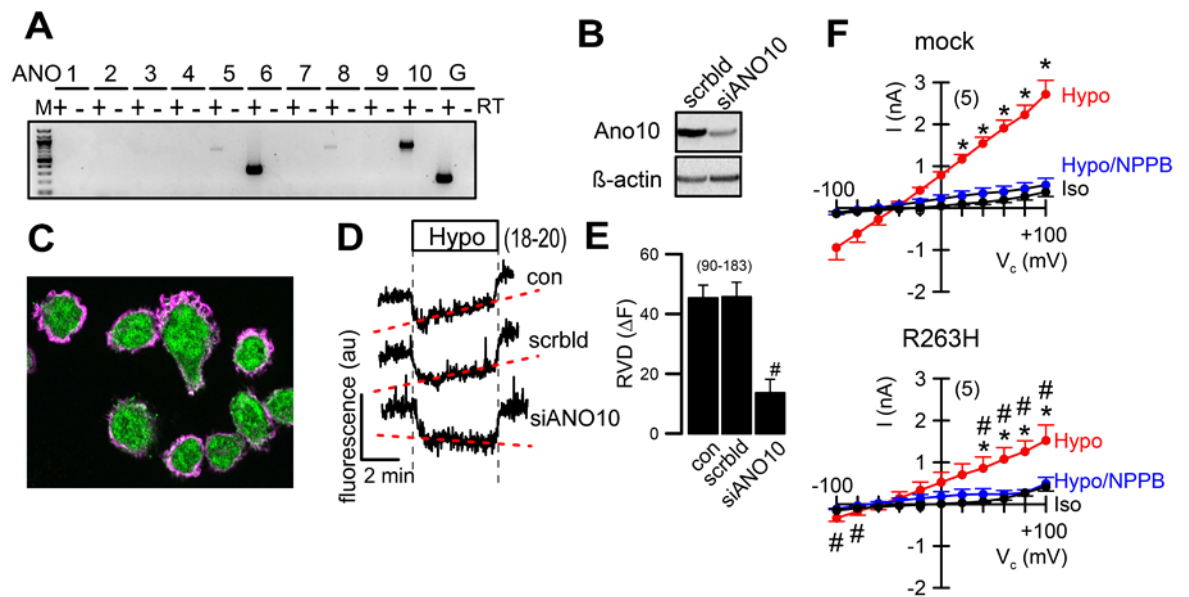
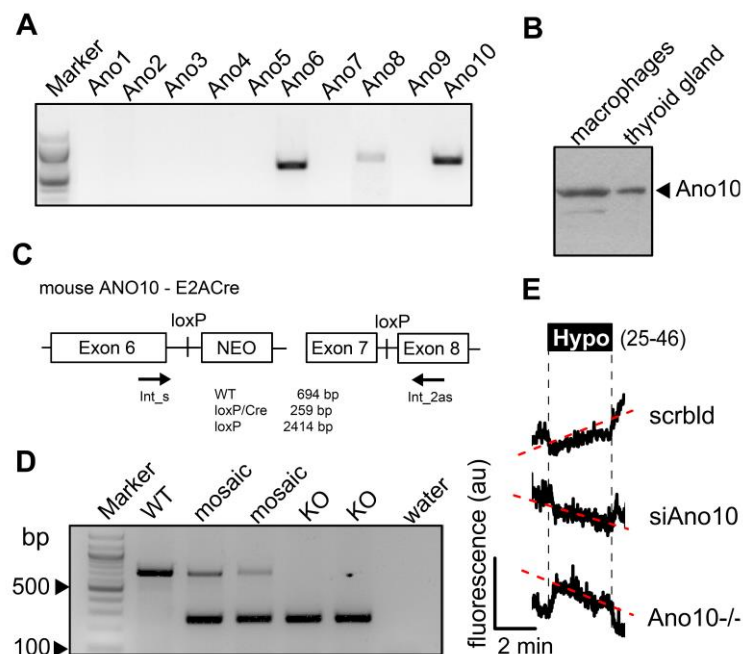


Figure 5: Role of ANO10 for volume regulation in macrophages. **A)** RT-PCR analysis of anoctamin expression in THP-1 macrophages. **B)** Western blot indicating knockdown of ANO10-expression by siRNA. **C)** ANO10 (green) and peripheral actin (rhodamin-phalloidin) of THP-1 cells suggesting dominant intracellular location of ANO10. **D)** Summary trace for re-shrinkage of cells exposed to hypotonic bath solution (RVD), measured in single cells loaded with calcein. RVD was abolished after siRNA-knockdown of ANO10. **E)** Summary of RVD measured by absolute fluorescence change. **F)** I/V curves indicating reduced I_{Hypo} in R263H-expressing cells.



Supplementary Figure 7: Role of ANO10 for volume regulation in mouse macrophages **A)** RT-PCR analysis of anoctamin expression in freshly isolated mouse peritoneal macrophages. **B)** Western blot indicating expression of Ano10 in mouse macrophages and thyroid gland, which is known to express high levels of

ANO10. **C)** Generation of *Ano10* KO animals by crossbreeding *Ano10*^{loxP/loxP} mice with E2A-Cre animals. **D)** Genomic analysis demonstrating *Ano10* knockout. **E)** Summary traces of single cell fluorescence in calcein loaded cells (arbitrary units, au). Exposure of macrophages to hypotonic bath solution (Hypo; 33% reduced tonicity) induced cell swelling (loss of fluorescence), from which control cells (treated with scrambled RNA; scrblld) quickly recovered (RVD; regulatory volume decrease). In contrast, siRNA-knockdown of *Ano10* or *Ano10* knockdown in *Ano10*^{loxP/loxP}/E2a-Cre animals) abolished RVD. (number of cells).

Similar to the experiments in oocytes, also in macrophages expression of ANO10-R263H inhibited I_{Hypo} (Fig. 5F). I_{Hypo} and volume regulation is a prerequisite for cell migration and thus crucial for eradication of spirochetes (125;129). We therefore examined migration of macrophages, which was induced by monocyte chemoattractant protein 1 (MCP-1). Migration was largely reduced by siRNA-knockdown of ANO10, and was inhibited by typical anoctamin blockers (Fig. 5G). Cell viability was not affected by these procedures (data not shown). Because cell migration and phagocytic activity of macrophages will determine the efficacy of spirochete eradication (125;129), we examined phagocytosis of red-fluorescent cherry-labeled *B. garinii* by THP-1 macrophages. Phagocytosis of *B. garinii* was significantly reduced after siRNA-knockdown of ANO10 (Fig. 5H,I). Exposure to *B. garinii* induced a strong release of the major cytokine TNF α by THP-1 cells, which was not affected by knockdown of ANO10 (Fig. 5J,K). No immediate cell death was observed upon exposure and phagocytosis of *B. garinii*, but apoptosis of THP-1 macrophages was reduced 6 days post-exposure to *B. garinii*, which may allow *B. garinii* to circumvent innate defense (data not shown). Taken together, the present results suggest that ANO10 is important for volume regulation of macrophages, and for their role in innate immunity. Eradication of spirochetes may be compromised in carriers of the ANO10 variant R263H.

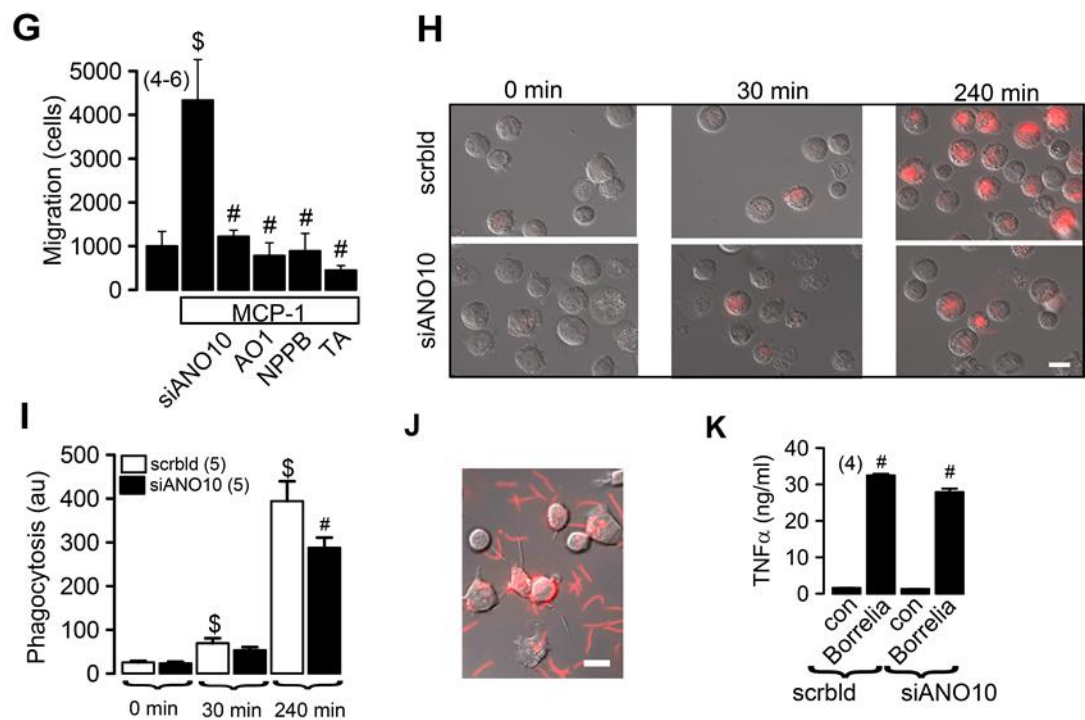


Figure 5: Role of ANO10 for volume regulation in macrophages. **G**) Migration assay in Boyden chambers. MCP-1 induced migration was inhibited by siRNA knockdown of ANO10, and anoctamin inhibitors T_{inh} AO1 (20 μ M), NPPB (50 μ M), or tannic acid (TA, 10 μ M). **H**) THP-1 cells exposed to red-fluorescent cherry-labeled *B. garinii*. Accumulation of cytosolic fluorescence, indicating progressing phagocytosis of *Borrelia* by THP-1 cells. **I**) Increase in fluorescence intensity as a measure of phagocytic activity. **J**) Exposure of THP-1 cells to cherry-labelled *B. garinii*. **K**) Release of TNF α upon exposure to *B. garinii* was not affected by siRNA-knockdown of ANO10. Mean \pm SEM (number of cells or assays). #significant difference when compared to scrambled, MCP-1 alone, mock, or con (ANOVA). §significant increase in migration and phagocytosis, respectively (unpaired t-test). Bar = 20 μ m.

Phenotypes in borreliosis patients

In a subsequent exploratory human study, we wondered whether patients with laboratory-confirmed borreliosis, carrying the ANO10-R263H variant would differ in any respect from non-carriers. Specifically, due to the potential association of both identified SNPs with cerebellar ataxia, we searched for a potential overrepresentation of cerebellar ataxia-like symptoms that have also been reported previously in cases of neuroborreliosis (130). To address this question, we recruited prospectively 100 patients with laboratory-confirmed diagnosis of borreliosis. Patients had a mean age of 56.3 years (standard deviation: 16.0 years, range: 15-86 years), 58% were male. Classical clinical correlates of neuroborreliosis

(including meningitis, radiculitis, cranial nerve palsy, ataxia, dizziness, encephalitis) were present in 30, of systemic Lyme borreliosis (including erythema migrans, arthralgia, myalgia, headache, malaise, nausea, dizziness) in 20 patients. A total of 50 patients had just a laboratory-based diagnosis without typical clinical signs and symptoms; 4 out of these 100 individuals carried the rs41289586 risk allele (T, ANO10-R263H variant), and 2 of 100 had the rs17850869 risk allele (T); all were heterozygous (CT) for these risk SNPs. Of the 6 (4+2) risk allele carriers, 5 had the diagnosis borreliosis without typical clinical symptoms (only laboratory signs of infection) in contrast to 45 of 94 non-carriers (5/6 versus 45/94: Fisher's exact $P=0.20$). Moreover, 3/6 had cerebellar symptoms in contrast to 28/94 (3/6 versus 28/94: Fisher's exact $P=0.37$). Apart from these potentially interesting hints that would need to be consolidated in larger follow-up studies, no prominent clinical differences were detected.

Discussion

In the first GWAS on *Borrelia* antibody serostatus, we identified two host genomic variants mediating differential susceptibility to *Borrelia* seropositivity. Interestingly, both variants, located on chromosomes 3 and 16, happen to be in some context with spinocerebellar ataxia (46;124). The SNP on chromosome 3, rs41289586, represents the missense variant ANO10-R263H, encoded by the gene *ANO10*. We provide here first evidence of this variant modifying normal host defense. The role of the variant on chromosome 16, rs17850869, a synonymous SNP in *ZNF821* is presently less clear. Addressing the second objective of the present study, i.e. to potentially relate *Borrelia* seropositivity to core phenotypes of neuropsychiatric disorders, we obtained a significantly higher symptom load of seropositive versus seronegative individuals in essentially all items of the BSI (119) self-rating scale.

Macrophage function is essential for eradication of *Borrelia* (128). We recently found a role of anoctamin 6 (ANO6) for immune functions of macrophages (76), while volume regulation by anoctamins has been reported earlier (12;34;37). We therefore analyzed the role of ANO10 for volume regulation and found that I_{Hypo} and RVD are depending on ANO10 in

oocytes, HEK293 cells, lymphocytes, and macrophages. The properties of ANO10-induced I_{Hypo} correspond well to those described for VRAC (reviewed in (1;78;79). How does ANO10 control I_{Hypo} and thereby affect RVD? It could be a binding partner of the essential VRAC component LRRC8A (13;14), although we did not find a potentiation of I_{Hypo} by coexpression of ANO10 and LRRC8A in oocytes, and in HEK293 cells exogenous LRRC8A was even inhibitory on I_{Hypo} . Interestingly, no I_{Hypo} was found when we expressed a LRRC8A mutant lacking the leucine-rich repeat (LRCC8A-D367stop; data not shown), suggesting a role of the LRR-motif for I_{Hypo} . Moreover, LRCC8A-D367stop inhibited ionomycin-activation (1 μM) of endogenous xANO1 currents by $43 \pm 5.8\%$ ($n = 27$), and abolished I_{Hypo} in ANO10 expressing oocytes. This suggests a functional relationship between LRRC8A and anoctamins. ANO10 may also control compartmentalized Ca^{2+} signals that have been shown to be important for activation of I_{Hypo} (98;127).

R263H-ANO10 had a dominant negative effect on this ANO10 function. Due to the location of R263 close to the dimer interface, the mutation could interfere with dimerization of ANO10 thereby affecting biosynthesis and/or protein function (21) (Supplementary Fig. 8b,C). R263H compromised volume regulation, migration and phagocytosis, thereby reducing spirochete clearance. Interestingly another member of the anoctamin family, ANO9 (*TMEM16J*) is of potential relevance for the defense against Mycobacteriae, because polymorphisms in the *PKP3-SIGIRR-TMEM16J* gene region were found to be associated with higher susceptibility to tuberculosis (131).

Notably, mutations in ANO10 were found to cause spinocerebellar ataxia (46;124), which is also a reported phenotype of neuroborreliosis (130). Similar to R263H, also these mutations inhibited I_{Hypo} in our present report. We may speculate that ANO10-R263H and putative further variants convey a genetic predisposition to cerebellar ataxia, possibly requiring an ‘additional hit’ in form of an infection to trigger symptoms. The second associated SNP, rs17850869, is a synonymous variant in *ZNF821*. As mentioned earlier, the gene upstream of *ZNF821* is *ATXNIL* (ataxin 1-like), a paralog of *ATXN1* (ataxin 1), which is associated with

spinocerebellar ataxia type 1 (SCA1) (123). In mice, a role of *Atxn1l* in SCA1 pathology was recently demonstrated (132).

Although half of our study participants carry a neuropsychiatric diagnosis, our study design did not allow us to investigate whether *Borrelia* can be (co-)causative of these diseases. Serotyping was performed after neuropsychiatric diagnosis and inclusion of the patients in the GRAS cohort. Thus, the increased seroprevalence in neuropsychiatric patients cannot be interpreted as direct contribution to disease etiology, but rather as disease-related deficits in personal hygiene or increased risk-taking behavior. Furthermore, considering the endemic pattern of *Borrelia* infections (133), the distribution of patient recruitment centers across Germany must also be taken into consideration (116). In contrast to patients, healthy volunteers were mainly from Lower Saxony with a relatively low incidence of borreliosis.

We did not find any evidence for a worse clinical outcome of schizophrenic antibody carriers (independent of genotypes) when compared to seronegative schizophrenia patients with respect to core symptoms of schizophrenia or to neurological deficits, as assessed by trained investigators. However, it is important to remember that antibody seropositivity cannot simply be equated with Lyme disease or neuroborreliosis. Nevertheless, when asked for self-assessment of their overall condition employing the BSI (119) seropositive schizophrenia patients rated more severe symptoms throughout all inventory items including the Global Severity Index (GSI). We cannot provide at this time a reliable interpretation of this data, but their non-specific nature may reflect the reputation of *Borrelia* as the ‘great imitator’ (134), and it is well known that subjective symptoms can persist after disappearance of objective criteria (109).

Conclusion

Our study identified a novel player in innate immune defense, anoctamin 10, which controls cellular volume and macrophage function. We also show that immune response in humans against *Borrelia* varies according to specific genotypes. In the context of further

studies, this might help to design of personalized therapeutic approaches. It is more and more evident that the identification of virulence factors of the pathogen and susceptibility variants of the host are both critical for our understanding of host-pathogen interaction. Joint association analyses of both genomes hold great potential to uncover footprints of natural selection, as shown recently for HIV (135) Progress in the isolation and culture of *Borrelia* from human serum might soon bring similar approaches within achievable range (136).

Acknowledgments

This work was supported by the Max Planck Society and the Max Planck Förderstiftung as well as by the DFGSFB699A12, DFG KU756/12-1, Volkswagenstiftung AZ 87499 and the Niedersachsen-Research Network on Neuroinfectiology (N-RENNT) of the Ministry of Science and Culture of Lower Saxony. C.H. acknowledges grant support by the Daimler & Benz Foundation as well as the Brain & Behavior Foundation.

Chapter 4

Bestrophin 1 is indispensable for volume regulation in human retinal pigment epithelium cells

Abstract

In response to cell swelling, volume-regulated anion channels (VRACs) participate in a process known as regulatory volume decrease (RVD). Only recently, first insight into the molecular identity of mammalian VRACs was obtained by the discovery of the leucine-rich repeats containing 8A (LRRC8A) gene. Here, we show that bestrophin 1 (BEST1) but not LRRC8A is crucial for volume regulation in human retinal pigment epithelium (RPE) cells. Whole-cell patch-clamp recordings in RPE derived from human induced pluripotent stem cells (hiPSC) exhibit an outwardly rectifying chloride current with characteristic functional properties of a VRAC. This current is severely reduced in hiPSC-RPE cells derived from macular dystrophy patients with pathologic BEST1 mutations. Disruption of the orthologous mouse gene (*Best1*^{-/-}) does not result in obvious retinal pathology but leads to a severe sub-fertility phenotype in agreement with minor endogenous expression of *Best1* in murine RPE but highly abundant expression in mouse testis. Sperm from *Best1*^{-/-} mice showed reduced motility and abnormal sperm morphology, indicating an inability in RVD. Together, our data suggest that the molecular identity of VRAC is more complex, i.e. instead of a single ubiquitous channel, VRAC could be formed by cell-type or tissue-specific subunit composition. Our findings provide the basis to further explore VRAC diversity in normal and diseased cell physiology, key to explore novel therapeutic approaches in VRAC-associated pathologies.

Key words: Bestrophin1, VRAC, induced pluripotent stem cells, RPE, mouse sperm

Published in: Andrea Milenkovic, Caroline Brandl Vladimir M. Milenkovic, Thomas Jendryke, **Lalida Sirianant**, Potchanart Wanitchakool, Stephanie Zimmermann, Charlotte M. Reiff, Franziska Horling, Heinrich Schrewe, Rainer Schreiber, Karl Kunzelmann, Christian H. Wetzel, Bernhard H.F. Weber. Bestrophin 1 is indispensable for volume regulation in human retinal pigment epithelium cells. *Proc Natl Acad Sci USA*. 2015 May 19;112(20)

Own experimental contribution: All double electrode voltage clamp experiments

Own written contribution: part of Methods and Results

Other contributions: Designed experiments and analyzed data.

Introduction

Tight regulation of cell volume is fundamental to proper cell function and survival. In general, rapid water influx across cell membranes leads to cell swelling which, in turn, activates net efflux of K^+ and Cl^- thereby triggering the release of osmotically obligated water from the cell. Essential to this process is the activation of a current primarily carried by chloride ions (I_{swell}). This current is gated by volume-regulated anion channels (VRACs), returning the cell to a controlled state of homeostatic integrity, a complex mechanism commonly referred to as regulatory volume decrease (RVD) (3;79). Although VRACs share common features in almost all cell types, it is unclear whether there is one ubiquitous channel or a diversity of chloride channels with slightly differing functional properties. In this context, three families of proteins, the Ca^{2+} and/or volume sensitive anoctamins, bestrophins, and the recently discovered LRRC8s are presently at the center of interest (13;14;137-139).

Bestrophin 1 (*BEST1*), a member of the human bestrophin family of four paralogous genes, encodes an integral membrane protein, strongly expressed in the human retinal pigment epithelium (RPE) (140). Mutations in BEST1 have been associated with various macular dystrophies most prominently represented by Best disease (BD), a central retinopathy with autosomal dominant inheritance but variable penetrance and expressivity (141;142); Key features of BD pathology include a striking lipofuscin accumulation in the macular RPE (143) and an abnormal light peak(LP)/dark trough ratio in the electro-oculogram (EOG) reflective of an impaired RPE (144). The abnormalities in the LP were suggested to be compatible with a function of BEST1 as a Ca^{2+} -activated Cl^- channel (CaCC) (50;56).

Addressing BEST1 function, several studies have suggested a role of the protein in distinct basic cellular processes such as Ca^{2+} homeostasis, neurotransmitter release and cell volume regulation. These studies mostly relied on BEST1 overexpression in HEK293 cells or conducted in vitro experiments with isolated cells from existing Best1 deficient mouse lines. In summarizing these data, BEST1 was shown to be (i) a calcium sensor localized to the endoplasmic reticulum of mouse RPE (145), (ii) an intracellular Cl^- channel activating

anoctamin 1 (ANO1) located at the plasma membrane of mouse trachea (139), (iii) a modulator of voltage-gated Ca^{2+} channels in murine RPE (57), and (iv) a channel for tonic GABA or slow glutamate release in mouse glia cells and astrocytes (146;147). To date, the functional role of Best1 has not been determined in mouse testis, the site of highest endogenous Best1 expression in the mouse (148). In addition, utilizing patient-derived hiRPE cells the role of BEST1 in mediating endoplasmic reticulum (ER) calcium release and/or uptake was shown (149). In contrast, two independent studies in S2R+ cells from *Drosophila melanogaster* strongly suggested the invertebrate dBest1 to act as a volume-regulated chloride channel although with biophysical characteristics clearly distinct from vertebrate VRAC (137;150). By small interfering RNA (siRNA)-mediated knockdown of BEST1 in HEK293 cells (13) and mBest1 disruption in murine peritoneal macrophages (151), two studies could not show a functional effect of BEST1 on I_{swell} , thus questioning this protein as candidate for mammalian VRAC in these cell types. Instead, two studies identified the LRRC8A gene as an essential component of a VRAC in various cultured cell lines (13;14). In these latter studies, the authors propose a scenario where LRRC8A and the isoforms LRRC8B to LRRC8E form variable cell type-specific hexamers explaining the variability of VRAC properties in different cell types.

Together, the rather disparate reports on BEST 1 function underscore the need to further clarify its role in mammalian VRAC. To this end, we focused on two tissues with strong endogenous BEST1 protein expression, namely human RPE (140) and mouse sperm (148). Major insight into BEST1 function was gained from (i) RPE cell culture models established via hiPSC technology from a healthy donor and two macular dystrophy patients with established pathologic mutations in BEST1, and (ii) a mouse strain deficient for Best1, the murine orthologue of the human BEST1 gene. When exposed to hypo-osmotic challenge, both the mutant hiPSC-RPE cells and Best1-deficient mouse spermatozoa exhibited severe phenotypes, suggesting BEST1 as a crucial component of VRAC function in these cell types. In addition, membrane rupture experiments and voltage-clamp recordings in oocytes from *Xenopus laevis*, co-expressing aquaporin-1 (AQP1) and BEST1 from mouse and human,

respectively, demonstrated identical functional properties of the mammalian BEST1 orthologues.

Materials and Methods

Chemicals: 4,4'-diisothiocyanostilbene-2,2'-disulfonic acid (DIDS), and adenosine 5'-triphosphate magnesium salt (ATP), (Sigma-Aldrich, Munich, Germany); cyclopiazonic acid (CPA) (Enzo Life Science, Lörrach, Germany); ionomycin (Biomol, Hamburg, Germany). Substances were prepared as stock solutions: DIDS (600 μ M), CPA (10 mM), each in dimethyl sulfoxide (DMSO). Immediately before starting the experiment, ATP (final concentration 100 μ M) was freshly prepared in the appropriate buffer solutions.

Antibodies: Two antibodies were generated against mouse Best1 and human BEST1, respectively. Anti-Best1 antisera were obtained by immunizing two rabbits with peptide PESPTTEHLQQRRLDQMSTNIQALMKEHAESYPYRDEAGTKPVLVE, representing the final 45 amino acids of the C-terminus of the mouse Best1 peptide sequence (ref.seq. no. NP_036043.2), coupled to carrier protein *glutathione-S-transferase* (GST). The polyclonal antibody, referred to as α -C45, was affinity-purified via HiTrap NHS-activated HP column (GE Healthcare, Uppsala, Sweden) and vigorously tested (see **SI Appendix, Fig. S1, A-C**). Human BEST1 rabbit polyclonal antibody, referred to as α -334, was raised against amino acids 572 to 585 of the human BEST protein (ref.seq. no. NP_004174.1) and affinity-purified with the synthetic peptide used for immunization (Davids Biotechnologie GmbH, Regensburg, Germany). By Western blot analysis, the antibody specifically detected a protein of the expected molecular weight of ~68 kD exclusively in tissue-lysates from human RPE. Antibody specificity was further evaluated by immunocytochemistry, revealing a basolateral membrane staining in hiRPE-cells, as previously reported (49;149). Anti C-45 or α -334 antibodies were used at 1:5000 and 1:2500 dilutions for Western blot analysis and 1:500 and 1:250 dilutions for immunofluorescence staining, respectively. Additional antibodies included rabbit polyclonal antibodies against Gfap (#G9269, Sigma-Aldrich, Munich, Germany; dilution 1:5000), mBest1(55) (referred to as α -KK, dilution 1:2,500), zonula occludens (ZO-1) (Invitrogen, Karlsruhe, Germany; dilution 1:500), LRRC8A (#HPA016811, Sigma-

Aldrich, Munich, Germany; dilution 1:500) and GST (#G7781, Sigma-Aldrich, Munich, Germany; dilution 1:10,000). Mouse monoclonal antibodies against β -actin (#5441, Sigma-Aldrich, Munich, Germany; dilution 1:10,000), Rpe65 (ab13826, Abcam, Cambridge, UK; dilution 1:2,500), acetylated tubulin (#T6793, Sigma-Aldrich, Munich, Germany; dilution 1:10,000) and Rs1 (RS1-3R10) (kindly provided by Dr. Robert Molday, University of British Columbia, Vancouver, Canada; dilution 1:10,000). Secondary antibody for immunofluorescence was Alexa 488-conjugated goat anti-rabbit (Dianova, Hamburg, Germany; 1:500). Western blot experiments were performed with horseradish peroxidase-conjugated secondary antibodies (Calbiochem/Merck, Darmstadt, Germany; 1:10000).

Construction of the Best1 Knock-out Targeting Vector: The pHM2 vector, containing the *LacZ* and neomycin resistant gene (*neor*) (152), was used as targeting vector. The 5'-fragment of the murine *Best1* gene, spanning exon 3 to exon 6, was fused in frame to the *lacZ* gene. The 3'-fragment, spanning *Best1* intron 6 to intron 9, was inserted into the *ClaI* site of the pHM2 vector. The final knock-out construct was linearized with restriction enzyme *XbaI*.

Homologous Recombination in ES Cells and Generation of Germ Line Chimeras: CJ7 ES cells were electroporated and ES cell clones were selected and screened for homologous recombination as described (153). Recombinant ES cells were injected into C57BL/6 blastocysts. Chimeric founders were bred to C57BL/6 mice, and heterozygous mice were backcrossed into either a C57BL/6 or a CD-1 genetic background (154;155) (Charles River Laboratories, Sulzfeld, Germany). Genotyping of animals was performed by PCR amplification using primer pairs mVMD2-KI-KO-F (5'-CAG CCA AAG CTG CTC CAT TAG-3') / lacZ-R2 (R2) (5'-GCT GCA AGG CGA TTA AGT TGG GT-3') for the knockout allele and mVMD2-KI-KO-F / mVMD2-KI-KO-R (R1) (5'-ACC ATC GTT GTG TGG CTG GTC C-3') for the wild type allele. Prior to analysis, mice deficient for *Best1* were backcrossed for at least 10 generations into C57BL/6 and CD-1 strains, respectively. For all animal experiments, with the exception of study series involving the developing mouse testis (postnatal stage P15 to P84), age-matched male mice were used between 2 to 6 months of age. All mice were maintained on a 12 hours light / 12 h dark cycle, housed under specific

pathogen-free conditions and generally maintained under guidelines established by the institution for their use. Mice were sacrificed by cervical dislocation after inhalation of carbon dioxide or *by decapitation* when younger than 14 days.

Sample Collection and Preparation for RNA and Protein Expression: For RNA and protein expression studies in mouse, all tissues were collected from CD1 animals, with the exception of RPE cells which were isolated from C57BL/6. The expression of BEST1 in RPE and testis across different mammalian species was investigated in tissues from human, pig, rabbit, rat and mouse. Human testis samples were allocated from the Department of Urology at St. Josef's Hospital, Regensburg (Director: Prof. Dr. Wieland). Human eyes from anonymous donors were provided by Prof. Dr. Tamm from the Department of Human Anatomy and Embryology, University of Regensburg. Pig tissue samples were obtained from a local slaughterhouse, tissues from rabbit and rat were provided by the "Zentrale Tierlaboratorien der Universität Regensburg". For Western blot analysis and RNA isolation, tissues of all species were cut into small pieces and homogenized using a TissueLyzer (QIAGEN, Hilden, Germany). For RPE sample preparation from human, pig and rabbit, cells were obtained mechanically. Briefly, after removal of the retina the RPE cell layer was isolated with a scalpel. RPE cells from mouse, rat and pig eyes were isolated enzymatically from a pool of twelve adult C57BL/6 mice, two adult rats and one pig, respectively, as described earlier (156). After enucleation of the eyes, bulbi were incised along the ora serrata and cornea, lens, iris and vitreous body were removed. After incubating the posterior eyecups in phosphate buffered saline (PBS, pH 7.4) at 37°C for 20 min the retina was removed. After 30 min incubation in PBS/1 mM EDTA, the eyecups were transferred to a dissociation buffer of 3 mM L-cysteine (Sigma-Aldrich, Munich, Germany) in PBS /1 mM EDTA, 1 U/ml papain (Sigma-Aldrich, Munich, Germany), and 1 mg/ml BSA (Sigma-Aldrich, Munich, Germany) for 23 min. RPE cells were rinsed in DMEM culture medium (PAA, Pasching, Austria) supplemented with 2 % FCS to stop the reaction (PAA, Pasching, Austria). After a washing step with PBS the isolated RPE cells were pelleted and subsequently stored at -80°C.

RNA Isolation and Reverse Transcription: Total RNA was extracted according to the

manufacturer's instructions applying the RNeasy Mini Kit (Qiagen, Hilden, Germany). Genomic DNA was removed by DNase treatment (Roche, Mannheim, Germany). The RNA was quantified spectrometrically with the ND-1000 NanoDrop (PeqLab, Erlangen, Germany) and stored at -80 °C. First strand cDNA synthesis from 1 µg of total RNA was performed with RevertAid™ H Minus First Strand cDNA Synthesis Kit (Fermentas, St. Leon-Rot, Germany) and random hexamer oligonucleotide primers. For RT-PCR reactions 50 ng of cDNA was used as templates for PCR with Go Taq Polymerase (Promega, Mannheim, Germany). Primer sequences are listed in **SI Appendix, Table S5**.

Quantitative Real-time RT-PCR: Amplification of 50 ng cDNA was performed with an ABI7900HT machine (Applied Biosystems, Darmstadt, Germany) in 10 µl reactions containing 1x TaqMan Universal PCR Master Mix (Applied Biosystems, Darmstadt, Germany), 200 nM of primers and 0.25 µl of dual-labeled probe (Roche ProbeLibrary, Roche Applied Science, Mannheim, Germany). Measurements were performed in triplicates and results were analyzed with an ABI sequence detector software version 2.3 (Applied Biosystems, Darmstadt, Germany) applying the $\Delta\Delta C_t$ method for relative quantification. Primer sequences for amplification of target genes and Roche Library Probes are listed in **SI Appendix, Table S7**.

Northern Blot: For Northern blot analysis, total RNA (10 µg) was isolated from frozen testis, electrophoretically separated on a 1,2 % agarose gel containing 1 % formaldehyde and blotted onto nylon membrane (Amersham, Freiburg, Germany). Hybridization probes were generated by RT-PCR encompassing exon 9 to 10 of the mBest1 gene (NM_011913.2) and mouse smooth muscle actin as a control. The fragments were randomly labeled in the presence of [α -³²P] dCTP (Redi Prime II DNA Labeling System, GE Healthcare, München, Germany). Removal of unincorporated nucleotides was achieved by Sephadex™ chromatography.

Protein Sample Preparation, SDS Page and Western Blot Analysis: Total protein extracts were prepared by homogenization in 1 x PBS supplemented with 1 x Protease inhibitor cocktail (Roche, Mannheim, Germany). SDS sample buffer was added and protein extracts were sheared on ice with fifteen 1-sec pulses at 30 % amplitude using a Vibra-Cell sonicator

(Sonic, Newtown, USA). Protein samples were separated by SDS-polyacrylamide gel electrophoresis on 8-10% gels and subsequently transferred onto PVDF membranes (Millipore, Bedford, MA, USA). Incubation of primary and secondary antibodies was carried out at 4°C over night (ON). Protein labeling was visualized by enhanced chemiluminescence (ECL) using AGFA medical X-ray film (AGFA, Kamp-Lintfort, Germany).

Measurement of Visual Acuity: A Virtual Optomotor System (OptoMotry, CerebralMechanics, Lethbride, Canada) was used to measure visual acuity as an index of visual function as described previously (157). To that purpose, animals were exposed to moving sine wave gratings of various spatial frequencies and reflexive head movements of mice were tracked. Acuity was assessed by starting with a low spatial frequency (0.1 cycle / degree) and incrementally increasing the spatial frequency of the grating until the animal failed to response. The threshold was defined as the highest spatial frequency obtained at 100% contrast. Each mouse was tested five times for acuity of the right and the left eye.

Histological Analysis of Retinal Sections by Light and Electron Microscopy: 18 to 21 one months old Best1 ^{-/-} mice and age matched littermate control animals were fixed by intracardiac perfusion with 1% paraformaldehyde (PFA) plus 1% glutaraldehyde containing 0.2 M cacodylate buffer. Eyes were enucleated and fixed overnight in Karnovsky buffer (2.5 % glutaraldehyde, 2.0 % paraformaldehyde in 0.1 M cacodylate buffer, pH 7.2), washed with 0.2 M cacodylate buffer pH 7.4 and post fixed for 2 h in 1 % osmium tetroxide and embedded in EPON (Serva, Heidelberg, Germany) after dehydration. Semithin sections (1 µm) from the central retina were cut along the vertical meridian of the eye at the optic nerve head (ONH) and counterstained with methylene blue and viewed on a Zeiss Axioskop-2 microscope (Zeiss, Göttingen, Germany) using AxioVision LE Rel. 4.5. software. Quantification of whole retinal thickness was assessed by dividing retinal areas into ten sections anterior and posterior of the ONH. Ultrathin sections (50 to 80 nm) were contrasted with 4 % uranyl acetate in 50 % EtOH and 2 % lead citrate in 1 M NaOH and viewed with an electron microscope (EM 902, Zeiss, Göttingen, Germany).

Diurnal RPE Phagocytosis Assay Using RPE Flat Mounting: Eyes from C57BL/6 or CD-1

Best1 ^{-/-} and corresponding littermate control mice were harvested at various times before and after light onset. After trimming the enucleated eyes, each eye was once pierced above the ora serrata (OS) and prefixed by immersing in 2 % PFA/PBS for 4 min at room temperature followed by incising along the OS to remove lens and vitreous body. The retina was peeled away after an incubation step in PBS for 20 min at 37 °C. After further 6 min fixation in 4% PFA/PBS immunofluorescence labeling was performed using primary antibody zonula occludens (ZO-1) and Rho 1D4 antibody. Incisions were made from the peripheral eye cup towards the optic nerve head to gain a flat mount preparation and mounted onto glass slides. Flat mounts were imaged on a Zeiss Axioskop-2 microscope (Zeiss, Göttingen, Germany) using AxioVision LE Rel. 4.1. software and confocal microscope LSM 510 (Zeiss, Göttingen, Germany). The number of Rho-1D4-positive phagosomes per RPE cell, defined by ZO-1 staining, was assessed.

Analysis of Retinal Docosahexaenoic Acid (DHA) Concentration: DHA concentration were measured from retinae of CD-1 Best1 ^{-/-} and wild type mice aged 10 to 12 months. Retinal protein concentrations were determined by a standard Bradford assay (Roti-quant®, Roth, Karlsruhe, Germany) after homogenization and DHA concentrations were analyzed by GC–mass spectrometry (MS). Briefly, 50 µg protein equivalents of each retinal homogenate were derivatized with acetyl chloride in methanol for 2 h at 80 °C (158). An internal DHA standard mixture was added prior to methylation, followed by an extraction of methyl esters by hexane and analyzed using a Shimadzu QP-2010 GC-MS. DHA quantification was performed by external calibration and DHA levels are given as DHA [mg] / total retinal protein [g].

Antibody Epitope Mapping: Four overlapping fragments within the last 45 C-terminal amino acid residues of mouse Best1 were cloned into the GST expression vector pGEX-4T3 and transformed into the BL21 bacterial strain. Recombinant protein expression was induced by IPTG and whole-cell SDS-lysates were prepared for Western blot analysis using α-GST antibody to test for protein expression. For oligonucleotide primer pair sequences see **SI Appendix, Table S6**.

Antigen Specific Affinity Purification: Murine antibody α-C45 was purified by immune

precipitation using testis from a Best1^{-/-} mouse to remove unspecific antigen binding. Testis tissue was homogenized in 250 µl lysis buffer (50 mM Tris pH 7.5, 1 mM EDTA, 150 mM NaCl, 1 % Triton-X, 1 mM Na₃VO₄, 5 mM NaF, 1 mM PMSF, 1 x Protease inhibitor cocktail) and incubated for 30 min on a rotating wheel at 4°C. After centrifugation at 16,000 g for 15 min, the supernatant was incubated with 5 µl of α-C45 overnight at 4°C. Unwanted pre-immune antibodies were precipitated with protein G-sepharose (GE Healthcare, Uppsala, Sweden) whereas the most specific antibody against Best1 was enriched in the unbound fraction for further immunofluorescence labeling.

Plasma Membrane Surface Biotinylation: For biotinylation of plasma membrane proteins, spermatozoa from 12 CD-1 mice were released in TYH290 media, pooled and washed 2 times with ice-cold PBS. Surface proteins were biotinylated with fresh 1 mg/ml solution of EZ-Link Sulfo-NHS-SS-Biotin (#89881, Pierce, Thermo Fisher Scientific, Waltham, USA) for 30 min at 4°C. Homogenization of cell lysates was performed in 1 ml lysis buffer (50 mM Tris, pH 7,5, 5 mM EDTA, 15 mM NaCl, 1% Triton, 1 x Protease inhibitor cocktail (#04693116001, Roche, Switzerland) by passing the lysate 6 times through a 27 and 5 times through a 30 gauge needle. After incubation with streptavidin beads (Thermo Fisher Scientific, Waltham, USA) biotinylated proteins were eluted and subjected to SDS-PAGE.

Immunofluorescence Labeling: A 20 µl drop of sperm suspension was air-dried on microscope slides. hiPSC-RPE cells were grown on transwell-filters (Corning Costar by Sigma-Aldrich, Munich, Germany) for 2-3 months. Samples were fixed in 4 % paraformaldehyde (PFA)/PBS for 10 minutes and blocked by PBS containing 0.3 % Triton X-100 and 10 % goat serum for 25 min. Incubation with primary antibody was performed ON and labelled with fluorescent-conjugated secondary antibody for 2h at room temperature. Stained spermatozoa or hiPSC-RPE cells were imaged on a Zeiss confocal microscope LSM 510 (Zeiss, Göttingen, Germany).

Mating and Fertility: Reproductive capacity was assayed by breeding eight CD-1 and twelve C57BL/6 males with two wild type females CD-1 Best1^{+/+} and C57BL/6 Best1^{+/+}, respectively. After 19 days females were removed and kept in holding cages. Two weeks after

giving birth (waiting period), CD-1 females were mated with CD-1 wild type males. C57BL/6 males were mated solely with females that produced pups in the first mating round to assure their fertility. The total number of litter and pups during the entire mating period was counted.

Sperm Incubation Media: We used Toyoda Yokoyama Hoshi (TYH) media (159) (138 mM NaCl, 4.8 mM KCl, 2 mM CaCl₂, 1.2 mM KH₂PO₄, 1.0 mM MgSO₄, 5.6 mM Glucose, 0.5 mM Sodium Pyruvate, 10 mM L-Lactat, 10 mM Hepes) adjusted to pH 7.4 with NaOH. Osmotic solutions TYH290, TYH350 and TYH420 were titrated with NaCl-free TYH media or media with high NaCl concentration (~ 700 mmol/kg) using a cryoscopic osmometer (OSMOMAT 030, Gonotec, Berlin, Germany).

Sperm Preparation: The epididymus was removed and cleaned of blood and connective tissue. Caput, corpus or cauda epididymis was placed in one well of a 4-well multidish (#176740, Thermo Fisher Scientific, Waltham, USA) and minced in 500 µl of the appropriate TYH media. Sperm were allowed to swim out for 15 min. After removing epididymal tissue the sperm suspension was transferred into a 2 ml cup and kept in a 37 °C incubator for further analysis.

Evaluation of Sperm Viability, Acrosome Integrity, Sperm Tail Morphology and Motility:

Sperm viability was performed with the eosin-nigrosin staining technique as described before (160). Stained spermatozoa on microscope slide were air dried, mounted and examined under oil immersion. 150 cells were analyzed for each sample by bright field microscopy. Acrosomal integrity was determined by lectin staining with Peanut Agglutinin (PNA) (161) coupled with Alexa Fluor 488 (Invitrogen, Karlsruhe, Germany). A 20 µl aliquot of sperm suspension was smeared on microscope slides and air dried. Spermatozoa on microscope slides were fixed in 4 % PFA, incubated in a 1 µg/ml PNA/DAPI solution for 20 minutes in the dark. The acrosomal status of 100 spermatozoa per sample was evaluated. The same slides were consecutively used to examine sperm morphology. A Zeiss Axioskop-2 microscope (Zeiss, Göttingen, Germany) was used for simultaneous fluorescence and differential interference contrast (DIC) imaging at 100X magnification using AxioVision LE Rel. 4.1. software.

Sample Preparation for Sperm Motility Analysis: Sperm suspensions were prepared from cauda epididymal sperm, released for 15 min in TYH media with an osmolality of 290 mmol/kg (TYH290), 350 mmol/kg (TYH350) or 420 mmol/kg (TYH420). Before loading the chamber, spermatozoa from wild type mice and CD-1 Best1^{-/-} mice were diluted 30 to 40 and 5 to 16 fold, respectively, into the corresponding TYH media (supplemented with 0.3% BSA). Movies were recorded for each osmotic condition within 2 hours in a time frame of 0, 30, 75, and 120 minutes after sperm collection. For all time points, 4 to 6 movies were recorded. After two recordings, the chamber was loaded continuously with freshly diluted sperm cells to avoid any decrease of sperm mobility caused by fluid evaporation from the recording chamber.

Optical Setup: Sperm cells were analyzed using an inverted microscope (IX71, Olympus, Hamburg, Germany) equipped with a dark-field condenser, a 10x objective (UPLSAPO; NA 0.4), and additional 1.6x magnification lenses (16x final magnification). The microscope was enclosed in an incubator (Life Imaging Services), and the temperature was adjusted to 37°C. Cell suspensions were placed in glass observation chambers with 150 µm depth. Stroboscopic illumination was achieved using a LED (M660L3-C1; Thorlabs, Munich, Germany) and a custom-made pulse generator. Images were collected at 200 frames per second using a CMOS camera (Dimax; PCO, Kelheim, Germany). The camera and the LED light-pulses were synchronized using a function generator (33220A; Agilent, Böblingen, Germany).

Quantitative Analysis of Sperm Motility: Quantification of sperm function parameters was performed using semiautomatic custom-made programs written in MATLAB (Mathworks, Ismaning, Germany). Motile and non-motile cells were set apart by their velocity along the average path (VAP) (162). Sperm cells with a VAP lower than 20 µm·s⁻¹ were considered non-motile.

Ca²⁺ Imaging: For Ca²⁺ imaging, spermatozoa were collected in TYH420 media and were allowed to attach onto glass cover slips with Cell-Tak (BD Biosciences, Heidelberg, Germany). After incubation with the Ca²⁺ indicator dye Fura-2-AM (Thermo Fisher Scientific, Waltham, USA) and 0.05% pluronic F-127 (Thermo Fisher Scientific, Waltham,

USA) for 1 hour at 37°C, 5% CO₂ in the dark, cells were mounted onto a Zeiss inverted microscope (Axio Observer Z.1). Changes in intracellular free Ca²⁺ ([Ca²⁺]_i) were recorded in the sperm head at 1 to 5-s intervals altering the wavelength of excitation light between 340 and 380 nm. Ca²⁺ images were acquired from 20-30 spermatozoa in an optical field and data were collected only from spermatozoa with their heads attached to the coverslip and their tails beating. Data were recorded and analyzed with ZEN 2012 software (ZEISS, Jena, Germany).

Construction of cRNA, Preparation and Injection of Xenopus Oocytes:

Full-length wild type and mutant BEST1 from human (NM_004183.3) and mouse (NM_011913.2) were cloned into the modified *X. laevis* oocyte expression vector pTLN and linearized with restriction enzyme MluI. Capped RNA was synthesized by in vitro transcription with Sp6 RNA polymerase (mMessage mMachine, Ambion, Thermo Fisher Scientific, Waltham, USA). Oocytes from *X. laevis* were prepared as described (163). Oocytes were thoroughly defolliculated and monitored for endogenous swelling-activated whole-cell currents (164).

X. laevis Oocyte Swelling Assay: Oocytes were injected with cRNA encoding aquaporin 1 (0.5ng) and/or bestrophins (5ng), and transferred from fresh ND96 isotonic 33% buffer into a chamber containing ND96 hypotonic 33% solution. Images were recorded every 20 seconds for a period of 8 minutes using a Zeiss STeREO Discovery V.12 microscope equipped with an AxioCam ICc1 camera. Time course and number of swelling-induced oocyte membrane rupture was determined from at least 20 oocytes.

Double Electrode Voltage Clamping in Oocytes from X. laevis: Two to four days after cRNA injection, oocytes were impaled with two electrodes (Clark Instruments Ltd, Salisbury, UK), which had a resistances of < 1 MΩ when filled with 2.7 mol/l KCl. Using two bath electrodes and a virtual-ground head stage, the voltage drop across the serial resistance was effectively zero. Membrane currents were measured by voltage clamping (oocyte clamp amplifier, Warner Instruments LLC, Hamden CT) in intervals from -80 to +60 mV, in steps of 20 mV, each 1 s. The bath was continuously perfused at a rate of 5 ml/min with ND96 isotonic 33% buffer. Oocyte swelling was induced with ND96 hypotonic 33% solution. All

experiments were conducted at 22°C. ND96 isotonic 33% buffer in mM: 60 NaCl, 72 mannitol, 2 KCl, 1.8 CaCl₂, 1 MgCl₂, 2 HEPES, 2.5 Pyruvic acid; ND96 hypotonic 33% solution was prepared without mannitol; pH was adjusted to 7.5 – 7.6.

Generation of hiPSC Cells and Differentiation to RPE: The procedure for reprogramming skin biopsy-derived human dermal fibroblasts into induced pluripotent stem cells (iPSCs) and their differentiation into retinal pigment epithelial (RPE) cells was described previously. Reprogramming of fibroblasts was performed via spinfection and polycistronic lentiviral transduction using the Lentivirus Reprogramming Kit (Merck Millipore, Darmstadt, Germany). For further analysis, hiPSC-derived RPE cells were cultivated on 6-well or 12-well transwell filter inserts (0.4 µm pore size, Corning Costar by Sigma-Aldrich, Munich, Germany) coated with gfr-Matrigel at a dilution of 1:30.

Patient Presentation: A healthy female, aged 26, with no known history of eye disease, normal visual acuity and normal fundus on ophthalmoscopy was recruited and referred to as “WT1”. In addition, two patients with BEST1-associated BD were included in the study. One male patient at 37 years of age, diagnosed with an atypical manifestation of BD, revealed a heterozygote mutation in BEST1 Exon 7, c.728C>T (p.Ala243Val). At the time of his last ophthalmological examination at the Department of Ophthalmology, University Hospital Regensburg, Germany, the patient still retained good visual acuity (0.1 logMAR on both eyes) and showed less pronounced bilateral macular findings on ophthalmoscopy, Spectral Domain-Optical Coherence Tomography (SD-OCT) and fundus autofluorescence (**SI Appendix, Fig. S5 A-C**). Electrophysiological examinations demonstrated a typically reduced Arden quotient in the electrooculogram (EOG) and a characteristically normal electroretinogram (ERG). A second male patient at 71 years of age was affected by a BD subtype known as adult vitelliform macula dystrophy (AVMD). DNA analysis revealed a heterozygous mutation in Exon 6 of the BEST1 gene, c713A>G (p.Gln238Arg). Visual acuity examined at the Department of Ophthalmology, University Hospital Freiburg, Germany, was poor in the right eye (1.3 logMAR) and had also decreased in the left eye (0.22 logMAR). Macular findings are shown in **SI Appendix, Fig. S5, D-F**. Electrophysiological examinations including EOG

and multifocal ERG verified extensive RPE damage and reduction of amplitudes by 50%.

Patch-Clamp Recordings of Whole-Cell Currents: HiPSC-RPE cells were trypsinized and seeded on poly-L-lysine coated glass cover slips for electrophysiological characterization. Patch pipettes had a tip resistance of 3-5 M Ω and were filled with isotonic solution of 290 mOsm/kg (145 mM CsCl, 2 mM MgCl₂, 11 mM EGTA, 1 mM CaCl₂, 2 mM Hepes). Cells were bathed in extracellular solution (isosmotic), and were recorded in the whole-cell voltage-clamp mode using an EPC-10 USB amplifier and the Patchmaster Software (HEKA, Lambrecht, Germany). The capacitance and series resistance were adjusted using the built-in compensation algorithm of the EPC-10 and the data were sampled at 2 to 5 kHz and filtered 1 to 3 kHz. Voltage-driven inward and outward currents were induced by applying voltage-ramps (500 ms duration) from -100 to +100 mV in 1 sec interval. The magnitude of inward and outward currents was analyzed at a period with constant voltage before and after the ramp (at -100 and +100 mV, respectively). Inactivation and recovery kinetics of currents were investigated by a two-pulse protocol applying a depolarizing voltage-step (from -60 to +120 mV, 1 s) followed by a second depolarizing pulse (100 ms) with varying delay. The delay in the first two-pulse recording was 10 ms, followed by recordings with delay intervals doubled in time (20, 40, 80, 160, 320, 640, 1280, 2560 and 5120 ms). Extracellular solutions: isotonic (290 mOsm/kg) in mM: 85 NaCl, 120 mannitol, 0.4 KH₂PO₄, 1.6 K₂HPO₄, 5 glucose, 1 MgCl₂, 1.3 Ca-gluconate buffered with NaOH to pH 7.3 - 7.4; hypotonic solution (250 mOsm/kg) was prepared by reducing mannitol to 80 mM. For solutions under Ca²⁺ free conditions Ca-gluconate was replaced by 5 mM EGTA; in experiments with reduced extracellular Cl⁻ concentration NaCl was substituted by 85 mM Na-gluconate.

Statistical analysis: Statistical analysis was performed applying the Wilcoxon signed rank test for non-normal distribution and Student's t-test for normal distribution by IGOR PRO software (WaveMetrics). To analyze the breeding performance in Best1^{-/-} and wild type mice, two-tailed Fisher's exact test was used. For box plots, the whiskers reach the 5th and 95th percentiles of the range. P<0.05 was considered statistically significant.

Short Hairpin RNA-Mediated Stable Gene Knockdown: Human LRRC8A shRNA using

forward 5'-CCG GAC CAA GCT CAT CGT CCT CAA CCT CGA GGT TGA GGA CGA TGA GCT TGG TTT TTT G-3' and reverse 5'-AAT TCA AAA AAC CAA GCT CAT CGT CCT CAA CCT CGA GGT TGA GGA CGA TGA GCT TGG T-3' oligonucleotides was inserted into the pLKO.1 vector (Addgene, Middlesex, UK). Lentivirus particles were produced by co-transfecting HEK293T cells with LRRC8A shRNA, and plasmids pMD2.G and psPAX2 using Fugene 6 transfection reagent (Promega, Mannheim, Germany). HiPSC-derived RPE cells from a healthy control, growing for 2 month on 12-well transwell filter, were consecutively transduced twice in a 4-day interval with LRRC8A shRNA and scrambled shRNA, respectively. Gene knockdown efficiency was determined by qRT-PCR after 1 week and 4 weeks posttransduction and Western blot analysis. Scrambled shRNA (Addgene, Middlesex, UK) was used as control.

Study approval: All experimental procedures involving mice and *Xenopus laevis* were conducted in accordance with the German Animal Welfare Act. The present human study has obtained approval of the ethics review board of the University of Regensburg, Germany (Reference No. 11-101-0228). Informed consent was given by each proband participating in the study.

Results

Expression Profiling Suggests a Role for BEST1 in Mouse Sperm and Human RPE

First, we performed RNA and protein expression profiling of Best1 in an extended panel of 14 mouse tissues by RT-PCR and Western blot analysis, respectively. Prominent mRNA expression was almost exclusively restricted to testis, while expression in the remaining tissues was weak (e.g. retina, RPE, trachea, lung) or absent (e.g. spleen, liver, colon, kidney) (**Fig. 1 A and B**). This was mirrored by antibody staining of Best1 protein which was evident only in whole-cell lysates of mouse testis but not in RPE or other tissues analyzed (**Fig. 1 C and D**). Specificity of Best1 polyclonal antibody a-C45 was vigorously tested and further enhanced by antigen specific affinity purification (see **SI Appendix, Fig. S1 A-C**).

We then explored the ratio of BEST1 expression in RPE relative to testis across phylogeny (**Fig. 1 B and D**). While human showed strong BEST1 mRNA expression in RPE

and weak expression in testis, an inverse pattern was observed in rat and mouse while in this semi-quantitative analysis, pig and rabbit revealed an almost equal ratio of BEST1 transcription in the two tissues. BEST1 antibody staining of RPE and testis in human, pig and mouse was strong in RPE of human and pig, while the protein was not detectable in the latter species in testis, despite a strong Best1 RNA expression in pig testis (Fig. 1 B and D).

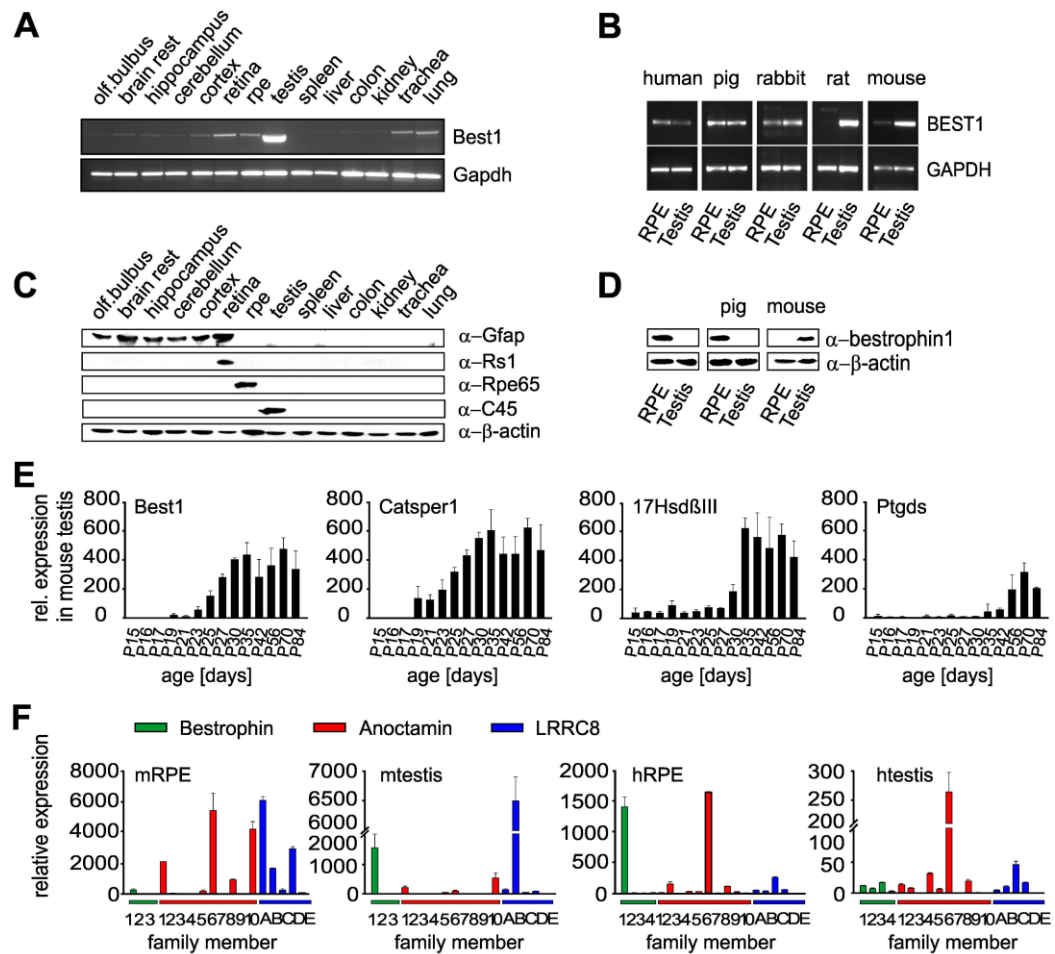


Figure 1. RNA and protein expression analysis of BEST1 (A) RNA expression of BEST1 in 14 mouse tissues and (B) RPE and testis across five mammalian species by RT-PCR. GAPDH served as a control for RNA integrity. Primer sequences see SI Appendix, Table S5. (C) Western blot analysis in 14 mouse tissues and (D) RPE and testis from human, pig and mouse using α -C45 or α -334 antibody, respectively. Co-staining was done with cell-specific markers for glia cells (α -Gfap), RPE (α -Rpe65) and retina (α -Rs1h). Anti-beta actin served as control. (E) Spatiotemporal RNA gene expression in mouse testis development by qRT-PCR at indicated postnatal time points. Testis samples ($n = 3$) were measured in triplicates and normalized to a fixed amount of extracted total RNA. For each sample, the mean \pm SD is given. (F) Relative mRNA expression of indicated chloride channels in mouse RPE ($n = 2$, prepared from 24 eyes), mouse testis ($n = 3$), human RPE ($n = 2$) and human testis ($n = 3$), normalized to Hprt1. For each sample, the mean \pm SD is given. Primer sequences and Roche library probes, see SI Appendix, Table S7.

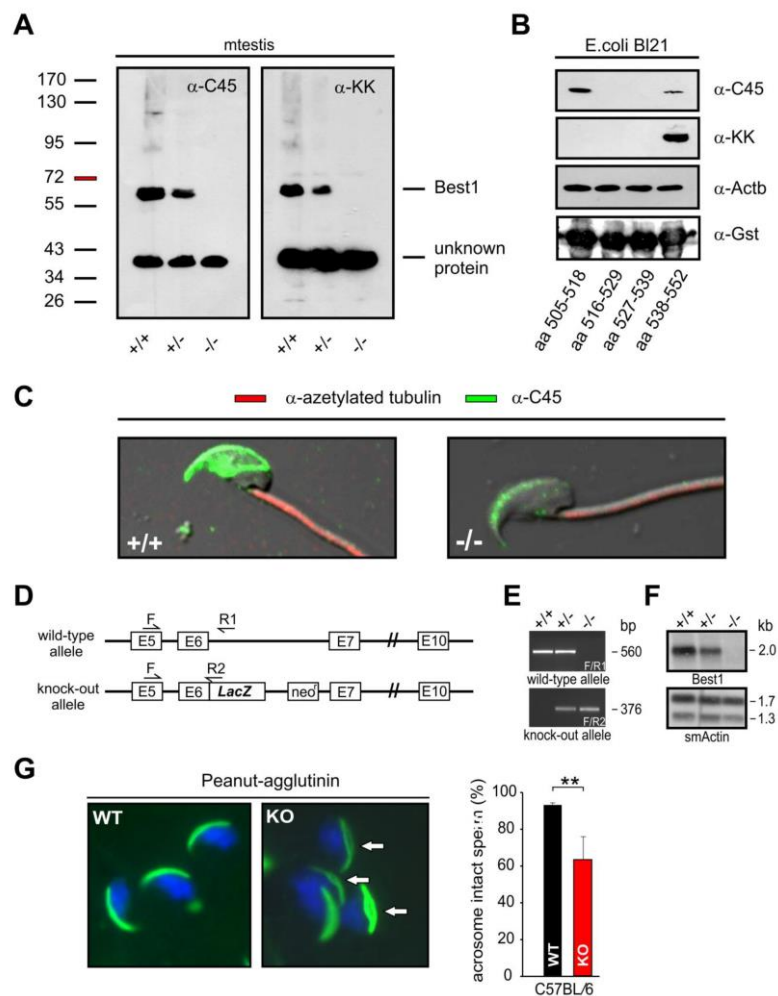


Figure S1. Characterization of polyclonal mouse antibody α -C45 and targeted disruption of the mouse *Best1* gene (A) Western blot analysis with two independently generated murine polyclonal antibodies, termed α -C45 and α -KK. *Best1* protein was present in testis extracts of *Best1*^{+/+} and *Best1*^{+/-} at the expected molecular weight (68 kDa) and absent in *Best1*^{-/-} mice. Of note, both antibodies cross-react with an approximately 40 kDa protein of unknown identity. (B) Epitope mapping within the C-terminal 45 amino acid residues of murine *Best1*. Antibodies α -C45 and α -KK map to different epitopes in the *Best1* protein sequence. Antibodies α -beta actin and α -GST served as control for equal loading. For primer sequences see SI Appendix, Table S6. (C) Immunofluorescence labeling of sperm cells from wild type (+/+) and *Best1*^{-/-} mice with antibody α -C45 revealed a weak non-specific staining in the cup-shaped acrosome. Antigen specific affinity purification prior to immunostaining successfully abolished non-specific tissue immunoreactivity as shown in Fig. 2 A. Further details see in SI Methods. (D) Schematic representation of the targeting strategy to generate ES cells which harbour a *LacZ* reporter gene in-frame in exon 6 of the murine *Best1* gene together with a neomycin-resistance cassette (*neor*). (E) Mice were genotyped by PCR amplification of DNA extracted from mouse tail resulting in a 560 bp fragment in wild type (+/+) and additionally, a 376 bp fragment in heterozygous (+/-) mice. The aberrant fragment of 376 bp is indicative of the correct targeting of the *Best1* allele. (F) To confirm successful germ line transmission of the correctly targeted allele, Northern blot analysis was performed using 10 μ g of total RNA from mouse testis by hybridization with a probe encompassing exon 9 to 10 of the murine *Best1* gene. Mouse smooth muscle actin served as control for loading and RNA integrity. (G) Caudal spermatozoa from C57BL/6 *Best1*^{-/-} males displayed a higher percentage of thickened acrosomal cups compared to wild type mice.

Percentages of acrosome intact cells (uniform apple-green fluorescence) from 797 spermatozoa of five Best1^{-/-} mice were compared to 522 spermatozoa from three wild type mice using PNA-488 staining. Sperm cells were released into TYH290 media. Values are given as mean + S.D, ** = significant differences ($P < 0.01$) compared to spermatozoa C57BL/6 from wild type mice (two-sided unpaired Student's t-test).

To determine gene expression in the transcriptionally silent spermatozoa, we devised an RNA expression assay in the developing testis tissue. Accordingly, increasing expression during testis development should reflect sperm maturation to acquire male fertility. Validation of this assay was carried out for several genes with known transcription profiles in sperm including CatSper1, Cftr, Slx11, Gabra1 and Gabrb3 (**Fig. 1 E and SI Appendix, Fig. S2 B**) (165-168). Best1 transcripts were first evident at mouse postnatal day (PN) 19 with a strong increase until PN30 where it reached steady-state adulthood levels. This pattern is similar to that of the known sperm-specific Ca^{2+} channel CatSper1 but not Leydig/Sertoli cell markers 17 β HsdIII and Ptgds (169) (**Fig. 1 E**). Together, these data suggested a sperm-specific expression of Best1.

To define the expression profile of known and putative anion channels in mouse and human RPE and testis, RNA expression was determined for paralogous bestrophin family members, known calcium-activated chloride channels (CACCs) such as the anoctamins and the recently discovered volume-sensitive LRRC8s (**Fig. 1 E**). While BEST1 was highly expressed in murine testis and human RPE, expression of BEST2 to BEST4 was similar in testis and RPE from both humans and mice. For the anoctamins, ANO6 consistently showed strong RNA expression in all tissues (see also \log_{10} -transformed data in **SI Appendix, Fig. S2 A**), while ANO1 and ANO10 exhibited similar strong expression only in mouse RPE and testis. The remaining anoctamin family members revealed variable, but mostly weak expression. For the LRRC8s, high mRNA expression was noted for LRRC8A in mouse RPE, for LRRC8C in the two human tissues and a remarkably strong expression of LRRC8B in murine testis. It is of note that in the developing mouse testis (PN15 to PN84), from the five LRRC8 family members only LRRC8B showed an RNA expression pattern largely overlapping CatSper1 and Best1 (**Fig. 1 E and SI Appendix, Fig. S2 B**), arguing for its presence in mouse spermatozoa.

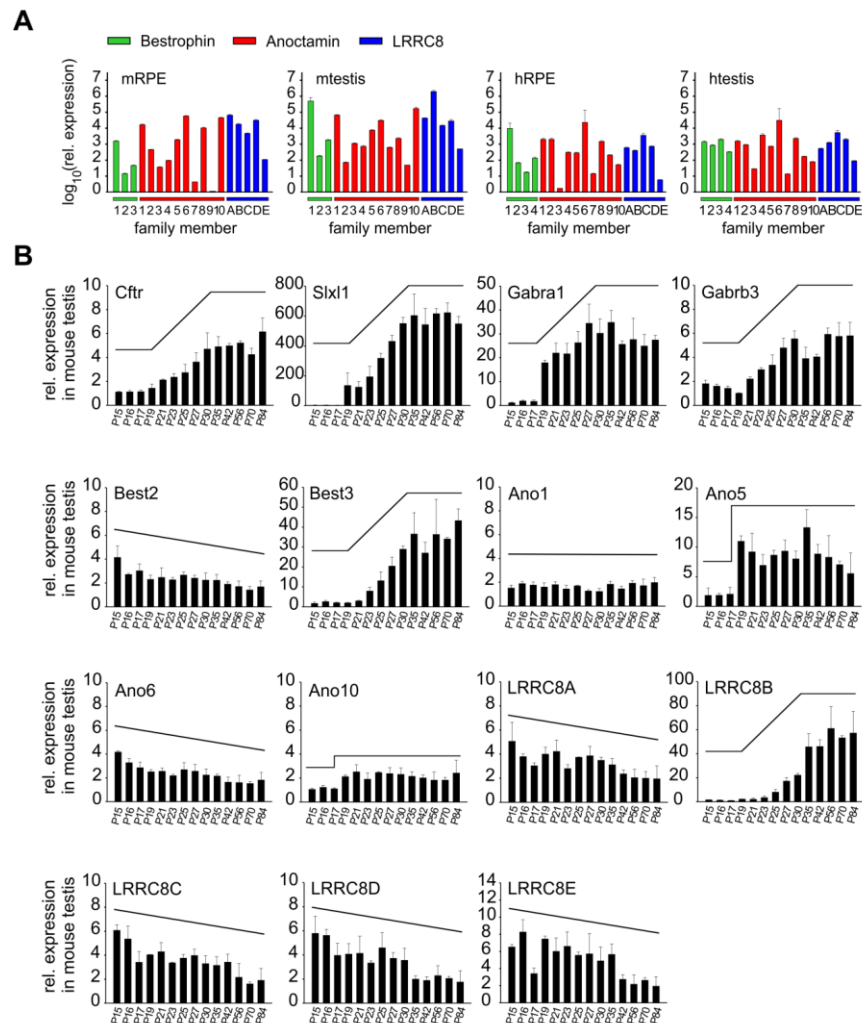


Figure S2. Relative mRNA expression of chloride channels in human and mouse tissue

(A) Comparison of mRNA expression levels of bestrophin, anoctamin and LRRC8 family members in RPE and testis tissue from mouse (m) and human (h), respectively. RPE cells from 24 mouse eyes were isolated enzymatically and pooled to obtain two independent RNA probes. Each bar of testis tissue represents mRNA from three human and three mouse samples, respectively. Bars from human RPE represent mRNA from two independent eyes. Data are LOG10-transformed. Primer sequences and Roche library probes are given in SI Appendix, Table S7. (B) RNA expression during postnatal mouse testis development of indicated genes. (related to Fig. 1F). Expression profile from genes known to be expressed in sperm: *Cftr*, *Slx1*, *Gabra1* and *Gabrb3*, compared to family members of the bestrophins, anoctamins and LRRC8. Sperm expression correlates with increasing gene expression from postnatal day 19, and reaching a steady-state adult expression at postnatal day 30. In comparison, only *Best3* and *LRRC8B* revealed a similar spatiotemporal expression pattern, strongly suggesting an expression of *Best3* and *LRRC8B* in sperm. For each time point, RNA was pooled from testis tissue of three mice. The mean + SD is given for each sample. All experiments were performed in triplicates and normalized to a fixed amount of extracted total RNA.

Best1 Deficiency in the Mouse Impairs Sperm Function and Results in Sub-Fertility

A gene-targeted knock-out mouse was generated (SI Appendix, Fig. S1 D-F) and crossed for over 10 generations onto a C57BL/6 (B6) and a CD-1 genetic background, respectively.

Offspring from heterozygous ($Best1^{+/-}$) matings of both genetic strains were born at the expected Mendelian ratio of 1:2:1 (**SI Appendix, Table S1**) and $Best1^{-/-}$ mice (male and female) developed normally. Initially, the $Best1^{-/-}$ mice were evaluated for their ocular phenotype with particular emphasis on retinal and RPE integrity. Analyses included measurement of visual acuity, light and electron microscopy, diurnal RPE phagocytosis, retinal docosahexaenoic acid levels and basal intracellular Ca^{2+} levels of cultured RPE cells, but revealed no signs of histological or functional pathology (**SI Appendix, Fig. S3 A-J**). In contrast, male mice deficient for $Best1$ revealed a severe sub-fertility phenotype (**Table 1**), although judged by the presence of vaginal plugs, no differences in mating behavior of homozygous knockout males versus wild type were noted. Wild type B6 females mated with B6 $Best1^{-/-}$ males gave birth to only 40 % of pups (mean litter size 4 ± 2.2 pups) when compared to wild type (8.5 ± 2.2 pups). Fertility problems were even more pronounced in CD-1 $Best1^{-/-}$ males with only 7 pups born out of 23 intercrosses (0.3 pups per mating), while control breedings resulted in an average of 12.1 pups per intercross (**Table 1**).

Table 1. Breeding performance of $Best1^{-/-}$ and wild-type mice

Genetic background	BEST1, genotype of parents		BEST1, offsprings		P value, Fisher exact t test
	Males (n)	Females (n)	Litter (n)	Pups (n)	
C5BL/6	+/+ (12)	+/+ (35)	23	195	1,5E-07
	-/- (12)	+/+ (35)	19	75	
CD-1	+/+ (8)	+/+ (23)	23	278	3,4E-08
	-/- (8)	+/+ (23)	4	7	

Supplemental Table 1. Mendelian distribution of offspring from matings with heterozygous males

genetic background	BEST1 genotype of parents		BEST1 offspring number of		genotype ratio WT:HET:HOM	P-value Fisher's exact test
	male	female	litter	pups		
C57BL/6	+ / -	+ / +	4	29	1.00 : 1.23 : 0.00	1.00
	+ / -	+ / -	100	472	1.00 : 2.30 : 1.03	0.97
CD-1	+ / -	+ / +	6	70	1.00 : 1.50 : 0.00	1.00
	+ / -	+ / -	43	348	1.00 : 2.13 : 0.96	0.98

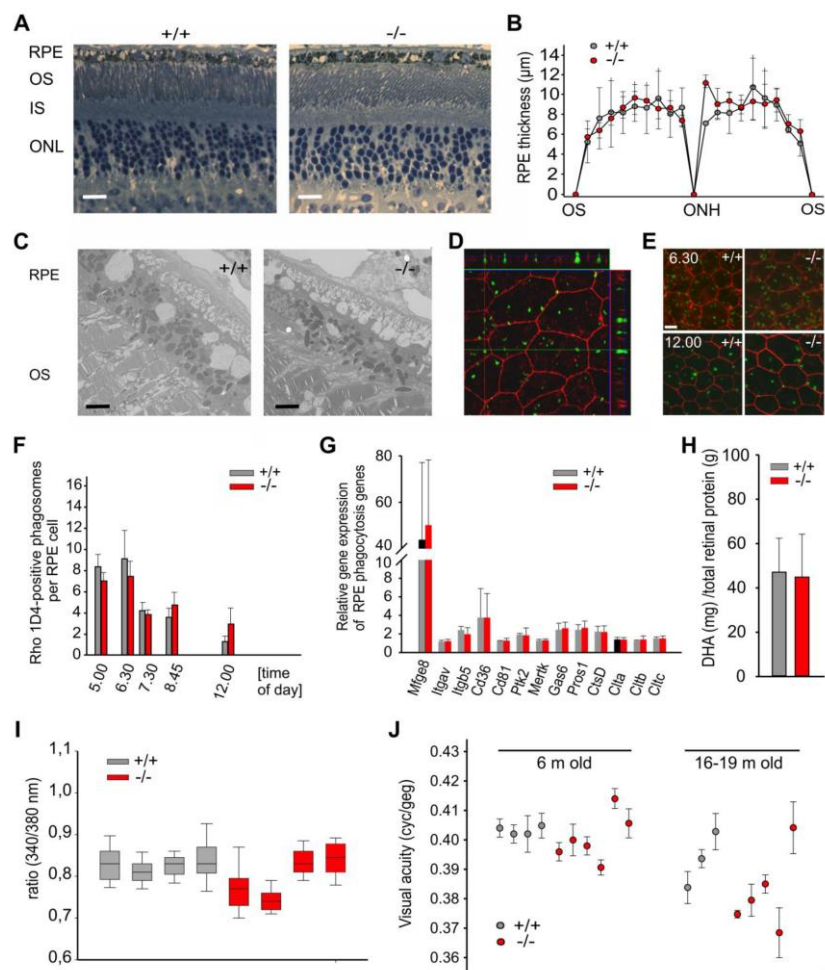


Figure S3. Retinal histology and visual functionality is not affected in Best1^{-/-} mice

(A) Light microscopy of retinal semithin sections of C57BL/6 wild type and Best1^{-/-} mice aged 18 to 21 months. Retinal sections from Best1^{-/-} mice displayed no morphological abnormalities in the RPE and the neuroretina (OS: outer segments, IS: inner segments, ONL: outer nuclear layer). Scale bar = 20 μm. (B) Quantification of RPE thickness in Best1^{-/-} revealed no significant difference when compared to wild type littermates. Retinae were divided in ten sections anterior and posterior of the optic nerve head (ONH), ending at the ora serrata (OS). The mean + SD is given for each sample; n = 1 – 5 mice per genotype, two retinal sections were analyzed per mouse. (C) Ultrathin sections showing the RPE layer with associated photoreceptor outer segments (OS). No abnormalities were found in the number of basal infoldings of the RPE underlying Bruch's membrane, the distribution and number of melanosomes and the general shape of the RPE cells in eyes from BL6-Best1^{-/-} mice compared to wild type. (D-G) Investigation of diurnal RPE phagocytosis. (D) Representative confocal x-z and x-y scan of an RPE flat mount showing binding and internalization of green stained rhodopsin-1D4-positive (Rho-1D4) photoreceptor outer segments (POS) at the apical RPE cell layer, indicated by red staining of zonula occludens-1 (ZO-1). (E) Representative microscopic images of RPE flat mounts at 6:30am and 12:00am of wild type and Best1^{-/-} mice, showing similar amount and distribution of rhodopsin-1D4-positive POS containing phagosomes (green) at the apical RPE cell layer, indicated by red staining with ZO-1. (F) Quantitative analysis of diurnal RPE phagocytosis of CD1 Best1^{-/-} and wild type mice. The mean of 1D4-positive phagosomes per RPE cell is given from six to eight immunostained flat mount regions at the indicated time points. Diurnal shedding and uptake of POS was found to be comparable between wild type and Best1^{-/-} mice. The mean + SD is given for each time point; n = 4 eyes from 2 independent mice. (G) Quantitative real-time expression analysis

of RPE genes involved in different steps of RPE phagocytosis, shortly after light onset at 6:30am. BL6 Best1^{-/-} and wild type mice displayed similar expression levels of genes associated with internalization and degradation of POS, i.e. Mfge8 (Milk fat globule-EGF factor 8 protein), Itgav (α VIntegrin), Itgb5 (β 5Integrin), CD36 and CD81, Gas6 (Growth arrest specific factor 6), PTK2 (Protein Tyrosine Kinase 2), MerTK (Mer Tyrosine Kinase), ProS1 (ProteinS1), CtsD (CathepsinD) and Clta, - b and - c (Clatherin light chains a and b and heavy chain). RNA was extracted from pooled RPE cells, enzymatically isolated from eyes of six Best1^{-/-} and wild type mice, respectively. The mean + SD is given for each sample. All samples were performed in triplicates. **(H)** Analysis of retinal metabolism. Levels of docosahexaenoic acid (DHA) in isolated retinæ of CD1 Best1^{+/+} and Best1^{-/-} mice were analyzed by gas chromatography-mass spectrometry (GC-MS). No statistical differences in DHA levels of Best1^{-/-} mice were found compared to wild type (n = 4 - 8). Data are given as mean DHA (mg) per total retinal protein (g) of mice aged 10 to 12 months. **(I)** Box and Whisker plots of basal [Ca²⁺]_i levels in cultured RPE cells. Each box plot shows the interquartile range of 20 to 50 single cells per well. Enzymatically isolated RPE cells from 4 Best1^{+/+} and 4 Best1^{-/-} mice were cultured for 7 days and [Ca²⁺]_i levels were analyzed using the Ca²⁺ indicator dye FURA-2. No statistical differences in [Ca²⁺]_i levels of Best1^{-/-} mice were found compared to wild type. **(J)** Visual acuity of wild type and Best1^{-/-} mice was analyzed by a virtual optomotor system. Mice of two different age groups were tested 5 times on subsequent days for acuity of the right and left eye. Data are given as mean acuity of two eyes per mouse. An age-dependent decrease in visual acuity was observed with no statistical differences between Best1^{-/-} and Best1^{+/+}

We next analyzed mouse Best1 expression in the male reproductive tract by immunolabelling spermatozoa (**Fig. 2 A**) and epididymus (**Fig. 2 B**) with α -C45 antibodies. Immunolabelling consistently stained the equatorial segment of the sperm head in wild type but not in Best1^{-/-} sperm (**Fig. 2 A**). In cell-surface biotinylation experiments, Best1 was identified in the biotin fraction whereas intracellular tubulin was absent (**Fig. 2 C**), indicating that Best1 is mainly localized to the plasma membrane.

To further characterize the sub-fertility phenotype, spermatozoa from CD-1 Best1^{-/-} males and wild type littermates were released from cauda epididymis into media with an osmolality of 290 mmol·kg⁻¹ (TYH290). In the epididymis, sperm are stored at an osmolality of about 420 mmol kg⁻¹. The release into TYH290 (Δ osmolality = -130 mmol kg⁻¹) mimics the osmotic shock that ejaculated sperm experience upon transfer into the female uterine tract (170). Sperm quality parameters such as morphology, acrosome integrity, viability, and motility were assessed (**Fig. 2 D-G**). By microscopic inspection, a high percentage of heads without tails was noted in the Best1^{-/-} sperm population indicative of enhanced decapitation (**Fig. 2 D**). Strikingly, a large fraction of CD-1 Best1^{-/-} sperm displayed severe coiling and angulation of the flagellum – a well-known phenotype referred to as curly tail. The curly-tail

phenotype reflects impaired sperm volume regulation (171). In addition, an approximately 30 % decline of viable sperm combined with an increase in the number of acrosome-reacted, vesiculated or thickened acrosomal structures were monitored (**Fig. 2 D-F**). Consistent with the milder sub-fertility phenotype of B6 Best1^{-/-} males, a high number of spermatozoa from B6 knockouts displayed a thickened acrosome but less vesiculated and less acrosome-reacted when compared to CD-1 Best1^{-/-}. Importantly, the fraction of sperm with tail abnormalities was lower in B6 Best1^{-/-} spermatozoa (**SI Appendix, Fig. S1 G**). In CD-1 Best1^{-/-}, the fraction of acrosome intact spermatozoa declined dramatically as the spermatozoa progressed from the caput to the corpus and cauda region of the epididymal duct (**Fig. 2 F**). Finally, sperm motility parameters such as curvilinear velocity (VCL), average path velocity (VAP), straight line velocity (VSL) and amplitude of lateral head displacement (ALH) were analyzed from video recordings, revealing a severe decrease in all motility parameters in CD-1 Best1^{-/-} sperm compared to wild type ($p < 0.001$) (**Fig. 2 G** and **SI Appendix, Table S2 and Movies S1 and 2**). Taken together, sperm characteristics of both CD-1 and, to a lesser extent, B6 Best1^{-/-} mice suggest that sperm suffer from an impaired volume regulation, similar to studies on analogous morphological abnormalities reported in other knockout mouse models upon cell swelling (172;173).

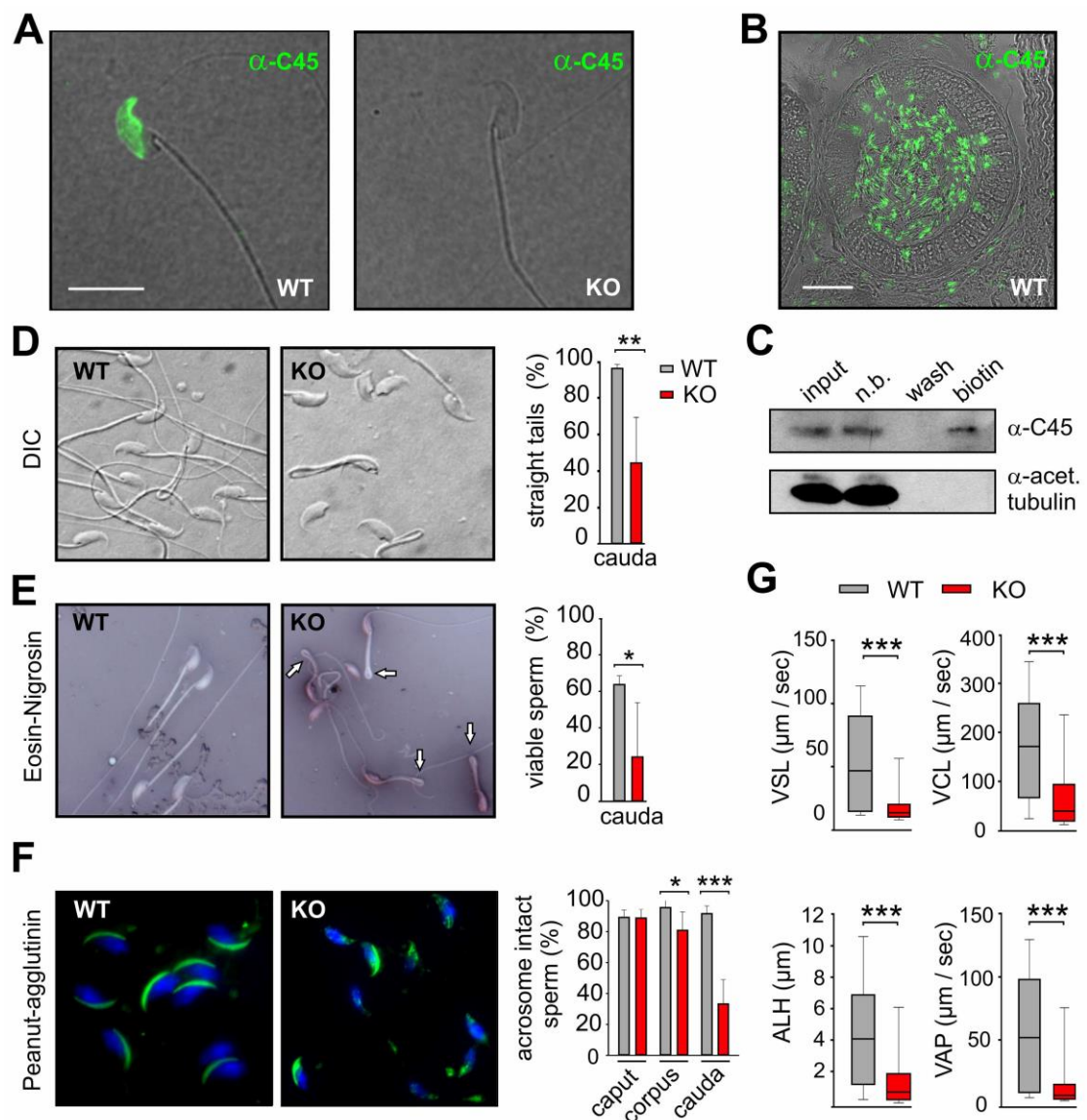


Figure 2. Effects of Best1-deficiency on sperm quality parameters in CD-1 mice (A) Immunofluorescence staining of spermatozoa from wild type and Best1^{-/-} mice and (B) epididymal cryosection with α -C45. Also see SI Appendix, Fig. S1 A-C. Scale bar = 10 μm and 40 μm , respectively. (C) Spermatozoa from 12 CD-1 male mice were subjected to cell surface biotinylation. Labelled sperm sample was immuno-precipitated with streptavidin, transferred to nylon membranes and probed as indicated. (n.b. = unbound fraction). (D) CD-1 Best1^{-/-} spermatozoa showing enhanced decapitation and angulated sperm tails. Percentages of straight tails and (E) stained (dead) and colorless (live) spermatozoa from cauda epididymis after eosin-nigrosin staining from 100 spermatozoa of wild type (n = 10) and CD-1 Best1^{-/-} (n = 5) mice. (F) CD-1 Best1^{-/-} mice showing acrosome reacted spermatozoa using PNA-488 staining. Percentages of acrosome intact cells (uniform apple-green fluorescence) to acrosome reacted sperm (perforated or absent acrosome cap) from 150 spermatozoa of wild type (n = 16) and Best1^{-/-} mice (n = 10) of spermatozoa from caput, corpus and cauda epididymis. (G) Box and Whisker plots of sperm velocity parameters including VSL, VCL, ALH and VAP. Each box plot shows the interquartile range of 382 spermatozoa from CD-1 wild type (n = 3) and 654 spermatozoa from Best1^{-/-} mice (n = 7). Further details, see SI Appendix, Table S2. Spermatozoa were released into TYH290 media. Values are given as mean + SD. Two-sided Student's t-test or Wilcoxon signed rank test: * = P<0.05; ** = P<0.01; *** =

P<0.001.

Supplemental Table 2. Velocity parameter means of spermatozoa from CD-1 wild type (WT) and Best1 ^{-/-} (KO) mice released in different osmotic solutions

TYH media mosmol/kg	Time point after sperm collection (min)	Genotype	Motile sperm (%)	VCL (µm/s)	VAP (µm/s)	VSL (µm/s)	ALH (µm)
290	0	WT	66 ± 13	174.92 ± 57.80	58.35 ± 20.79	54.45 ± 19.27	4.55 ± 1.77
		KO	19 ± 4	70.97 ± 32.08	17.34 ± 9.71	16.89 ± 8.52	1.64 ± 0.83
290	30	WT	65 ± 6	170.97 ± 31.02	52.50 ± 7.82	48.07 ± 6.72	4.47 ± 1.12
		KO	19 ± 8	62.49 ± 17.49	15.73 ± 4.63	14.42 ± 2.96	1.58 ± 0.74
290	75	WT	64 ± 5	166.80 ± 43.72	51.36 ± 14.77	45.28 ± 13.66	4.58 ± 1.29
		KO	13 ± 4	53.69 ± 6.07	11.88 ± 1.9	12.03 ± 12.01	1.16 ± 0.22
290	120	WT	72 ± 5	176.05 ± 35.96	57.55 ± 12.3	46.67 ± 8.29	5.36 ± 1.12
		KO	12 ± 3	47.33 ± 12.63	10.77 ± 2.9	11.07 ± 2.53	1.06 ± 0.24

Values are mean ± standard deviation. VCL = curvilinear velocity in µm/sec, VAP = average path velocity in µm/sec, VSL = straight line velocity in µm/sec, ALH = amplitude of lateral head displacement in µm.

Supplemental Table 2. cont'd

TYH media mosmol/kg	Time point after sperm collection (min)	Genotype	Motile sperm (%)	VCL (µm/s)	VAP (µm/s)	VSL (µm/s)	ALH (µm)
350	0	WT	63 ± 7	161.62 ± 33.66	52.51 ± 28.41	42.1 ± 4.72	5.09 ± 1.01
		KO	28 ± 19	91.28 ± 54.42	26.93 ± 20.62	24.12 ± 16.5	2.60 ± 2.04
350	30	WT	67 ± 4	158.79 ± 24.36	54.35 ± 7.91	40.35 ± 3.84	5.37 ± 0.96
		KO	19 ± 8	68.25 ± 23.75	20.09 ± 9.83	16.58 ± 6.63	1.92 ± 0.94
350	75	WT	61 ± 9	139.90 ± 12.39	48.28 ± 5.15	36.14 ± 1.83	4.51 ± 0.58
		KO	20 ± 5	70.46 ± 16.39	17.3 ± 5.65	14.3 ± 4.65	1.80 ± 0.58
350	120	WT	55 ± 13	123.78 ± 13.41	42.58 ± 7.05	32.16 ± 2.32	3.78 ± 0.75
		KO	12 ± 9	48.83 ± 17.58	12.86 ± 26.91	12.82 ± 5.41	1.10 ± 0.52

Values are mean ± standard deviation. VCL = curvilinear velocity in µm/sec, VAP = average path velocity in µm/sec, VSL = straight line velocity in µm/sec, ALH = amplitude of lateral head displacement in µm.

An Impaired Tolerance to Osmotic Change Could Underlie the Sperm Defect in CD-1 Best1^{-/-}

To functionally delineate the sub-fertility phenotype which, in principle, could be attributed to disturbances in RVD, but also to defects in other signaling mechanisms, e.g. Ca²⁺ homeostasis, changes in intracellular Ca²⁺ concentration ([Ca²⁺]_i) in CD-1 Best1^{-/-} sperm were examined. Sperm were released into TYH420 medium and stimulated by (1) hypotonic swelling in TYH290 medium, (2) 100 µM ATP or (3) 50 µM cyclopiazonic acid (CPA), a

potent inhibitor of calcium ATPase (SERCA) activity. Changes in Ca^{2+} levels in sperm heads were recorded as a ratio of fura-2 fluorescence emission upon excitation at 340 nm and 380 nm (**Fig. 3 A**). Prior to the application of a stimulus no significant differences in fluorescence ratio was observed, suggesting that basal Ca^{2+} levels were similar in wild type and CD-1 $\text{Best1}^{-/-}$ sperm (**Fig. 3 B**). Hypotonic swelling in TYH290 evoked a transient Ca^{2+} increase. The peak amplitude (**Fig. 3 C and D**) and the recovery rate (**Fig. 3 E**) of the swelling-induced Ca^{2+} transient was similar in wild type and CD-1 $\text{Best1}^{-/-}$ sperm. Treatment of sperm with 100 μM ATP to activate P2X receptors (174) evoked a transient Ca^{2+} increase, whose characteristics were similar in wild type and CD-1 $\text{Best1}^{-/-}$ mice (**Fig. 3 D and F**), whereas no calcium increase was detected upon 50 μM CPA application (**SI Appendix, Fig. S4 A and B**).

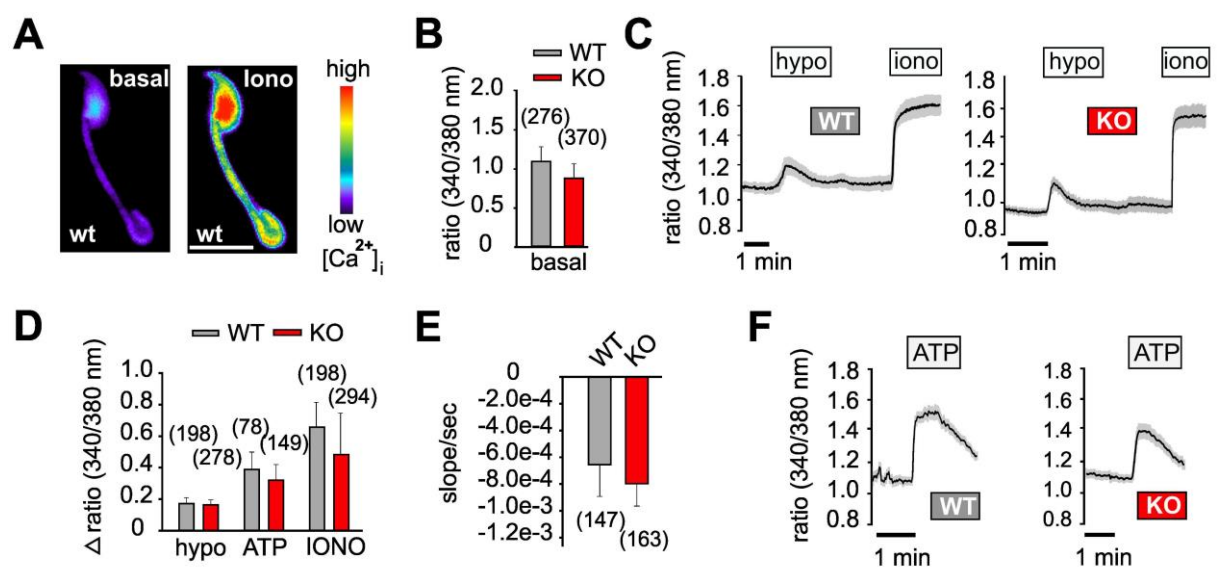


Figure 3. Consequences of Best1-deficiency on calcium signaling and osmotic tolerance in mouse sperm

(**A-F**) Ca^{2+} imaging in the sperm head from spermatozoa of corpus epididymis from CD-1 wild type and CD-1 $\text{Best1}^{-/-}$ mice ($n = 3 - 6$) released into TYH420 media. (**A**) Representative images of cytosolic Ca^{2+} levels $[\text{Ca}^{2+}]_i$ in mouse sperm, unstimulated (left panel) or upon ionomycin application (right panel). The pseudocolor image shows the $[\text{Ca}^{2+}]_i$ increase in sperm head. (**B**) Bar graphs showing basal $[\text{Ca}^{2+}]_i$ levels. (**C**) Averaged graphs of $[\text{Ca}^{2+}]_i$ increase upon hypotonic stimulation. (**D**) Summary of basal $[\text{Ca}^{2+}]_i$ levels, ATP-induced and swelling-activated increases in $[\text{Ca}^{2+}]_i$ obtained from experiments shown in (B-C) and (F). Ionomycin was used for determination of maximum $[\text{Ca}^{2+}]_i$. Black lines indicate the averaged responses of at least 30 spermatozoa; grey area indicates S.E.M. Also see SI Appendix, Fig. S4. (**E**) Bar graphs showing recovery rates ($\text{slope} \cdot \text{sec}^{-1}$) from swelling-induced $[\text{Ca}^{2+}]_i$ maximum peak to initial levels. (**F**) Averaged graphs of $[\text{Ca}^{2+}]_i$ increase in response to 100 μM ATP

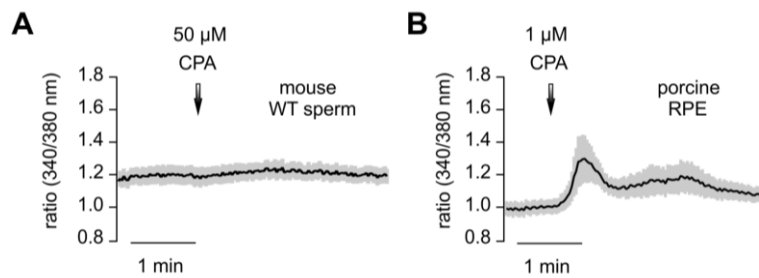


Figure S4. Effect of cyclopiazonic acid (CPA) on $[Ca^{2+}]_i$ in mouse spermatozoa

(A) Spermatozoa of corpus epididymis from four CD-1 wild type mice were released into TYH420 media and intracellular Ca^{2+} concentration was measured using Fura-2-AM. Representative graph of $[Ca^{2+}]_i$ responses to 50 μ M cyclopiazonic acid (CPA). Related to Fig.3. (B) Control experiment with porcine primary RPE cells, enzymatically isolated with papain/L-cystein dissociation buffer (Further details see in SI Methods). RPE cells were grown on coverslips for 3 days and loaded with Fura-2-AM. A \sim 30 % increase in the 340 nm to 380 nm ratio was detected upon stimulation with as little as 1 μ M CPA. Black lines indicate the averaged responses of at least 24 spermatozoa and porcine RPE cells, respectively; grey area indicates S.E.M

To address osmotic tolerance and its possible impairment as the basis for the severe sperm phenotype in CD-1 Best^{-/-} mice, total motility and sperm velocity parameters VAP, VSL, VCL and ALH were evaluated from caudal spermatozoa. In a time lapse experiment, caudal spermatozoa were exposed to solutions with increasing osmolalities. The percentage of motile sperm was relatively stable for up to two hours within all osmotic solutions with the possible exception of wild type sperm at 420 mmol kg⁻¹ (**Fig. 3 G**). Although CD-1 Best1^{-/-} mice showed a significant lower percentage of motile sperm compared to wild type at all osmotic conditions tested ($22 \pm 8\%$ versus $65 \pm 7\%$), statistics on pooled data from the three osmotic conditions revealed a rescue of total motility in spermatozoa from CD-1 Best1^{-/-} mice with increasing osmolality (THY290 : THY350 : THY420 = $16 \pm 4\%$: $20 \pm 7\%$: $31 \pm 6\%$) (**Fig. 3 H and SI Appendix, Table S2**). Notably, in CD-1 Best1^{-/-} mice the percentages of motile spermatozoa reflected the number of viable cells (**Fig. 2 E**), indicating that those sperm that are alive are motile. From these data, we conclude that lack of Best1 in mouse spermatozoa does not affect Ca^{2+} homeostasis, but rather renders sperm unable to cope with changes in osmotic pressure.

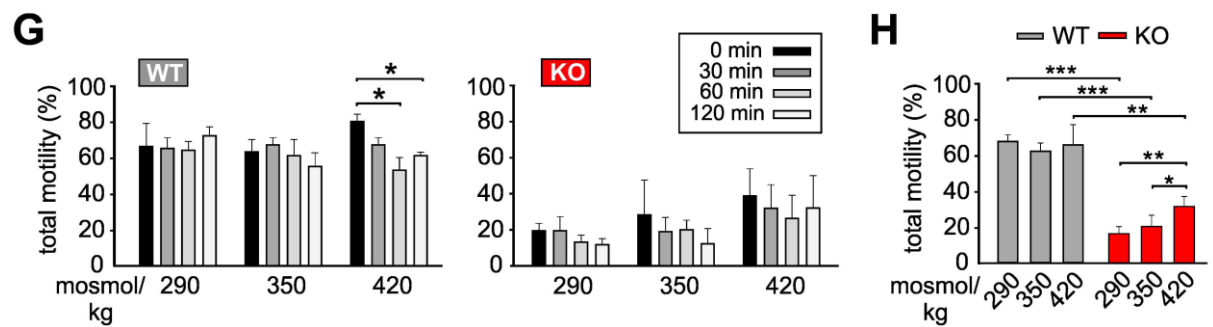


Figure 3 (cont.). Consequences of Best1-deficiency on calcium signaling and osmotic tolerance in mouse sperm (G) Percentages of total sperm motility from caudal spermatozoa of three CD-1 wild type and seven Best1^{-/-} mice exposed to defined osmotic conditions. Recordings were taken at indicated time points after initial exposure to TYH290, TYH350 or TYH420 media. **(H)** Summary of (G). Mean values were pooled for the three indicated osmotic conditions. For further details see SI Appendix, Table S2. Values are given as mean \pm S.E.M. Two-sided unpaired Student's t-test, * = $P < 0.05$, ** = $P < 0.01$, *** = $P < 0.005$; n = number of spermatozoa.

Cell Swelling Activates Identical Currents in *X. laevis* Oocytes Expressing Human and Mouse BEST1

Next, we explored whether BEST1 function is evolutionarily conserved between mouse and man. To this end, *X. laevis* oocytes were exposed to hypotonic bath solution which induced cell swelling and rupture of the oocyte membrane in cells expressing the water channel AQP1 (**Fig. 4 A**). Cell swelling and rupture of the oocyte membrane was significantly delayed in oocytes co-expressing human BEST1 or mouse Best1 (**Fig. 4 B**). In contrast, expression of mutant proteins BEST1-R218C or BEST1-Y227N did not delay oocyte bursting (**Fig. 4 B**). Notably, 50% of the oocytes expressing AQP1, AQP1/R218C and AQP1/Y227N burst within the first 30 seconds ($T_{50} = 0.25$ min, 0.4 min and 0.25 min, respectively), while expression of human BEST1 or mouse Best1 significantly increased T_{50} to 2.5 min and 4.5 min, respectively (**Fig. 4 B and C**).

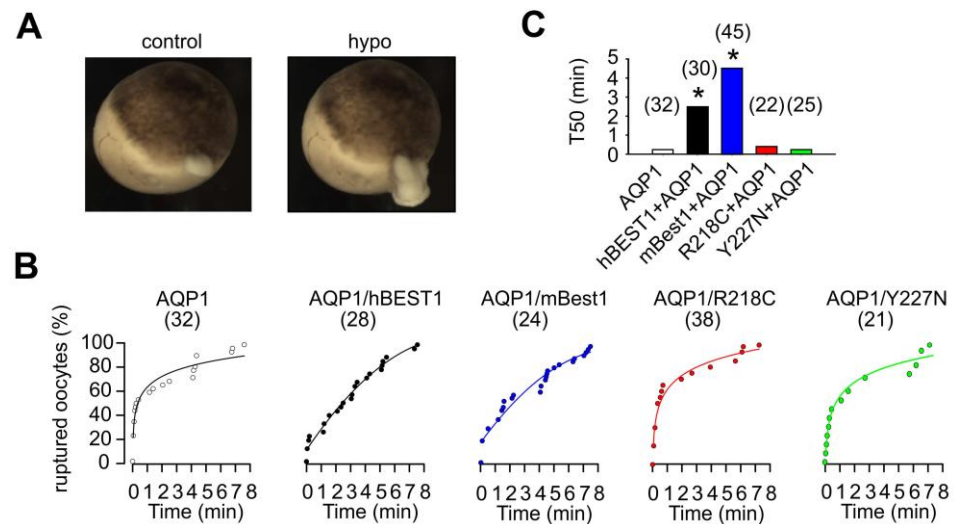


Figure 4. Rescue of swelling-induced membrane rupture of AQP1-expressing *X. laevis* oocytes by co-expression of hBEST1 or mBest1 (A) Photomicrograph showing two *X. laevis* oocytes under hypotonic condition injected with water as control (left panel) or AQP1 (right panel). (B) Cumulative plot of ruptured *X. laevis* oocytes, co-expressing AQP1 and the indicated BEST1-constructs in a time-course of 0 to 8 min after exposure to hypotonic media. Data were plotted as colored circles and fitted by double-exponential regression. (C) Bar graph summarizing (B). (T50) = time to burst 50% of the total number of oocytes is indicated.

We then examined whether hypotonic cell swelling in the presence of BEST1 also activates membrane currents in *X. laevis* oocytes. Defolliculated oocytes were thoroughly monitored for endogenous swelling-activated whole-cell currents as reported earlier (164). Three days after injection, oocyte rupture and volume-activated whole-cell currents were virtually absent in water-injected control oocytes similar to earlier studies (175). In AQP1-injected oocytes hypotonic bath solution activated only a small endogenous whole-cell current before membrane bursting (**Fig. 4 D and E**). In AQP1/hBEST1 and AQP1/mBest1 co-expressing cells the volume-activated currents were twice as large as in control oocytes expressing AQP1 only (**Fig. 4 D-G**). The swelling-activated current was inhibited by 200 μ M DIDS (inhibition by 48 ± 7.9 %; $n = 5$), but not by other known Ca^{2+} -activated Cl^- channel blockers, such as NPPB (50 μ M) (inhibition by 9 ± 1.1 %; $n = 5$), or CaCCinh-AO1 (20 μ M) (inhibition by 3 ± 0.4 %; $n = 4$) (34;176). Notably, volume activated whole-cell currents in AQP1/hBEST1 and AQP1/mBest1 co-expressing cells were rather linear and showed only little time-dependent inactivation, as reported earlier (150;175). Together, these experiments suggest that human and mouse BEST1 are both activated by cell swelling thereby leading to

RVD and delay in hypotonic cell rupture. The disease-associated BEST1 mutations, BEST1-R218C, BEST1-Y227N, BEST1-Q238R, and BEST1-A243V abolished ion channel function (Fig. 4 B-C and G). In addition, co-expression of AQP1/hBEST1 and BEST1-A243V also leads to significant reduction in VRAC currents in agreement with a dominant-negative mode of action of BEST1 mutations on wild type BEST1 as suggested earlier (177).

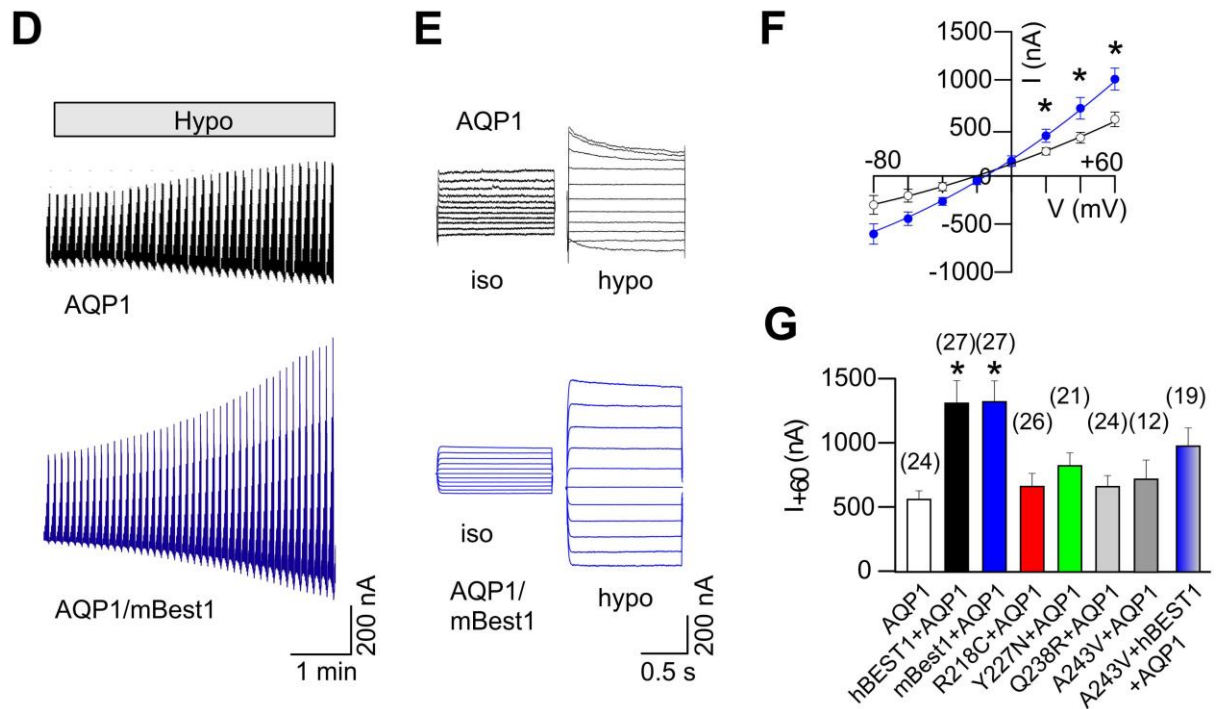


Figure 4. Rescue of swelling-induced membrane rupture of AQP1-expressing *X. laevis* oocytes by co-expression of hBEST1 or mBest1 (D-F) Voltage-clamp recordings of *X. laevis* oocytes, expressing AQP1 (black) or AQP1/mBest1 (blue). **(D)** Kinetic of swelling-induced anion currents (I_{swell}) at -80 and +60 mV over time. **(E)** Current traces in response to voltage steps (20 mV intervals from -80 to +60 mV) in isotonic solution ($290 \text{ mmol}\cdot\text{kg}^{-1}$) and after 5 min in hypotonic solution ($200 \text{ mmol}\cdot\text{kg}^{-1}$). **(F)** Current-voltage relationship under hypo-osmotic conditions. **(G)** Summary of I_{swell} from oocytes, co-expressing AQP1 and the indicated BEST1-constructs at +60 mV. AQP1-expressing oocytes served as control. Values are given as mean \pm S.E.M., (n) = number of measured cells, * significant differences compared to AQP1-expressing oocytes (two-sided unpaired Student's t-test; * = $P < 0.05$). Defolliculated oocytes were carefully monitored for endogenous I_{swell} before experiments.

HiRPE Cells from Two Macular Dystrophy Patients Reveal Aberrant BEST1 Localization

To analyze functional aspects of BEST1 in human RPE, we resorted to RPE differentiated from human induced pluripotent stem cells. Such cell lines reveal properties largely overlapping those of native cells (178) and were generated from a healthy donor and two macular dystrophy patients harboring the heterozygous mutations BEST1-A243V and BEST1-Q238R, respectively (SI Appendix, Fig. S5 A-F). Upon visual inspection, the three cell lines were morphologically identical, all revealing hexagonal cell shape and strong pigmentation, unique features of differentiated RPE cells (Fig. 5 A). Epithelial integrity of the hiRPE cells was established by measuring transepithelial resistance (TER) with a mean TER of $241 \pm 57 \Omega \cdot \text{cm}^2$ for the three cell lines after correction for background.

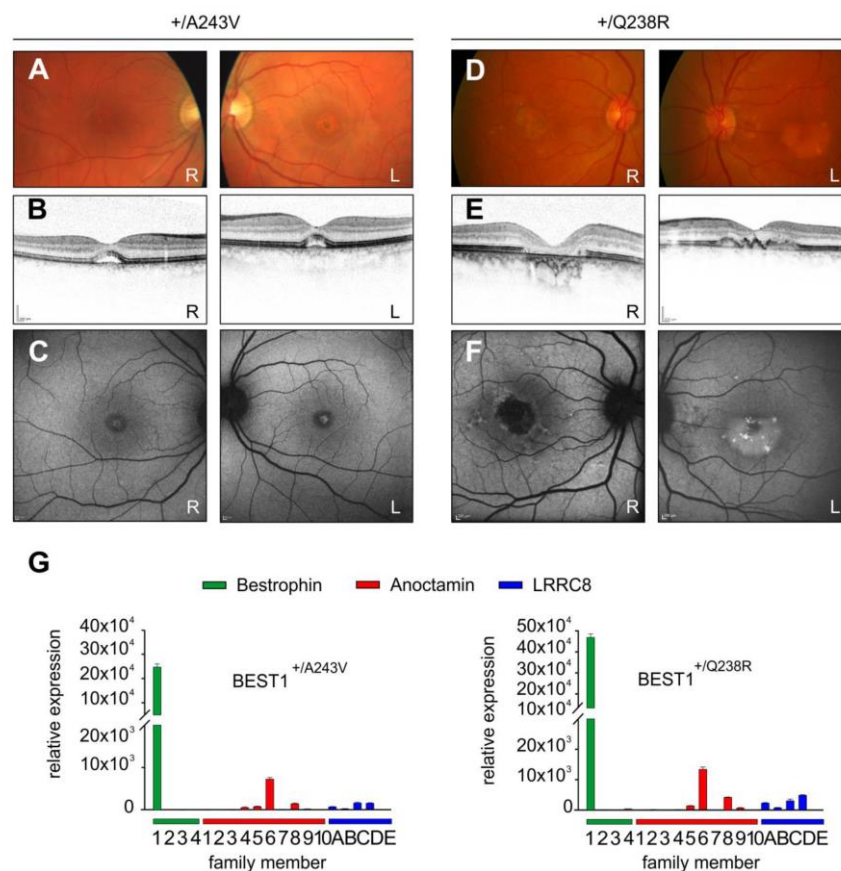


Figure S5. Ophthalmological findings in BD patients with defined mutations in BEST1 (A-C) A 37-year old male patient with a heterozygous mutation in BEST1: c.728C>T, p.A243V. (A) Color fundus photographs of the right (R) and left (L) eye revealing small roundish central lesions with subretinal material deposits (dark-yellowish aspect) surrounded by depigmentation of the RPE. (B) Spectral Domain-Optical Coherence

Tomography (SD-OCT) of the right and left eye depicting a small area of subretinal material deposits and serous detachment of the neurosensory retina. (C) Fundus autofluorescence (FAF) of the right and left eye revealing a distinct increase of autofluorescence surrounded by a dark margin, corresponding to the region of the dark-yellowish deposits. (D-F) A 71-year old male patient with a heterozygous mutation in BEST1: c.713A>G, p.Q238R. (D) Color fundus photographs of the right (R) and left (L) eye revealing central areolar atrophy with loss of RPE in the right eye and vast drusenoid/drusen-like deposits in the left eye. (E) SD-OCT confirming areolar atrophy with major loss of photoreceptors and RPE in the right eye and drusenoid sub-RPE deposits in the left eye. (F) FAF showing a decrease with a margin of increased FAF corresponding to areolar atrophy in the right eye and marked increase of central FAF due to drusenoid accumulations and stress of RPE in the left eye. (G) Relative mRNA expression of bestrophins, anoctamins and LRRC8s in hiPSC- RPE cells from patients carrying the mutation BEST1-A243V or BEST1-Q238R, respectively. Rates of mRNA expression were normalized to HPRT1. Primer sequences and Roche library probes are given in SI Appendix, Table S7. For a comparison to a healthy control individual (BEST1+/+) see Fig. 5E.

Immunostaining of control hiRPE cells with a-334 BEST1 antibody confirmed correct protein localization to the basolateral plasma membrane relative to a-ZO-1, a tight junction marker localized at the apical side of RPE cell clusters (**Fig. 5 B**). In contrast, BEST1-A243V cells revealed localization of BEST1 to both the plasma membrane but also to the cytoplasm, while in BEST1-Q238R, the mutant protein appeared grossly reduced compared to normal RPE and to an even larger extend localized within the cytoplasm with only minor staining of the plasma membrane (**Fig. 5 B**). These findings supported a dominant-negative effect of the mutant protein on wild type BEST1. Semi-quantitative Western blot analysis confirmed reduced expression of BEST1 protein in BEST1-Q238R while RNA expression levels appeared similar in the three cell lines analyzed (**Fig. 5 C and D**).

We further tested RNA expression for bestrophins, known CaCCs and volume-sensitive LRRC8s and confirmed that the profiles are similar for the three hiRPE cell lines when compared to native RPE (**Fig. 1 F and Fig. 5 E and SI Appendix, Fig. S5 G**), suggesting that the hiRPE cell lines represent suitable cellular models to investigate BEST1 function in a setting similar to native RPE.

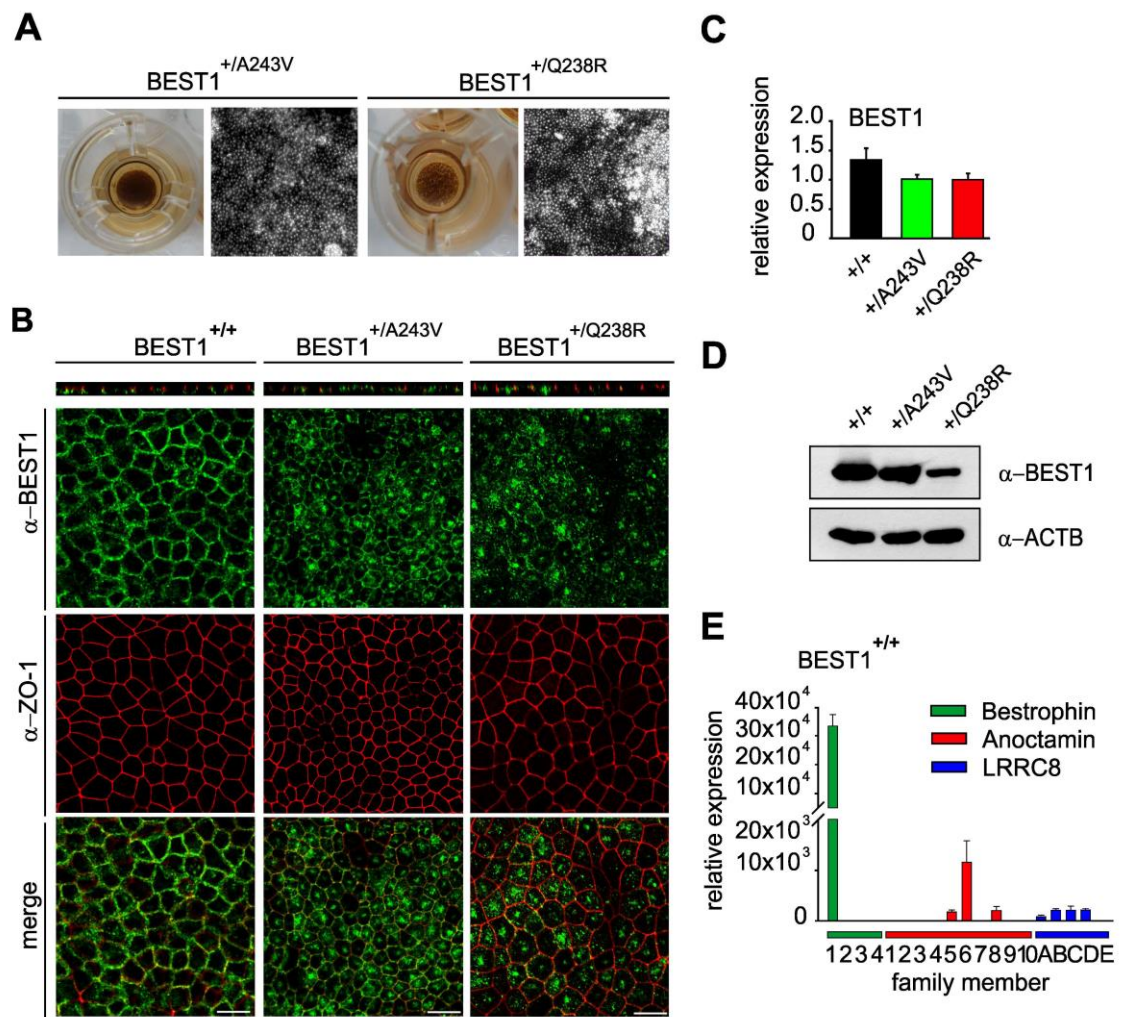


Figure 5. Expression and localization of normal and macular dystrophy associated mutant BEST1 in hiRPE cells (A) Images of hiRPE cells from two BD patients (+/A243V or +/Q238R) after 2 months grown on 12-well-transwell filter (left panel). Bright field microscopy of pigmented hiRPE cells (right panel). Scale bar = 100 μ m. (B) Flat mount immunofluorescence imaging of BEST1 and ZO-1 proteins. Shown are x-y and x-z projections of confocal image stacks. Scale bars: 20 μ m. (C) Quantification of BEST1 RNA expression by qRT-PCR of total RNA extracted from hiRPE transwell filters. Samples were performed in triplicates and normalized to HPRT1. (D) Western blot analysis of hiRPE cell lysates using BEST1 antibody a-334 for detection. ACTB served as loading control. (E) Relative mRNA expression of indicated genes in hiRPE cells from a healthy donor (BEST1^{+/+}) (n = 3) normalized to HPRT1. Results from patient-derived RPE cells see SI Appendix, Fig. S5 G. Primer sequences and Roche library probes are given in SI Appendix, Table S7.

Swelling-Induced Anion Currents are Absent in hiRPE Cells from Macular Dystrophy Patients with Heterozygous BEST1 Mutations

To characterize swelling-induced currents in hiRPE cells, whole-cell voltage-clamp recordings were performed in isosmotic bath solution (intra- and extracellular solution at 290 mmol \cdot kg⁻¹) (SI Appendix, Fig. S6 A). First, wild type hiRPE cells ((+/+), n = 18) were

challenged by exchanging the extracellular bath for a hyposmotic solution (260 mmol kg^{-1}). The resulting difference in osmotic pressure led to an increase in conductance, as monitored by increased inward and outward currents in response to voltage ramps (**Fig. 6 A and B**). Functional properties of this current were analyzed in a subset of cells ($n = 7$) using an extended protocol. Under the given ionic conditions, currents were slightly outward rectifying and reversed polarity at $+4 \pm 2 \text{ mV}$ (**Fig. 6 C and SI Appendix, Fig. S6 B**). The osmotic pressure-induced currents increased with a half-time of $3.3 \pm 0.2 \text{ min}$ (**SI Appendix, Fig. S6 B**) to reach a plateau on average of $2.3 \pm 0.7 \text{ nA}$ (**Fig. 6 D**). Reducing extracellular Cl^- concentration to 2 mM by replacing Cl^- with gluconate, led to a marked decrease of outward currents to $0.6 \pm 0.2 \text{ nA}$ (compatible with a diminished influx of anions due to a lower permeability for gluconate compared to Cl^-) (**Fig. 6 A and D**), paralleled by a shift of the reversal potential to positive values ($+22 \pm 6 \text{ mV}$) (**Fig. 6 C**). This indicates that the swelling-activated current is carried by anions. Moreover, adding DIDS ($300\text{-}600 \mu\text{M}$) to the external bath solution also markedly reduced currents, by stronger affecting outward currents (**Fig. 6 A and C-D**), pointing to an anion permeable pore that conducts the swelling-induced current in hiRPE (+/+) cells.

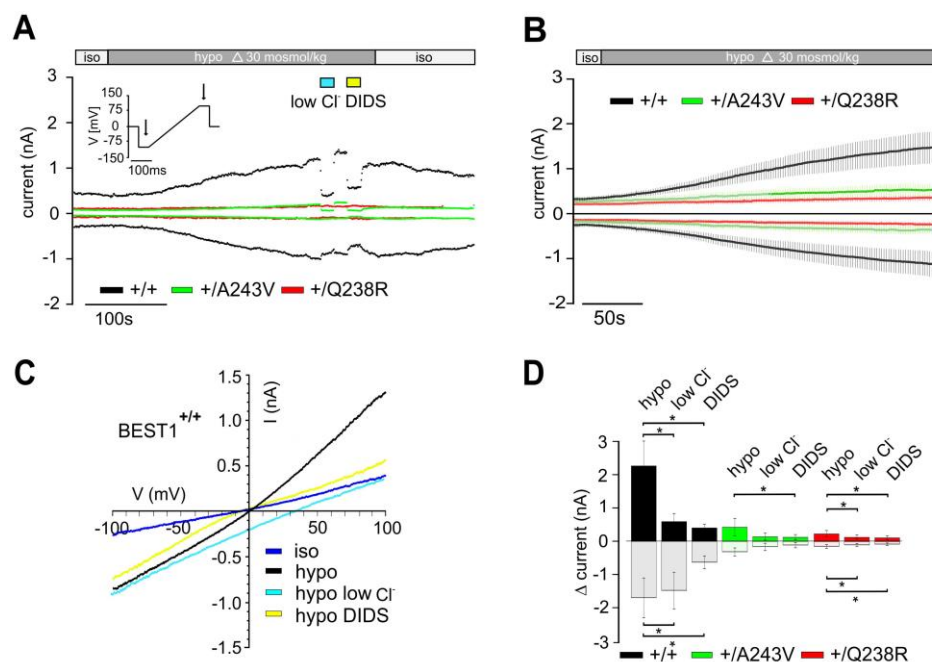


Figure 6. Swelling-induced anion currents in hiRPE cells are greatly reduced in patients with macular

dystrophy (A-D) Whole-cell voltage-clamp recordings of hiRPE cells from a healthy donor (+/+) and two macular dystrophy patients (+/A243V or +/Q238R) under indicated conditions. **(A)** Activation of endogenous anion currents upon hypotonic challenge ($260 \text{ mmol}\cdot\text{kg}^{-1}$) over time. Data were extracted from recordings of voltage ramps at -100 and $+100$ mV. **(B)** Averaged currents recorded at -100 to $+100$ mV upon hypotonic challenge for 5 min. **(C)** IV plot of selected recordings from **(A)**. Also see SI Appendix, Fig. S6 C-D. **(D)** Statistical analysis of I_{swell} obtained from experiments **(A-C)**. Data points are corrected for baseline currents under isotonic conditions ($290 \text{ mmol}\cdot\text{kg}^{-1}$). Values are given as mean \pm S.E.M. Two-sided paired Student's t-test; * = $P < 0.05$

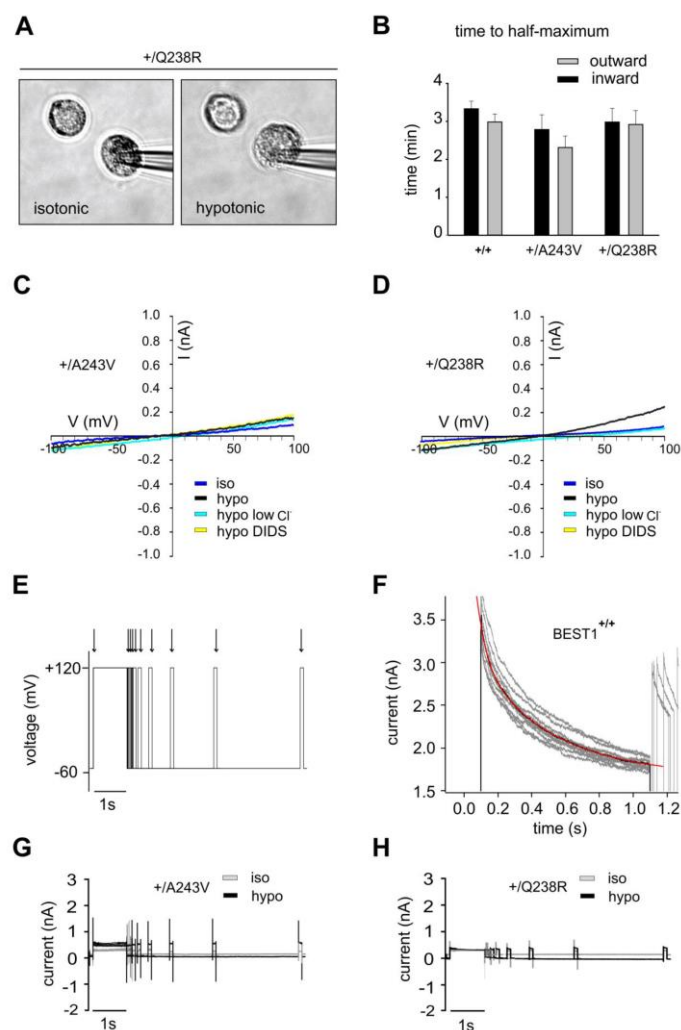


Figure S6. Characteristic features of VRACs are lost in hiPSC-derived RPE cells from Best disease patients **(A)** Photomicrograph showing two hiPSC-derived RPE cells (BEST1-Q238R) under iso- (left panel) or hypotonic conditions (right panel). One cell is attached by a recording pipette. **(B)** Bar diagram depicting the activation kinetics of swelling-induced currents of hiPSC-derived RPE cells from a healthy control (+/+) or from patients carrying the BEST1-A243V (+/A243V) or BEST1-Q238R (+/Q238R) mutation, respectively. The time to reach 50% of the maximum amplitude (inward or outward direction) is indicated. For further details see SI Appendix, Table S4. **(C-D)** Current-voltage relationship of hiPSC-derived RPE cells from patients with mutation BEST1-A243V (c) or BEST1-Q238R (d). Traces represent currents induced by voltage-ramps from -100 to $+100$ mV under the conditions indicated (iso: unstimulated $290 \text{ mmol}\cdot\text{kg}^{-1}$, hypo: stimulated with $260 \text{ mmol}\cdot\text{kg}^{-1}$, hypo low Cl⁻: hypotonic solution containing 2 mM Cl^- , hypo DIDS: hypotonic solution containing

300-600 μ M DIDS). Related to Fig. 6C. (E) Two-pulse protocol. A one-second depolarizing voltage pulse (from -60 to +120 mV) is followed by a second depolarizing pulse after a variable delay (20, 40, 80, 160, 320, 640, 1280, 2560 or 5120 ms). (F) Whole-cell voltage-clamp recording showing an array of currents recorded from a wildtype hiPSC-derived RPE cell (BEST1+/+). Currents were induced by depolarizing voltage steps from -60 to +120 mV (1 sec) (see SI Appendix Fig. S6 E). The red curve indicates the mono-exponential fit of the average trace obtained from the mathematical average of 10 current recordings. This current relaxation shows the voltage-dependent inactivation of the swelling-induced VRAC. (G-H) Current recordings of hiPSC-derived RPE cells from patients carrying the BEST1-A243V (G) or BEST1-Q238R mutation (H), performed with the 2-pulse protocol shown in SI Appendix, Fig. S5 E. Currents were recorded under isotonic (grey traces) or hypotonic (black traces) conditions. Currents did not show relaxation during the 1-sec depolarizing voltage step and did not show any voltage- or time-dependent recovery. Related to Fig. 7B.

Additionally, osmotic pressure-induced I_{swell} in hiRPE (+/+) cells featured a characteristic time- and voltage-dependent inactivation at strong positive voltages (**Fig. 7 A and B**). After activation of I_{swell} by application of hyposmotic bath solution, currents showed pronounced current relaxation (inactivation) during a depolarizing voltage step (+120 mV, 1s) with a decay following a double-exponential time course (time constant $t_1 = 0.22 \pm 0.13$ s and $t_2 = 0.9 \pm 0.15$ s). Currents recovered from inactivation at negative voltages (-60 mV) with a time constant of $t = 1.57$ s. The time and voltage-dependent inactivation can be modulated by extracellular cations (179) and is absent in extracellular Ca^{2+} -free bath solution (**Fig. 7 C**), whereas the activation of I_{swell} remained unaffected (**Fig. 7 D**). Together, these data argue for the presence of an I_{swell} in hiRPE (+/+) cells which exhibits the functional properties of a typical VRAC (79).

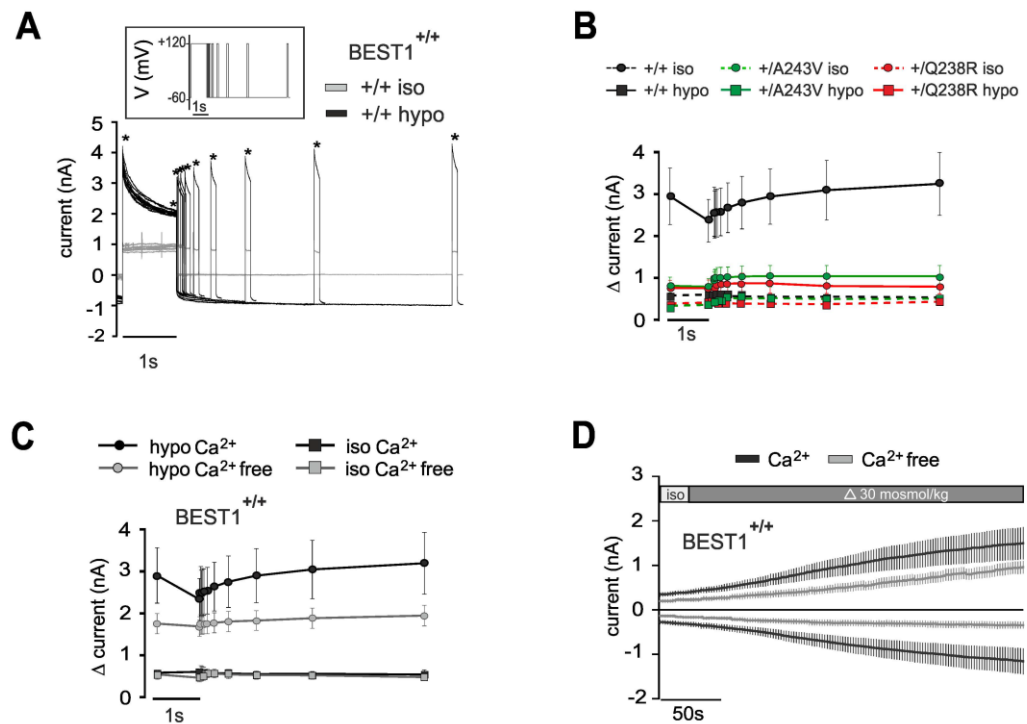


Figure 7. Swelling-induced anion currents in hiRPE cells display time- and voltage-dependent inactivation (A-D) Voltage-dependent inactivation and recovery from inactivation of I_{swell} during a 2-voltage step experiment. After inactivation of I_{swell} during the first voltage step to +120 mV for 1 s, the cell was held at -60 mV with increasing time intervals and then stepped back to +120 mV. (A) Representative recording from a control (BEST1^{+/+}). Asterisks indicate time points of current amplitudes analyzed in (B) and (C). (B) Summary of experiments from hiRPE cells of control and BD patients. Also see SI Appendix, Fig. S6 E-H. (C) Kinetics of I_{swell} (at -100 mV and +100 mV) in hiRPE cells (BEST1^{+/+}) under the Ca²⁺ conditions indicated. A one second lasting depolarizing prepulse lead to voltage-dependent inactivation. A second pulse with varying delay revealed time-dependent recovery from inactivation. (D) Summary of voltage-dependent inactivation and time-dependent recovery from inactivation of I_{swell} in 2-pulse experiments in hiRPE cells (BEST1^{+/+}) under the Ca²⁺ conditions indicated. The currents are corrected for baseline. Values are given as mean \pm S.E.M.

HiRPE cells from BD patients carrying mutations BEST1-A243V or BEST1-Q238R, respectively, showed voltage-driven currents under isosmotic conditions that were similar (BEST1-A243V) or slightly smaller (BEST1-Q238R) when compared to hiRPE (+/+) cells (Fig. 6 B and SI Appendix, Table S3). Notably, challenging the cells with hypotonic bath solution induced only small voltage-driven currents (Fig. 6 A-D and SI Appendix, Fig. S6 C and D and SI Appendix, Table S3 and S4) in a fraction of cells (8 out of 22 in BEST1-Q238R and 6 out of 14 cells in BEST1-A243V). The remaining cells did not significantly change conductance upon treatment with hypotonic solution. The residual currents in responsive cells were still sensitive to the application of low Cl⁻ containing solution or DIDS

(**Fig. 6 A and D**). However, currents induced by depolarizing voltage steps during hypotonic challenge did not show any inactivation or current relaxation, similar to the situation found under isosmotic conditions (**SI Appendix, Fig. S6 E-H**).

Supplemental Table 3. Mean values of Cl⁻ currents in hiPSC-RPE cells

osmolality mosmol/kg	genotype	current (+100 mV) (nA)	current (-100 mV) (nA)	n
	WT	0.314 ± 0.05	-0.263 ± 0.05	18
290 (iso)	Q238R	0.199 ± 0.04	-0.141 ± 0.04	22
	A243V	0.268 ± 0.06	-0.188 ± 0.04	14
260 (hypo)	Q238R	0.332 ± 0.10	-0.221 ± 0.06	13
	A243V	0.605 ± 0.31	-0.462 ± 0.15	6
260 (delta hypo)	Q238R	0.226 ± 0.10	-0.157 ± 0.06	13
	A243V	0.422 ± 0.26	-0.326 ± 0.12	6

Stable Knockdown of LRRC8A in hiRPE Cells Has No Effect on I_{swell}

Motivated by two recent publications which identified LRRC8A as an essential component of VRAC in several cell lines (13;14), we analyzed a potential role of LRRC8A in hiRPE volume regulation. We therefore established a stable short-hairpin RNA (shRNA)-mediated knockdown of LRRC8A expression in hiRPE cells of healthy control. After two rounds of lentiviral transduction with shRNA against LRRC8A (hiRPE_{shLRRC8A}), qRT-PCR analysis revealed a 76 % mRNA decrease of LRRC8A expression compared to control cells treated with lentivirus coding for scrambled RNA (hiRPE_{scramble}) (**Fig. 8 A**). This was confirmed by antibody staining of LRRC8A which was markedly reduced in whole-cell lysates of hiRPE_{shLRRC8A} cells (**Fig. 8 B**). A standardized protocol of hypotonic current activation and subsequent isotonic inactivation was used for whole-cell voltage-clamp recordings (**Fig. 8 C**). Challenging the cells with hypo-osmotic bath solution led to activation of I_{swell} in 54% of hiRPE_{shLRRC8A} (27/50 cells) and in 40% of the hiRPE_{scramble} (25/63 cells), while the average magnitude of I_{swell} in hiRPE_{shLRRC8A} cells was somewhat larger compared to

hiRPE_{scramble} controls (outward: 150%, $p=0.03$; inward: 150%, $p=0.3$, n.s.) (**Fig. 8 D**). Taken together, the shRNA-mediated knockdown of LRRC8A in hiRPE cells led to a reduction in both, the level of LRRC8A mRNA and protein, while no significant difference in I_{swell} between hiRPE_{shLRRC8A} and hiRPE_{scramble} was observed (neither in number of responders, nor in magnitude of current).

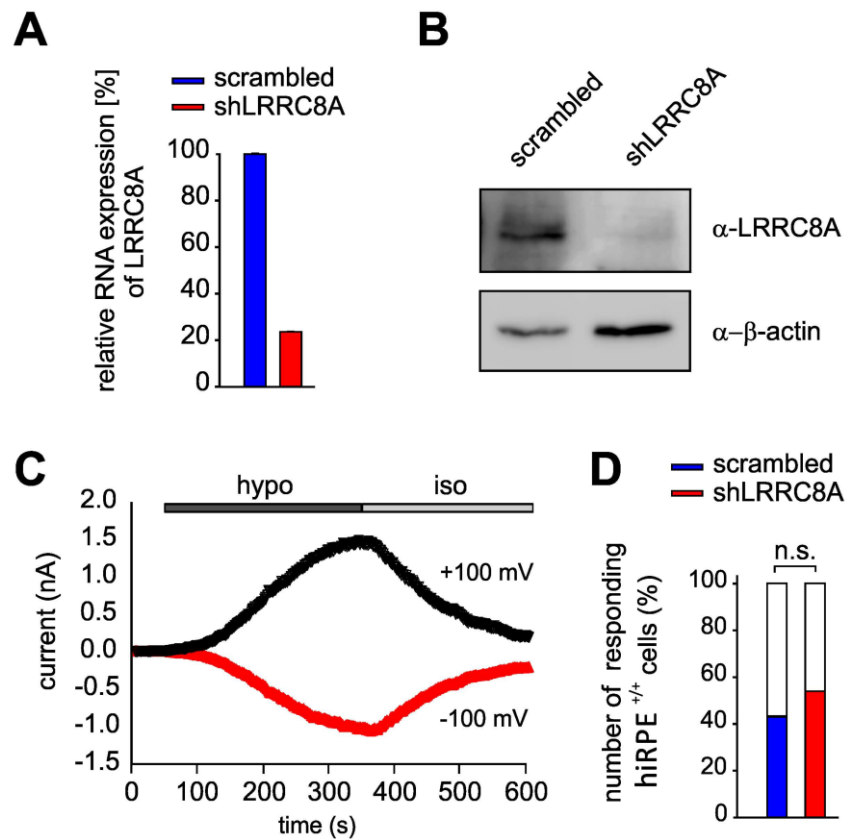


Figure 8. Stable knockdown of LRRC8A in hiRPE cells has no effect on I_{swell} (A) Relative mRNA expression of hLRRC8A in hiRPE^{+/+} cells virally transduced with scrambled (hiRPE_{scrambled}) and LRRC8A shRNA (hiRPE_{shLRRC8A}), normalized to Hprt1 expression. (n = 2, pooled data from analysis after 1 and 4 weeks of lentiviral transduction; mean \pm SD). (B) Western blot analysis of hiRPE_{scrambled} and hiRPE_{shLRRC8A} lysates using α -LRRC8A. Per lane, three 12-well-transwell filters were pooled. Anti-beta actin served as control. (C) Representative graph showing swelling-induced whole-cell currents of a hiRPE_{scrambled} cell using a standardized protocol with current activation at 260 mmol kg⁻¹ for 300 sec and inactivation at 290 mmol kg⁻¹ for at least 200 sec. Data were extracted from recordings of voltage ramps at -100 and +100 mV. (D) Bar graph depicting the fraction of responders vs. non-responders of analyzed hiRPE_{scrambled} (n = 63) and hiRPE_{shLRRC8A} (n = 50) cells.

Discussion

The present study provides several lines of direct and indirect evidence arguing for BEST1 as a crucial component of VRAC in mouse sperm and human RPE. Our findings show

that lack or dysfunction of these properties have vital implications on both mouse sperm resulting in a severe sub-fertility phenotype and human RPE cells strongly reducing swelling-induced anion currents. Moreover, heterologous overexpression of both human and mouse BEST1 in AQP1-co-expressing *X. laevis* oocytes results in a significant rescue in a membrane rupture assay and an increase of I_{swell} upon hypotonic stimulation. Importantly, the latter set of experiments demonstrates that mouse and human BEST1 have a similar if not identical role in volume regulation, despite the fact that the two orthologues proteins operate in highly diverse and specialized cell types.

Until now, the mammalian bestrophins and their functional role in classical VRAC activity were rather controversial. Essentially, three main arguments were brought forward. Strikingly, BEST1 whole-cell currents behaved largely insensitive toward hypotonic challenges after heterologous overexpression of bestrophin family members in HEK293 cells (138). We argue that the HEK293 cell system is ill-suited for addressing this particular question as these cells are known to retain a large proportion of overexpressed BEST1 protein intracellularly (180). Upon hypotonic stimulation, the simultaneous activation of the endogenous LRRC8A-mediated VRAC current in HEK293 cells (13;14) renders it impossible to distinguish endogenous VRAC from heterologously expressed BEST1 currents. To avoid these methodological difficulties, we resorted to *Xenopus* oocytes, a polarized cell system which provides an important precondition for plasma membrane localization of BEST1 (181). After manual defolliculation and careful monitoring of each single batch for endogenous swelling-activated whole-cell currents, we recorded BEST-mediated swelling-sensitive currents which were significantly enlarged relative to endogenous I_{swell} . Together, these experiments demonstrated that (i) mouse and human BEST1 are functionally interchangeable, and (ii) BEST1 current indeed is activated by hypo-osmotic solution.

Secondly, the *Drosophila* dBest1 was suggested as VRAC (137;150), but the biophysical characteristics of endogenous dBest1 in S2R+ cells from *Drosophila* differed significantly from properties of I_{swell} in mammalian VRAC (79). This further questioned the role of mammalian BEST1 as VRAC although the discrepant channel characteristics may best be

explained by an obvious sequence diversity of bestrophins from arthropod to vertebrate. Specifically, dBest1 reveals a sequence identity to human paralogs BEST1, BEST2, BEST3 and BEST4 of 52%, 53%, 51% and 49%, respectively. On the basis of such close sequence identities, a human orthologue to *Drosophila* dBest1 cannot be assigned which makes it rather difficult to compare functional aspects between the phylogenetically related bestrophin families.

Further arguments contradicting a role of BEST1 as VRAC developed from findings in a knockout mouse model demonstrating that Best1 deficiency failed to eliminate VRAC in peritoneal macrophages (151). Additionally, siRNA-mediated knockdown of endogenous BEST1 in HEK293 cells had no effect on hypotonicity-induced YFP quenching responses (56). These findings, however, do not contradict the results presented in the present study. In fact, no or very weak RNA and protein expression is not in favor of a functional role of mBest1 in macrophages or hBEST1 in HEK293 cells further supporting our hypothesis of cell- or tissue-specific VRAC channel diversity.

While mutations in the *BEST1* gene cause an ocular phenotype in human, our thorough analysis of a Best1-deficient mouse has not revealed a comparable retinal pathology in the murine model. This is in agreement with lack of Best1 expression in the murine RPE and findings in an independent *Best1*^{-/-} knockout mouse revealing no effect on RPE chloride conductance (57). Conversely, high expression of Best1 in mouse sperm is associated with a strong fertility phenotype. Unfortunately, our evidence linking the observed sperm phenotype to a defect in volume regulation is rather indirect and is not based on direct measurements of ion currents. Particularly for mouse sperm, the latter experimental approach is most challenging, due to the low volume of sperm cytoplasm and the fact that the plasma membrane of intact spermatozoa is extremely rigid (182). In our hands, shifting to hypotonic solution repeatedly resulted in loss of the whole-cell configuration between the patch-clamp pipette and the cytoplasmic droplet membrane of the sperm tail. We also tested optical methods to study sperm ion channels via fluorescent indicators. Specifically, we used fluorescent chloride indicator MQAE and the volumetric indicator Calcein-AM. Again, the

results were little encouraging due to the miniscule volume of the sperm cytoplasm and the resulting weak fluorescence.

Unexpectedly, sperm motility of *Best1*^{-/-} mice was not fully rescued by hypertonic solution, in contrast to reports e.g. for spermatozoa from the *Slo*^{-/-} mouse (183). As suggested by Voets et al. (8), this finding may be explained by VRAC activation in *Best1*^{-/-} spermatozoa before ejaculation and could be triggered by reduced intracellular ionic strength. As spermatozoa pass from the testis to the cauda of the epididymis, before ejaculation they are stored in a concentrated environment of high osmolality and low intracellular ionic strength when compared to the testical environment (184). Upon ejaculation, the hypotonic environment of the female tract could still enhance an epididymal *Best1*^{-/-} sperm defect which would then be reflected by the significantly reduced motility compared to the higher osmotic condition.

Recently, *LRRC8A* was suggested as an integral component of VRAC or, alternatively, crucial for its activation as shown in siRNA-mediated knockdown and CRISPR/Cas9 genome editing experiments (13;14). In this model, VRAC is formed by *LRRC8* hexamers of *LRRC8A* and at least one other family member. Hence, small variations of biophysical and biochemical features of VRAC in different cell types (79) may be explained by a variable cell type- or tissue-specific combination of *LRRC8A* with different *LRRC8* isoforms (14). Our findings are not in support of such a model which is exclusively based on *LRRC8A* and its family members as the sole components of VRAC. We show that in mouse sperm, only *LRRC8B* but no other *LRRC8* isoform is sufficiently expressed to account for a crucial functional role in this cell type. Considering that disruption or overexpression of isoform *LRRC8B* alone did not alter I_{swell} in HEK293 and HCT116 cells (14), a sole function of *LRRC8B* appears insufficient to mediate VRAC pore properties in mouse sperm. Furthermore, our data demonstrate that hiRPE cells are well capable of regulating cell volume although *LRRC8A* is significantly reduced in our shRNA knockdown experiments.

In conclusion, the identification of *BEST1* as an essential component of VRAC in human RPE and the restricted expression of the protein in human RPE and mouse sperm, led us to

propose a model scenario where VRAC is a cell type- or tissue-specific complex rather than a single ubiquitous channel. A refined knowledge about protein expression in the different cell types and species might help to find additional components of the vertebrate family of VRACs. Particularly, other members of the bestrophins family need to be assessed for their possible role in volume regulation in specifically defined cells or tissues. Together, our findings provide the basis to further explore the mechanisms of cell volume regulation in normal and diseased cell physiology possibly delineating novel therapeutic treatment strategies for BEST1- and other VRAC-associated pathologies.

Acknowledgments

We thank Timo Strünker, Luis Alvarez, and Christoph Brenker (Department of Molecular Sensory Systems, Caesar, Bonn, Germany) for help with sperm motility experiments and for critically reading the manuscript, M. Landthaler (Department of Dermatology, University Hospital Regensburg, Germany), L. Bruckner-Tuderman and J.S. Kern (Department of Dermatology, University Hospital Freiburg, Germany) for providing human skin biopsies, M. Breunig and A. Göpferich (Department of Pharmaceutical Technology, University of Regensburg, Germany) for help with confocal microscopy, T. Jahner for technical assistance and E. Röhrl for help with ocular phenotyping of Best^{-/-} mice. This work was supported in part by a grant from Novartis Pharma, Germany (Reference No. 3625340 to CB and BHFw), grants from the German Research Foundation (DFG WE1259/20-1 to BHFw and WE2298/4-1 to CHW), DFG SFB699 projects A7 and A12 (to KK), and the Volkswagenstiftung (#87499 to KK)

Chapter 5

TMC8 (EVER2) attenuates intracellular signaling by Zn^{2+} and Ca^{2+} and suppresses activation of Cl^- currents

Abstract

Eight paralogues members form the family of transmembrane channel-like (TMC) proteins that share considerable sequence homology to anoctamin 1 (Ano1, TMEM16A). Ano1 is a Ca^{2+} activated Cl^- channel that is related to head and neck cancer, often caused by human papilloma virus (HPV) infection. Mutations in TMC 6 and 8 (EVER1, EVER2) cause epidermodysplasia verruciformis. This rare skin disease is characterized by abnormal susceptibility to HPV infection and cancer. We found that in contrast to Ano1 the common paralogues TMC4 – TMC8 did not produce Ca^{2+} activated Cl^- currents when expressed in HEK293 cells. On the contrary, TMC8 was found to be localized in the endoplasmic reticulum (ER), where it inhibited receptor mediated Ca^{2+} release, activation of Ano1 and volume regulated LRRC8-related Cl^- currents. Zn^{2+} is co-released from the ER together with Ca^{2+} and thereby further augments Ca^{2+} store release. Because TMC8 is required to lower cytosolic Zn^{2+} concentrations by the Zn^{2+} transporter ZnT-1, we hypothesize that HPV infections and cancer caused by mutations in TMC8 are related to upregulated Zn^{2+}/Ca^{2+} signaling and activation of Ano1.

Key words: Transmembrane channel-like protein, TMC8, EVER2, Zn^{2+} signaling, LRRC8A, anoctamin 1

Published in: Lalida Sirianant, Jiraporn Ousingsawat, Yuemin Tian, Rainer Schreiber, Karl Kunzelmann. TMC8 (EVER2) attenuates intracellular signaling by Zn^{2+} and Ca^{2+} and suppresses activation of Cl^- currents. *Cellular signaling*. 2014 Dec;26(12):2826-33

Own experimental contribution: All patch clamping experiments

Own written contribution: Methods, Results, Parts of Introduction and Discussion.

Other contributions: Designed experiments and analyzed data.

Introduction

The transmembrane channel-like (TMC) family of proteins consists of 8 members in mammals. These proteins have been implicated in human diseases like hearing loss and human papillomavirus (HPV) infections, leading to epidermodysplasia verruciformis and cancer (62;185;186). There is a noticeable overlap between TMC proteins and anoctamins, which suggested that these proteins may form a super family (65). Ten paralogous proteins form the anoctamin family of proteins (Ano1-10, TMEM16A-K). It was shown for Ano1, 2, and 6 that they can produce Ca²⁺ activated Cl⁻ channels (20;22;23;29;36;187;188), while Ano6 and other anoctamins have additional functions (29;39;189). Overexpression of anoctamin 1 is observed in head and neck cancer (HNSCC) and other tumors, where they support proliferation and tumor development (190-194). Notably, about half of all HNSCC are caused by infection with HPV (195-197).

TMC4 – 7 but not TMC8 show relatively broad expression (186). Individuals with mutations in TMC6 or TMC8 (EVER1, EVER2) demonstrate high susceptibility towards infections with HPV, which turns into uncontrolled HPV infections, growth of scaly macules and papules, which have a high risk to turn into cancer (69;198). It was shown that TMC6 and TMC8 activate the ER-located zinc transporter ZnT-1, thereby facilitating Zn²⁺ uptake into the endoplasmic reticulum, a mechanism that appears essential to protect from HPV-infections. Mutations in TMC6 and TMC8 may therefore lead to enhanced cytosolic Zn²⁺ levels with leakage of Zn²⁺ into the nucleus and enhanced transcription of Zn²⁺-dependent viral proteins (68;69). Noticeable similarities exist between HNSCC and epidermodysplasia verruciformis, which suggests common pathogenic pathways (199).

Because of the potential structural similarities between anoctamins and TMC proteins, we asked whether TMC proteins are able to produce Ca²⁺ activated Cl⁻ currents. However, while activation of Cl⁻ currents was not observed, we found for TMC8 suppression of Ca²⁺ and volume activated Cl⁻ currents. Suppression of Ano1 currents was due to attenuation of intracellular Ca²⁺ signaling, which was controlled by cytosolic Zn²⁺ levels. The data demonstrate for the first time that TMC8 limits activation of Ca²⁺-dependent and volume activated whole cell currents, probably by controlling compartmentalized intracellular Ca²⁺

signaling.

Materials and Methods

Cell culture, cloning of TMCs, siRNA: HEK293, Fisher rat thyroid (FRT), HT₂₉, and Cal33 cells were grown in DMEM-F12 and OptiMEM medium, respectively. All media were supplemented with 10% FBS. Cells were incubated in 5% CO₂ at 37°C. Plasmids were transfected into cells using standard methods (Lipofectamine, Invitrogen). Cells were examined 48 or 72 h after transfection. cDNA of TMC4 (IRAU_p969G1081D); TMC5 (IRAK_p961O07168Q), TMC6 (IRAU_p969E0379D), TMC7 (IRAT_p970H0474D) and TMC8 (IRAT_p970F12109D) (imaGenes; Berlin, Germany) were subcloned into pcDNA31. Fusion proteins with EGFP were generated by PCR techniques. All cDNAs were verified by sequencing. TMC8-siRNA (Stealth RNAi™; Life technologies) had the sequence 5'-GGGAGGAGCUGUACAAGCUGAGUAU-3'.

Immunocytochemistry: HEK293 cells or Fisher rat thyroid cells were transfected with TMC-GFP fusion proteins. F-actin was labeled with phalloidin-conjugated AlexaFluor®647 (1:40, Molecular Probes, Invitrogen). TMC4-GFP – TMC8-GFP proteins were localized using polyclonal rabbit anti-GFP antibody (Invitrogen A11122). Cells were mounted on glass slides with fluorescent mounting medium (DAKO Cytomation, Hamburg, Germany) and examined under confocal conditions using ApoTome Axiovert 200 M fluorescence microscope (Zeiss, Göttingen, Germany). Nuclei were counterstained with Hoe33342 (0.1 µg/ml PBS, Aplichem, Darmstadt, Germany).

Flow cytometry: After transfection cells were trypsinized and exposed to control isotonic (Iso) solution containing (mM): NaCl 72.5, KH₂PO₄ 0.4, K₂HPO₄ 1.6, D-glucose 6, MgCl₂ 1, Ca-gluconate 1.3, Mannitol 145, pH 7.4. Hypotonic solution (Hypo) was generated by removing mannitol (145 mosm/l). Cell volume was determined continuously for 20 minutes, after exposure to isotonic or hypotonic bath solution, using CASY-TT (Roche, Germany).

Patch clamping: Cells grown on cover slips were mounted in a perfused bath on the stage of an inverted microscope (IM35, Zeiss) and kept at 37°C The bath was perfused continuously with Ringer solution (mM: NaCl 145, KH₂PO₄ 0.4, K₂HPO₄ 1.6, D-glucose 6, MgCl₂ 1, Ca-

gluconate 1.3, pH 7.4) at about 10 ml/min. Experiments were performed in the fast whole-cell configuration. Patch pipettes had an input resistance of 3-5 M Ω , when filled with an intracellular like solution containing (mM) KCl 30, K-gluconate 95, NaH₂PO₄ 1.2, Na₂HPO₄ 4.8, EGTA 1, Ca-gluconate 0.758, MgCl₂ 1.034, D-glucose 5, ATP 3. pH was 7.2, the Ca^{2+} activity was 0.1 μ M. Access conductances were measured continuously and were between 90-140 nS (EPC 9 amplifier, List Medical Electronics, Darmstadt, Germany). In regular intervals, membrane voltages (V_c) were clamped in steps of 20 mV from -100 to +100 mV.

Ca²⁺ measurements: For single cell fluorescence measurements cells were grown on glass covers slips, mounted in a cell chamber and perfused with ringer solution at 37°C, as described previously (29). To measure intracellular Ca^{2+} levels, cells were loaded with 2 μ M Fura-2, AM and 0.02% pluronic (Life technologies) for 1h at RT. Fura-2 was excited at 340/380 nm, and emission was recorded between 470 and 550 nm. For measurements of changes in intracellular Zn^{2+} levels, Cal33 cells were loaded with 25 μ M zinquin (2h, 37°C; Enzo Life Sciences (Plymouth, PA) and fluorescence was collected at an emission wavelength of 470 nm.

Iodide Quenching:

Quenching of the intracellular fluorescence generated by the iodide-sensitive enhanced yellow fluorescent protein (EYFP-I152L) was used to measure anion conductance. YFP-I152L fluorescence was excited at 490 nm using a high speed polychromatic illumination system for microscopic fluorescence measurement (Visitron Systems, Puchheim, Germany) and the emitted light at 535 ± 25 nm was detected with a Coolsnap HQ CCD camera (Roper Scientific). Quenching of YFP-I152L fluorescence by I^{-} influx was induced by replacing 20 mM extracellular Cl^{-} by I^{-} . Images were analyzed with Metafluor software (Universal Imaging). Background fluorescence was subtracted, and autofluorescence was negligible. Changes in fluorescence induced by I^{-} are expressed as initial rates of maximal fluorescence decrease ($\Delta RF/\Delta t$). Slopes for fluorescence quenching were independent on absolute YFP fluorescence.

Compounds and Statistic: All compounds used were of the highest available grade of purity

and were from Sigma or Calbiochem. Statistical analysis was performed using Student *t*-test (for paired or unpaired samples) or, if appropriate, ANOVA. *P* < 0.05 was accepted as significant.

Results

TMC proteins do not produce Ca²⁺ activated Cl⁻ currents in HEK293 cells:

Anoctamin 1 (Ano1, TMEM16A) is a Ca²⁺ activated Cl⁻ channel (20;22;23). Because of its strong homology to transmembrane channel-like (TMC) proteins, we examined if the TMC paralogues 4, 5, 6, 7, and 8 generate Ca²⁺ activated Cl⁻ currents when expressed in HEK293 cells. However, no currents could be detected upon stimulation of TMC-overexpressing cells with either ionomycin (1 μM) or ATP (100 μM) (Fig. 1). Interestingly, in TMC6 and TMC8 expressing cells, membrane currents appeared smaller, suggesting an inhibitory effect on endogenous membrane channels (Fig. 1). We examined cellular localization of GFP-tagged TMC proteins when expressed in HEK293 and Fisher rat thyroid (FRT) cells, and found expression exclusively in intracellular compartments (Fig. 2,3). Earlier studies showed that TMC6 and TMC8 (EVER1 and EVER2) are located in the endoplasmic reticulum (ER) (185). We focused on TMC8 and found that overexpressed TMC8 is also located in the ER, as indicated by co-labeling with ER tracker (Fig. 4A). No endogenous TMC8 was detected in HEK293 cells by RT-PCR, and only weak expression was found for TMC6 and TMC7 (Fig. 4B).

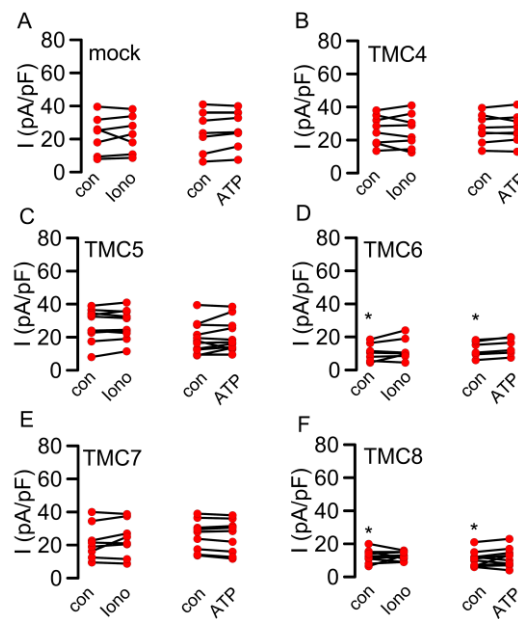


Fig. 1: TMC proteins do not produce Ca^{2+} activated Cl^- channels. Summary of current densities ($V_c = +100$ mV) measured in whole cell patch clamp experiments with mock transfected HEK293 cells (A) or cells overexpressing TMC4 (B), TMC5 (C), TMC6 (D), TMC7 (E) or TMC8 (F). Cells were stimulated with either the Ca^{2+} ionophore ionomycin ($1 \mu M$) or the purinergic ligand ATP ($100 \mu M$). No whole cell currents were activated, while baseline currents appeared reduced in TMC6 and TMC8 expressing cells. Mean \pm SEM (Number of experiments). *indicates significant difference to mock transfected cells (unpaired t-test).

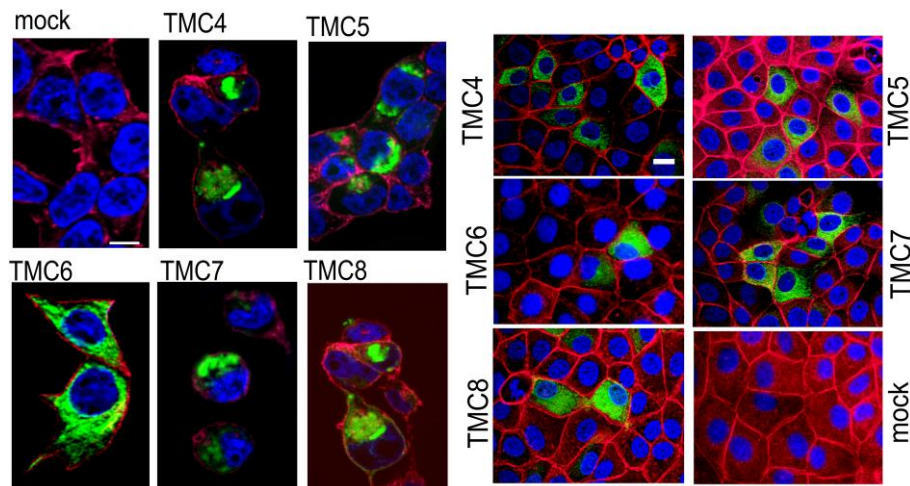


Fig. 2: Expression of TMC proteins in HEK293 cells. Intracellular localization of GFP tagged TMC proteins overexpressed in HEK293 cells. Confocal live imaging of GFP fluorescence (Green). Membrane localized F-actin was visualized using fluorescence labeled phalloidin (Red). Nuclei were stained by DAPI (Blue). Mock = cells transfected with empty plasmid. Bar = $10 \mu m$.

Fig. 3: Expression of TMC proteins in FRT cells. Intracellular localization of GFP tagged TMC proteins overexpressed in FRT cells. Confocal live imaging of GFP fluorescence (Green). Membrane localized F-actin was visualized using fluorescence - labeled phalloidin (Red). Nuclei were stained by DAPI (Blue). Mock cells were transfected with empty plasmid. Bar = $20 \mu m$.

TMC8 inhibits Ca^{2+} activated and volume regulated chloride channels and attenuates intracellular Ca^{2+} signals:

Stimulation of HEK293 cells by the Ca^{2+} ionophore ionomycin (1 μ M) activated whole cell Cl^- currents. The current was outwardly rectifying in the absence of permeable cations (CsCl in bath and pipette), but was rather linear in the presence of a “cytosolic-like” pipette solution containing 130 mM K^+ , and with NaCl in the bath (29) (Fig. 5 left). To maintain proper Ca^{2+} signaling (outlined below), we performed further experiments in the presence of physiological ion concentrations. Activation of Ano1 by ionomycin was unaffected by coexpression of TMC8 (Fig. 5 right). We further asked whether coexpression of TMC8 does affect activation of Ano1 through stimulation of G-protein coupled receptors (GPCRs). Remarkably, stimulation of Ano1 by the purinergic agonist ATP (100 μ M) was completely inhibited by coexpression of TMC8 (Fig. 4C,D). GPCR mediated activation of Ano1 requires release of Ca^{2+} from ER-stores and influx through store operated Ca^{2+} channels (SOCE). We hypothesized that TMC8 may affect intracellular Ca^{2+} transients and therefore examined ATP-induced Ca^{2+} signals in the absence or presence of coexpressed TMC8. We found that the ATP-induced Ca^{2+} signal relaxed significantly faster in the presence TMC8 (Fig. 4E).

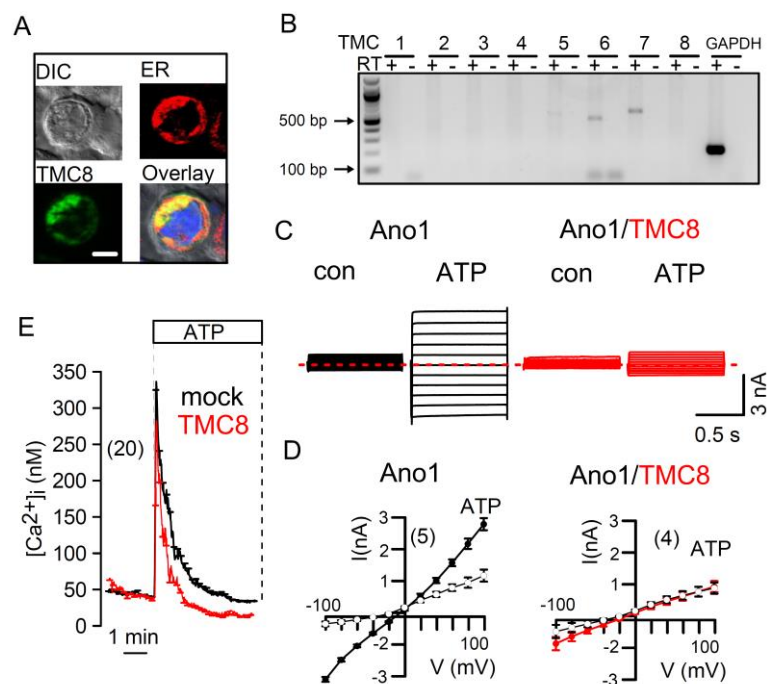


Fig. 4: Inhibition of Ano1-activation and intracellular Ca^{2+} signaling by TMC8 in HEK293 cells: A) Live

imaging of TMC8-GFP (GFP, green) and ER (ER tracker, red). Bar = 10 μ m. B) Expression (RT-PCR) of endogenous TMC paralogues. C) Whole cell current overlays before and after stimulation with 100 μ M ATP in Ano1 and Ano1/TMC8 expressing cells. D) Corresponding current/voltage (I/V) relationships. E) ATP-induced Ca^{2+} increase (Mean \pm SEM) in Ano1 and Ano1/TMC8 expressing cells. Mean \pm SEM (number of experiments).

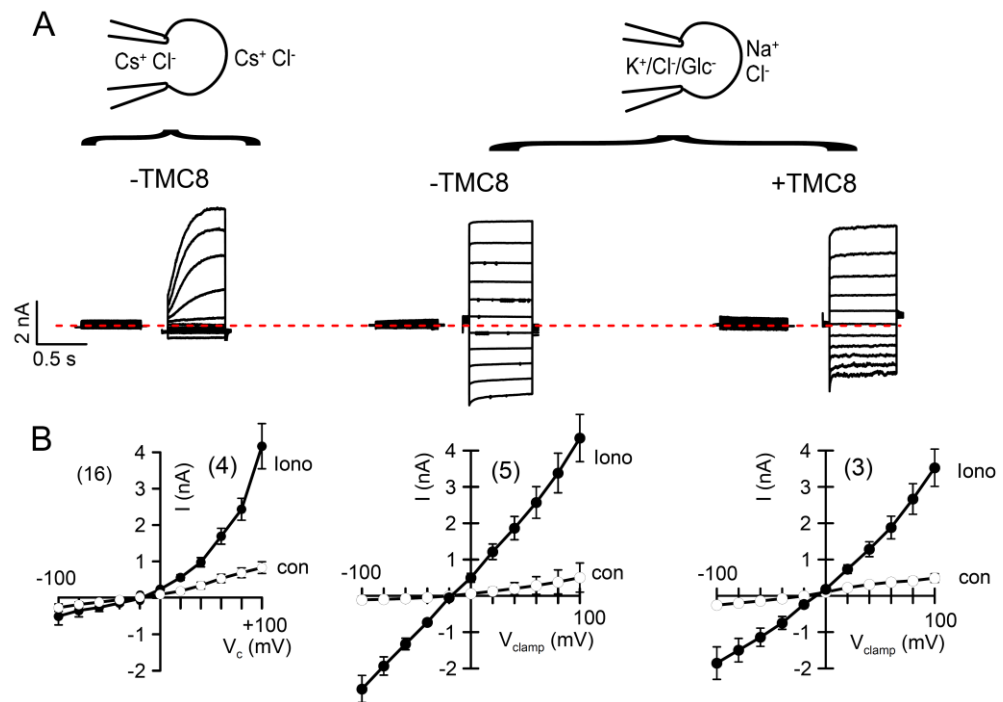


Fig. 5: The Ca^{2+} ionophore ionomycin activates Ano1 independent of coexpression of TMC8. A) Original overlay currents ($V_c = \pm 100$ mV in steps of 20 mV) indicating activation of anoctamin 1 (Ano1) expressed in HEK293 cells by stimulation with ionomycin (1 μ M). Currents were outwardly rectifying in the absence of permeable cations (CsCl in patch pipette and bath), but were linear in the presence of K^+ and Na^+ . Coexpression of TMC8 did not interfere with activation of Ano1. B) Corresponding current/voltage relationships. Mean \pm SEM (number of experiments).

Ca^{2+} dependence has also been demonstrated earlier for volume activated Cl^- currents (98). Similar to other mammalian cells, also HEK293 cells express volume regulated anion channels (VRAC), and the recently identified VRAC channel component LRRC8A (12-14) (unpublished data). VRAC was activated in HEK293 cells by exposure to a hypotonic bath solution (Hypo) (Fig. 6A,B). However, activation of VRAC was largely compromised in cells coexpressing TMC8. Abrogation of VRAC by coexpression of TMC8 also inhibited volume regulation in HEK293 cells: Recovery from Hypo-induced cell swelling (regulatory volume decrease; RVD) in HEK293 cells was abolished by coexpression of TMC8 (Fig. 6C,D).

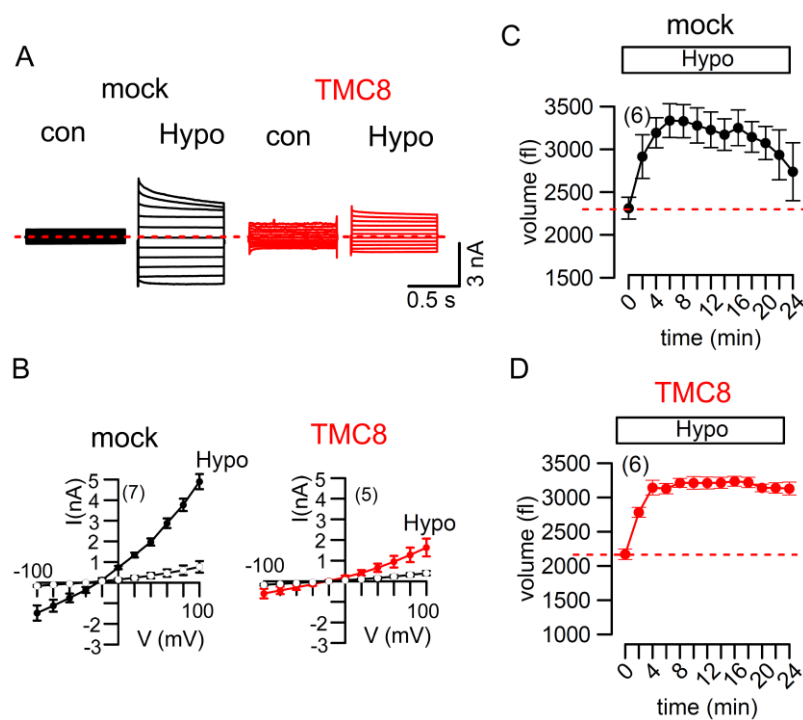


Fig. 6: Suppression of volume regulation by TMC8 in HEK293 cells: A) Whole cell current overlays before and after exposure of mock transfected or TMC8 expressing cells to hypotonic solution (Hypo, 150 mosmol/l). B) Corresponding I/V relationships. C,D) Cell volume assessed in mock transfected or TMC8 expressing cells using flow cytometry. Mean \pm SEM (number of experiments or assays).

TMC8 inhibits endogenous Ano1 and VRAC in Cal33 cells:

We examined whether endogenous Ano1 currents and are equally inhibited by expression of TMC8. Cal33 cells strongly express endogenous Ano1 and large Ca^{2+} activated Cl^- currents found in these cells are entirely due to Ano1 expression (194). Although Cal33 cells express some of the other TMC proteins, they do not express endogenous TMC8 (Fig. 7A). They may therefore be an ideal system to further look into the role of TMC8 for Cl^- transport and Ca^{2+} signaling. Comparable to the results obtained in HEK293 cells, also activation of endogenous Ano1 currents by ATP was largely inhibited by expression of TMC8 (Fig. 7B,C). This was also demonstrated using a sensitive independent cell contact-free technique. Cal33 cells were transfected with I^- sensitive yellow fluorescent protein (YFP). Application of I^- induced strong fluorescence quenching, which was further augmented by activation of Ano1 with ATP (Fig. 7C). Both basal and ATP-induced quenching was dramatically reduced in cells expressing TMC8 (Fig. 7C,D). This confirms data from overexpressing HEK293 cells and indicates that

baseline currents and acutely activated currents are controlled by TMC8. Moreover, also Hypo-induced Cl^{-} currents were inhibited by expression of TMC8 (Fig. 7E).

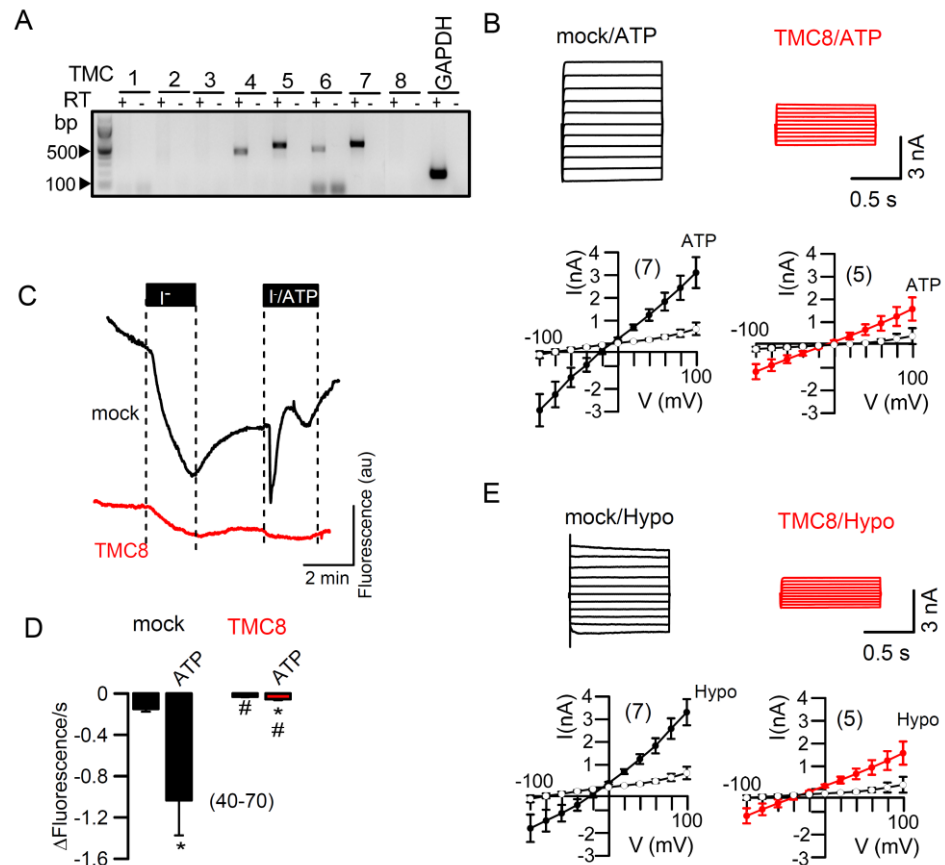


Fig. 7: TMC8 inhibits endogenous Ano1 and VRAC in Cal33 cells: A) Expression (RT-PCR) of endogenous TMC paralogs. B) Whole cell current overlays after stimulation with 100 μ M ATP of mock transfected and TMC8 expressing cells with corresponding I/V curves. C) YFP-fluorescence quenching by 20 mM I^{-} and increase of initial rate of quenching by stimulation with ATP of mock-transfected and TMC8-expressing cells. E) Whole cell current overlays after exposure to Hypo of mock transfected and TMC8 expressing cells with corresponding I/V curves. Mean \pm SEM (number of cells). *significant effects of ATP; $p < 0.05$; paired t-test. #significant difference when compared to mock; $p < 0.05$; unpaired t-test.

TMC8 controls ATP-induced release of Zn^{2+} and Ca^{2+} from ER:

Expression of TMC8 strongly attenuated ATP-induced Ca^{2+} release from ER (Fig. 8A). We examined whether this effect is due to reduced store Ca^{2+} by exposing the cell to the sarcoplasmic endoplasmic reticulum ATPase (SERCA)-inhibitor cyclopiazonic acid (CPA; 10 μ M) in Ca^{2+} free solution. However, emptying of the ER Ca^{2+} store by CPA caused equal Ca^{2+} increase in mock transfected and TMC8 overexpressing cells (Fig. 8B,C). Moreover, re-addition of extracellular Ca^{2+} in the presence of CPA induced a similar Ca^{2+} increase in

TMC8-expressing and control cells, suggesting unaffected SOCE (Phase 3 in Fig. 8B,C).

It was reported earlier that Ca²⁺ influences Zn²⁺ homeostasis and vice versa, and that Zn²⁺ dynamics modulate Ca²⁺ signaling (200). Using the Zn²⁺ sensitive dye zinquin, we found that stimulation with ATP increases intracellular Zn²⁺ levels (Fig. 8D). Preincubation of the cells with the Zn²⁺ chelator N, N, N', N'-tetrakis (2-pyridylmethyl) ethylenediamine (TPEN, 25 μM, 20 min) abolished ATP-induced Zn²⁺ increase. Remarkably, chelation of Zn²⁺ by TPEN also strongly suppressed ATP-induced Ca²⁺ increase (Fig. 8E,G), while basal Ca²⁺ levels were increased (Fig. 8E,F). As a result, activation of Ano1 by ATP was strongly reduced (Fig. 9). This result suggest that ATP-induced store release of Ca²⁺ is augmented by co-release of Zn²⁺. TMC8 limits Ca²⁺ signals by activating Zn²⁺ re-uptake into the ER through the Zn²⁺ transporter ZnT-1 (68;200).

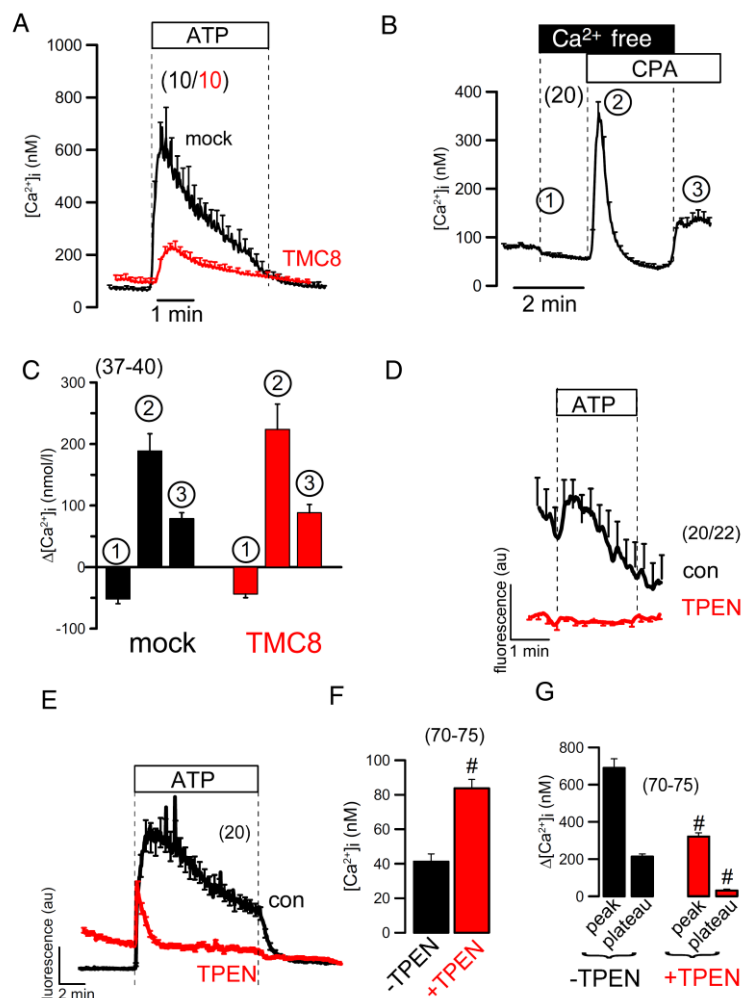


Fig. 8: TMC8 controls ATP-induced release of Zn²⁺ and Ca²⁺ from ER in Cal33 cells: A) ATP-induced Ca²⁺

increase (Mean \pm SEM) in mock transfected and TMC8 expressing cells B) CPA (10 μ M) induced emptying of ER-Ca²⁺ stores and Ca²⁺ influx after re-increase of Ca²⁺ to the extracellular solution in the continuous presence of CPA. C) Identical effects of Ca²⁺ free bath solution (1), CPA (2) and re-increase of Ca²⁺ in the presence of CPA (3) in mock transfected or TMC8-expressing cells. D) Increase of intracellular Zn²⁺ concentrations (zincin fluorescence) by ATP (Mean \pm SEM) and effect of preincubation by Zn²⁺ chelator TPEN. E) ATP-induced Ca²⁺ increase (Mean \pm SEM) in the absence or presence of TPEN. F) Basal Ca²⁺ concentrations in the absence (con) or presence of TPEN. G) Peak and plateau Ca²⁺ increase upon ATP stimulation in the absence or presence of TPEN. Mean \pm SEM (number of cells). #significant difference when compared to con; p < 0.05; unpaired t-test.

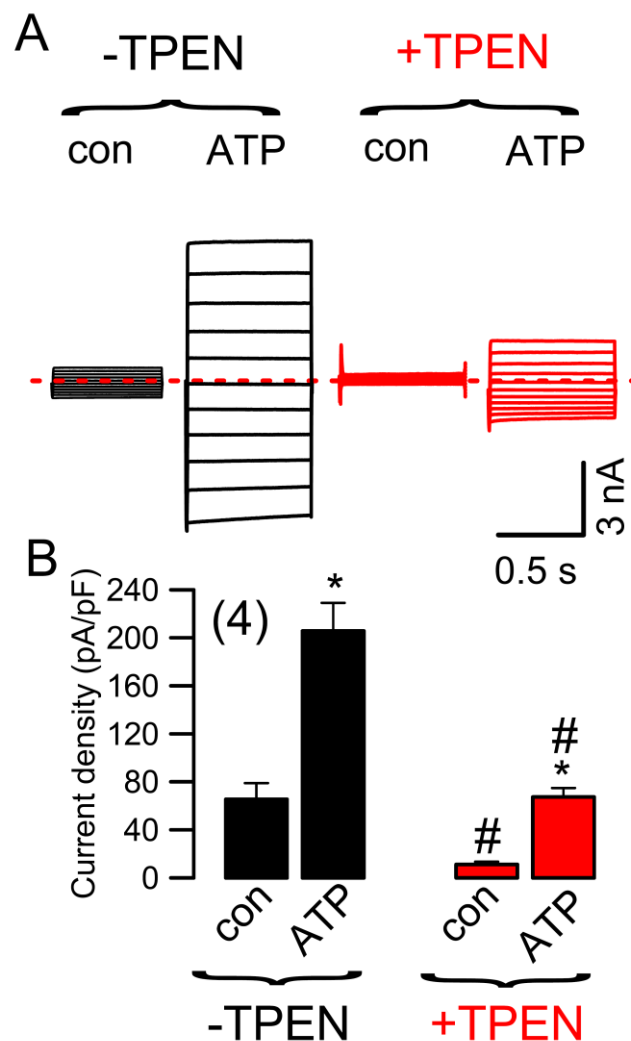


Fig. 9: Inhibition of basal and ATP-activated Ano1 currents by TPEN in Cal33 cells: A) Whole cell current overlays before and after ATP-stimulation in the absence or presence of TPEN. B) Effect of ATP and TPEN on current densities. Mean \pm SEM (number of cells). * significant effects of ATP; p < 0.05; paired t-test. # significant difference when compared to -TPEN; p < 0.05; unpaired t-test.

Discussion

Despite remarkable structural similarity particularly in the putative pore region of the Ca²⁺ activated Cl⁻ channel Ano1, we could not find evidence that TMC proteins may act as or

support Ca^{2+} activated Cl^{-} currents (65). On the contrary, the data indicate that TMC8 is controlling receptor-mediated Ca^{2+} release from ER stores, and is thus counteracting activation of Ano1. Not surprisingly, TMC8 also inhibits swelling activated Cl^{-} currents in HEK293 and Cal33 cells, emphasizing on the relevance of Ca^{2+} for activation of VRAC in these cells and other cell types (1;10;12;93;98;99;201). Also volume regulation was strongly attenuated in TMC8 expressing cells (Fig: 2D). It will be interesting to determine in future studies, whether the activity of the recently identified VRAC subunit LRRC8 is controlled by intracellular Ca^{2+} (13;14). Because we present evidence that TMC8 controls intracellular Zn^{2+} levels which in turn regulates Ca^{2+} signals, it is noteworthy that hypoosmotic swelling has been shown to increase intracellular Zn^{2+} levels in rat astrocytes (202).

Earlier reports showed that TMC8 interacts physically with the Zn^{2+} transporter ZnT-1, which is located in ER and plasma membrane. Loss of TMC8 activity due to mutations leads to reduced transport activity of ZnT-1 and disturbances in the cellular Zn^{2+} distribution with enhanced Zn^{2+} levels in the nucleus (68;200). Abrogated cellular Zn^{2+} homeostasis is believed to cause persistent HPV infections with the risk of developing skin cancer. The present report and earlier studies demonstrate an intimate connection between Zn^{2+} homeostasis and Ca^{2+} signaling, with both messengers being released from IP3-sensitive stores (200;203) (Fig. 10). We therefore speculate that disturbed intracellular Ca^{2+} signaling might be equally important for the observed increase in proliferation and development of cancer. The enhanced activity of Ano1 due to disturbed Zn^{2+}/Ca^{2+} homeostasis could be a major factor that promotes proliferation and cancer development as shown recently in several studies (190-194;204). We and others found that Ano1 and possibly Ano6 activity is directly related to oncogenic signaling (190;204;205).

The role of HPV in cancer is increasingly recognized. HPV is not only causally related to anogenital cancer (206) and epidermodysplasia verruciformis (62;185;186), is also involved in a large fraction of HNSCC (195-197). Because VRAC was found to be enhanced in papilloma virus infected cells (207), it should be worthwhile looking more closely into the role of LRRC8 and Ano1 in papilloma virus infected cells.

Acknowledgments

Supported by DFG SFB699A7. The technical assistance by Ms. Ana M. Romao, Tian, Dr. Diana Faria, Ms. Ernestine Tartler and Ms. Patricia Seeberger is gratefully acknowledged.

CHAPTER 6

DISCUSSION

LRRC8A is not the only VRAC

The molecular identity of VRAC was unclear for more than 25 years, until in 2014 when two independent groups identified LRRC8A or SWELL1 as the major and essential component of this channel (13;14). However, a study in RPE cells, where LRRC8A is barely present but Best1 is abundantly expressed, shows that these cells could generate a remarkably swelling-activated whole cell current and performed RVD in the absence of LRRC8A. On the other hand, Scott lymphocytes which lack of ANO6 expression showed a reduction of swelling-activated whole cell currents and demonstrated a defective RVD as well. Moreover, the data obtained from *Xenopus laevis* oocytes show that ANO10 clearly augments swelling-activated whole cell currents and that the hypotonic-induced *Xenopus laevis* oocytes bursting is largely reduced. Taken together, these data suggest that besides LRRC8A, Best1 and anoctamins play a role for volume-regulated anion channels and may be components of VRAC required for the full activation. LRRC8A has been shown to require other proteins to form a complete functional VRAC (14). Because the LRR motif of LRRC8 proteins was reported to play a role in protein-protein interactions (19), we studied the role of the LRR motif by co-expressing a LRRC8A mutant lacking LRR with ANO10 and found that swelling-activated whole cell currents were largely reduced in both *Xenopus laevis* oocyte and HEK293 cells. This result suggests the functional relationship between LRRC8A and ANO10 through the LRR motif, but how this relationship contributes to volume regulation needs to be further investigated. Even though we could show the contribution of Best1 on volume regulation in human RPE cells and mouse sperms, heterologous expression or siRNA knockdown of Best1 in HEK293 cells did not affect swelling-activated whole cell currents (13;138). One of the reasons could be the lacking of membrane specific chaperone in this cell type, since a large proportion of this protein is localized intracellularly (58;180). Hence, the role of Best1 as VRAC is perhaps cell- or tissue specific.

In this thesis, we show that the properties of swelling-activated whole cell currents

generated by ANO6 and ANO10 resemble that of the classical VRAC. For example the inhibitor of VRAC, NS3728, could largely inhibit swelling-activated whole cells currents generated by ANO6 and ANO10 as well (82). The currents obtained from ANO6 and ANO10 show outwardly rectification, a typical characteristic of VRAC. The only, however, remarkable difference to the typical VRAC currents we observed in our studies was the lack of the VRAC-typical time-dependent inactivation. Swelling activation of ANO6 and ANO10 demonstrated hardly any time-dependent inactivation. In one of our studies we suggested a relationship between Ca^{2+} accessibility of ANO6 and time-dependent inactivation. We observed more pronounced time-dependent inactivation when Ca^{2+} access was limited (data is shown in Chapter 2)

Activation of VRAC and Anoctamins

Since the role of Ca^{2+} on volume regulation is still controversial we conducted the experiment in the absence of Ca^{2+} and found that swelling-activated whole currents were completely abolished. It is well recognized that the TRP channels are activated during cell swelling (1;10;97). Our study in ANO6 overexpressing HEK293 cells found that the inhibition of Ca^{2+} entry through TRP channels largely affected swelling-activated whole cell currents and RVD. In addition, cell swelling can activate Ca^{2+} -induced Ca^{2+} release from ryanodine and IP3-sensitive Ca^{2+} stores. These results clearly point out a role of Ca^{2+} for VRAC activation. Ca^{2+} measurement using the Ca^{2+} sensors GCaMP2 and Fura-2 display that overexpression of ANO10 augmented hypo-induced transient increase in intracellular Ca^{2+} without disturbing the Ca^{2+} content in the ER store. In parallel we found that ANO10 mainly colocalizes with the ER marker, thus suggesting that ANO10 may also regulate Ca^{2+} signaling that is required for swelling- activated whole cell currents.

Another evidence that explains the importance of Ca^{2+} for VRAC activation is a study in TMC8 overexpressing cells. Our study presents the role of TMC8 in regulating receptor-mediated Ca^{2+} release from the ER. In fact co-release of Zn^{2+} together with Ca^{2+} is required in order to generate large Ca^{2+} release peaks. TMC8 is known to interact with ZnT-1 at ER membranes and mediates Zn^{2+} re-uptake via ZnT-1 transporter (68;200). Hence a reduction of

Ca^{2+} signaling is observed when TMC8 is overexpressed in HEK293 and Cal33 cells, consequently swelling-activated whole cell currents and RVD are reduced in these overexpressing cells (Fig. 1).

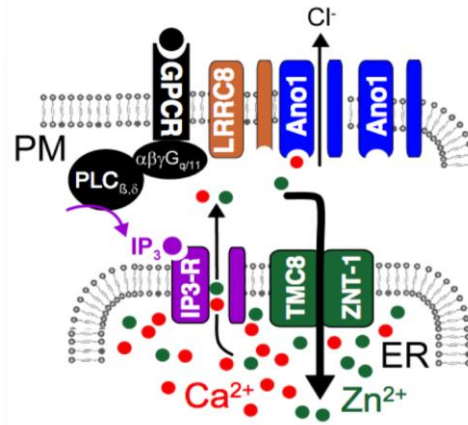


Fig 1. TMC8 controls compartmentalized Ca^{2+} signaling: hypothetical model proposing release of Zn^{2+} and Ca^{2+} from the ER upon stimulation of G-protein coupled receptors (GPCR). Co-released Zn^{2+} further augments Ca^{2+} release and activation of Ano1 and possibly swelling activated LRRRC8-related channels.

Our results suggest a functional role of PLA_2 upon cell swelling. Inhibition of PLA_2 results in largely reduced hypo-induced Ca^{2+} signaling, swelling-activated whole cell currents, and RVD. In fact, it is known that PLA_2 is a mechanosensor that is involved in VRAC and RVD activation (1;100). Our study revealed for the first time that ANO6 could be activated by PLA_2 . One may speculate that activation of ANO6 by PLA_2 is due to the activation of Ca^{2+} influx through TRP channels since some of PLA_2 inhibitors may also inhibit TRP channels (87;208). However, mellitin, a potent PLA_2 activator, shows no interference with Ca^{2+} signaling but induced robust whole cell currents could activate ANO6 in overexpressing HEK293 cells and wt lymphocytes, in contrast to non-transfected HEK293 cells and Scott lymphocytes lacking expression of ANO6. Swelling activation of currents was completely inhibited by PLA_2 inhibitors (1). In addition, ANOs inhibitors such as $\text{CaCC}_{\text{inh}}\text{-AO1}$ and niflumic acid can inhibit swelling activated currents. It is well known that activation of PLA_2 releases fatty acid such as arachidonic acid (ArA) from the phospholipids of the plasma membrane resulting in the accumulation of lysophospholipids (LPL) on the plasma membrane and causing membrane tension (95). Since some ion channels are known to be gated by membrane tension and are therefore called mechanosensitive channels (209), we speculate

that membrane tension may also lead to the opening of ANO6. Inhibitors of metabolic downstream pathway of PLA₂ showed no effect on ANO6 activation, excluding an essential contribution of the arachidonic (ArA) pathway to channel activation. However re-added ArA, resulted in immediate inhibition of ANO6, while, direct application of LPL generated anion currents. These results speak in favor of ANO6 being activated by PLA₂ through accumulation of plasma membrane LPL and induction of membrane tension (Fig. 2).

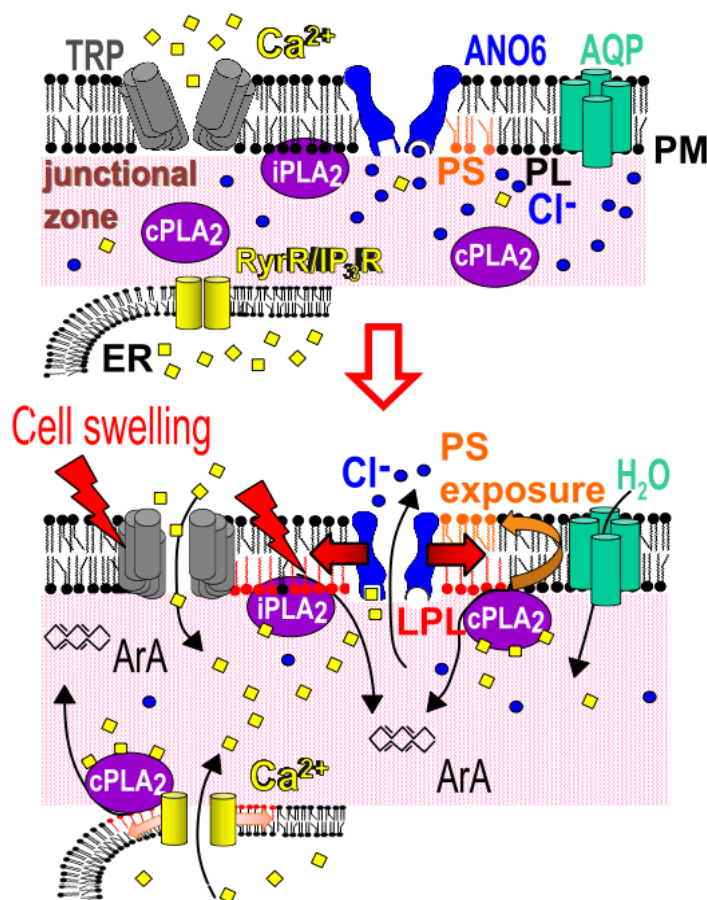


Fig. 2 Activation of ANO6 by hypotonic cell swelling. Possible mechanisms for hypotonic activation of ANO6. During cell swelling, water enters the cell through AQP water channels and reduces osmolarity and Cl⁻ concentration within the junctional zone, thereby releasing ANO6 from Cl⁻ inhibition. Cell swelling activates mechanosensitive TRP channels such as TRPC1 through Ca²⁺ insensitive, stretch-activated iPLA₂, which releases fatty acids, like arachidonic acid (ArA), from plasma membrane phospholipids (PL). Accumulation of lysophospholipids (LPL) causes membrane tension and, together with local increase of Ca²⁺ in the junctional zone, activates ANO6. Increase in intracellular Ca²⁺ further recruits Ca²⁺-dependent cytosolic cPLA₂ to ER membranes and induces a transient ER store release of Ca²⁺. Exposure of phosphatidylserine (PS) by the phospholipid scrambling property of ANO6 may lead to a conformational change allowing Cl⁻ transport by ANO6 or may lead to exocytosis of submembraneous channel pools

As mentioned earlier, changes in the intracellular concentration of certain ions could trigger VRAC activation, so we tested whether ANO6 can be triggered by this phenomenon (8;9). We mimicked the condition where intracellular Cl^- concentration is diluted during cell swelling. With low (5mM) Cl^- in the patch pipette and isotonic bath condition, large whole cell currents in ANO6 overexpressing HEK293 cells were observed. These currents were not affected by TRP channels inhibitor but were largely reduced when the extracellular Cl^- concentration was reduced. On the other hand, with high concentration of Cl^- (125mM) in the patch pipette, whole cell currents are found to be smaller under both isotonic and hypotonic bath condition. These result display the regulation of ANO6 by intracellular Cl^- concentration without the involvement of Ca^{2+} and cell swelling. Therefore, we proposed that ANO6 might operate as an osmosensor during cell swelling by sensing the changing of intracellular Cl^- concentration.

Involvement of VRAC in physiology and Pathophysiology

VRAC has been reported to be an important player in many physiological and pathophysiological processes. For example, a study in a hypertensive mouse model showed that the VRAC activity is enhanced in cerebrovascular smooth muscle cells during the development of hypertension (210). Cell proliferation was also reported as a VRAC dependent process, since VRAC-inhibitors could inhibit cell proliferation in various cell types. In contrast upregulation of VRAC was found to promote cell proliferation in rat aortic smooth muscle cells (83;211;212). Moreover, cell migration is another process that requires activation of ion channels and volume regulation. Cell migration occurs when the front part (leading edge) of cells is swelling while the rear part of the cell is retracting (125); hence this process depends largely on volume regulation.

The present study revealed that lack of ANO10 causes a defect in cell migration in THP-1 macrophages as cellular volume regulation is compromised. ANO10-R263H, a missense variant of ANO10 is found to be related with high borreliosis susceptibility. Overexpression of this mutant leads to a reduction of swelling-activated whole cell currents

and also RVD. Since lack of ANO10 leads to impairment of cell volume regulation and cell migration, we investigated the phagocytic activity of macrophages. We found that phagocytosis of the red-fluorescent cherry labeled *B.garinii* by THP-1 macrophages was largely reduced in ANO10 knock-down cells. Macrophages are known to be responsible for phagocytosis of pathogens, thus initiating the cascades of immune response (213) therefore representing the first line of defense against *borrelia* infection (128). Our study proposed that ANO10 is necessary for volume regulation, which is required for macrophages migration and their role in immunity response. Patients who carry the missense variant ANO10-R263H have a high susceptibility to *borrelia* infection maybe because the elimination of spirochetes is compromised in these patients. ANO6 is not shown to be related with borreliosis, but deletion of ANO6 also results in deterioration of macrophages functions. Cell migration, ATP-induced cell shrinkage and phagocytic activity were significantly reduced in ANO6 knock down cells (76).

VRAC is important for RVD, the process occur when the cells is swollen under hypotonic condition. Another process, which requires the activation of VRAC under normotonic condition is AVD, the apoptotic volume decrease (214). AVD is a prerequisite for the cells that will undergo to apoptotic cell death. Various studies in several cell types revealed that VRAC is the anion channels that play a role in AVD (1;215;216). Previous studies from our group revealed that apoptosis-inducing compound such as staurosporine, was not able to activate whole cell currents in siANO6 treated jurkat cells. Moreover staurosporine activated whole cell currents in control jurkat cells were completely inhibited by ANOs inhibitors (34). These results taken together with our observations confirm the thesis that ANO6 is another essential component of VRAC.

Even though the role of LRRC8A was described as molecular subunit essential for VRAC, by two independent groups (13;14), our data obtained from a highly differentiated human RPE cells and mouse sperms question this conclusion. In fact ion currents studied in human RPE, where Best1 is highly expressed but LRRC8A is almost absent, show normal swelling-activated whole cell currents. In contrast human RPE cells isolated from macular

dystrophy patients carrying heterozygous mutation of Best1, show a clear defect in swelling-activated whole cell currents. Moreover knocking down of LRRC8A in human RPE cells did not have any effects on swelling-activated whole cell currents. Therefore we proposed that in RPE cells, Best1 is an essential component of VRAC. In contrast to human RPE cells, ion currents studies in RPE cells isolated from Best1 knockout mice do not show any difference from those isolated from wild type mice. In addition, retinal pathology was not observed in Best1 knockout mice because there is no Best1 expression in murine RPE cells (57). However Best1 is abundantly expressed in mouse sperms. Severe defects in fertility that is not involved with mating behavior, was observed in Best1 knockout mice. Sperms from Best1 knockout mice display a curly tail phenotype; this phenotype is known to be involved with the defect of sperm volume regulation mechanism (171). Sperm motility measured under hypotonic condition, shows a severe decrease in Best1 knockout mice. However this result is not surprising since VRAC is known to play a role in cell movement (1). Our studies suggest that Best1 plays a major role in volume regulation, and is required for mouse sperm functionality (171-173). However the role of Best1 in the human reproductive system has not been investigated, since the expression of Best1 is very low.

In the present thesis, we also show that TMC8 plays a role in the regulation of intracellular Zn^{2+} and Ca^{2+} signaling. TMC8 unlike TMC1 and TMC2 does not have any role in mechano-electrical signal transduction in the inner ear hair cells (62;63). However TMC8 is well documented as an interacting protein of ZnT-1, zinc transporter, on the ER. TMC8/ZnT-1 complex is known to mediate influx of Zn^{2+} into the ER (69). Zn^{2+} is a trace element important for proteins function and signal transduction and it is also known as a crucial transcription factor for viruses (217). Under physiological condition intracellular Zn^{2+} level is kept very low but in 2007, Yamasaki *et al.* discovered that upon activation of membrane receptor free Zn^{2+} are released from its pool, which is the ER. The release is followed by a Zn^{2+} wave, a process where Zn^{2+} is diffuses throughout the cell (218). Mutation of TMC8 leads to an impaired activity of ZnT-1 transporter and to a consequently rise in the intracellular Zn^{2+} level (Fig. 3). Human papillomavirus (HPV) was reported to have certain

genes and proteins that contain Zn^{2+} binding sites (219;220).

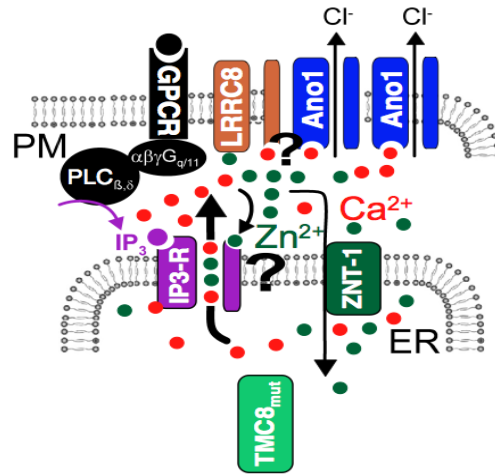


Fig 3. The functional TMC8/ZNT-1 transporter complex maintains low cytosolic Zn^{2+} levels, but is not working properly when TMC8 is mutated. This leads to enhanced cytosolic Zn^{2+}/Ca^{2+} concentrations, with the result of augmented Ano1 and VRAC activity, and increase in proliferation and viral replication.

Therefore the rise of Zn^{2+} distribution and Zn^{2+} level inside the cells due to a mutation of TMC8 could lead to the activation of HPV gene expression and also signal transduction. Abolition of Zn^{2+} homeostasis due to a mutation of TMC8 is reported to cause endless HPV infection with the risk of developing skin cancer (69). The present thesis demonstrates the relationship between Zn^{2+} homeostasis and Ca^{2+} signaling. Since the upregulation of ANO1 and VRAC activity is known to be involved in cell proliferation and cancer development (190;204), further investigations of Ca^{2+}/Zn^{2+} homeostasis and the role of anoctamin channels in HPV infection and skin cancer will be interesting.

Concluding Remarks

We have herein provided evidences that anoctamins and bestrophin1 play major roles in volume regulation. Lack of these proteins largely affects both swelling-activated whole cell currents and regulatory volume decrease (RVD). Anoctamins have biophysical and pharmacological properties which are similar to that of VRAC. For example the activation of ANO6 by hypotonic solution give us an outward rectifying currents and a specific VRAC inhibitor, NS3728 (72), is shown to inhibit swelling-activated currents generated by anoctamins. However most of anoctamins members are located in cytosolic compartment including ANO10. Therefore to elucidate whether these anoctamins play a role in volume regulation or not, and if so, how do they control the activity of VRAC and RVD would be interesting.

The role of Best1 as VRAC has been under controversy for years since overexpression of this protein often led to its retention intracellularly (58). Moreover, peritoneal macrophages isolated from Best1-knockout mice do not show any defect in VRAC activation (151). However, our studies in highly differentiated tissues, such as human RPE cells and mouse sperms point out that Best1 is an essential component of VRAC and its function is rather tissue specific. Due to the fact that the expression level of each member of bestrophin family is different among tissues therefore the role of other members in volume regulation would be interesting for further investigate.

It is well known that alteration of Zn^{2+} homeostasis that caused by mutation of TMC8 lead to high susceptibility for HPV infection (69). Since the present work provides a significance role of TMC8 in controlling Zn^{2+} homeostasis and Ca^{2+} signaling which further regulates ANO1 and VRAC activity, hence further study of the role of these channels and Ca^{2+} on HPV infection and cancer related to HPV will be interesting.

REFERENCES

1. Hoffmann, E. K., Lambert, I. H., Pedersen, S. F. (2009) Physiology of cell volume regulation in vertebrates. *Physiol Rev.* 89, 193-277
2. Nilius, B., Prenen, J., Voets, T., Eggermont, J., Bruzik, K. S., Shears, S. B., Droogmans, G. (1998) Inhibition by inositoltriphosphates of calcium- and volume-activated Cl⁻ currents in macrovascular endothelial cells. *Pflugers Arch.* 435, 637-644
3. Lang, F., Busch, G. L., Ritter, M., Volkl, H., Waldegger, S., Gulbins, E., Haussinger, D. (1998) Functional significance of cell volume regulatory mechanisms. *Physiol Rev* 78, 247-306
4. Stauber, T. (2015) The volume-regulated anion channel is formed by LRRC8 heteromers - molecular identification and roles in membrane transport and physiology. *Biol Chem.* j/bchm-2015
5. Sardini, A., Amey, J. S., Weylandt, K. H., Nobles, M., Valverde, M. A., Higgins, C. F. (2003) Cell volume regulation and swelling-activated chloride channels. *Biochim.Biophys Acta.* 1618, 153-162
6. Ellis, R. J. (2001) Macromolecular crowding: obvious but underappreciated. *Trends Biochem Sci.* 26, 597-604
7. Pedersen, S. F., Hoffmann, E. K., Mills, J. W. (2001) The cytoskeleton and cell volume regulation. *Comp Biochem Physiol A Mol Integr.Physiol.* 130, 385-399
8. Voets, T., Droogmans, G., Raskin, G., Eggermont, J., Nilius, B. (1999) Reduced intracellular ionic strength as the initial trigger for activation of endothelial volume-regulated anion channels. *Proc.Natl.Acad.Sci U.S.A.* 96, 5298-5303
9. Sabirov, R. Z., Prenen, J., Tomita, T., Droogmans, G., Nilius, B. (2000) Reduction of ionic strength activates single volume-regulated anion channels (VRAC) in endothelial cells. *Pflugers Arch.* 439, 315-320
10. McCarty, N. A., O'Neil, R. G. (1992) Calcium signalling in volume regulation. *Physiol.Rev.* 72, 1037-1061
11. Wehner, F. (2006) Cell volume-regulated cation channels. *Contrib.Nephrol.* 152, 25-53
12. Almaca, J., Tian, Y., AlDehni, F., Ousingawat, J., Kongsuphol, P., Rock, J. R., Harfe, B. D., Schreiber, R., Kunzelmann, K. (2009) TMEM16 proteins produce volume regulated chloride currents that are reduced in mice lacking TMEM16A. *J Biol Chem* 284, 28571-28578

13. Qiu, Z., Dubin, A. E., Mathur, J., Tu, B., Reddy, K., Miraglia, L. J., Reinhardt, J., Orth, A. P., Patapoutian, A. (2014) SWELL1, a Plasma Membrane Protein, Is an Essential Component of Volume-Regulated Anion Channel. *Cell*. 157, 447-458
14. Voss, F. K., Ullrich, F., Munch, J., Lazarow, K., Lutter, D., Mah, N., Andrade-Navarro, M. A., von Kries, J. P., Stauber, T., Jentsch, T. J. (2014) Identification of LRRC8 Heteromers as an Essential Component of the Volume-Regulated Anion Channel VRAC. *Science*. 344, 634-638
15. Milenkovic, A., Brandl, C., Milenkovic, V. M., Jendrike, T., Sirianant, L., Wanitchakool, P., Zimmermann, S., Reif, C. M., Horling, F., Schrewe, H., Strünker, T., Alvarez, L., Schreiber, R., Kunzelmann, K., Wetzel, C. H., Weber, B. H. F. (2015) Bestrophin1 is the volume-regulated anion channel in mouse sperm and human retinal pigment epithelium. *Proc.Natl.Acad.Sci U.S.A.(in press)* 112,
16. Verdon, B., Winpenny, J. P., Whitfield, K. J., Argent, B. E., Gray, M. A. (1995) Volume-activated chloride currents in pancreatic duct cells. *J.Membr.Biol.* 147, 173-183
17. Christensen, O. (1987) Mediation of cell volume regulation by Ca²⁺ influx through stretch-activated channels. *Nature*. 330, 66-68
18. Abascal, F., Zardoya, R. (2012) LRRC8 proteins share a common ancestor with pannexins, and may form hexameric channels involved in cell-cell communication. *Bioessays*. 34, 551-560
19. Kobe, B., Kajava, A. V. (2001) The leucine-rich repeat as a protein recognition motif. *Curr.Opin.Struct.Biol.* 11, 725-732
20. Yang, Y. D., Cho, H., Koo, J. Y., Tak, M. H., Cho, Y., Shim, W. S., Park, S. P., Lee, J., Lee, B., Kim, B. M., Raouf, R., Shin, Y. K., Oh, U. (2008) TMEM16A confers receptor-activated calcium-dependent chloride conductance. *Nature*. 455, 1210-1215
21. Brunner, J. D., Lim, N. K., Schenck, S., Duerst, A., Dutzler, R. (2014) X-ray structure of a calcium-activated TMEM16 lipid scramblase. *Nature*. 516, 207-212
22. Caputo, A., Caci, E., Ferrera, L., Pedemonte, N., Barsanti, C., Sondo, E., Pfeiffer, U., Ravazzolo, R., Zegarra-Moran, O., Galletta, L. J. (2008) TMEM16A, A Membrane Protein Associated With Calcium-Dependent Chloride Channel Activity. *Science*. 322, 590-594
23. Schroeder, B. C., Cheng, T., Jan, Y. N., Jan, L. Y. (2008) Expression cloning of TMEM16A as a calcium-activated chloride channel subunit. *Cell*. 134, 1019-1029
24. Stephan, A. B., Shum, E. Y., Hirsh, S., Cygnar, K. D., Reisert, J., Zhao, H. (2009)

- ANO2 is the ciliary calcium-activated chloride channel that may mediate olfactory amplification. *Proc.Natl.Acad.Sci.U.S.A.* 106, 11776-11781
25. Hengl, T., Kaneko, H., Dauner, K., Vocke, K., Frings, S., Mohrlen, F. (2010) Molecular components of signal amplification in olfactory sensory cilia. *Proc.Natl.Acad.Sci.U.S.A.* 107, 6052-6057
 26. Rasche, S., Toetter, B., Adler, J., Tschapek, A., Doerner, J. F., Kurtenbach, S., Hatt, H., Meyer, H., Warscheid, B., Neuhaus, E. M. (2010) Tmem16b is Specifically Expressed in the Cilia of Olfactory Sensory Neurons. *Chem.Senses.* 35, 239-245
 27. Schreiber, R., Faria, D., Skryabin, B. V., Rock, J. R., Kunzelmann, K. (2014) Anoctamins support calcium-dependent chloride secretion by facilitating calcium signaling in adult mouse intestine. *Pflügers Arch* 467, 1203-1213
 28. Charlesworth, G., Plagnol, V., Holmstrom, K. M., Bras, J., Sheerin, U. M., Preza, E., Rubio-Agusti, I., Ryten, M., Schneider, S. A., Stamelou, M., Trabzuni, D., Abramov, A. Y., Bhatia, K. P., Wood, N. W. (2012) Mutations in ANO3 cause dominant craniocervical dystonia: ion channel implicated in pathogenesis. *Am.J Hum.Genet.* 91, 1041-1050
 29. Tian, Y., Schreiber, R., Kunzelmann, K. (2012) Anoctamins are a family of Ca²⁺ activated Cl⁻ channels. *J Cell Sci* 125, 4991-4998
 30. Maniero, C., Zhou, J., Shaikh, L. H., Azizan, E. A., McFarlane, I., Neogi, S., Scudieri, P., Galietta, L. J., Brown, M. J. (2015) Role of ANO4 in regulation of aldosterone secretion in the zona glomerulosa of the human adrenal gland. *Lancet.* 385 Suppl 1, -4
 31. Hicks, D., Sarkozy, A., Muelas, N., Koehler, K., Huebner, A., Hudson, G., Chinnery, P. F., Barresi, R., Eagle, M., Polvikoski, T., Bailey, G., Miller, J., Radunovic, A., Hughes, P. J., Roberts, R., Krause, S., Walter, M. C., Laval, S. H., Straub, V., Lochmuller, H., Bushby, K. (2011) A founder mutation in Anoctamin 5 is a major cause of limb-girdle muscular dystrophy. *Brain.* 134, 171-182
 32. Tran, T. T., Tobiume, K., Hirono, C., Fujimoto, S., Mizuta, K., Kubozono, K., Inoue, H., Itakura, M., Sugita, M., Kamata, N. (2014) TMEM16E (GDD1) exhibits protein instability and distinct characteristics in chloride channel/pore forming ability. *J.Cell Physiol.(in press)* 229, 181-190
 33. Kunzelmann, K., Tian, Y., Martins, J. R., Faria, D., Kongsuphol, P., Ousingsawat, J., Thevenod, F., Roussa, E., Rock, J. R., Schreiber, R. (2011) Anoctamins. *Pflugers Arch.* 462, 195-208
 34. Martins, J. R., Faria, D., Kongsuphol, P., Reisch, B., Schreiber, R., Kunzelmann, K. (2011) Anoctamin 6 is an essential component of the outwardly rectifying chloride

- channel. *Proc.Natl.Acad.Sci.U.S.A.* 108, 18168-18172
35. Yang, H., Kim, A., David, T., Palmer, D., Jin, T., Tien, J., Huang, F., Cheng, T., Coughlin, S. R., Jan, Y. N., Jan, L. Y. (2012) TMEM16F Forms a Ca(2+)-Activated Cation Channel Required for Lipid Scrambling in Platelets during Blood Coagulation. *Cell.* 151, 111-122
 36. Grubb, S., Poulsen, K. A., Juul, C. A., Kyed, T., Klausen, T. K., Larsen, E. H., Hoffmann, E. K. (2013) TMEM16F (Anoctamin 6), an anion channel of delayed Ca²⁺ activation. *J Gen.Physiol.* 141, 585-600
 37. Juul, C. A., Grubb, S., Poulsen, K. A., Kyed, T., Hashem, N., Lambert, I. H., Larsen, E. H., Hoffmann, E. K. (2014) Anoctamin 6 differs from VRAC and VSOAC but is involved in apoptosis and supports volume regulation in the presence of Ca. *Pflugers Arch* 466, 1899-1910
 38. Bevers, E. M., Williamson, P. L. (2010) Phospholipid scramblase: an update. *FEBS Lett.* 584, 2724-2730
 39. Suzuki, J., Umeda, M., Sims, P. J., Nagata, S. (2010) Calcium-dependent phospholipid scrambling by TMEM16F. *Nature* 468, 834-838
 40. Kunzelmann, K. (2015) TMEM16, LRRC8A, bestrophin: chloride channels controlled by Ca and cell volume. *Trends Biochem.Sci.* 40, 535-543
 41. Bera, T. K., Das, S., Maeda, H., Beers, R., Wolfgang, C. D., Kumar, V., Hahn, Y., Lee, B., Pastan, I. (2004) NGEF, a gene encoding a membrane protein detected only in prostate cancer and normal prostate. *Proc.Natl.Acad.Sci.U.S.A.* 101, 3059-3064
 42. Das, S., Hahn, Y., Nagata, S., Willingham, M. C., Bera, T. K., Lee, B., Pastan, I. (2007) NGEF, a prostate-specific plasma membrane protein that promotes the association of LNCaP cells. *Cancer Res.* 67, 1594-1601
 43. Duran, C., Qu, Z., Osunkoya, A. O., Cui, Y., Hartzell, H. C. (2011) ANOs 3-7 in the anoctamin/tmem16 Cl⁻ channel family are intracellular proteins. *Am J Physiol Cell Physiol.*
 44. Kunzelmann, K., Schreiber, R., Kmit, A., Jantarajit, W., Martins, J. R., Faria, D., Kongsuphol, P., Ousingsawat, J., Tian, Y. (2012) Expression and function of epithelial anoctamins. *Exp.Physiol.* 97, 184-192
 45. Li, C., Cai, S., Wang, X., Jiang, Z. (2015) Identification and characterization of ANO9 in stage II and III colorectal carcinoma. *Oncotarget.*
 46. Vermeer, S., Hoischen, A., Meijer, R. P., Gilissen, C., Neveling, K., Wieskamp, N., de Brouwer, A., Koenig, M., Anheim, M., Assoum, M., Drouot, N., Todorovic, S., Milic-

- Rasic, V., Lochmuller, H., Stevanin, G., Goizet, C., David, A., Durr, A., Brice, A., Kremer, B., van de Warrenburg, B. P., Schijvenaars, M. M., Heister, A., Kwint, M., Arts, P., van der, W. J., Veltman, J., Kamsteeg, E. J., Scheffer, H., Knoers, N. (2010) Targeted next-generation sequencing of a 12.5 Mb homozygous region reveals ANO10 mutations in patients with autosomal-recessive cerebellar ataxia. *Am J Hum. Genet.* 87, 813-819
47. Balreira, A., Boczonadi, V., Barca, E., Pyle, A., Bansagi, B., Appleton, M., Graham, C., Hargreaves, I. P., Rasic, V. M., Lochmuller, H., Griffin, H., Taylor, R. W., Naini, A., Chinnery, P. F., Hirano, M., Quinzii, C. M., Horvath, R. (2014) ANO10 mutations cause ataxia and coenzyme Q deficiency. *J Neurol.* 261, 2192-2198
48. Yang, T., Liu, Q., Kloss, B., Bruni, R., Kalathur, R. C., Guo, Y., Kloppmann, E., Rost, B., Colecraft, H. M., Hendrickson, W. A. (2014) Structure and selectivity in bestrophin ion channels. *Science.* 346, 355-359
49. Marmorstein, A. D., Marmorstein, L. Y., Rayborn, M., Wang, X., Hollyfield, J. G., Petrukhin, K. (2000) Bestrophin, the product of the Best vitelliform macular dystrophy gene (VMD2), localizes to the basolateral plasma membrane of the retinal pigment epithelium. *Proc.Natl.Acad.Sci.U.S.A* 97, 12758-12763
50. Sun, H., Tsunenari, T., Yau, K. W., Nathans, J. (2001) The vitelliform macular dystrophy protein defines a new family of chloride channels. *Proc.Natl.Acad.Sci.U.S.A.* 2002 Mar; 99, 4008-4013
51. Qu, Z., Wei, R. W., Mann, W., Hartzell, H. C. (2003) Two bestrophins cloned from *Xenopus laevis* Oocytes express Ca-activated Cl currents. *J Biol Chem* 278., 49563-49572
52. Tsunenari, T., Sun, H., Williams, J., Cahill, H., Smallwood, P., Yau, K. W., Nathans, J. (2003) Structure-function analysis of the bestrophin family of anion channels. *J Biol Chem* 278, 41114-41125
53. Qu, Z., Fischmeister, R., Hartzell, H. C. (2004) Mouse bestrophin-2 is a bona fide Cl(-) channel: identification of a residue important in anion binding and conduction. *J Gen Physiol* 123, 327-340
54. Hughes, B. A., Gallemore, R. P., Miller, S. M. (1998) Transport mechanisms in the retinal pigment epithelium. In: *The Retinal Pigment Epithelium-Function and Disease*. Marmor, M.F. and Wolfensberger, T.J. (eds). *Oxford University Press* 1, 103-134
55. Barro Soria, R., Spitzner, M., Schreiber, R., Kunzelmann, K. (2009) Bestrophin 1 enables Ca²⁺ activated Cl⁻ conductance in epithelia. *J Biol Chem* 284, 29405-29412
56. Hartzell, H. C. (2008) Molecular Physiology of Bestrophins: Multifunctional

- Membrane Proteins Linked to Best Disease and Other Retinopathies. *Physiological Reviews* 88, 639-672
57. Marmorstein, L. Y., Wu, J., McLaughlin, P., Yocom, J., Karl, M. O., Neussert, R., Wimmers, S., Stanton, J. B., Gregg, R. G., Strauss, O., Peachey, N. S., Marmorstein, A. D. (2006) The Light Peak of the Electroretinogram Is Dependent on Voltage-gated Calcium Channels and Antagonized by Bestrophin (Best-1). *J Gen.Physiol.* 127, 577-589
 58. Barro Soria, R., AlDehni, F., Almaca, J., Witzgall, R., Schreiber, R., Kunzelmann, K. (2009) ER localized bestrophin1 acts as a counter-ion channel to activate Ca²⁺-dependent ion channels TMEM16A and SK4. *Pflügers Arch* 459, 485-497
 59. Zhang, S. L., Yu, Y., Roos, J., Kozak, J. A., Deerinck, T. J., Ellisman, M. H., Stauderman, K. A., Cahalan, M. D. (2005) STIM1 is a Ca²⁺ sensor that activates CRAC channels and migrates from the Ca²⁺ store to the plasma membrane. *Nature.* 437, 902-905
 60. Roos, J., DiGregorio, P. J., Yeromin, A. V., Ohlsen, K., Lioudyno, M., Zhang, S., Safrina, O., Kozak, J. A., Wagner, S. L., Cahalan, M. D., Velicelebi, G., Stauderman, K. A. (2005) STIM1, an essential and conserved component of store-operated Ca²⁺ channel function. *J Cell Biol.* 169, 435-445
 61. Strauss, O., Muller, C., Reichhart, N., Tamm, E. R., Gomez, N. M. (2014) The role of bestrophin-1 in intracellular Ca²⁺ signaling. *Adv.Exp.Med.Biol.* 801, 113-119
 62. Kawashima, Y., Geleoc, G. S., Kurima, K., Labay, V., Lelli, A., Asai, Y., Makishima, T., Wu, D. K., Della Santina, C. C., Holt, J. R., Griffith, A. J. (2011) Mechanotransduction in mouse inner ear hair cells requires transmembrane channel-like genes. *J Clin.Invest.* 121, 4796-4809
 63. Kurima, K., Ebrahim, S., Pan, B., Sedlacek, M., Sengupta, P., Millis, B. A., Cui, R., Nakanishi, H., Fujikawa, T., Kawashima, Y., Choi, B. Y., Monahan, K., Holt, J. R., Griffith, A. J., Kachar, B. (2015) TMC1 and TMC2 Localize at the Site of Mechanotransduction in Mammalian Inner Ear Hair Cell Stereocilia. *Cell Rep.* 12, 1606-1617
 64. Kurima, K., Peters, L. M., Yang, Y., Riazuddin, S., Ahmed, Z. M., Naz, S., Arnaud, D., Drury, S., Mo, J., Makishima, T., Ghosh, M., Menon, P. S., Deshmukh, D., Oddoux, C., Ostrer, H., Khan, S., Riazuddin, S., Deiningner, P. L., Hampton, L. L., Sullivan, S. L., Battey, J. F., Jr., Keats, B. J., Wilcox, E. R., Friedman, T. B., Griffith, A. J. (2002) Dominant and recessive deafness caused by mutations of a novel gene, TMC1, required for cochlear hair-cell function. *Nat.Genet.* 30, 277-284
 65. Hahn, Y., Kim, D. S., Pastan, I. H., Lee, B. (2009) Anoctamin and transmembrane channel-like proteins are evolutionarily related. *Int.J.Mol.Med.* 24, 51-55

66. Labay, V., Weichert, R. M., Makishima, T., Griffith, A. J. (2010) Topology of transmembrane channel-like gene 1 protein. *Biochemistry*. 49, 8592-8598
67. Pan, B., Geleoc, G. S., Asai, Y., Horwitz, G. C., Kurima, K., Ishikawa, K., Kawashima, Y., Griffith, A. J., Holt, J. R. (2013) TMC1 and TMC2 Are Components of the Mechanotransduction Channel in Hair Cells of the Mammalian Inner Ear. *Neuron*. 79, 504-515
68. Lazarczyk, M., Pons, C., Mendoza, J. A., Cassonnet, P., Jacob, Y., Favre, M. (2008) Regulation of cellular zinc balance as a potential mechanism of EVER-mediated protection against pathogenesis by cutaneous oncogenic human papillomaviruses. *J.Exp.Med.* 205, 35-42
69. Lazarczyk, M., Cassonnet, P., Pons, C., Jacob, Y., Favre, M. (2009) The EVER proteins as a natural barrier against papillomaviruses: a new insight into the pathogenesis of human papillomavirus infections. *Microbiol.Mol.Biol.Rev.* 73, 348-370
70. Okada, Y. (2006) Cell volume-sensitive chloride channels: phenotypic properties and molecular identity. *Contrib.Nephrol.* 152, 9-24
71. Nilius, B., Eggermont, J., Voets, T., Droogmans, G. (1996) Volume-activated Cl⁻ channels. *Gen.Pharmacol.* 27, 1131-1140
72. Pedemonte, N., Galletta, L. J. (2014) Structure and Function of TMEM16 Proteins (Anoctamins). *Physiol Rev.* 94, 419-459
73. Malvezzi, M., Chalat, M., Janjusevic, R., Picollo, A., Terashima, H., Menon, A. K., Accardi, A. (2013) Ca²⁺-dependent phospholipid scrambling by a reconstituted TMEM16 ion channel. *Nat.Comm.* 4, 2367
74. Kmit, A., van Kruchten, R., Ousingsawat, J., Mattheij, N. J., Senden-Gijsbers, B., Heemskerk, J. W., Bevers, E. M., Kunzelmann, K. (2013) Calcium-activated and apoptotic phospholipid scrambling induced by Ano6 can occur independently of Ano6 ion currents. *Cell death and disease* 25, 4:e611
75. Shimizu, T., Iehara, T., Sato, K., Fujii, T., Sakai, H., Okada, Y. (2013) TMEM16F is a component of a Ca²⁺-activated Cl⁻ channel but not a volume-sensitive outwardly rectifying Cl⁻ channel. *Am.J Physiol Cell Physiol.* 304, C748-C759
76. Ousingsawat, J., Wanitchakool, P., Kmit, A., Romao, A. M., Jantarajit, W., Schreiber, S., Kunzelmann, K. (2015) Anoctamin 6 mediates effects essential for innate immunity downstream of P2X7-receptors in macrophages. *Nat.Comm.* 6, 6245
77. Sztejn, K., Schmid, E., Nurbaeva, M. K., Yang, W., Munzer, P., Kunzelmann, K.,

- Lang, F., Shumilina, E. (2012) Expression and Functional Significance of the Ca-Activated Cl(-) Channel ANO6 in Dendritic Cells. *Cell Physiol Biochem.* 30, 1319-1332
78. Strange, K., Emma, F., Jackson, P. S. (1996) Cellular and molecular physiology of volume-sensitive anion channels. *Am J Physiol.* 270, C711-C730
79. Nilius, B., Eggermont, J., Voets, T., Buyse, G., Manolopoulos, V., Droogmans, G. (1997) Properties of volume-regulated anion channels in mammalian cells. *Prog.Biophys Mol.Biol.* 68, 69-119
80. Ehlen, H. W., Chinenkova, M., Moser, M., Munter, H. M., Krause, Y., Gross, S., Brachvogel, B., Wuelling, M., Kornak, U., Vortkamp, A. (2012) Inactivation of Anoctamin-6/Tmem16f, a regulator of phosphatidylserine scrambling in osteoblasts, leads to decreased mineral deposition in skeletal tissues. *J Bone Miner.Res.* 28, 246-259
81. Ousingsawat, J., Martins, J. R., Schreiber, R., Rock, J. R., Harfe, B. D., Kunzelmann, K. (2009) Loss of TMEM16A causes a defect in epithelial Ca²⁺ dependent chloride transport. *J Biol Chem* 284, 28698-28703
82. Helix, N., Strobaek, D., Dahl, B. H., Christophersen, P. (2003) Inhibition of the endogenous volume-regulated anion channel (VRAC) in HEK293 cells by acidic di-aryl-ureas. *J Membr.Biol.* 196, 83-94
83. Klausen, T. K., Bergdahl, A., Hougaard, C., Christophersen, P., Pedersen, S. F., Hoffmann, E. K. (2007) Cell cycle-dependent activity of the volume- and Ca²⁺-activated anion currents in Ehrlich lettre ascites cells. *J Cell Physiol.* 210, 831-842
84. Namkung, W., Phuan, P. W., Verkman, A. S. (2011) TMEM16A inhibitors reveal TMEM16A as a minor component of CaCC conductance in airway and intestinal epithelial cells. *J Biol.Chem.* 286, 2365-2374
85. Preston, G. M., Carroll, T. P., Guggino, W. B., Agre, P. (1992) Appearance of water channels in *Xenopus* oocytes expressing red cell CHIP28 protein. *Science* 256, 385-387
86. Harteneck, C., Gollasch, M. (2011) Pharmacological modulation of diacylglycerol-sensitive TRPC3/6/7 channels. *Curr.Pharm.Biotechnol.* 12, 35-41
87. Harteneck, C., Frenzel, H., Kraft, R. (2007) N-(p-amylicinnamoyl)anthranilic acid (ACA): a phospholipase A(2) inhibitor and TRP channel blocker. *Cardiovasc.Drug Rev.* 25, 61-75
88. Fischer, K. G., Leipziger, J., Rubini-Illes, P., Nitschke, R., Greger, R. (1996)

- Attenuation of stimulated Ca^{2+} influx in colonic epithelial (HT₂₉) cells by cAMP. *Pflügers Arch.* 432, 735-740
89. Lee, M. Y., Song, H., Nakai, J., Ohkura, M., Kotlikoff, M. I., Kinsey, S. P., Golovina, V. A., Blaustein, M. P. (2006) Local subplasma membrane Ca^{2+} signals detected by a tethered Ca^{2+} sensor. *Proc.Natl.Acad.Sci.U.S.A.* 103, 13232-13237
 90. Nilius, B., Oike, M., Zahradnik, I., Droogmans, G. (1994) Activation of a Cl^- current by hypotonic volume increase in human endothelial cells. *J.Gen.Physiol.* 103, 787-805
 91. Ishii, T., Hashimoto, T., Ohmori, H. (1996) Hypotonic stimulation induced Ca^{2+} release from IP_3 -sensitive internal stores in a green monkey kidney cell line. *J Physiol.* 493, 371-384
 92. Mohanty, M. J., Ye, M., Li, X., Rossi, N. F. (2001) Hypotonic swelling-induced Ca^{2+} release by an $\text{IP}(3)$ -insensitive Ca^{2+} store. *Am.J Physiol Cell Physiol.* 281, C555-C562
 93. Akita, T., Okada, Y. (2011) Regulation of bradykinin-induced activation of volume-sensitive outwardly rectifying anion channels by Ca^{2+} nanodomains in mouse astrocytes. *J.Physiol.* 589, 3909-3927
 94. Berridge, M. J. (2004) Conformational coupling: a physiological calcium entry mechanism. *Sci STKE.* 2004, e33
 95. Yoo, J., Cui, Q. (2009) Curvature generation and pressure profile modulation in membrane by lysolipids: insights from coarse-grained simulations. *Biophys.J.* 97, 2267-2276
 96. Dawson, D. C., Van Driessche, W., Helman, S. I. (1988) Osmotically induced basolateral K^+ conductance in turtle colon: lidocaine-induced K^+ channel noise. *Am J Physiol.* 254, C165-C174
 97. Pedersen, S. F., Nilius, B. (2007) Transient receptor potential channels in mechanosensing and cell volume regulation. *Methods Enzymol.* 428, 183-207
 98. Lemonnier, L., Prevarskaya, N., Shuba, Y., Vanden Abeele, F., Nilius, B., Mazurier, J., Skryma, R. (2002) Ca^{2+} modulation of volume-regulated anion channels: evidence for colocalization with store-operated channels. *FASEB J.* 16, 222-224
 99. Zholos, A., Beck, B., Sydorenko, V., Lemonnier, L., Bordat, P., Prevarskaya, N., Skryma, R. (2005) Ca^{2+} - and volume-sensitive chloride currents are differentially regulated by agonists and store-operated Ca^{2+} entry. *J.Gen.Physiol.* 125, 197-211
 100. Lehtonen, J. Y., Kinnunen, P. K. (1995) Phospholipase A2 as a mechanosensor. *Biophys.J.* 68, 1888-1894

101. Yu, K., Whitlock, J. M., Lee, K., Ortlund, E. A., Yuan, C. Y., Hartzell, H. C. (2015) Identification of a lipid scrambling domain in ANO6/TMEM16F. *Elife*. 4. doi, 10
102. Pedersen, S. F., Poulsen, K. A., Lambert, I. H. (2006) Roles of phospholipase A2 isoforms in swelling- and melittin-induced arachidonic acid release and taurine efflux in NIH3T3 fibroblasts. *Am.J.Physiol Cell Physiol*. 291, C1286-C1296
103. Pedersen, S., Lambert, I. H., Thoroed, S. M., Hoffmann, E. K. (2000) Hypotonic cell swelling induces translocation of the alpha isoform of cytosolic phospholipase A2 but not the gamma isoform in Ehrlich ascites tumor cells. *Eur.J.Biochem*. 267, 5531-5539
104. Thoroed, S. M., Lauritzen, L., Lambert, I. H., Hansen, H. S., Hoffmann, E. K. (1997) Cell swelling activates phospholipase A2 in Ehrlich ascites tumor cells. *J.Membr.Biol*. 160, 47-58
105. Murakami, M., Kudo, I. (2002) Phospholipase A2. *J Biochem*. 131, 285-292
106. Bessac, B. F., Fleig, A. (2007) TRPM7 channel is sensitive to osmotic gradients in human kidney cells. *J Physiol*. 582, 1073-1086
107. Forrest, L. R., Tavoulari, S., Zhang, Y. W., Rudnick, G., Honig, B. (2007) Identification of a chloride ion binding site in Na⁺/Cl⁻-dependent transporters. *Proc.Natl.Acad.Sci U.S.A*. 104, 12761-12766
108. Cruz-Rangel, S., Gamba, G., Ramos-Mandujano, G., Pasantes-Morales, H. (2012) Influence of WNK3 on intracellular chloride concentration and volume regulation in HEK293 cells. *Pflugers Arch*. 464, 317-330
109. Shapiro, E. D. (2014) Clinical practice. Lyme disease. *N.Engl.J Med*. 370, 1724-1731
110. Stanek, G., Wormser, G. P., Gray, J., Strle, F. (2012) Lyme borreliosis. *Lancet*. 379, 461-473
111. Fallon, B. A., Nields, J. A. (1994) Lyme disease: a neuropsychiatric illness. *Am J Psychiatry*. 151, 1571-1583
112. Hess, A., Buchmann, J., Zettl, U. K., Henschel, S., Schlaefke, D., Grau, G., Benecke, R. (1999) *Borrelia burgdorferi* central nervous system infection presenting as an organic schizophrenialike disorder. *Biol Psychiatry*. 45, 795
113. Hanincova, K., Mukherjee, P., Ogden, N. H., Margos, G., Wormser, G. P., Reed, K. D., Meece, J. K., Vandermause, M. F., Schwartz, I. (2013) Multilocus sequence typing of *Borrelia burgdorferi* suggests existence of lineages with differential pathogenic properties in humans. *PLoS.ONE*. 8, e73066
114. Casjens, S. R., Mongodin, E. F., Qiu, W. G., Luft, B. J., Schutzer, S. E., Gilcrease, E.

- B., Huang, W. M., Vujadinovic, M., Aron, J. K., Vargas, L. C., Freeman, S., Radune, D., Weidman, J. F., Dimitrov, G. I., Khouri, H. M., Sosa, J. E., Halpin, R. A., Dunn, J. J., Fraser, C. M. (2012) Genome stability of Lyme disease spirochetes: comparative genomics of *Borrelia burgdorferi* plasmids. *PLoS ONE*. 7, e33280
115. Chapman, S. J., Hill, A. V. (2012) Human genetic susceptibility to infectious disease. *Nat.Rev.Genet.* 13, 175-188
116. Ribbe, K., Friedrichs, H., Begemann, M., Grube, S., Papiol, S., Kastner, A., Gerchen, M. F., Ackermann, V., Tarami, A., Treitz, A., Flogel, M., Adler, L., Aldenhoff, J. B., Becker-Emner, M., Becker, T., Czernik, A., Dose, M., Folkerts, H., Freese, R., Gunther, R., Herpertz, S., Hesse, D., Kruse, G., Kunze, H., Franz, M., Lohrer, F., Maier, W., Mielke, A., Muller-Isberner, R., Oestereich, C., Pajonk, F. G., Pollmacher, T., Schneider, U., Schwarz, H. J., Kroner-Herwig, B., Havemann-Reinecke, U., Frahm, J., Stuhmer, W., Falkai, P., Brose, N., Nave, K. A., Ehrenreich, H. (2010) The cross-sectional GRAS sample: a comprehensive phenotypical data collection of schizophrenic patients. *BMC.Psychiatry*. 10, 91-10
117. Hammer, C., Stepniak, B., Schneider, A., Papiol, S., Tantra, M., Begemann, M., Siren, A. L., Pardo, L. A., Sperling, S., Mohd, J. S., Gurvich, A., Jensen, N., Ostmeier, K., Luhder, F., Probst, C., Martens, H., Gillis, M., Saher, G., Assogna, F., Spalletta, G., Stocker, W., Schulz, T. F., Nave, K. A., Ehrenreich, H. (2014) Neuropsychiatric disease relevance of circulating anti-NMDA receptor autoantibodies depends on blood-brain barrier integrity. *Mol.Psychiatry*. 19, 1143-1149
118. Begemann, M., Grube, S., Papiol, S., Malzahn, D., Krampe, H., Ribbe, K., Friedrichs, H., Radyushkin, K. A., El Kordi, A., Benseler, F., Hannke, K., Sperling, S., Schwerdtfeger, D., Thanhauser, I., Gerchen, M. F., Ghorbani, M., Gutwinski, S., Hilmes, C., Leppert, R., Ronnenberg, A., Sowislo, J., Stawicki, S., Stodtke, M., Szuszies, C., Reim, K., Riggert, J., Eckstein, F., Falkai, P., Bickeboller, H., Nave, K. A., Brose, N., Ehrenreich, H. (2010) Modification of cognitive performance in schizophrenia by complexin 2 gene polymorphisms. *Arch Gen.Psychiatry*. 67, 879-888
119. Franke, G. H. (2000) Brief Symptom Inventory. Göttingen. *Beltz*
120. Yang, J., Lee, S. H., Goddard, M. E., Visscher, P. M. (2011) GCTA: a tool for genome-wide complex trait analysis. *Am J Hum.Genet.* 88, 76-82
121. Purcell, S., Neale, B., Todd-Brown, K., Thomas, L., Ferreira, M. A., Bender, D., Maller, J., Sklar, P., de Bakker, P. I., Daly, M. J., Sham, P. C. (2007) PLINK: a tool set for whole-genome association and population-based linkage analyses. *Am J Hum.Genet.* 81, 559-575
122. Abecasis, G. R., Auton, A., Brooks, L. D., DePristo, M. A., Durbin, R. M., Handsaker, R. E., Kang, H. M., Marth, G. T., McVean, G. A. (2012) An integrated map of genetic

- variation from 1,092 human genomes. *Nature*. 491, 56-65
123. Zoghbi, H. Y., Orr, H. T. (2009) Pathogenic mechanisms of a polyglutamine-mediated neurodegenerative disease, spinocerebellar ataxia type 1. *J Biol Chem*. 284, 7425-7429
 124. Chamova, T., Florez, L., Guergueltcheva, V., Raycheva, M., Kaneva, R., Lochmuller, H., Kalaydjieva, L., Tournev, I. (2012) ANO10 c.1150_1151del is a founder mutation causing autosomal recessive cerebellar ataxia in Roma/Gypsies. *J Neurol*. 259, 906-911
 125. Schwab, A., Fabian, A., Hanley, P. J., Stock, C. (2012) Role of ion channels and transporters in cell migration. *Physiol Rev*. 92, 1865-1913
 126. Gosling, M., Poyner, D. R., Smith, J. W. (1996) Effects of arachidonic acid upon the volume-sensitive chloride current in rat osteoblast-like (ROS 17/2.8) cells. *J.Physiol*. 493, 613-623
 127. Wu, X., Yang, H., Iserovich, P., Fischbarg, J., Reinach, P. S. (1997) Regulatory volume decrease by SV40-transformed rabbit corneal epithelial cells requires ryanodine-sensitive Ca²⁺-induced Ca²⁺ release. *J Membr.Biol*. 158, 127-136
 128. Berende, A., Oosting, M., Kullberg, B. J., Netea, M. G., Joosten, L. A. (2010) Activation of innate host defense mechanisms by *Borrelia*. *Eur.Cytokine Netw*. 21, 7-18
 129. Steere, A. C., Coburn, J., Glickstein, L. (2004) The emergence of Lyme disease. *J Clin.Invest*. 113, 1093-1101
 130. Arav-Boger, R., Crawford, T., Steere, A. C., Halsey, N. A. (2002) Cerebellar ataxia as the presenting manifestation of Lyme disease. *Pediatr.Infect.Dis.J*. 21, 353-356
 131. Horne, D. J., Randhawa, A. K., Chau, T. T., Bang, N. D., Yen, N. T., Farrar, J. J., Dunstan, S. J., Hawn, T. R. (2012) Common polymorphisms in the PKP3-SIGIRR-TMEM16J gene region are associated with susceptibility to tuberculosis. *J Infect.Dis*. 205, 586-594
 132. Bowman, A. B., Lam, Y. C., Jafar-Nejad, P., Chen, H. K., Richman, R., Samaco, R. C., Fryer, J. D., Kahle, J. J., Orr, H. T., Zoghbi, H. Y. (2007) Duplication of *Atxn11* suppresses SCA1 neuropathology by decreasing incorporation of polyglutamine-expanded ataxin-1 into native complexes. *Nat.Genet*. 39, 373-379
 133. Dehnert, M., Fingerle, V., Klier, C., Talaska, T., Schlaud, M., Krause, G., Wilking, H., Poggensee, G. (2012) Seropositivity of Lyme borreliosis and associated risk factors: a population-based study in Children and Adolescents in Germany (KiGGS). *PLoS.ONE*. 7, e41321

134. Pachner, A. R. (1988) *Borrelia burgdorferi* in the nervous system: the new "great imitator". *Ann.N.Y.Acad.Sci.* 539, 56-64
135. Bartha, I., Carlson, J. M., Brumme, C. J., McLaren, P. J., Brumme, Z. L., John, M., Haas, D. W., Martinez-Picado, J., Dalmau, J., Lopez-Galindez, C., Casado, C., Rauch, A., Gunthard, H. F., Bernasconi, E., Vernazza, P., Klimkait, T., Yerly, S., O'Brien, S. J., Listgarten, J., Pfeifer, N., Lippert, C., Fusi, N., Kutalik, Z., Allen, T. M., Muller, V., Harrigan, P. R., Heckerman, D., Telenti, A., Fellay, J. (2013) A genome-to-genome analysis of associations between human genetic variation, HIV-1 sequence diversity, and viral control. *Elife.* 2, e01123
136. Liveris, D., Schwartz, I., Bittker, S., Cooper, D., Iyer, R., Cox, M. E., Wormser, G. P. (2011) Improving the yield of blood cultures from patients with early Lyme disease. *J Clin.Microbiol.* 49, 2166-2168
137. Chien, L. T., Zhang, Z. R., Hartzell, H. C. (2006) Single Cl⁻ channels activated by Ca²⁺ in *Drosophila* S2 cells are mediated by bestrophins. *J Gen.Physiol.* 128, 247-259
138. Fischmeister, R., Hartzell, H. C. (2005) Volume sensitivity of the bestrophin family of chloride channels. *J.Physiol* 562, 477-491
139. Kunzelmann, K., Kongsuphol, P., Chootip, K., Toledo, C., Martins, J. R., Almaca, J., Tian, Y., Witzgall, R., Ousingsawat, J., Schreiber, R. (2011) Role of the Ca(2+)-activated Cl(-) channels bestrophin and anoctamin in epithelial cells. *Biol Chem.* 392, 125-134
140. Stohr, H., Marquardt, A., Nanda, I., Schmid, M., Weber, B. H. (2002) Three novel human VMD2-like genes are members of the evolutionary highly conserved RFP-TM family. *Eur.J.Hum.Genet.* 10, 281-284
141. Marquardt, A., Stohr, H., Passmore, L. A., Kramer, F., Rivera, A., Weber, B. H. (1998) Mutations in a novel gene, VMD2, encoding a protein of unknown properties cause juvenile-onset vitelliform macular dystrophy (Best's disease). *Hum.Mol.Genet.* 7, 1517-1525
142. Petrukhin, K., Koisti, M. J., Bakall, B., Li, W., Xie, G., Marknell, T., Sandgren, O., Forsman, K., Holmgren, G., Andreasson, S., Vujic, M., Bergen, A. A., McGarty-Dugan, V., Figueroa, D., Austin, C. P., Metzker, M. L., Caskey, C. T., Wadelius, C. (1998) Identification of the gene responsible for Best macular dystrophy. *Nat.Genet.* 19, 241-247
143. Mohler, C. W., Fine, S. L. (1981) Long-term evaluation of patients with Best's vitelliform dystrophy. *Ophthalmology* 88, 688-692
144. Cross, H. E., Bard, L. (1974) Electro-oculography in Best's macular dystrophy.

- Am.J.Ophthalmol.* 77, 46-50
145. Neussert, R., Muller, C., Milenkovic, V. M., Strauss, O. (2010) The presence of bestrophin-1 modulates the Ca(2+) recruitment from Ca (2+) stores in the ER. *Pflugers Arch.* 460, 163-175
 146. Lee, S., Yoon, B. E., Berglund, K., Oh, S. J., Park, H., Shin, H. S., Augustine, G. J., Lee, C. J. (2010) Channel-mediated tonic GABA release from glia. *Science.* 330, 790-796
 147. Woo, D. H., Han, K. S., Shim, J. W., Yoon, B. E., Kim, E., Bae, J. Y., Oh, S. J., Hwang, E. M., Marmorstein, A. D., Bae, Y. C., Park, J. Y., Lee, C. J. (2012) TREK-1 and Best1 Channels Mediate Fast and Slow Glutamate Release in Astrocytes upon GPCR Activation. *Cell.* 151, 25-40
 148. Kramer, F., Stohr, H., Weber, B. H. (2004) Cloning and characterization of the murine Vmd2 RFP-TM gene family. *Cytogenet.Genome Res.* 105, 107-114
 149. Singh, R., Shen, W., Kuai, D., Martin, J. M., Guo, X., Smith, M. A., Perez, E. T., Phillips, M. J., Simonett, J. M., Wallace, K. A., Verhoeven, A. D., Capowski, E. E., Zhang, X., Yin, Y., Halbach, P. J., Fishman, G. A., Wright, L. S., Pattnaik, B. R., Gamm, D. M. (2013) iPS cell modeling of Best disease: insights into the pathophysiology of an inherited macular degeneration. *Hum.Mol.Genet.* 22, 593-607
 150. Stotz, S. C., Clapham, D. E. (2012) Anion-sensitive fluorophore identifies the Drosophila swell-activated chloride channel in a genome-wide RNA interference screen. *PLoS.ONE.* 7, e46865
 151. Chien, L. T., Hartzell, H. C. (2008) Rescue of volume-regulated anion current by bestrophin mutants with altered charge selectivity. *J Gen.Physiol.* 132, 537-546
 152. Kaestner, K. H., Montoliu, L., Kern, H., Thulke, M., Schutz, G. (1994) Universal beta-galactosidase cloning vectors for promoter analysis and gene targeting. *Gene* 148, 67-70
 153. Swiatek, P. J., Gridley, T. (1993) Perinatal lethality and defects in hindbrain development in mice homozygous for a targeted mutation of the zinc finger gene Krox20. *Genes Dev.* 7, 2071-2084
 154. Schrewe, H., Gendron-Maguire, M., Harbison, M. L., Gridley, T. (1994) Mice homozygous for a null mutation of activin beta B are viable and fertile. *Mech.Dev.* 47, 43-51
 155. Weber, B. H., Lin, B., White, K., Kohler, K., Soboleva, G., Herterich, S., Seeliger, M. W., Jaissle, G. B., Grimm, C., Reme, C., Wenzel, A., Asan, E., Schrewe, H. (2002) A

156. Gomez, N. M., Tamm, E. R., Straubeta, O. (2013) Role of bestrophin-1 in store-operated calcium entry in retinal pigment epithelium. *Pflugers Arch.* 465, 481-495
157. Prusky, G. T., Alam, N. M., Beekman, S., Douglas, R. M. (2004) Rapid quantification of adult and developing mouse spatial vision using a virtual optomotor system. *Invest Ophthalmol. Vis. Sci.* 45, 4611-4616
158. Lepage, G., Roy, C. C. (1986) Direct transesterification of all classes of lipids in a one-step reaction. *J. Lipid Res.* 27, 114-120
159. Toyoda, Y., Chang, M. C. (1974) Fertilization of rat eggs in vitro by epididymal spermatozoa and the development of eggs following transfer. *J. Reprod. Fertil.* 36, 9-22
160. Bjorndahl, L., Soderlund, I., Kvist, U. (2003) Evaluation of the one-step eosin-nigrosin staining technique for human sperm vitality assessment. *Hum. Reprod.* 18, 813-816
161. Mortimer, D., Curtis, E. F., Miller, R. G. (1987) Specific labelling by peanut agglutinin of the outer acrosomal membrane of the human spermatozoon. *J. Reprod. Fertil.* 81, 127-135
162. Mortimer, S. T. (2000) CASA--practical aspects. *J. Androl* 21, 515-524
163. Kongsuphol, P., Schreiber, R., Kraidth, K., Kunzelmann, K. (2011) CFTR induces extracellular acid sensing in *Xenopus* oocytes which activates endogenous Ca(2+)-activated Cl (-) conductance. *Pflugers Arch.* 462, 479-487
164. Ackerman, M. J., Wickman, K. D., Clapham, D. E. (1994) Hypotonicity activates a native chloride current in *Xenopus* oocytes. *J. Gen. Physiol.* 103, 153-179
165. Ren, D., Navarro, B., Perez, G., Jackson, A. C., Hsu, S., Shi, Q., Tilly, J. L., Clapham, D. E. (2001) A sperm ion channel required for sperm motility and male fertility. *Nature* 413, 603-609
166. Xu, W. M., Shi, Q. X., Chen, W. Y., Zhou, C. X., Ni, Y., Rowlands, D. K., Liu, G. Y., Zhu, H., Ma, Z. G., Wang, X. F., Chen, Z. H., Zhou, S. C., Dong, H. S., Zhang, X. H., Chung, Y. W., Yuan, Y. Y., Yang, W. X., Chan, H. C. (2007) Cystic fibrosis transmembrane conductance regulator is vital to sperm fertilizing capacity and male fertility. *Proc. Natl. Acad. Sci. U.S.A.* .,
167. Darszon, A., Acevedo, J. J., Galindo, B. E., Hernandez-Gonzalez, E. O., Nishigaki, T., Trevino, C. L., Wood, C., Beltran, C. (2006) Sperm channel diversity and functional multiplicity. *Reproduction.* 131, 977-988
168. Cocquet, J., Ellis, P. J., Yamauchi, Y., Riel, J. M., Karaacs, T. P., Rattigan, A., Ojarikre, O. A., Affara, N. A., Ward, M. A., Burgoyne, P. S. (2010) Deficiency in the multicopy

- Sycp3-like X-linked genes *Slx* and *Slx11* causes major defects in spermatid differentiation. *Mol.Biol.Cell* 21, 3497-3505
169. O'Shaughnessy, P. J., Fleming, L., Baker, P. J., Jackson, G., Johnston, H. (2003) Identification of developmentally regulated genes in the somatic cells of the mouse testis using serial analysis of gene expression. *Biol.Reprod.* 69, 797-808
170. Yeung, C. H., Sonnenberg-Riethmacher, E., Cooper, T. G. (1998) Receptor tyrosine kinase *c-ros* knockout mice as a model for the study of epididymal regulation of sperm function. *J.Reprod.Fertil.Suppl* 53, 137-147
171. Yeung, C. H., Sonnenberg-Riethmacher, E., Cooper, T. G. (1999) Infertile spermatozoa of *c-ros* tyrosine kinase receptor knockout mice show flagellar angulation and maturational defects in cell volume regulatory mechanisms. *Biol.Reprod.* 61, 1062-1069
172. Joseph, A., Shur, B. D., Ko, C., Chambon, P., Hess, R. A. (2010) Epididymal hypo-osmolality induces abnormal sperm morphology and function in the estrogen receptor alpha knockout mouse. *Biol.Reprod.* 82, 958-967
173. Yeung, C. H., Anapolski, M., Sipila, P., Wagenfeld, A., Poutanen, M., Huhtaniemi, I., Nieschlag, E., Cooper, T. G. (2002) Sperm volume regulation: maturational changes in fertile and infertile transgenic mice and association with kinematics and tail angulation. *Biol.Reprod.* 67, 269-275
174. Navarro, B., Miki, K., Clapham, D. E. (2011) ATP-activated P2X2 current in mouse spermatozoa. *Proc.Natl.Acad.Sci.U.S.A* 108, 14342-14347
175. Morin, X. K., Bond, T. D., Loo, T. W., Clarke, D. M., Bear, C. E. (1995) Failure of P-glycoprotein (MDR1) expressed in *Xenopus* oocytes to produce swelling-activated chloride channel activity. *J Physiol.* 486, 707-714
176. de la Fuente, R., Namkung, W., Mills, A., Verkman, A. S. (2007) Small molecule screen identifies inhibitors of a human intestinal calcium activated chloride channel. *Mol Pharmacol.* 73, 758-768
177. Johnson, A. A., Lee, Y. S., Stanton, J. B., Yu, K., Hartzell, C. H., Marmorstein, L. Y., Marmorstein, A. D. (2013) Differential effects of Best disease causing missense mutations on bestrophin-1 trafficking. *Hum.Mol.Genet.* 22, 4688-4697
178. Brandl, C., Zimmermann, S. J., Milenkovic, V. M., Rosendahl, S. M., Grassmann, F., Milenkovic, A., Hehr, U., Federlin, M., Wetzel, C. H., Helbig, H., Weber, B. H. (2014) In-depth characterisation of Retinal Pigment Epithelium (RPE) cells derived from human induced pluripotent stem cells (hiPSC). *Neuromolecular.Med.* 16, 551-564
179. Anderson, J. W., Jirsch, J. D., Fedida, D. (1995) Cation regulation of anion current

- activated by cell swelling in two types of human epithelial cancer cells. *J Physiol.* 483, 549-557
180. Kunzelmann, K., Milenkovic, V. M., Spitzner, M., Barro Soria, R., Schreiber, R. (2007) Calcium dependent chloride conductance in epithelia: Is there a contribution by Bestrophin? *Pflügers Arch* 454, 879-889
181. Milenkovic, V. M., Rohrl, E., Weber, B. H., Strauss, O. (2011) Disease-associated missense mutations in bestrophin-1 affect cellular trafficking and anion conductance. *J.Cell Sci.* 124, 2988-2996
182. Kirichok, Y., Lishko, P. V. (2011) Rediscovering sperm ion channels with the patch-clamp technique. *Mol.Hum.Reprod.* 17, 478-499
183. Zeng, X. H., Yang, C., Kim, S. T., Lingle, C. J., Xia, X. M. (2011) Deletion of the Slo3 gene abolishes alkalization-activated K⁺ current in mouse spermatozoa. *Proc.Natl.Acad.Sci.U.S.A* 108, 5879-5884
184. Cooper, T. G. (2011) The epididymis, cytoplasmic droplets and male fertility. *Asian J.Androl* 13, 130-138
185. Ramoz, N., Rueda, L. A., Bouadjar, B., Montoya, L. S., Orth, G., Favre, M. (2002) Mutations in two adjacent novel genes are associated with epidermodysplasia verruciformis. *Nat.Genet.* 32, 579-581
186. Keresztes, G., Mutai, H., Heller, S. (2003) TMC and EVER genes belong to a larger novel family, the TMC gene family encoding transmembrane proteins. *BMC.Genomics.* 4, 24
187. Billig, G. M., Pál, B., Fidzinski, P., Jentsch, T. J. (2011) Ca²⁺-activated Cl⁻ currents are dispensable for olfaction. *Nature neurosc.* 14, 763-769
188. Schreiber, R., Uliyakina, I., Kongsuphol, P., Warth, R., Mirza, M., Martins, J. R., Kunzelmann, K. (2010) Expression and Function of Epithelial Anoctamins. *J.Biol.Chem.* 285, 7838-7845
189. Suzuki, J., Fujii, T., Imao, T., Ishihara, K., Kuba, H., Nagata, S. (2013) Calcium-dependent Phospholipid Scramblase Activity of TMEM16 Family Members. *J Biol Chem.* 288, 13305-13316
190. Duvvuri, U., Shiwarski, D. J., Xiao, D., Bertrand, C., Huang, X., Edinger, R. S., Rock, J. R., Harfe, B. D., Henson, B. J., Kunzelmann, K., Schreiber, R., Seethala, R. R., Egloff, A. M., Chen, X., Lui, V. W., Grandis, J. R., Gollin, S. M. (2012) TMEM16A, induces MAPK and contributes directly to tumorigenesis and cancer progression. *Cancer Res.* 72, 3270-3281

191. Shiwarski, D. J., Shao, C., Bill, A., Kim, J., Xiao, D., Bertrand, C., Seethala, R. R., Sano, D., Myers, J. N., Ha, P. K., Grandis, J. R., Gaither, L. A., Puthenveedu, M. A., Duvvuri, U. (2014) To "Grow" or "Go": TMEM16A Expression as a Switch between Tumor Growth and Metastasis in SCCHN. *Clin.Cancer Res.* 20, 4673-4688
192. Berglund, E., Akcakaya, P., Berglund, D., Karlsson, F., Vukojevic, V., Lee, L., Bogdanovic, D., Lui, W. O., Larsson, C., Zedenius, J., Frobom, R., Branstrom, R. (2014) Functional role of the Ca-activated Cl channel DOG1/TMEM16A in gastrointestinal stromal tumor cells. *Exp.Cell Res.* 326, 315-325
193. Wanitchakool, P., Wolf, L., Koehl, G., Sirianant, L., Gaumann, A., Schreiber, R., Duvvuri, U., Kunzelmann, K. (2014) Role of Anoctamins in Cancer and Apoptosis. *Philos Trans R Soc Lond B Biol Sci* 369, 20130096
194. Ruiz, C., Martins, J. R., Rudin, F., Schneider, S., Dietsche, T., Fischer, C. A., Tornillo, L., Terracciano, L. M., Schreiber, R., Bubendorf, L., Kunzelmann, K. (2012) Enhanced Expression of ANO1 in Head and Neck Squamous Cell Carcinoma Causes Cell Migration and Correlates with Poor Prognosis. *PLoS.ONE.* 7, e43265
195. Bisht, M., Bist, S. S. (2011) Human papilloma virus: a new risk factor in a subset of head and neck cancers. *J Cancer Res.Ther.* 7, 251-255
196. Chaudhary, A. K., Singh, M., Sundaram, S., Mehrotra, R. (2009) Role of human papillomavirus and its detection in potentially malignant and malignant head and neck lesions: updated review. *Head Neck Oncol.* 25, 1-22
197. Liang, C., Marsit, C. J., McClean, M. D., Nelson, H. H., Christensen, B. C., Haddad, R. I., Clark, J. R., Wein, R. O., Grillone, G. A., Houseman, E. A., Halec, G., Waterboer, T., Pawlita, M., Krane, J. F., Kelsey, K. T. (2012) Biomarkers of HPV in Head and Neck Squamous Cell Carcinoma. *Cancer Res.* 72, 5004-5013
198. Lazarczyk, M., Dalard, C., Hayder, M., Dupre, L., Pignolet, B., Majewski, S., Vuillier, F., Favre, M., Liblau, R. S. (2012) EVER Proteins, Key Elements of the Natural Anti-Human Papillomavirus Barrier, Are Regulated upon T-Cell Activation. *PLoS.ONE.* 7, e39995
199. Mullen, D. L., Silverberg, S. G., Penn, I., Hammond, W. S. (1976) Squamous cell carcinoma of the skin and lip in renal homograft recipients. *Cancer.* 37, 729-734
200. Qin, Y., Dittmer, P. J., Park, J. G., Jansen, K. B., Palmer, A. E. (2011) Measuring steady-state and dynamic endoplasmic reticulum and Golgi Zn²⁺ with genetically encoded sensors. *Proc.Natl.Acad.Sci U.S.A.* 108, 7351-7356
201. Akita, T., Fedorovich, S. V., Okada, Y. (2011) Ca²⁺ nanodomain-mediated component of swelling-induced volume-sensitive outwardly rectifying anion current triggered by

- autocrine action of ATP in mouse astrocytes. *Cell Physiol Biochem.* 28, 1181-1190
202. Kruczek, C., Gorg, B., Keitel, V., Pirev, E., Kronke, K. D., Schliess, F., Haussinger, D. (2009) Hypoosmotic swelling affects zinc homeostasis in cultured rat astrocytes. *Glia.* 57, 79-92
203. Stork, C. J., Li, Y. V. (2010) Zinc release from thapsigargin/IP3-sensitive stores in cultured cortical neurons. *J Mol.Signal.* 5, 5
204. Britschgi, A., Bill, A., Brinkhaus, H., Rothwell, C., Clay, I., Duss, S., Rebhan, M., Raman, P., Guy, C. T., Wetzell, K., George, E., Popa, M. O., Lilley, S., Choudhury, H., Gosling, M., Wang, L., Fitzgerald, S., Borawski, J., Baffoe, J., Labow, M., Gaither, L. A., Bentires-Alj, M. (2013) Calcium-activated chloride channel ANO1 promotes breast cancer progression by activating EGFR and CAMK signaling. *Proc.Natl.Acad.Sci U.S.A.* 110, E1026-E1034
205. Zhao, P., Torcaso, A., Mariano, A., Xu, L., Mohsin, S., Zhao, L., Han, R. (2014) Anoctamin 6 Regulates C2C12 Myoblast Proliferation. *PLoS.ONE.* 9, e92749
206. zur, H. H. (1991) Human papillomaviruses in the pathogenesis of anogenital cancer. *Virology.* 184, 9-13
207. Abdullaev, I. F., Sabirov, R. Z., Okada, Y. (2003) Upregulation of swelling-activated Cl⁻ channel sensitivity to cell volume by activation of EGF receptors in murine mammary cells. *J Physiol.* 549, 749-758
208. Kraft, R., Grimm, C., Frenzel, H., Harteneck, C. (2006) Inhibition of TRPM2 cation channels by N-(p-amylcinnamoyl)anthranilic acid. *Br.J Pharmacol.* 148, 264-273
209. Iscla, I., Blount, P. (2012) Sensing and responding to membrane tension: the bacterial MscL channel as a model system. *Biophys.J.* 103, 169-174
210. Shi, X. L., Wang, G. L., Zhang, Z., Liu, Y. J., Chen, J. H., Zhou, J. G., Qiu, Q. Y., Guan, Y. Y. (2007) Alteration of volume-regulated chloride movement in rat cerebrovascular smooth muscle cells during hypertension. *Hypertension* 49, 1371-1377
211. He, D., Luo, X., Wei, W., Xie, M., Wang, W., Yu, Z. (2012) DCPIB, a specific inhibitor of volume-regulated anion channels (VRACs), inhibits astrocyte proliferation and cell cycle progression via G1/S arrest. *J Mol.Neurosci.* 46, 249-257
212. Wondergem, R., Gong, W., Monen, S. H., Dooley, S. N., Gonce, J. L., Conner, T. D., Houser, M., Ecay, T. W., Ferslew, K. E. (2001) Blocking swelling-activated chloride current inhibits mouse liver cell proliferation. *J Physiol* 532, 661-672
213. Underhill, D. M., Bassetti, M., Rudensky, A., Aderem, A. (1999) Dynamic interactions

- of macrophages with T cells during antigen presentation. *J Exp.Med.* 190, 1909-1914
214. Okada, Y., Maeno, E., Shimizu, T., Manabe, K., Mori, S., Nabekura, T. (2004) Dual roles of plasmalemmal chloride channels in induction of cell death. *Pflugers Arch* 448, 287-295
215. Shimizu, T., Numata, T., Okada, Y. (2004) A role of reactive oxygen species in apoptotic activation of volume-sensitive Cl(-) channel. *Proc.Natl.Acad.Sci.U.S.A.* 101, 6770-6773
216. Okada, Y., Shimizu, T., Maeno, E., Tanabe, S., Wang, X., Takahashi, N. (2006) Volume-sensitive chloride channels involved in apoptotic volume decrease and cell death. *J Membr.Biol.* 209, 21-29
217. Lazarczyk, M., Favre, M. (2008) Role of Zn²⁺ ions in host-virus interactions. *J.Virol.* 82, 11486-11494
218. Yamasaki, S., Sakata-Sogawa, K., Hasegawa, A., Suzuki, T., Kabu, K., Sato, E., Kurosaki, T., Yamashita, S., Tokunaga, M., Nishida, K., Hirano, T. (2007) Zinc is a novel intracellular second messenger. *J.Cell Biol.* 177, 637-645
219. Barbosa, M. S., Lowy, D. R., Schiller, J. T. (1989) Papillomavirus polypeptides E6 and E7 are zinc-binding proteins. *J.Virol.* 63, 1404-1407
220. Barbosa,M.S.,Schlegel,R.(1989)The E6 and E7 genes of HPV-18 are sufficient for inducing two-stage in vitro transformation of human keratinocytes.*Oncogene* 4,1529-1532

ACKNOWLEDGEMENTS

Firstly, I would like to express my sincere gratitude to my advisor Prof. Dr. Karl Kunzelmann for the continuous support of my Ph.D study and related research, for his patience, motivation, and immense knowledge. His guidance helped me in all the time of research and writing of this thesis. I could not have imagined having a better advisor for my Ph.D study.

Besides my advisor, I would like to thank Prof. Dr. Rainer Schreiber for his insightful comments, encouragement, and grateful helps. I would also like to thank Dr. Jiraporn Ousingsawat for her kindness. It is whole-heartedly expressed that your advices for everything proved to be a landmark effort towards the success of my Ph.D. life. I don't know if I can make it this far without you. Special thanks to our lovely technicians Tini, Brigitte, and Patricia, their supports made our lives easier in every way. I sincerely thank all my labmates particularly Kip, Ines, and Robie for all the fun we have had in the last year. Having all of you in the lab made my life more enjoyable (even though sometimes I find it a bit too much). Besides the fun we had at our setups, I would like to thank Robie again for all her help during thesis preparations. I would like to show my gratitude to all the grants that support my present work: DFG SFB699-A7/A12, DFG KU756/12-1, Sander-Stiftung 2013.031.1 and Volkswagenstiftung AZ 87 499

Last but not the least, I am deeply thankful to my precious family: my parents and my sister for their love, support and encouragement. I would never become the person I am today without all of you in my life.

Sirianant Lalida

ERKLÄRUNGEN**Erklärung:**

Hiermit erkläre ich, gem. § 6 Abs. 2, Nr. 6 der Promotionsordnung der Math.-Nat.-
Fachbereiche zur Erlangung des Dr. rer. nat., dass ich die vorliegende Dissertation
selbständig verfasst und mich keiner anderen als der angegebenen Hilfsmittel
bedient habe.

Regensburg, den 09.12.15

Sirianant Lalida

Curriculum Vitae

PERSONAL INFORMATION

Name Miss Lalida Sirianant
Date of birth February 2nd, 1985
Nationality Thai
Current address Hochweg 56A, Regensburg, 93049, Germany
Email lalida@live.com, lalida.sirianant@vkl.uni-regensburg.de

EDUCATIONS

2012 - present Ph.D., Faculty of Natural Sciences III: Biology and Preclinical Medicine, University of Regensburg, Germany
2007 - 2010 M.Sc. (Toxicology), Toxicology Graduate Program, Faculty of Science, Mahidol University, Thailand.
2003 – 2006 B.Sc. (Biology), Department of Biology, Faculty of Science, Mahidol University, Thailand.

RESEARCH EXPERIENCES

2009 -2010 Visiting student, Graduate School of Frontier Biosciences, Osaka University, Japan (Scholarship from Japanese Student Service Organization: JASSO)
2011 – 2012 Research assistant, Department of Physiology, Faculty of Science, Mahidol University, Thailand

PUBLICATIONS

1. Kunzelmann K, Cabrita I, Wanitchakool P, Ousingsawat J, **Sirianant L**, Benedetto R, Schreiber R. Modulating Ca²⁺ signals: a common theme for TMEM16, Ist2, and TMC. *Pflugers Arch.* 2015 Dec 23.
2. **Sirianant L**, Ousingsawat J, Wanitchakool P, Schreiber R, Kunzelmann K. Cellular volume regulation by anoctamin 6:Ca²⁺, phospholipase A₂ and osmosensing. *Pflugers*

Arch. 2015 Oct 6.

3. Milenkovic A, Brandl C, Milenkovic VM, Jendryke T, **Sirianant L**, Wanitchakool P, Zimmermann S, Reiff CM, Horling F, Schrewe H, Schreiber R, Kunzelmann K, Wetzel CH, Weber BH. Bestrophin 1 is indispensable for volume regulation in human retinal pigment epithelium cells. *Proc Natl Acad Sci U S A.* 2015 May 19;112(20):E2630-9.
4. Botelho HM, Uliyakina I, Awatade NT, Proença MC, Tischer C, **Sirianant L**, Kunzelmann K, Pepperkok R, Amaral MD. Protein traffic disorders: an effective high-throughput fluorescence microscopy pipeline for drug discovery. *Sci Rep.* 2015 Mar 12;5:9038.
5. Hammer C, Wanitchakool P, **Sirianant L**, Papiol S, Monnheim M, Faria D, Ousingsawat J, Schramek N, Schmitt C, Margos G, Michel A, Kraiczky P, Pawlita M, Schreiber R, Schulz TF, Fingerle V, Tumani H, Ehrenreich H, Kunzelmann K. A Coding Variant of ANO10, Affecting Volume Regulation of Macrophages, Is Associated with Borrelia Seropositivity. *Mol Med.* 2015 Feb 23;21:26-37.
6. **Sirianant L**, Ousingsawat J, Tian Y, Schreiber R, Kunzelmann K. TMC8 (EVER2) attenuates intracellular signaling by Zn²⁺ and Ca²⁺ and suppresses activation of Cl⁻ currents. *Cell Signal.* 2014 Dec;26(12):2826-33.
7. Schurek EM, Völker LA, Tax J, Lamkemeyer T, Rinschen MM, Ungruue D, Kratz JE 3rd, **Sirianant L**, Kunzelmann K, Chalfie M, Schermer B, Benzing T, Höhne M. A disease-causing mutation illuminates the protein membrane topology of the kidney-expressed prohibitin homology (PHB) domain protein podocin. *J Biol Chem.* 2014 Apr 18;289(16):11262-71.
8. Wanitchakool P, Wolf L, Koehl GE, **Sirianant L**, Schreiber R, Kulkarni S, Duvvuri U, Kunzelmann K. Role of anoctamins in cancer and apoptosis. *Philos Trans R Soc Lond B Biol Sci.* 2014 Feb 3;369(1638):20130096.
9. Almaça J, Faria D, Sousa M, Uliyakina I, Conrad C, **Sirianant L**, Clarke LA, Martins JP, Santos M, Heriché JK, Huber W, Schreiber R, Pepperkok R, Kunzelmann K, Amaral MD. High-content siRNA screen reveals global ENaC regulators and potential cystic fibrosis

- therapy targets. *Cell*. 2013 Sep 12;154(6):1390-400.
10. Kunzelmann K, Nilius B, Owsianik G, Schreiber R, Ousingsawat J, **Sirianant L**, Wanitchakool P, Bevers EM, Heemskerk JW. Molecular functions of anoctamin 6 (TMEM16F): a chloride channel, cation channel, or phospholipid scramblase? *Pflugers Arch*. 2014 Mar;466(3):407-14.
 11. Rahmati N, Kunzelmann K, Xu J, Barone S, **Sirianant L**, De Zeeuw CI, Soleimani M. 10. Slc26a11 is prominently expressed in the brain and functions as a chloride channel: expression in Purkinje cells and stimulation of V H⁺-ATPase. *Pflugers Arch*. 2013 Nov;465(11):1583-97.
 12. Muanprasat C, **Sirianant L**, Sawasvirojwong S, Homvisasevongsa S, Suksamrarn A, Chatsudthipong V. Activation of AMP-activated protein kinase by a plant-derived dihydroisosteviol in human intestinal epithelial cell. *Biol Pharm Bull*. 2013;36(4):522-8.
 13. Muanprasat C, **Sirianant L**, Soodvilai S, Chokchaisiri R, Suksamrarn A, Chatsudthipong V. Novel action of the chalcone isoliquiritigenin as a cystic fibrosis transmembrane conductance regulator (CFTR) inhibitor: potential therapy for cholera and polycystic kidney disease. *J Pharmacol Sci*. 2012;118(1):82-91.
 14. Wongsamitkul N, **Sirianant L**, Muanprasat C, Chatsudthipong V. A plant-derived hydrolysable tannin inhibits CFTR chloride channel: a potential treatment of diarrhea. *Pharm Res*. 2010 Mar;27(3):490-7

